Geochemistry of the Tussaap Ultramafic Complex, Southern West Greenland

By

Timothy McIntyre

A thesis submitted in partial fulfillment of the requirements for the degree

Master of Science

Department of Earth and Atmospheric Sciences

University of Alberta

Abstract

The Tussaap ultramafic complex (TUC) is located within the ~3.65 to 3.81 Ga Itsaq Gneiss complex of southern West Greenland. The TUC is part of numerous ultramafic enclaves in the Itsaq Gneiss complex that are thought to predate the gneisses. Some of these enclaves have been interpreted as lithospheric mantle material while others are interpreted as layered cumulates. In this study, measurements of mineral chemistry and whole rock major-, trace-, and platinum-group-element abundances of the previously unstudied TUC were used to evaluate its origin as cumulate or residual mantle material. Rhenium-Os isotopic systematics were used to place chronological constraints on the enclave.

The TUC comprises dunites, ol-clinopyroxenites, amphibolites, and hornblende gabbros. The mineral chemistry of the TUC largely reflects secondary processes, and, where possibly shielded from these processes, show no indication of partial melting. The whole-rock FeO contents of the dunites are high, up to 15.5 wt%, and with variable iridium group platinum group elements (IPGE: Os, Ir, and Ru) are not consistent with a depleted mantle origin for the rocks. Inter-element variations in major- and trace-element geochemistry of the TUC fit well with fractional crystallization models. In such models the dunites are explicable as olivine and chromite cumulates, the ol-clinopyroxenites as clinopyroxene, olivine, and chromite cumulates, the amphibolites as clinopyroxene and Cr-magnetite cumulates, and the hornblende gabbros as crystallized melts. Variable relative and absolute IPGE abundances and enrichments in IPGEs relative to palladium group platinum group elements (PPGE: Pd and Pt) in the cumulate lithologies are accounted for if the parental melts of the TUC were sulphide undersaturated and platinum-group-element contents in the cumulates were controlled by their compatibility in fractionating silicate, oxide, and platinum group minerals. In contrast to cumulate lithologies, one hornblende

gabbro sample was PPGE enriched relative to IPGEs, consistent with these samples originating as crystallized melts.

Major-element variations in ol-clinopyroxenites and trace-element systematics in all rocks of the TUC suggest their parental melts had arc-like affinities. However, Re-Os isotopic measurements revealed that these melts were moderately enriched in ^{187}Os relative to estimates for primitive upper mantle at 3.8 Ga. This largely contrasts with other less evolved refractory peridotite enclaves in the area which have less radiogenic Os isotopic compositions. These differences are interpreted to reflect the proportionally higher degree of assimilation of basaltic crust experienced by the parental melts of the TUC. In addition, relative to Phanerozoic intra-plate magmas the Pd content was high, which was not considered to be a melt source characteristic, but likely due to crustal assimilation by the parental melts of the TUC. The extent to which crustal assimilation was responsible for generating arc-like signatures in major and trace elements is unclear. Thus, there is no strong evidence that parental melts of the TUC formed in a subduction-zone environment.

Relative to primitive upper mantle at 3.8 Ga, the TUC is moderately enriched in ^{187}Os, resulting in inconclusive age determinations. Although this radiogenic Os isotopic composition is interpreted to be the result crustal assimilation, resulting T_{MA} and T_{RD} ages are younger than ~2.85 Ga, which places some uncertainty on the inferred Eoarchean age of the TUC and, therefore, other enclaves in the Itsaq Gneiss complex.

Acknowledgements

I’d like to thank Professor Graham Pearson for accepting me as a master student, his guidance and support, and his time and effort spent editing my thesis. I’d also like to thank Pedro Waterton for training me in the methods of PGE and Re-Os isotopic analyses, Kris Szilas for his help with interpretations, and Sarah Woodland and Chiranjeeb Sarkar for their help in the lab when I needed it.

Table of Contents

Chapter 1

List of Tables

List of Figures

Chapter 1

Introduction

1.1. Background

The development of Earth's geochemical reservoirs in the Hadean and Eoarchean remains poorly understood. The timing and extent of crustal differentiation (e.g., Kemp et al., 2010; Hoffmann et al., 2011; Rizo et al., 2013; Griffin et al., 2014; Fisher and Vervoort, 2018), and the nature of early Earth's tectonic regimes (Stern, 2005; Bedard, 2006; Nair and Chacko, 2008; van Hunen and Moyen, 2012; Griffin et al., 2014; Polat et al., 2015) are topics of uncertainty and debate. Remnants of Eoarchean or Hadean crust and lithospheric mantle are invaluable sources of information on the development of these reservoirs during this time. Yet, these rocks are rarely preserved at the surface of the Earth (Nutman et al., 1996). Eoarchean and Hadean crust is thought to be dominantly mafic in composition (Griffin et al., 2014; Reimink et al., 2014), and fragments of such a crust (Chadwick and Crewe, 1986; Nutman et al., 1996; Nutman and Friend, 2009) and possible associated lithospheric mantle (Bennett et al., 2002; Friend et al., 2002; Rollinson, 2007; van de Locht et al., 2018) are preserved in the Itsaq Gneiss Complex (IGC) of southern West Greenland (Fig. 1-1). As these fragments have been hosted in gneisses for >3.8 Byr, they have not been subject to late convective mixing and homogenization experienced by much of the Earth's silicate system, and, thus, offer a unique opportunity to understand the Eoarchean and Hadean crust-mantle system.

Although, remnants of lithospheric mantle in the IGC may offer a clear view of the composition of the early mantle and the processes affecting it, studies of ultramafic lithologies, potential mantle material, within the IGC are few and there is uncertainty concerning the true nature of this material, i.e., whether it represents mantle restite materials or ultramafic cumulates (cf. Dymek et al., 1988; Bennett et al., 2002; Friend et al., 2002; Rollinson et al., 2007; Friend and Nutman, 2011; Szilas et al., 2015; van de Locht et al., 2018). This uncertainty may, in part, be due to alteration, as the ancient crustal residence time (>3.65 Byr) for such rocks means that they have typically undergone high-grade metamorphism, arguably altering many geochemical characteristics and obscuring many petrogenetic indicators (Rollinson, 2007). In addition, globally, mantle xenoliths older than ~3.2 Ga are rare (Carlson et al., 2005) and absent from the West Greenland mantle xenolith suite

(Wittig et al, 2010). As such, there is currently no reliable proxy of Eoarchean lithospheric mantle with which to make comparisons.

Ultramafic lithologies in the IGC which have been interpreted as pristine mantle material, have some contradictory geochemical characteristics. This has led some authors to hypothesize that the lithospheric mantle was different from typical cratonic mantle (Friend et al., 2002). These ultramafic lithologies are dunitic and harzburgitic, which implies that, to be of restite origin, such lithologies must have experienced high degrees of melt extraction (Wittig et al., 2008). This is supported by the platinum group element (PGE) composition of some of the ultramafic rocks (van de Locht et al., 2018). However, whole rock Mg #'s average 88 ± 1 (Friend et al., 2002; van de Locht et al., 2018), which is inconsistent with a depleted mantle origin, unless significantly altered through metasomatism (Wittig et al., 2008). Given that questions surrounding the origin of ultramafic enclaves in the IGC, there is a need to investigate further their geochemical and isotopic composition.

The nature of the Eoarchean lithospheric mantle associated with the North Atlantic craton is further complicated by the isotopic systematics of its crustal magmatic/metamorphic rocks. The Lu-Hf isotopic record preserved in zircons from the tonalites implies a chondritic source for the tonalites (Fischer and Vervoort, 2018). Similarly, potentially unaltered whole rock Lu-Hf isotopes of tholeiitic basalts indicate a chondritic source for the basalts (Polat et al., 2003; Hoffmann et al., 2011; Rizo et al., 2011). This is in contrast to the ^{146,147}Sm - ^{142,143}Nd record of the tonalites and basalts (Bennet et al., 2007; Rizo et al., 2011 and 2013; O'Neill et al., 2016) and with the ^{190}Pt - ^{186}Os isotopic systematics of ultramafic cumulate rocks (Coggon et al., 2013), which imply that the basalts and tonalitic gneisses formed from a melt extracted from a long-lived depleted reservoir. This emphasizes our limited current understanding of the crust-mantle system during Eoarchean times and illustrates the potential benefit of evaluating ultramafic enclaves in the IGC.

An additional rationale for studying Eoarchean ultramafic rocks from West Greenland revolves around gaining a better understanding of the tectonic setting of early Earth rocks. Although there is some contention over whether Phanerozoic-style plate tectonics was operating in the Archean (Stern, 2005; Bedard, 2006), with few exceptions (e.g. Komiya et al., 2004), the mafic and ultramafic lithologies of the IGC are interpreted as having formed at convergent plate margins (Polat et al., 2002; Polat and Hofmann, 2003; Jenner et al., 2009; Nutman and Friend, 2009; Furnes et al., 2009; Szilas et al., 2015; Polat et al., 2015). Although, this assertion is widely accepted, further evaluation of the tectonic setting of Eoarchean rocks, is warranted given the attention to the topic in the literature and the importance to understanding early Earth (e.g. Stern, 2005; Bedard, 2006; Nair and Chacko, 2008; van Hunen and Moyen, 2012; Griffin et al., 2014; Polat et al., 2015).

Finally, analysis of potential Eoarchean mantle rocks is important from the perspective of understanding the highly siderophile element evolution of the Earth. The abundances and chondritic siderophile element composition of the modern mantle is inconsistent with extraction of these elements into the early Earth's core (Chou, 1978), with no replenishment. To reconcile this, Chou (1978) proposed that the addition ~1% chondritic material to the bulk silicate earth (BSE) following core differentiation could account for modern siderophile element abundances in the BSE, a concept known as the "late-veneer" hypothesis. The timing of the addition and mixing of the late-veneer into the mantle is uncertain, but can be evaluated using PGE contents and ^{182}W isotopes in crustal rocks (e.g. Maier et al., 2009; Willbold et al., 2015; Rizo et al., 2016).

Crust that formed prior to ~3.65 Ga has small excesses in ^{182}W relative to that of the modern day (e.g. Touboul et al., 2014; Willbold et al., 2015; Rizo et al., 2016; Dale et al., 2017) and this has been suggested to be a result of the extraction of this crust from a mantle lacking late veneer contributions of chondritic material (Willbold et al., 2015). However, using ^{182}W to estimate the timing of the late veneer is questionable for two reasons. 1) Many crustal rocks with ^{182}W excesses also have modern BSE PGE concentrations and relative abundances (e.g. Touboul et al., 2014; Rizo et al., 2016; van de Locht et al., 2018). 2) The high mobility of W in crustal fluids makes evaluations of ^{182}W excesses in ancient terranes composed of different lithologies with large temporal gaps questionable (Liu et al., 2018).

Maier et al. (2009) proposed that broad temporal trends in the PGE abundances of komatiites suggest that the lower mantle did not have PGE re-enrichment prior to ~3.3 Ga. However, in the IGC, the inference of late veneer contributions to the melt source for the crustal rocks based on PGEs and ^{182}W is in some contention. The mafic and ultramafic lithologies in the IGC have ^{182}W excesses (Rizo et al., 2016; Dale et al., 2017) which may imply a source lacking a late veneer component (Willbold et al., 2015). This is supported by Dale et al., (2017) who argue that the source had only received a partial late veneer component to its PGE budget by Eoarchean times. However, other authors (Bennett et al., 2002; Szilas et al., 2015; Rizo et al., 2016; van de Locht et al., 2018) argue that the source for mafic-ultramafic crustal lithologies had modern BSE-like PGE concentrations and relative abundances, implying a well-mixed mantle with a full compliment of HSEs at that time. This problem is far from resolved and further evaluation of PGE systematics in Eoarchean crustal rocks is required.

1.2 Research Objectives

To address the above issues this study undertook a mineral and whole rock major-, trace-, and platinum-group element and Re-Os isotopic study of a previously unstudied large ultramafic enclave in the IGC. Due to its proximity to Lake Tussaap Tasia, the enclave is named the Tussaap ultramafic complex (TUC). The initial goal of this research was to determine whether the enclave was an ultramafic cumulate sequence or fragment of depleted lithospheric mantle. In the past, interpretations based on mineral chemistry and whole-rock major- and trace element geochemistry have been controversial (e.g. Dymek et al., 1988; Bennett et al., 2002; Friend et al., 2002; Rollinson et al., 2007; Friend and Nutman, 2011; Szilas et al., 2015; van de Locht et al., 2018). However, platinum group elements were deemed to be a good approach to this problem, as they are relatively resistant to alteration (Szilas et al., 2015) and their inter-element fractionation patterns can used to distinguish mantle rocks from cumulates crystallized from mafic or ultrmaifc magmas (e.g. Pearson et al., 2004; Szilas et al., 2015).

In addition to determining the process responsible for forming the ultramafic rocks of the TUC, the study attempts to constrain the nature of the parent magma or source with respect to

a) Determining whether an accurate estimate can be made of the HSE abundances in the mantle at the time of formation, and
b) Attempting to constrain the tectonic setting that the TUC formed within.

Lastly, the study tries to assess the age of formation of the TUC and its subsequent evolution within the context of the host IGC.

1.3 Geological Overview

1.3.1 The Godthåbsfjord Region

The Godthåbsfjord region is an amalgamation of Mesoarchean to Eoarchean terranes forming part of the North Atlantic Craton in southern West Greenland (Fig. 1-1). What is referred to here as the Godthåbsfjord region (Nutman et al., 1996) is also referred to in the literature as the Akulleq

Terrane (McGregor et al., 1991) or the Nuuk region (Friend and Nutman, 2005). The Region is fault bounded to the north by the ~3220 to 2970 Ma Akia Terrain and to the south by the ~ 2920 to 2860 Ma Tasiusarsuaq terrane (Friend and Nutman, 2005; Crowley et al., 2002). The Godthåbsfjord region consists of four terranes: the Faeringhavn terrane, the Isukasia terrane, the Kapisilik terrane, and the Tre Brodre terrane (Friend and Nutman, 2005). As the area of interest in this study is the Isukasia terrane in which the TUC is located (Fig. 1-2), only a brief description of the Godthåbsfjord region is given here.

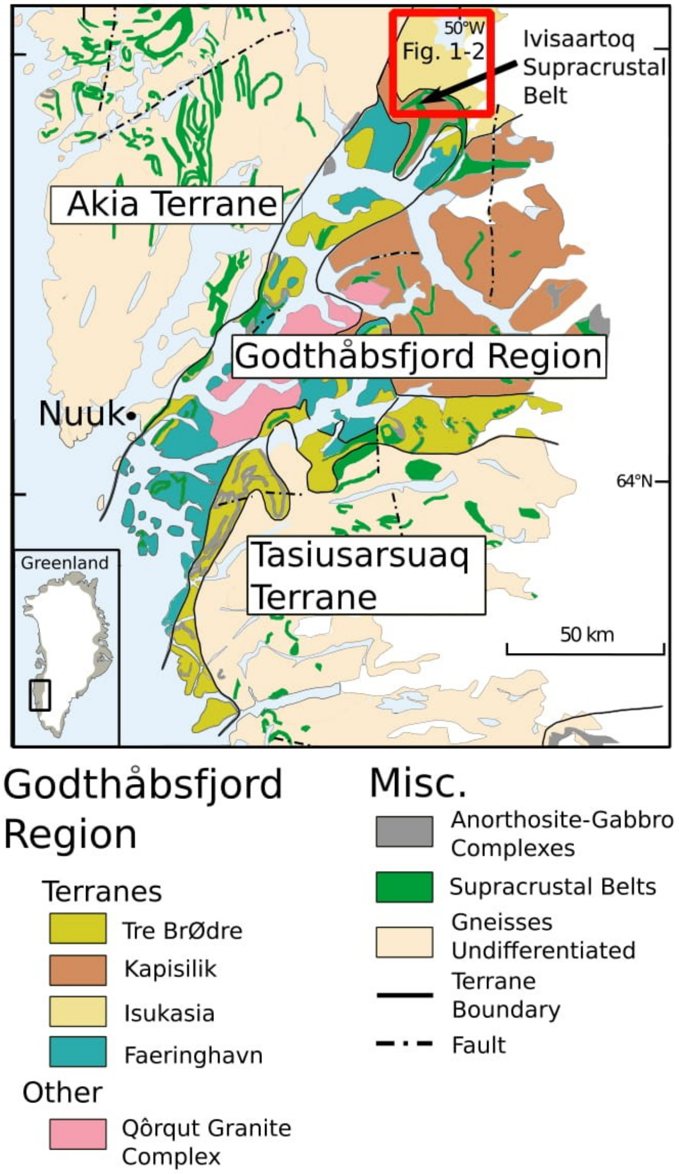

Fig. 1-1. Geology of the Godsthabfjord region in southern West Greenland modified from Koppelberg et al. (2013). The area in the red square is expanded in Fig. 1-2.

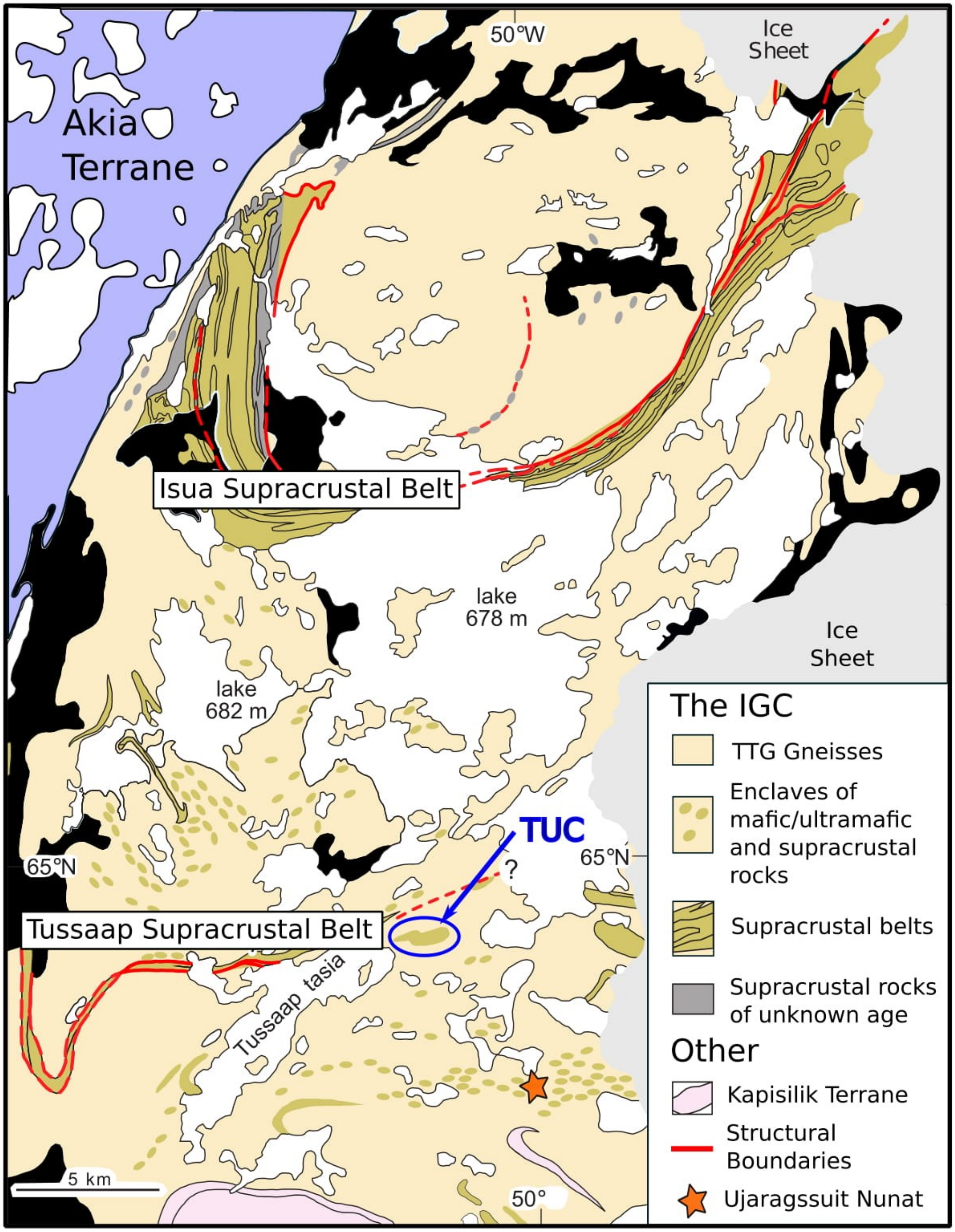

Fig. 1-2. Geology of the Isukasia terrane modified from Nutman and Friend (2002). Black areas are surficial cover.

The terranes of the Godthåbsfjord region are largely composed of rocks of the tonalite-trondhjemite-granodirorite suite (TTG) with lesser sedimentary and mafic-ultramafic belts and enclaves (Friend and Nutman, 2005). The terranes range in age from ~2825 Ma to 3850 Ma and partially amalgamated by horizontal tectonics throughout this time interval (Nutman and Friend, 2002; Friend and Nutman, 2005; Polat et al., 2007; Friend et al., 2009; Nutman et al., 2015). Renewed zircon growth during metamorphism in crustal rocks from the Godthåbsfjord region, the Akai terrane, and Tasiusarsuaq terrane at ~2700 Ma has been suggested to be the result of the final amalgamation of all the terranes in the area (McGregor et al., 1991; Crowley, 2002; Friend and Nutman, 2005).

The term IGC refers to all crustal rocks in the Godthåbsfjord region that are >3600 Ma and does not refer to rocks of a specific lithology, petrogenesis, or association (Nutman et al., 1996). In this regard the IGC refers to both the Faeringhavn terrane and the Isukasia terrane (cf. Nutman et al., 1996; Friend and Nutman, 2005). The dominant lithology of the IGC is the TTG suite. However, the IGC also hosts Eoarchean or older supracrustal enclaves and belts and potential lithospheric mantle fragments (Nutman et al., 1996).

The IGC in the Faeringhavn terrane is located in the southern west portion of the Godthåbsfjord region (Fig. 1-1). The protolith age for the TTG gniesses are ~3850 Ma and the gneisses experienced granulite-facies metamorphism between 3660 and 3600 Ma (Nutman et al., 2007). The terrane is in tectonic contact with the Tre Brodre terrane throughout the Godthåbsfjord region (Fig. 1-1). The Tre Brodre terrane (Fig. 1-1) is composed of minor layered anorthosite complexes (Owens and Dymek, 1997) intruded by the more voluminous 2.82 Ga Ikkattoq gneiss (Friend et al., 2009).

The Faeringhavn and Tre Brodre terranes are tectonically juxtaposed with the Tasiusarsuaq terrane along the southeastern margin of the Godthåbsfjord region (Fig. 1-1) (Friend et al., 2009). Uncertainty in cross-cutting relationships in the area has led to some doubt asto the the exact timing of the intercalation of these three terranes in this area but this may have occurred by ~2720 Ma (Crowley, 2002). The northeastern portion of the Faeringhavn and Tre Bodre terranes are in tectonic contact with the Kapisilik terrane and Akai terrain (Fig. 1-1). The timing of these events is also poorly constrained but has an upper limit of 2825 Ma, constrained by the age of the Ikkatoq gneisses of the Tre Brodre terrain (Friend et al., 2009) and a lower limit of ~2700 Ma by a shared amphibolite-facies metamorphic event in the Godsthabsfjord region, Akai terrane, and the Tasiusarsuaq terrane (McGregor et al., 1991; Friend and Nutman, 2005).

The Kapisilik terrane, located in the central to northeastern portion of the region (Fig. 1-1), contains orthogneisses, granites, and the region's largest supracrustal belt, the Ivisaartoq supracrustal belt (Friend and Nutman, 2005; Polat et al., 2007; Nutman et al., 2015). The Ivisaartoq supracrustal belt has an age of 3075 Ma and is composed of pillow basalts, ultramafic flows, gabbros, and serpentinized ultramafic rocks, and has been suggested to represent a Mesoarchean supra-subduction zone ophiolite (Polat et al., 2007). Arc-like trace element signatures in the 3070 to 3000 Ma tonalitic gneisses suggest continued subduction zone development (Nutman et al., 2015). The granites of the terrane are younger, ~2970 Ma, and have εHf values in zircons at this age of -15.1 to -3.8 (Nutman et al., 2015). These εHf values are distinct from the older tonalitic gneisses which range from +2.1 to +4.6 (Nutman et al., 2015). On this evidence, Nutman et al. (2015) suggest that the older supracrustal belt and tonalitic gneisses developed as an island arc complex which collided with and overrode the southern portion of the Isukasia terrane at ~2970 Ma. The granites resulted from the melting of the underlying Eoarchean Isukasia terrane (Nutman et al., 2015). The overriding Kapisilik terrane may have extended as far north as the Tussaap surpacrustal belt (TSB) in the Isukasia terrane (Fig. 1-2) (Nutman et al., 2015). The Isukasia terrain is the most north easterly extension of the Godthåbsfjord region and the IGC and is discussed in more detail below.

Finally, the ~2530 Ma Qorqut granite complex intruded the central part of the Godthåbsfjord region (McGregor, 1991). This has been suggested to be the result of partial melting of the crust in the southern parts of the region where there are high abundances of radiogenic heat producing elements, K, U, and Th in the crust (McGregor, 1991).

1.3.2 Overview of the Isukasia Region:

The Isukasia terrane of southern West Greenland refers to the northern most outcropping of the IGC in the Godthåbsfjord region (Fig. 1-1 and 1-2). The terrane is composed of three gneissic TTG domains separated by two surpa crustal belts, the Isua supracrustal belt (ISB) and the TSB (Fig. 1-2) (Nutman et al., 2002). Uranium-Pb zircon analyses from the gneissic domains range from 3650 to 3810 Ma (Nutman et al., 1996; Nutman et al., 2002). These domains are separated by structural boundaries that cut the two supracrustal belts (Fig. 1-2), and these boundaries were active between

3600 and 3650 Ma (Nutman et al., 2002). Nutman et al. (2002) suggest that these gneissic domains and associated supracrustal belts formed before ~3650 Ma and amalgamated in a convergent plate setting between 3600 and 3650 Ma.

The ISB consist of variably strained, stacked, and fault-bounded tectonic domains (Polat et al., 2002). The lithologies of the different domains within the ISB are similar and consist of volcanic and distal facies volcano/chemical-sedimentary packages, which include pillowed basalts intercalated with ultramafic rocks (of unknown origin), banded iron-formation, chert, siliciclastic turbidites and conglomerates (Polat et al., 2002). The lithotectonic domains within the belt are separated by structural boundaries (Fig. 1-2) (Nutman and Friend, 2002; Nutman et al., 2009). On the most southernly side of the belt (Fig. 1-2) the volcano-sedimentary units are cut by tonalitic dykes with an age of ~3.8 Ga, whereas those north of the most southernly structural boundary are cut by 3.7 Ga tonalitic dykes. The most detailed synthesis of the ISB is given in (Nutman et al., 2009). The TSB is less studied, but the lithologies in the belt are like those in the ISB; intercalated basalts and ultramafic rocks and distal chemical and siliciclastic sedimentary rocks. In addition, the TSB contains tectonic domains that potentially vary in age (Nutman and Friend, 2002).

The gneisses are host to abundant sedimentary and mafic-ultramafic enclaves in addition to the volcanic and volcano/chemical-sedimentary supracrustal belts (Nutman et al., 1996). In places, the enclaves and supracrustal belts are intruded by the protolith of the gneiss and, thus, predate them (Nutman et al., 1996). Like the supracrustal belts, the enclaves are largely composed of mafic (basaltic in origin) and distal facies chemical and siliciclastic sedimentary sequences (Chadwick and Crewe, 1986; Nutman et al., 1996). Ultramafic lithologies occur as concordant ultramafic sheets within mafic lithologies or layered and massive dunitic-harzburgitic enclaves (Chadwick and Crewe, 1986; Nutman et al., 1996). The enclaves and supracrustal belts are likely fragments of an earlier crust that was largely composed of oceanic basalts and volcano/chemical-sedimentary rocks (Chadwick and Crewe, 1986; Polat et al., 2002). However, some of the massive dunitic or harzburgitic enclaves may be mantle fragments (Nutman et al., 1996; Bennett et al., 2002; Friend et al., 2002; Nutman et al., 2002; Rollinson, 2007; van de Locht et al., 2018).

Of these pre-TTG supracrustal enclaves and belts, an overwhelming majority of the work has been focused on the ISB (e.g. Dymek et al., 1988; Rosing et al., 1996; Blichert-toft et al., 1999; Polat et al., 2002 and 2003; Polat and Hofmann, 2003; Frei et al., 2003; Furnes et al., 2009; Nutman and

Friend, 2009; Polat et al., 2014; Rizo et al., 2011, 2013, and 2016) with only minor focus on a limited number of enlcaves south of the ISB (Chadwick and Crewe, 1986; Bennett et al., 2002; Friend et al., 2002; Rollinson et al., 2002; Coggon et al., 2013; Coggon et al., 2015; van de Locht et al., 2018). In part, the dearth of studied ultramafic enclaves in the IGC is the reason that the focus of this project is on a previously unstudied ultramafic enclave in the IGC.

These earlier studies on both the ISB and enclaves south of the belt provide a solid platform of geochemical characteristics of the mafic-ultramafic rocks that may have formed part of the early crust and lithospheric mantle. In terms of basaltic rocks in the area, there are both tholeiitic and boninitic basalts (Polat et al., 2002; Polat and Hofmann, 2003; Jenner et al., 2009; Szilas et al., 2015). Unfortunately, the rocks have undergone metamorphic alteration up to at least amphibolite facies, overprinting many isotopic systems (Lu-Hf, Sm-Nd, and U-Th-Pb) that otherwise would have been ideal for assessing mantle source characteristics (e.g. Gruau et al., 1996; Blichert-Toff et al., 1999; Frei et al., 2002; Polat et al., 2003; Boyet et al., 2003). Some studies have inferred that Lu-Hf isotope systematics may have been preserved in rocks with a low degree of alteration (Polat et al., 2003; Hoffmann et al., 2011; Rizo et al., 2011). Notably, the Hf isotope signatures of such whole-rock studies vary far more widely than those conducted on zircon where the effects of alteration are less (e.g., Heiss et al., 2009; Fisher and Vervoort, 2018). From these whole-rock studies, the tholeiitic basalts are thought to have formed from sources with chondritic Hf isotopic ratios and the boninitic basalts from one that was severely Hf depleted. If the difference in Hf isotope compositions between these two groups of rocks is primary, it is somewhat odd that both types of basalts share a similar ^{142}Nd excess (Rizo et al., 2011 and 2016; O'Neill, 2016). Given that the more volumetrically important gneisses in the area share this ^{142}Nd excess and that Nd may have been added to the basalts by fluids derived from the gneisses (Frei et al., 2002), these data do not provide a consistent history of Eoarchean mantle melting events.

With respect to lithospheric mantle material in the area, based on rare earth elements (REE) abundances, Dymek et al. (1988) suggested that some ultramafic units in the ISB may be metasomatized mantle material, but that the results were somewhat inconclusive. Similarly, Friend and Nutman (2011) suggested a mantle origin for some of the dunitic units in the ISB, based on whole-rock major- and trace- element compositions and the trace-element composition of clinohumite. Using PGE analyses of the same ultramafic units as those of Friend and Nutman

(2011), Szilas et al. (2015) found no evidence for any melt depletion history for the dunites and interpreted them as cumulates.

Bennett et al. (2002) and Friend et al. (2002) interpreted some ultramafic enclaves located between the ISB and the TSB to be unmodified lithospheric mantle material. Based on whole-rock, major- and trace-element chemistry and mineral chemistry in chromite, Rollinson (2007) argued that not all these enclaves could be unmodified mantle material but conceded that the area south of ISB potentially preserves fragments of Eoarchean mantle. As an extension of the earlier work of Friend et al. (2002), van de Locht et al. (2018) applied PGE data to four of these samples, assessing the PGE systematics to reflect depleted lithospheric mantle (Fig. 1-3).

These potential lithospheric mantle fragments have similarities with Eoarchean TTG-hosted ultramafic enclaves within the North Atlantic Craton in the Saglek-Hebron area of northeastern Labrador (e.g. Collerson et al., 1991; Ishikawa et al., 2017). This area is an eastern extension of the North Atlantic Craton and these enclaves were first interpreted as lithospheric mantle material by Collerson et al. (1991). Major, trace, and platinum group element compositions of these mantle fragments closely resemble those hosted within the IGC (Fig. 1-3) (cf. Collerson et al., 1991; Bennett et al., 2002; Friend et al., 2002; Ishikawa et al., 2017; van de Locht et al., 2018). This resemblance further supports the contention that ultramafic enclaves south of the ISB may be

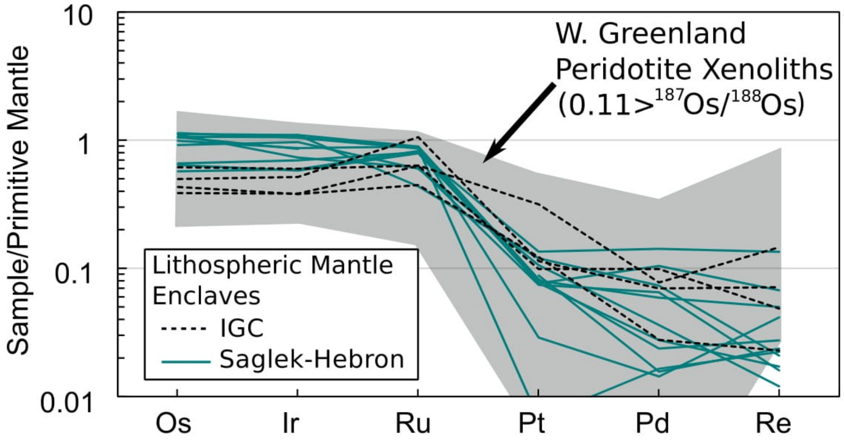

Fig. 1-3. Primitive mantle normalized PGE abundances of mantle xenoliths from the North Atlantic Craton (NAC) (Wittig et al., 2010) and possible mantle enclaves in the IGC (van de Locht et al., 2018) and Saglek-Hebron block (Ishikawa et al., 2017). Only data from PPGE depleted peridotites south of the ISB are shown from van de Locht et al., (2018) and only PPGE depleted lithospheric mantle peridotites are shown from Ishikawa et al., (2017). The W. Greenland peridotite data is constrained as suggested by Ishikawa et al. (2017) by 0.11>^{187}Os/^{188}Os. Normalization values are from Becker et al. (2006).

representative of Eoarchean lithospheric mantle. This potential for the preservation of Eoarchean lithospheric mantle remnants was the main reason for the targeting of an IGC ultramafic enclave in this study. The TUC is located south of the TSB (Fig. 1-2) and has not previously been studied.

1.4 Thesis Outline

The main body of this work is encompassed in Chapter 2 and is intended for publication in a peer reviewed journal. The layout follows the typical layout for any geological scientific work: local geology, methods, unbiased representation of the data, interpretation and discussion, and conclusions. The data includes petrographic observations, and measured mineral chemistry, whole-rock major- and trace- element abundances, PGE abundances, and Re-Os isotopic ratios. The initial portion of the discussion largely focuses on differentiating secondary and primary geochemical characteristics and how these can be applied to assessing a potential cumulate vs. mantle origin for the rocks. Trace-element characteristics are then applied to discussing the operation of Archean plate tectonics. Platinum group elements are applied to assessing the effects of Eoarchean cumulate processes on the distribution of these elements in the TUC. These observations on PGE processes in the TUC are then used to estimate the PGE abundance in the source. Finally, potential chronological constraints are placed on the TUC using the distribution of Re-Os isotopes in the rocks.

Chapter 3 encompasses the broader conclusions, how the work answered the research objectives and where future work should be directed in terms of targeting potential mantle enclaves, the operation of plate tectonic processes in the Eoarchean, and the timing of modern BSE and chondritic relative PGE abundances in the mantle.

References

Bédard, J.H. (2006). A catalytic delamination-drivenmodel for coupled genesis of Archaean crust and sub-continental lithospheric mantle. *Geochim. Cosmochim. Acta*, 70, 1188-1214.

Bennett, V.C., Nutman, A.P., and Esat, T.M., (2002). Constraints on mantle evolution from 187Os/188Os isotopic compositions from Archaean ultramafic rocks from southern west Greenland (3.8 Ga) and western Australia (3.46 Ga). *Geochim. Cosmochim. Acta*, 66, 2615-2630.

Bennett, V.C., Brandon, A.D., and Nutman, A.P. (2007). Coupled 142Nd–143Nd isotopic evidence for Hadean mantle dynamics. *Science*, 318, 1907-1910.

Blichert-Toft J., Albarede F., Rosing M., Frei R., and Bridgwater D. (1999). The Nd and Hf isotopic evolution of the mantle through the Archean. Results from the Isua Supracrustals, West Greenland, and from the Birimian terranes of West Africa. *Geochim. Cosmochim. Acta*, 63, 3901-3914.

Boyet, M., Blichert-Toft, J., Rosing, M., Storey, M., Télouk, P., Albarède, F. (2003). 142Nd evidence for early Earth differentiation. *Earth Planet. Sci. Lett.*, 214, 427-442.

Carlson, R.W., Pearson, D.G., and James, D.E. (2005). Physical, chemical and chronological characteristics of continental mantle. *Reviews of Geophysics*, 43, RG1001.

Chadwick, B. and Crewe, M.A. (1986). Chromite in the early Archean Akilia Association (ca. 3,800 m.y.), Iviartoq region, inner Godthåbsfjord, southern West Greenland. *Econ. Geol.* 81,184-191.

Chou, C. L. (1978). Fractionation of siderophile elements in the Earth's upper mantle. Proc. 9th *Lunar Planet. Sci. Conf.*, 9, 219-230.

Coggon, J.A., Luguet A., Nowell, G.M., and Appel, P.W.U. (2013). Hadean mantle melting recorded by southwest Greenland chromitite 186Os signatures. *Nat. Geo.*, 6, 871-874.

Coggon, J.A., Luguet, A., Fonseca, R.O.C., Lorand, J.-P., Heuser, A., and Appel, P.W.U. (2015). Understanding Re-Os systematics and model ages in metamorphosed Archean ultramafic rocks: A single mineral to whole-rock investigation: *Geochim. Cosmochim. Acta*, 167, 205-240.

Collerson, K.D., Campbell, L.M., Weaver, B.L., and Palacz, Z.A. (1991). Evidence for extreme mantle fractionation in earlyArchean ultramafic rocks from northern Labrador. *Nature*, 349, 209-214.

Crowley, J.L. (2002). Testing the model of late Archaean terrane accretion in southern West Greenland: a comparison of the timing of geological events across the Qarliit Nunaat fault, Buksefjorden region. *Precambrian Res.*, 116, 57-80.

Dale, C.W., Kruijer, T.S., and Burton, K.W. (2017). Highly siderophile element and 182W evidence for a partial late veneer in the source of 3.8 Ga rocks from Isua, Greenland: *Earth Planet. Sci. Lett.*, 458, 394–404.

Dymek, R.F., Brothers, S.C., and Schiffries, C.M., (1988). Petrogenesis of ultramafic metamorphic rocks from the 3800 Ma Isua supracrustal belt, West Greenland. *J. Petrology*, 29, 1353-1397.

Fisher, C.M. and Vervoort, J.D. (2018). Using the magmatic record to constrain the growth of continental crust—The Eoarchean zircon Hf record of Greenland. *Earth Planet. Sci. Lett.*, 488, 79-91.

Frei, R., Rosing, M., Waight, T.E., and Ulfbeck D.G. (2002). Hydrothermal-metasomatic and tectono-metamorphic processes in the Isua greenstone belt (West Greenland): A multi-isotopic investigation of their effects on the Earth's oldest oceanic crustal sequence. *Geochim. Cosmochim. Acta*, 66, 467–486.

Friend, C.R.L., Bennett, V.C., and Nutman, A.P., (2002). Abyssal peridotites >3,800 Ma from southern west Greenland: field relationships, petrography, geochronology, wholerock and mineral chemistry of dunite and harzburgite inclusions in the Itsaq Gneiss Complex. *Contributions to Mineralogy and Petrology*, 143, 71–92.

Friend, C.R. and Nutman, A.P. (2005). Newpieces to the Archaean terrane jigsawpuzzle in the Nuuk region, southernWest Greenland: steps in transforming a simple insight into a complex regional tectonothermal model. *Journal of the Geological Society*, 162, 147–162.

Friend, C.R.L., Nutman, A.P., Baadsgaard, H., and Duke, M.J.M. (2009). The whole rock Sm–Nd 'age' for the 2825 Ma Ikkattoq gneisses (Greenland) is 800 Ma too young: Insights into Archaean TTG petrogenesis. *Chem. Geol.*, 261, 62-72.

Friend, C.R.L. and Nutman, A.P. (2011). Dunites from Isua, Greenland: a ca. 3720 Ma window into subcrustal metasomatism of depleted mantle. *Geology*, 39, 663-666.

Furnes, H., Rosing, M., Dilek, Y., and DeWit, M. (2009). Isua supracrustal belt (Greenland) - A vestige of a 3.8 Ga suprasubduction zone ophiolite, and the implications for Archean geology. *Lithos*, 113, 115-132.

Griffin, W.L., Belousova, E.A., O'Neill, C.O., O'Reilly, S.Y., Malkovets, V., Pearson, N.J., Spetsius, S., and Wilde, S.A. (2014). The world turns over: Hadean–Archean crust–mantle evolution. *Lithos*, 189, 2-15.

Gruau, G., Rosing, M., Bridgwater, D., and Gill, R.C.O. (1996). Resetting of Sm–Nd systematics during metamorphism of >3.7-Ga rocks: implications for isotopic models of early Earth differentiation. *Chem. Geol.*,133, 225-240.

Hiess, J., Bennet, V.C., Nutman, A.P., and William, I.S. (2009). In situ U–Pb, O and Hf isotopic compositions of zircon and olivine from Eoarchaean rocks, West Greenland: New insights to making old crust. *Geochim. Cosmochim. Acta*, 73, 4489-4516.

Hoffmann, J.E., Münker, C., Polat, A., Rosing, M.T., and Schulz, T. (2011). The origin of decoupled Hf-Nd isotope compositions in Eoarchean rocks from southern West Greenland: *Geochim. Cosmochim. Acta*, 75, 6610-6628.

Ishikawa, A., Suzuki, K., Collerson, K.D., Liu, J., Pearson, D.G., and Komiya, T. (2017). Rhenium-osmium isotopes and highly siderophile elements in ultramafic rocks from the Eoarchean Saglek Block, northern Labrador, Canada: implications for Archean mantle evolution. *Geochim. Cosmochim. Acta*, 216, 286-311.

Kopplberg, M., Dziggel, A., Schlatter, D.M., Kolb, J., and Meyer, F.M. (2013). Geochemistry and petrology of gold-bearing hydrothermal alteration zones on Qilanngaarsuit, southern West Greenland. *Geological Survey of Denmark and Greenland Bulletin*, 28, 49-52.

Jenner, F.E., Bennett, V.C., Nutman, A.P., Friend, C.R.L., Norman, M.D., and Yaxley, G. (2009). Evidence for subduction at 3.8 Ga: geochemistry of arclike metabasalts from the southern edge of the Isua Supracrustal Belt. *Chem. Geol.*, 261, 82-99.

Kemp, A.I.S., Wilde, S.A., Hawkesworth, C.J., Coath, C.D., Nemchin, A., Pidgeon, R.T., Vervoort, J.D., and DuFrane, S.A. (2010). Hadean crustal evolution revisited: new constraints from Pb–Hf isotope systematics of the Jack Hills zircons. *Earth Planet. Sci. Lett.*, 296, 45-56.

Komiya, T., Maruyama, S., Hirata, T., Yurimoto, H., Nohda, S. (2004). Geochemistry of the oldest MORB and OIB in the Isua Supracrustal Belt, southern West Greenland: implications for the composition and temperature of early Archean upper mantle. *Island Arc*, 13, 47-72.

Maier, W.D., Barnes, S.J., Campbell, I.H., Fiorentini, M.L., Peltonen, P., Barnes, S.J., and Smithies, R.H. (2009). Progressive mixing of meteoritic veneer into the early Earth's deep mantle. *Nature*, 460, 620-623.

McGregor, V.R., Friend, C.R.L., and Nutman, A.P. (1991). The late Archaean mobile belt through Godthåbsfjord, southern West Greenland: a continent–continent collision zone? *Bulletin of the Geological Society, Denmark*, 39, 179-197.

Nair, R. and Chacko, T. (2008). Role of oceanic plateaus in the initiation of subduction and origin of continental crust. *Geological Soc. America*, 36, 583-586.

Nutman, A.P., Mcgregor, V.R., Friend, C.R.L., Bennett, V.C., and Kinny, P.D. (1996). The Itsaq Gneiss Complex of southern West Greenland; the world's most extensive record of early crustal evolution (3900–3600). *Precambrian Res.*, 78, 1-39.

Nutman, A.P., Friend, C.R.L., and Bennett, V.C. (2002). Evidence for 3650–3600 Ma assembly of the northern end of the Itsaq Gneiss Complex, Greenland: implication for early Archean tectonics. *Tectonics*, 21, No. 1, 1005.

Nutman, A.P., Friend, C.R.L., Horie, K., and Hidaka, H. (2007). The Itsaq Gneiss Complex of southern West Greenland and the construction of Eoarchaean crust at convergent plate boundaries, in van Kranendonk, M., et al., eds., *Earth's oldest rocks: Developments in Precambrian Geology*, Volume 15: Amsterdam, Elsevier, 187-218.

Nutman, A.P. and Friend, C.R.L. (2009). New 1:20,000 scale geological maps, synthesis and history of investigation of the Isua supracrustal belt and adjacent orthogneisses, southern West Greenland: a glimpse of Eoarchaean crust formation and orogeny. *Precambrian Res.*, 172, 189-211.

Nutman, A.P., Bennett, V.C., Friend, C.R.L., Keewook, Y., and Lee, S.R. (2015). Mesoarchaean collision of Kapisilik terrane 3070 Ma juvenile arc rocks and >3600 Ma Isukasia terrane continental crust (Greenland). *Precambrian Res.*, 258, 146-160.

O'Neil, J., Rizo, H., Boyet, M., Carlson, R.W., and Rosing, M.T. (2016). Geochemistry and Nd isotopic characteristics of Earth's Hadean mantle and primitive crust. *Earth Planet. Sci. Lett.*, 442, 194-205.

Owens, B.E. and Dymek, R.F. (1997). Comparative petrology of Archaean anorthosites in amphibolite and granulite facies terranes, SW Greenland. *Contrib. Mineral Petrol.*, 128, 371-384.

Pearson, D.G., Irvine, G.J., Ionov, D.A., Boyd, F.R., and Dreibus, G.E. (2004). Re–Os isotope systematics and platinum group element fractionation during mantle melt extraction: a study of massif and xenolith peridotite suites. *Chem. Geol.*, 208, 29–54.

Polat, A., Hoffmann, A.W., and Rosing, M. (2002). Boninite-like volcanic rocks in the 3.7–3.8 Ga Isua greenstone belt, West Greenland: geochemical evidence for intra-oceanic subduction zone processes in the early Earth. *Chem. Geol.*, 184, 231-254.

Polat, A., Hofmann, A.W., Münker, C., Regelous, M., Appel, P.W.U., (2003). Contrasting geochemical patterns in the 3.7–3.8 Ga pillow basalt cores and rims, Isua greenstone belt, Southwest Greenland: implications for postmagmatic alteration processes. *Geochim. Cosmochim. Acta*, 441-457.

Polat, A. and Hoffmann, A.W. (2003). Alteration and geochemical patterns in the 3.7–3.8 Ga Isua greenstone belt, West Greenland. *Precambrian Res.*, 126, 197-218.

Polat, A., Appel, P.W.U., Frei, R., Pan, W.M., Dilek, Y., Ordonez-Calderon, J.C., Fryer, B., Hollis, J.A., and Raith, J.G. (2007). Field and geochemical characteristics of theMesoarchean (~3075 Ma) Ivisaartoq greenstone belt, southern West Greenland: Evidence for seafloor hydrothermal alteration in supra-subduction oceaniccrust. *Gondwana Res.*, 11, 69-91.

Polat, A., Wang, L., and Appel, P.W.U. (2015). A review of structural patterns and melting processes in the Archean craton of West Greenland: Evidence for crustal growth at convergent plate margins as opposed to non-uniformitarian models: *Tectonophysics*, 662, 67-94.

Reimink, J.R., Chacko, T., Stern, R.A., and Heaman, L.M. (2014). Earth's earliest evolved crust generated in an Iceland-like setting. *Nature Geoscience*, 7, 529-533.

Rizo, H., Boyet, M., Blichert-Toft, J., and Rosing, M. T. (2011). Combined Nd and Hf isotope evidence for deep-seated source of Isua lavas. *Earth Planet. Sci. Lett.*, 312, 267-279.

Rizo, H., Boyet, M., Blichert-Toft, J., and Rosing, M. T. (2013). Early mantle dynamics inferred from 142Nd variations in Archean rocks from southwest Greenland. *Earth Planet. Sci. Lett.*, 377, 324-335.

Rizo, H., Walker, R.J., Carlson, R.W., Touboul, M., Horan, M.F., Puchtel, I.S., Boyet, M., and Rosing, M.T. (2016). Early Earth differentiation investigated through 142Nd, 182W, and highly siderophile element abundances in samples from Isua, Greenland: *Geochim. Cosmochim. Acta*, 175, 319-336.

Rollinson, H., Appel, P.W.U., and Frei, R. (2002). A metamorphosed, early Archean chromitite from West Greenland: Implications for the genesis of Archean anorthositic chromitites. *J. Petrol.*, 43, 2143-2170.

Rollinson, H., (2007). Recognizing early Archaean mantle: a reappraisal. *Contributions to Mineralogy and Petrology*, 154, 241-252.

Rosing, M.T., N.M., Rose, D., Bridgwater, H. S., and Thomsen, H.S. (1996). Earliest part of the Earth's stratigraphic record: A reappraisal of the >3.7 Ga Isua (Greenland) supracrustal sequence. *Geology*, 24, 43-46.

Stern, R.J., (2005). Evidence from ophiolites, blueschists, and ultrahigh-pressure metamorphic terranes that the modern episode of subduction tectonics began in Neoproterozoic time. *Geology*, 33, 557-560.

Szilas, K., Kelemen, P.B., and Rosing, M.T. (2015). The petrogenesis of ultramafic rocks in the >3.8 Ga Isua supracrustal belt, southern West Greenland: Geochemical evidence for two distinct magmatic cumulate trends: *Gondwana Res.*, 28, 565-580.

Touboul, M., Liu, J., O'Neil, J., Puchtel, I.S., and Walker, R.J. (2014). New insights into the Hadean mantle revealed by 182W and highly siderophile element abundances of supracrustal rocks from the Nuvvuagittuq Greenstone Belt, Quebec, Canada: *Chem. Geol.*, 383, 63-75.

van de Löcht, J., Hoffmann, J.E., Wang, C.L.Z., Becker, H., Rosing, M.T., Kleinschrodt, R., and Munker, C (2018). Earth's oldest mantle peridotites show entire record of late accretion. *Geo. Society of America*, 46, 199-202.

Van Hunen, J. and Moyen, J.F. (2012). Archean Subduction: Fact or Fiction? *Annual Rev. of Earth and Planet. Sci.*, 40, 195-29.

Willbold, M., Mojzsis, S.J., Chen, H.-W., and Elliott, T. (2015). Tungsten isotope composition of the Acasta Gneiss Complex: *Earth Planet. Sci. Lett.*, 419, 168-177.

Wittig, N., Pearson, D.G., Webb, M., Ottley, C.J., Irvine, G.J., Kopylova, M.G., Jensen, S.M., and Nowell, G.M. (2008). Origin of cratonic lithospheric mantle roots: a geochemical study of peridotites from the North Atlantic Craton, West Greenland. *Earth Planet. Sci. Lett.*, 274, 24-33.

Wittig, N., Webb, M., Pearson, D.G., Dale, C.W., Ottley, C.J., Hutchison, M., Jensen, S.M., and Laguet, A. (2010). Formation of the North Atlantic Craton: Timing and mechanisms constrained from Re–Os isotope and PGE data of peridotite xenoliths from S.W. Greenland. *Chem. Geol.,* 276, 166-187

Chapter 2

A Newly Studied Ultramafic Enclave of the Itsaq Gneiss Complex

2.1 Regional Geology

2.1.1 South of the Tussaap supracrustal belt*:*

The Tussaap ultramafic complex (TUC) is a large (about 1 km long and 400 m wide) enclave hosted within the northern portion of the Itsaq Gneiss Complex (IGC) in southern West Greenland (Fig. 1-2). The enclave is located in Archean gneisses just south of the Tussaap supracrustal belt at 64°58.81 N and 50°04.00 W (Fig. 1-2) and is composed of massive dunite, clinopyroxenites, and amphibolite with minor hornblende gabbro. A review of the geology of the IGC in this area, referred to as the Isukasia terrane, is given by Nutman et al. (2002). The terrane comprises of two supracrustal belts; the Tuvssaap supracrustal belt (TSB) and the Isua supracrustal belt (ISB). These are intercalated with three gneissic geologic domains; the area south of the TSB, the area between the TSB and the ISB, and the area north of the ISB (Nutman et al., 2002). The rocks of the geological domains are between 3650 and 3810 Ma in age and were tectonically juxtaposed between 3650 and 3600 Ma (Nutman et al., 2002).

The gneisses south of the TSB are predominantly tonalitic with lesser volumes of trondhjemites, diorites, granodiorites, and granites (Nutman et al., 1996). Trains of ultramafic pods, hosted in the gneiss, range from a few meters wide to up to 800 m long and 200 m wide and can be traced for several km along the foliation of the gneiss (Chadwick and Crewe, 1983 and 1986). The TUC comprises an exceptionally large pod belonging to this train of ultramafic exposures. The ultramafic pods of the gneisses south of the TSB are variably altered to tremolite-talc-chlorite schists (Chadwick and Crewe, 1986). Many of the pods are zoned, showing strong metasomatic alteration toward the contact with the gneiss (Chadwick and Crewe, 1983). Dunite is the most common lithology of the ultramafic pods (Chadwick and Crewe, 1983). Some enclaves are also composed of layered chromitite and dunite (Chadwick and Crewe, 1986; Appel et al., 2002; Rollinson et al., 2002; Lowry et a., 2003; Coggon et al 2015) or harzburgite (Chadwick and Crewe, 1986). Some of the massive dunite and harzburgite pods have been interpreted as upper mantle "xenoliths" in the gneiss (Nutman et al., 1996; Nutman et al., 2002).

More abundant in the gneiss south of the TSB are enclaves of supracrustal packages composed of amphibolites, gabbros, garnet paragneisses, and metamorphosed banded iron formations

(Chadwick and Crewe, 1986). Concordant ultramafic sheets are commonly found within the supracrustal enclaves (Chadwick and Crewe, 1986). The above lithological associations have led to the interpretation that the enclaves once formed a large layered complex that was intruded and disaggregated by the protolith of the gneiss (Chadwick and Crewe, 1986). Later tectonic interleaving resulted in further disaggregation and the pod-like shape of the enclaves (Chadwick and Crewe, 1986).

The most well studied ultramafic enclave in the gneisses south of the TSB is the Ujaragssuit nunat layered intrusion (Chadwick and Crewe, 1986; Appel et al., 2002; Rollinson et al., 2002; Lowry et al., 2003; Coggon et al., 2013; Coggon et al 2015). The enclave is located ~5 km SE of the TUC (Fig. 1) and is composed of layered dunite and chromite fractionated from a basaltic, boninitic, or komatiitic magma (Rollinson et al., 2002). A tonalite band in the gneiss from this area yielded a U-Pb zircon age of 3810 ± 7 Ma with metamorphic zircon growth recorded at 3630 ± 6 Ma (Nutman et al., 2002). Platinum-Os isotopic model ages from the Ujaragssuit nunat layered intrusion are as old as 4360 ± 421 Ma (Coggon et al., 2013). These provide useful age constraints on the TUC. The minimum age for the gneiss in the area is ~3810 Ma (Nutman et al., 2002). However, some of the enclaves may be much older, or may have recorded older mantle melting events.

The Isukasia region experienced polyphase metamorphism, but likely never reached granulite-facies conditions (Nutman et al., 1996). A pre-3600 Ma metamorphic event is inferred from the renewed zircon growth in the gneisses south of the TSB and may be related to the juxtaposition of the different geological domains in the area during this time (cf. Nutman et al., 2002). Additional thermal events caused regional folding between 3560 and 3580 Ma (Nutman et al., 2002). Further regional metamorphism occurred between 2800 and 3000 Ma reaching pressures of ~5 kbar and a minimum temperature of 550°C (Gruau et al., 1996; Frei et al., 2002; Cruz et al., in prep). The Mesoarchean event is possibly related to the collision of the Kapisilik terrane with the gneisses south of the TSB at ~2960 Ma (cf. Nutman et al., 2015). Additional metamorphism occurred during the amalgamation of the Godthåbsfjord region, the Akai terrane, and the Tasiusarsuaq terrane at ~2700 Ma. Further metamorphic events reset the K-Ar isotopic system in the gneisses hosting the TUC at about 2500 Ma and between 1800 and 2000 Ma (Cruz et al., in prep). Table 2.1 summarizes these metamorphic events.

Table 2. 1 – An abbreviated history of metamorphic events in the Isukasia terrane.

Timing of Event (Ma)	Technique	Possible Relevant Geological Events	Reference
>3810	Cross cutting relationships	Formation of the mafic-ultramafic crust and lithospheric mantle.	Nutman et al. (1996 and 2002)
~3810	U-Pb zircon in Gneiss	Protolith of the Gneiss intrudes the crust and lithospheric mantle.	Nutman et al. (1996 and 2002)
~3600 to 3650	U-Pb zircon overgrowths in Gneisses	Intercalation of gneissic domains in the Isukasia terrane.	Nutman et al. (1996 and 2002)
~3500 to 3580	U-Pb zircon overgrowths and reset Ar-Ar isotopic system in gneisses	Regional folding.	Nutman et al. (2002) and Cruz et al. (in prep.)
~2800 to 3000	Reset U-Th-Pb and Sm-Nd isotopic systems in mafic rocks and Ar-Ar isotopic system in the gneisses	Accretion of the Kapisilik terrane to the southern margin of the Isukasia terrane.	Gruau et al. (1996), Frei et al. (2002), and Cruz et al. (in prep.)
~2700	U-Pb zircon overgrowth and metamorphic monazite.	Intercalation of the Godthåbsfjord region, the Akai terrane, and the Tasiusarsuaq terrane.	Friend and Nutman, (2005)
~2500	Reset Ar-Ar isotopic system	Intrusion of the Qôrqut granite.	McGregor et al. (1991) and Cruz et al. (in prep.)
~1800 to 2000	Reset Ar-Ar isotopic system	Unknown	Cruz et al. (in prep.)

2.2 Methods

2.2.1 Mineral chemistry

Analysis by electron probe micro analysis (EPMA) were performed at the University of Alberta EPMA laboratory. Olivine, chromite, clinopyroxene, and orthopyroxene were measured on a JEOL JXA-8900R instrument, and amphiboles on a Cameca SX-100 instrument. Operating conditions were 20 kV accelerating potential, 100 nA current, and 2 μm spot size for all minerals except amphiboles, which were measured with operating conditions of 15 kV accelerating potential, 20 nA current, 5 μm spot size. Counting times for most elements was 30 s on each of peak and background. Mineral standards were measured at regular intervals within each analytical session to monitor accuracy and precision and the standards used are given in Appendix 1. Matrix corrections were done using ZAF or phi rho Z algorithms. Interference corrections were applied to Cr for interferences by V, Mn for interferences by Cr, V for interferences by Ti, and Co for interferences by Fe.

2.2.2 Sample preparation for whole-rock analyses

For whole-rock analyses, the samples were first cut into rectangular chunks of approximately 2.5 cm across by a diamond impregnated saw. To remove any residual metal left by the saw blade, the cut sample material was first washed with distilled water and then sanded with corundum paper. Then the samples were put in a sonic bath of distilled water for about 20 minutes. To crush the samples, the cut and washed material was then placed in at least three plastic sample bags and crushed on a metal plate with a sledge hammer. If the bags were broken, the sample was carefully removed and placed in new bags and crushed further. This process was continued until the samples were crushed to fragments of approximately <0.8 cm. The samples were then further pulverized to a fine powder in an agate mill.

2.2.3 Major and trace element geochemistry

Whole rock major- and minor- element compositions were determined by X-ray fluorescence on fused $Li_2B_4O_7$ disks at Franklin and Marshall College. Five replicate analyses of the certified reference material MUH-1 were performed to monitor accuracy and precision and the results are given in Appendix 2. Most oxides below 0.12 wt % in MUH-1 (TiO_2, K_2O, and P_2O_5) had poor reproducibilities of 12 to 33 % relative standard deviation (RSD). The more abundant major elements, MgO, CaO, and Al_2O_3 were reproducible to 5 %RSD or better. Most oxides were accurate to within 3.5 % the certified reference values for MUH-1. The average of TiO_2 analyses was 12 % less than the certifie reference value. However, if the analyses of the TUC were inaccurate to such an extent, petrogenetic interpretations made in this study based on TiO_2 would remain the same. Minor elements Ni, and Cr were reproducible to <3 % RSD. While the precision of Ni was very good, the measured value was ~30 % higher than the accepted value for MUH-1.

Trace elements were measured at the Arctic Resources Laboratory at the University of Alberta. Sample aliquots of 0.1 ± 0.01 g were dissolved in Savillex PFA beakers with 4 ml of 28.7 M HF and 1 ml of 15.4 M HNO_3 for 144 hrs at 150 °C. The samples were evaporated to near dryness and re-dissolved in 15.4 M HNO_3 three times. The final solution was spiked with In as an internal standard and diluted to 3.5 % HNO_3 for mass spectrometry.

The samples were measured with a Nu Attom inductively coupled plasma mass spectrometer (ICPMS) equipped with a Peltier cooled quartz spray chamber. Twelve replicate analyses of the certified reference material OKUM where used to monitor accuracy and precision and are given in Waterton et al. (2018). The precision for most elements was to ≤3 % RSD, while Th, Nb, and Zr were to ≤5.5% RSD. Most elements were reproducible to within 5 % of the certified reference values, except Zr which was reproducible to 9 %. In addition, Th was reproducible only to within 14% of the certified values. However, recent analyses (Peters and Pettke, 2017) yielded Th values of 0.027 ppm, within 1% of the average analyses here.

2.2.4 Platinum group elements

Platinum group elements and Re were measured at the Arctic Resources Laboratory at the University of Alberta. Approximately 1 g samples were equilibrated with a mixed PGE and Re spike, enriched in isotopes ^{190}Os, ^{191}Ir, ^{99}Ru,^{106}Pd, ^{194}Pt, and ^{185}Re, using inverse aqua regia (6mL 15.4 M HNO_3 and 3.5 mL 10.6 M HCl). Samples were equilibrated in quartz vials in an Anton-Paar high pressure asher at 290 °C and 100 bars for 16 hrs. Osmium was extracted from the inverse aqua regia in CCl_3, back extracted into HBr, and further micro distilled using HBr. After Os extraction, PGEs and Re in the inverse aqua regia were separated from the sample matrix via the method of Pearson and Woodland (2000). The above procedures were performed on three sets of samples. With each sample batch, the certified reference material OKUM and a procedural blank were included.

Osmium was measured on a Thermo Triton Plus thermal ionization mass spectrometer in negative ion mode. Spike unmixing was calculated offline with corrections for mass fractionation and O isotopic variation and interferences using an in-house Excel spread sheet. The Durham Romil Os standard (DROsS) was measured in each analytical session with load sizes of between 0.5 and 2.5 ng. The resulting mean $^{187}Os/^{188}Os$ value of 0.16096 ± 35 (n=14) is in good agreement with values published by Luguet et al. (2008) and Dale et al. (2012). In addition, OKUM was measured three times, resulting in a mean $^{187}Os/^{188}Os$ of 0.275 ± 0.007 and a mean Os concentration of 0.78 ± 0.02 ppb. Both measurements agree well with the results of Chen et al. (2016), and references therein and are consistent with longer term results within the UofA laboratory (e.g., Waterton, 2018).

Following chromatographic separation, the remaining PGEs and Re were measured using a Nu Attom ICPMS. Separate solutions of both natural PGEs plus Re and mixed oxides where measured within each analytical session to monitor for mass fractionation and oxide production rates. Isobaric and oxide interferences were measured within each sample analysis and corrected for. In addition, the reference material OKUM was measured three times averaging Ir of 0.88 ± 0.07 ppb, Ru of 4.56 ± 0.02 ppb, Pt of 11.6 ± 0.3 ppb, Pd of 11.9 ± 0.3 ppb, and Re of 0.51 ± 0.02 ppb, in agreement with certified values. Offline mass fractionation and interference corrections for PGEs and Re were performed with an in-house Excel spread sheet.

The average of the three procedural blanks are as follows: Os 1 ± 0.7 ppt, Ir of 0.7 ± 0.3 ppt, Ru estimated to be less than oxide interferences, Pt of 108 ± 13 ppt, Pd of 40 ± 38 ppt, and Re of 1 ± 0.6 ppt. These blank values were applied as corrections to all measured samples.

2.3 Results:

2.3.1 Samples and petrography

Based on mineralogy, the samples of the TUC have been grouped into four lithologies; dunite, ol-clinopyroxenite, amphibolite, and hornblende gabbro. Excluding alteration minerals, the dunites contain 97 to 99 % olivine, 1 to 3 % chromite, and minor orthopyroxene. Where preserved, the dunites are typically characterized by a granoblastic texture composed of olivine and chromite with grain sizes of 2 to 15 mm and 30 to 200 μm, respectively. However, in some samples olivine grains have been extensively replaced along grain boundaries by alteration minerals which has obscured this texture. Some dunites have a porphyroclastic texture in which 1 to 10 mm olivine porphyroclasts are surrounded by a matrix of smaller 0.1 to 1 mm grains of olivine extensively altered by hydrous phases.

The most abundant large (greater than 10 µm) inclusions in olivine are chromites that are rounded to euhedral grains up to 200 µm (Figs. 2-1 A and B), and these are locally associated with tremolite and phlogopite that form portions of larger inclusions up to 500 µm (Figs. 2-1 A and B). In addition, large inclusions of tremolite up to 800 µm in length occur in the olivine grains (Figs. 2-1 A and B). Olivine grains also contain inclusions that are elongate parallel to the crystallographic axes of the olivine grains and are typically less than 10 µm long and 1 µm wide (Fig. 2-1 C). These inclusions are tremolite, chromite, and magnetite and are abundant giving the olivine grains a cloudy appearance in transmitted light (Fig. 2-1 A).

Chromite also occurs interstitial to olivine and is euhedral to anhedral in shape, in places having lath-like inclusions of chlorite (Fig. 2-1 D). With the exception of one serpentinite, alteration minerals constitute about 5 to 25 % of the dunites and consist predominantly of tremolite, minor talc, phlogopite, and serpentine, with subordinate apatite. The alteration minerals locally form large irregular shaped aggregates up to 10 mm in size that are interstitial to olivine. These are largely composed of tremolite, magnetite, and talc. However, in some instances, orthopyroxene is found in these interstitial areas, being replaced by tremolite. In addition, a mesh texture is present in the dunites forming networks of serpentine which cross cuts other metamorphic minerals and is a late alteration characteristic.

Olivine-clinopyroxenites occur as two types; hydrous and anhydrous. Excluding secondary minerals, the anhydrous ol-clinopyroxenites contain 70 to 85 % clinopyroxenite, 15-30% olivine, and less than 1 % chromite. Minor pargasite, phlogopite, and plagioclase occur locally (Fig. 2-1 E). Clinopyroxene grains are 0.5 to 3 mm in size and have highly irregular grain boundaries ubiquitously inundated by orthopyroxene. These grains have extensive inclusions of chromite approximately 1 µm in size (Fig. 2-1 E), giving the grains a brownish colour in transmitted light. In addition, clinopyroxene has exsolved abundant orthopyroxene (Fig. 2-1 E). Orthopyroxene also forms large poikiloblastic crystals up to 2 mm in size (Fig. 2-1 F) and usually rims both clinopyroxene and olivine. Rarely, less than 10 µm inclusions of pargasite are hosted in clinopyroxene grains (Fig. 2-1 E). Chromite also occurs as inclusions in olivine with similar characteristics as those in the dunites. Inclusions in olivine that host chromite usually also contain pargasite, orthopyroxene, and phlogopite. Although lath like inclusions occur in olivine in these samples, none are large enough to accurately identify.

Hydrous ol-clinopyroxenites have been altered to tremolite, talc, phlogopite, and magnetite, to the extent that up to 80% of the samples consist of these minerals. Olivine is being replaced by

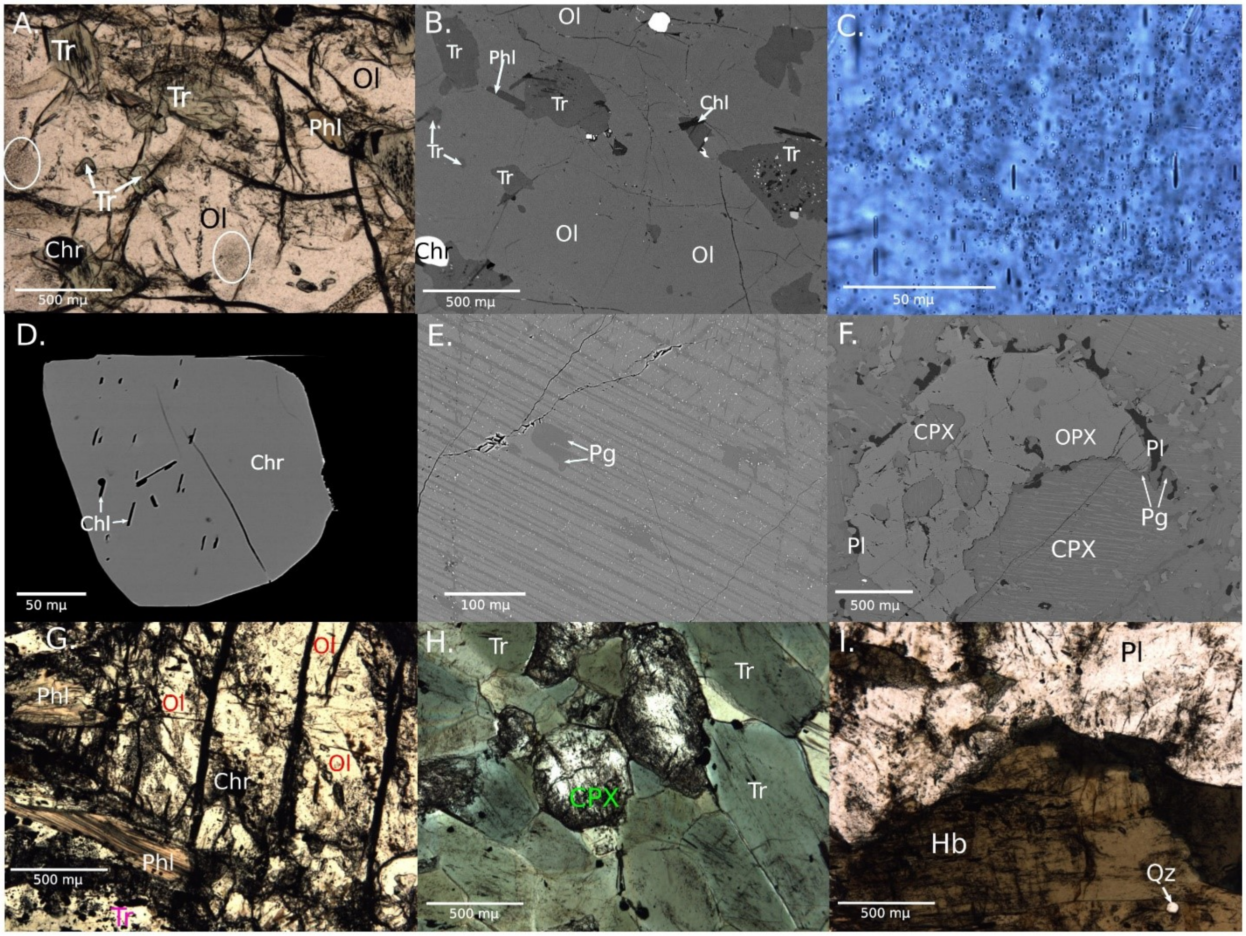

Fig. 2-1. Representative transmitted light (TL) and back-scatter electron (BSE) images for samples from the TUC. A) TL image of a large olivine grain in a dunite sample with inclusions of tremolite, chromite, phlogopite, and chlorite. White circles show areas that are "cloudy" from elongate micro inclusions discussed in text and in C. B) BSE image of A. C) TL image of elongate micro inclusions in olivine. Inclusions are tremolite, chromite, and magnetite. D) BSE image of subhedral unzoned chromite with chlorite laths. E) BSE image of clinopyroxene (light lamellae) exsolving orthopyroxene (dark lamellae) and chromite (white flecks). F) BSE image of large poikiloblast of orthopyroxene containing inclusions of clinopyroxene and rimmed by plagioclase and pargasite. G) TL image of olivine in hydrous ol-clinopyroxenite samples being cross cut by phlogopite and tremolite. H) TL image of amphibolite sample largely composed of tremolite and clinopyroxene. I) TL image of hornblende gabbro sample consists of hornblende and plagioclase. Minor blebs of quartz occur in this sample. Abbreviations: Ol – olivine, Chr – chromite, CPX – clinopyroxene, OPX – orthopyroxene, Tr – tremolite, Phl – phlogopite, Chl – chlorite, Hb – hornblende, Qz – quartz, and Pl – plagioclase.

alteration minerals (Fig. 2-1 G). Relic clinopyroxene is now replaced by tremolite, which pseudomorphs the exsolution lamellae. In addition, clinopyroxene occurs as aggregates of grains 0.2 to 1.5 mm in size, with irregular grain boundaries lacking exsolution lamellae. Clinopyroxene lacking exsolution lamellae often has extensive inclusions of tremolite, phlogopite, magnetite, and minor orthopyroxene and, thus, is secondary after these minerals.

Amphibolites consist of approximately 95 % tremolite, 5 % clinopyroxene, and minor apatite (Fig. 2-1 H). The grain size of tremolite is variable between 0.5 and 2.5 mm and grain boundaries exhibit ~120° triple junctions (Fig. 2-1 H). Clinopyroxene occurs in groups of grains that are 0.2 to 0.7 mm across and have straight and sharp grain boundaries with adjacent tremolite. Clinopyroxene lacks orthopyroxene exsolution. In addition, apatite forms aggregates of grains that are 0.2 to 0.5 mm in size.

The hornblende gabbros consist of 55 to 80 % hornblende, 20 to 45 % plagioclase, and minor quartz. Grain boundaries between hornblende and plagioclase are sutured. Both minerals have grain sizes of 0.5 to 10 mm. Where hornblende has a high modal proportion, grain boundaries between adjacent grains of this mineral are polygonal. Both hornblende and plagioclase contain inclusions of each other. Quartz occurs as small blebs that are less than 50 μm across in hornblende crystals (Fig. 2-1 I).

2.3.2 Mineral chemistry

Mineral chemistry of the TUC is tabulated in Appendix 1. The Mg # (Mg/(Mg+Fe)) of olivine in the dunites range from 81.3 to 84.0 and are lower in the ol-clinopyroxenites, ranging from 77.5 to 81.7. Similarly, the concentration of NiO in olivine is generally higher in the dunites (0.34 to 0.47 wt%) and lower in the ol-clinopyroxenites (0.23 to 0.39 wt%). The concentration of MnO in olivine is invariant between dunites (0.24 to 0.40 wt%) and ol-clinopyroxenites that have a mostly anhydrous mineralogy (0.27 to 0.30 wt%). However, in ol-clinopyroxenites, in which amphibole has extensively replaced precursor phases, the MnO concentration of olivine is very high, from 0.86 to 1.38 wt%. In addition, the lowest olivine Mg # and concentration of NiO in olivine of all the samples is in the hydrous ol-clinopyroxenites (Fig. 2-2). These mineral-scale variations do not extend to a whole-rock scale where anhydrous and hydrous ol-clinopyroxenites have similar major- and trace-element characteristics (Appendix 2).

Oxides in the TUC are dominated by Cr-rich spinel (chromite) variably rimmed by magnetite. Where present, magnetite rims are generally narrow (less than 5 μm). However, when in contact with amphibole, chlorite, or phlogopite, the magnetite proportion of the grains may be large or the chromite may be completely replaced by magnetite. In the dunites, chromite cores have Fe^{2+} numbers (molar $Fe^{2+}/Mg + Fe^{2+}$) of 0.87 to 0.94, Fe^{3+} numbers (molar $Fe^{3+}/Al + Cr + Fe^{3+}$) of 0.21 to 0.39, and Cr numbers (molar Cr/Al + Cr) of 0.72 to 0.91 (one outlier excluded and Fe^{3+} was calculated as in Droop (1987)). In the ol-clinopyroxenites chromite compositions show significant variations depending on the proportion of secondary amphibole present. In samples that have a nearly anhydrous mineralogy, chromite cores have Fe^{2+} numbers of 0.79 to 0.83, Fe^{3+} numbers of 0.09 to 0.12, and Cr numbers of 0.57 to 0.61. In contrast, oxides in the ol-clinpoyroxenite samples with a high modal proportion of amphibole are mostly ferrichromite with Fe^{2+} numbers of 0.93 to 0.99, Fe^{3+} numbers of 0.44 to 0.99, and Cr numbers of 0.87 to 1. Between all samples Cr numbers covary with Fe^{2+} numbers (Fig. 2-3). Relative to Eastern Pacific Rise MORB chromites, those of

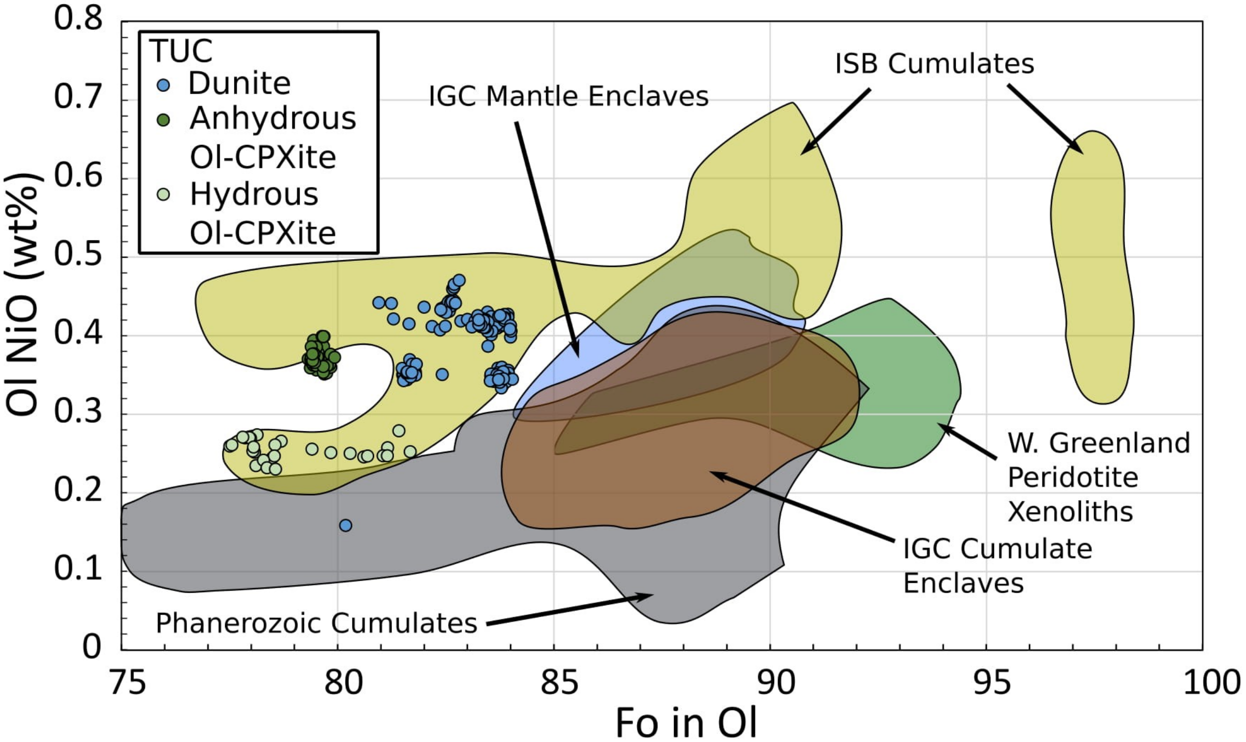

Fig. 2-2. Forsterite vs NiO content in olivine for samples from the TUC, ISB, Ujaragsuuit nunat layered intrusion, peridotite enclaves in the IGC, and West Greenland cratonic mantle. Sources are as follows: ISB from Dymek et al. (1988) and Szilas et al. (2015); West Greenland mantle from Bernstein et al. (2013); IGC cumulate enclaves from Rollinson et al. (2002); IGC mantle enclaves in the IGC from Friend et al. (2002).

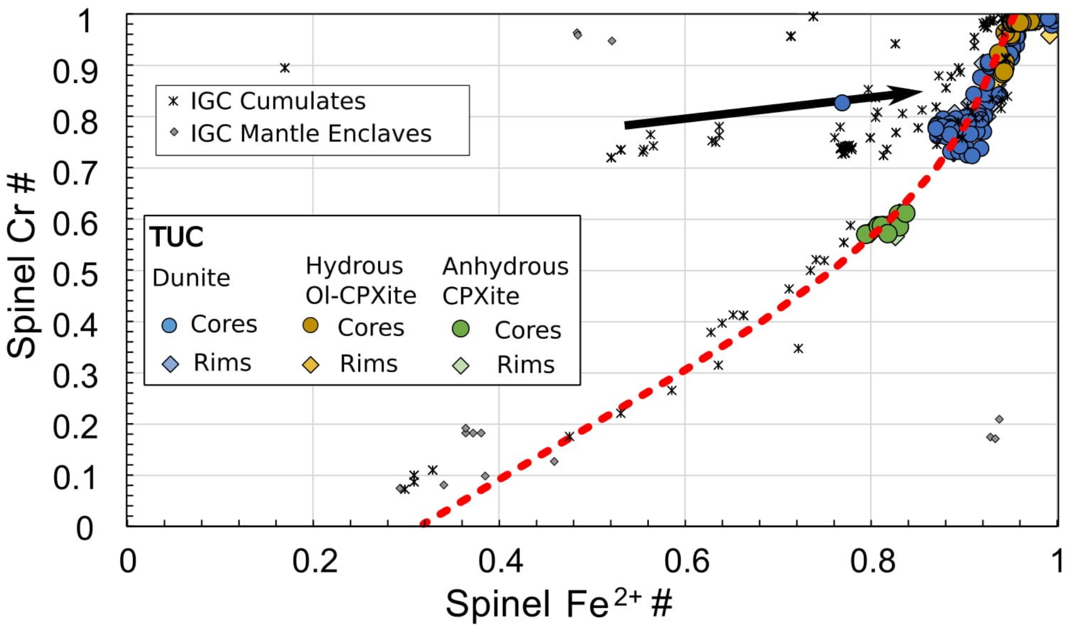

Fig. 2-4. Spinel Fe^{2+} # vs Cr # for samples from the TUC and spinel analyses from the literature for other samples in the Isukasia area. Data sources are the same as in Fig. 2-2 with additional chromite analyses from Coggon et al. (2015) for the Ujaragssuit nunat layered intrusion. Cumulate rocks in the IGC include those from the ISB. Red dashed line follows chromite equilibration with olivine of forsterite 83 at 550 °C from Wlotzka (2005). Black arrow is the main chromite trend of Rollinson (2002) for the Ujaragssuit nunat layered intrusion interpreted as magmatic in origin.

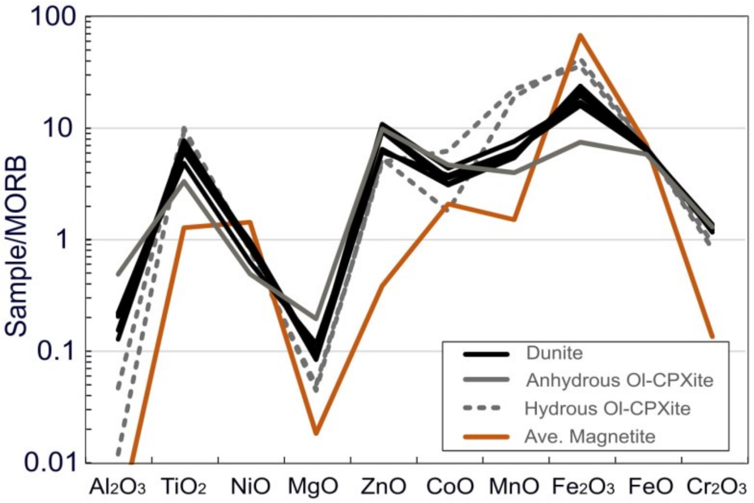

Fig. 2-3. Average chromite cores from each sample and average magnetite from the TUC normalized to MORB spinel from Page and Barnes (2009).

the TUC display enrichment in TiO_2, ZnO, MnO, CoO, Fe_2O_3, and FeO and depletions in Al_2O_3 and MgO (Fig. 2-4).

The pyroxene compositions of rocks from the TUC classify as diopside and clinoenstatite (Fig. 2-5). Clinopyroxenes from anhydrous ol-clinopyroxenite samples have lower Mg #'s (0.80 to 0.90) and higher TiO_2 (0.11 to 0.25 wt%) and Al_2O_3 (1.45 to 2.24 wt%). Clinopyroxene from hydrous ol-clinopyroxenites have high Mg #'s (0.90 to 0.93) and low TiO_2 (0.02 to 0.05 wt%) and Al_2O_3 (0.12 to 0.26 wt%). The clinopyroxenes from the amphibolites have Mg #'s from 81 to 82, and similar TiO_2 (0.03 to 0.06 wt%) and Al_2O_3 (0.27 to 0.3 wt%) to clinopyroxenes from the hydrous ol-clinopyroxenites.

Orthopyroxene occurs in ol-clinopyroxenites as an exsolution phase, reaction coronas on olivine and clinopyroxene, as a poikiloblastic phase. It occurs rarely in dunites as an interstitial phase partially replaced by amphibole. In the ol-clinopyroxenites, two populations of orthopyroxene exist with high En contents ranging from 78 to 81 and low En contentsranging from 67 to 70 (one outlier excluded) (Fig. 2-5). These correspond to higher and lower Mg/Fe ratios in the clinopyroxenes from which the orthopyroxene exsolved. Secondary orthopyroxene, forming reaction coronas and poikiloblastic phases, have higher Wo components than exsolved orthopyroxene (Fig. 2-5). In addition, orthopyroxene in the dunites has the highest En contents of all orthopyroxenes in the TUC ranging from 83 to 84.

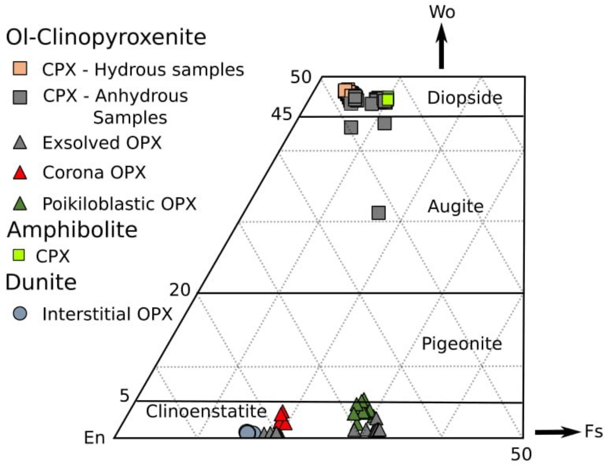

Fig. 2-5. Classification of pyroxenes from the TUC based on a portion of the Mg-Fe-Ca quadrilateral triangle of Morimoto (1988).

2.3.3 Major-element geochemistry

The major-element geochemical data is given in Appendix 2. The whole-rock geochemistry of the TUC largely reflects that of the mineral constituents which characterize the samples. The dunites (n=7) have a high concentration of refractory elements MgO (37.6 to 41.5 wt%), FeO (12.5 to 15.2 wt%), Ni (1794 to 2865 ppm), and Cr (4508 to 16545 ppm) and low SiO_2 (40.5 to 45.6 wt%), CaO (1.04 to 2.88 wt%), Al_2O_3 (1.18 to 1.63 wt%), and TiO_2 (0.10 to 0.14 wt%).

The ol-clinopyroxenites have significantly less MgO (17.8 to 23.7 wt%) than the dunites, a gap which separates the dunites from the other lithologies of the TUC (Fig. 2-6). In addition, the ol-clinopyroxenites have lower FeO (8.07 to 9.90 wt%), Ni (437 to 810 ppm), and Cr (1384 to 4274 ppm) and higher SiO_2 (50.8 to 53.1), CaO (13.2 to 15.5 wt%), Al_2O_3 (1.56 to 2.66 wt%), and TiO_2 (0.12 to 0.25 wt%).

Relative to the ol-clinopyroxenites, amphibolites (n=2) have similar CaO (13.8 and 14.1 wt%), lower MgO (17.1 and 18.5 wt%), Ni (397 and 423 ppm) and Cr (1398 and 1816 ppm) and higher SiO_2 (53.5 and 54.5 wt%), Al_2O_3 (2.51 and 3.29 wt%), and TiO_2 (0.26 and 0.28 wt%). There is some overlap between the ol-clinopyroxenites and amphibolites, in that one of the ol-clinopyroxenites (565467) is similar to amphibolites (Figs. 2-6 and 2-7).

Relative to the amphibolites, the hornblende gabbros (n=2) have lower SiO_2 (52.6 and 52.7 wt%), MgO (9.77 and 13.7 wt%), and CaO (10.0 and 11.2 wt%) and higher FeO (11.7 and 12.0 wt%), Al_2O_3 (7.33 and 11.7 wt%), TiO_2 (0.45 and 0.71 wt%), Ni (177 and 324 ppm), and Cr (446 and 739 ppm).

Fig. 2-6. Whole rock MgO vs major elements in the TUC samples compared with mineral chemistry and data from the literature for ISB, mantle enclaves in the IGC, West Greenland cratonic mantle, and clinopyroxenite cumulates from arc environments. Where not classified as tholeiitic or boninitic, samples from the ISB have been grouped into these affinities based on $(Gd/Yb)_{PM}$ and/or Al_2O_3/TiO_2 ratios discussed in text. The green star is the most magnesian rich olivine measured in this study and the orange star is an analysis of clinopyroxene in this study furthest from orthopyroxene exsolution lamellae. Red and Blue arrows are from MELTS modelling discussed in text. The gap in MgO in the cumulates is due to the rapid transition from olivine accumulation (high MgO) to clinopyroxene accumulation (lower MgO) in the model. Data sources are as follows: for the ISB from Dymek et al. (1988), Rosing and Rose (1993), Polat et al. (2002), Polat et al. (2003), Polat and Hofmann (2003), Frei and Jensen, (2003), Komiya et al. (2004), Furnes et al. (2009), Jenner et al. (2009), Hoffmann et al. (2011), Rizo et al. (2013), and Szilas et al. (2015); Mantle enclaves in the IGC are from Friend et al. (2002); clinopyroxenite cumulates from Himmelberg and Loney (1995), Helmy and Mahallawi (2003), Jagoutz and Schmidt (2012), Li et al. (2013), and Tilhac et al. (2016); West Greenland cratonic mantle from Wittig et al. (2008).

In the dunites MgO and CaO are negatively correlated, however, other elements in these samples do not covary with MgO (Fig. 2-6). Between the ol-clinopyroxenite, amphibolite and hornblende gabbros there is an inverse relationship between MgO and FeO, Al_2O_3, TiO_2, and Na_2O, and positive relationship between MgO and CaO. In addition, there is a positive relationship between MgO, Ni, and Cr between all samples.

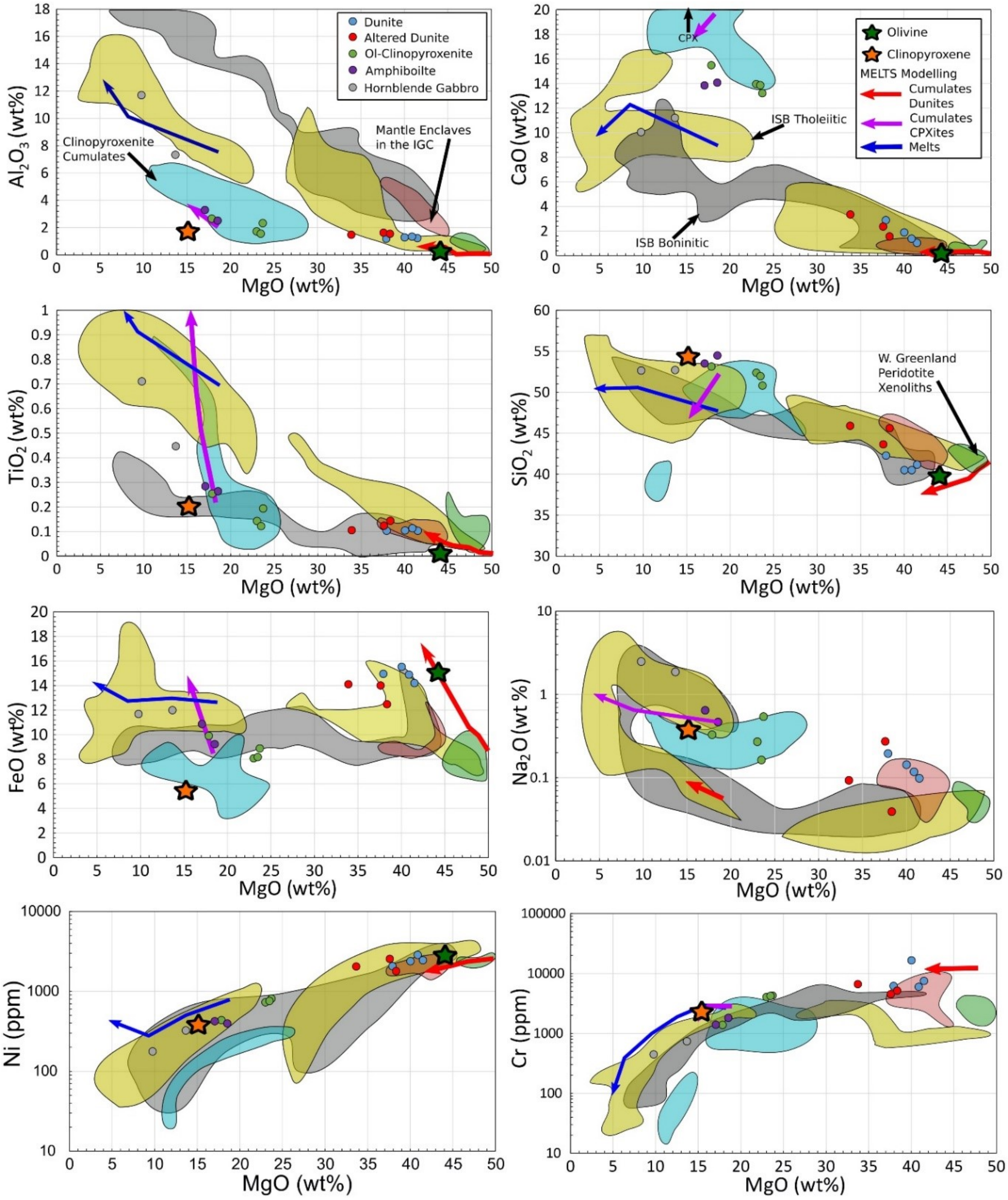

2.3.4 Trace-element geochemistry

The trace element geochemical data is given in Appendix 3. Most samples from the TUC have primitive mantle normalized trace-element patterns that are characterized by depletions in high field strength elements (HFSEs) relative to rare earth elements (REEs), enrichments in Th relative to Nb, and fractionated REEs such that light REEs (LREEs) are enriched relative to heavy REEs (HREEs) (Fig. 2-7). In some samples, LREEs are fractionated such that PUM-normalised abundances of Nd are greater than La. With some overlap, the dunites tend to have the lowest concentrations of trace elements, followed by ol-clinopyroxenites, amphibolites, and hornblende gabbros.

One hornblende gabbro sample does not have negative Th, Hf, or Zr anomalies, and is characterized by a slightly negatively sloped trace-element pattern, enriched in LREEs and with negative Nb and Ti anomalies. In addition, sample 565462, a serpentinite from a narrow shear zone near the edge of the TUC, displays Zr, Hf, and Nb enrichment and depletions in LREE and Eu relative to other samples, and shows inconsistent behavior in plots of Zr and Hf vs Al_2O_3 (Figs. 2-7 and 2-8), which are characteristics of samples in the ISB that have suffered significant alteration by CO_2-rich fluids (Polat and Hofmann, 2003). In addition, sample 565455 (a dunite) plots towards the serpentinite, and these samples have likely undergone significant alteration (Fig. 2-8). In addition to these samples, dunite 565453 is adjacent to an intrusive pegmatite vein and has enriched Ta, Nb, and HREE, which are not characteristic of any other samples in the TUC, and hence this sample is characterized as altered. As such, these samples have been excluded from any petrogenetic interpretations.

In plots of Al_2O_3 vs REEs, dunite, ol-clinopyroxenite, and amphibolites show good correlations (Fig. 2-8). However, hornblende gabbros fall away from such trends. Thorium and Nb are generally poorly correlated with Al_2O_3. Plots of Al_2O_3 vs TiO_2 are well correlated, and, with the exception of altered samples, so are Hf and Zr with Al_2O_3.

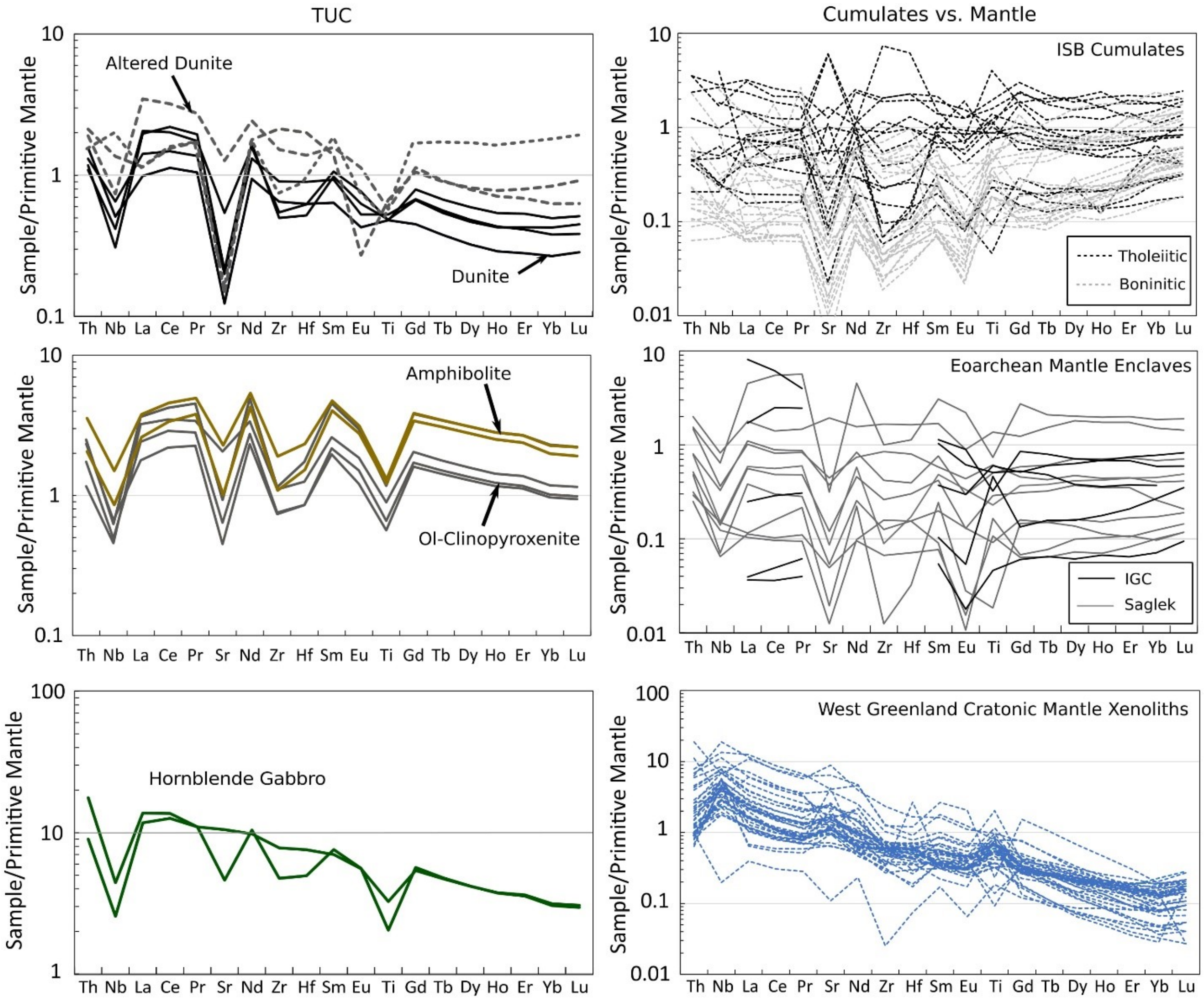

Fig. 2-7. Primitive mantle normalized trace element patterns for samples from the TUC, ISB, mantle enclaves form the Saglek-Hebron block of the North Atlantic craton, IGC mantle encalves, and West Greenland cratonic mantle. Data source are as follows: ISB from Szilas et al. (2015); Saglek-Hebron area from Ishikawa et al. (2017); IGC from Friend et al. (2002); West Greenland cratonic mantle from Wittig et al. (2008) Primitive mantle values from McDonough and Sun (1995).

2.3.5 Platinum group element geochemistry

Platinum group element data are given in Appendix 4. Iridium group PGEs (IPGEs) behave as compatible elements in the TUC rocks (Fig. 2-9), having the highest concentration in the dunites (n=5; Os; 6.2 ± 5.0 ppb, Ir; 4.8 ± 4.5 ppb, Ru; 13.8 ± 9.0 ppb) followed by ol-clinopyroxenite (n=4; Os; 1.65 ± 0.7 ppb, Ir; 1.2 ± 0.6 ppb, Ru; 4.4 ± 1.3 ppb), amphibolite (n=2; Os; 0.28 and 0.29 ppb, Ir; both at 0.31 ppb, Ru; 0.98 and 1.71 ppb), and hornblende gabbros (n=1; Os; 0.12 ppb, Ir; 0.17 ppb, Ru; 0.28 ppb). In contrast, platinum group PGEs (PPGEs) and Re show little variability between dunites, ol-clinopyroxenites, and amphibolites in the TUC. The dunites have Pt of 2.4 ±

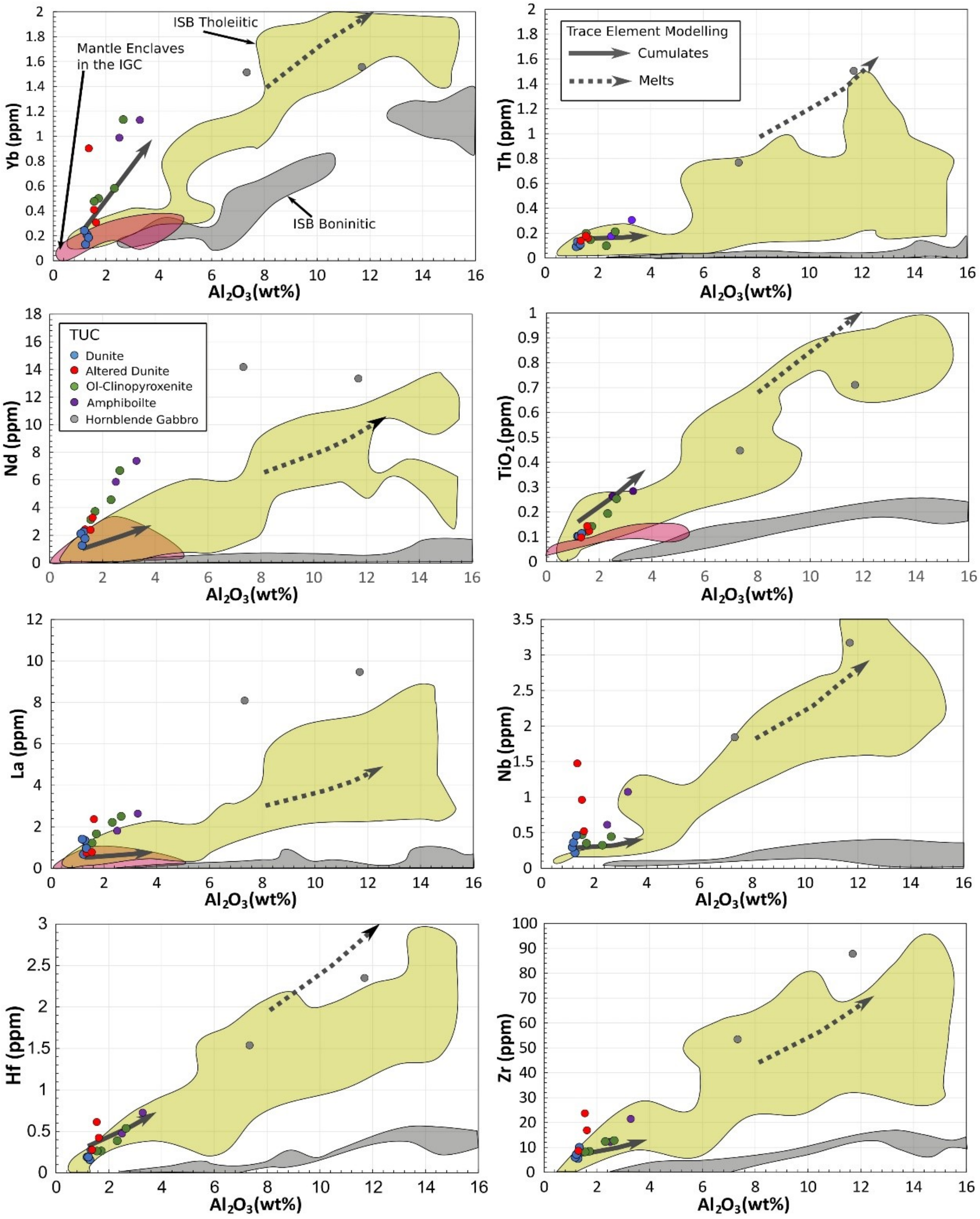

Fig. 2-8. Plots of Al_2O_3 vs trace elements in the TUC. Data sources for boninitic and tholeiitic fields are the same sources as in Fig. 2-6. Solid and dashed grey arrows are modelled cumulate and melt discussed in text. Both modelled cumulate and melt were extrapolated through the three stages of fractional crystallization. Partition coefficients and methods for the model are given in Appendix 6.

1.9 ppb, Pd of 0.76 ± 0.46 ppb, and Re of 0.02 ± 0.01 ppb; the ol-clinopyroxenites have Pt of 0.34 ± 0.17 ppb, Pb of 0.47 ± 0.21 ppb, and Re of 0.02 ± 0.01 ppb; the amphibolites have Pt of 0.03 and 0.87 ppb, Pd of 0.15 and 0.21 ppb, and Re of 0.004 and 0.009. Platinum group PGEs in the hornblende gabbro sample are relatively enriched compared with other samples, with Pt of 4.2 ppb, Pd of 5.1 ppb, and Re of 0.177 ppb.

Dunite, ol-clinopryoxenite, and amphibolites from the TUC display inter-element PGE fractionation such that primitive mantle normalized abundances are characterized by positive Ru anomalies and an enrichment in IPGEs relative to PPGEs (Fig. 2-10). Positive Ru anomalies in some samples are likely due to Cr-based interferences (Appendix 5). In contrast, the one hornblende gabbro sample analyzed displays relatively flat primitive mantle normalized I-PGE patterns and IPGE abundances that are depleted relative to PPGEs (Fig. 2-10). In addition, most samples in the TUC are characterized by a depletion in Pt relative to Pd (Fig. 2-10).

2.3.6 Re-Os isotopes and model ages

Re-Os isotope systematics within the TUC and associated rocks (Table 2.2) vary systematically with lithofacies. The dunites have the lowest ^{187}Os/^{188}Os (0.109 to 0.114) and ^{187}Re/^{188}Os (0.003 to 0.039) ratios. The ol-clinopyroxenites have ^{187}Os/^{188}Os from 0.112 to 0.123 and ^{187}Re/^{188}Os from 0.044 to 0.174. The amphibolites have ^{187}Os/^{188}Os of 0.115 and 0.126 and ^{187}Re/^{188}Os of 0.079 and 0.152. The one hornblende gabbro sample measured has a ^{187}Os/^{188}Os of 0.904 and ^{187}Re/^{188}Os of 7.79, much more radiogenic than the other samples.

Ratios of ^{187}Os/^{188}Os are moderately radiogenic relative to estimates for primitive upper mantle (PUM) (Meisel et al., 2001; Becket et al., 2006) at 3.8 Ga. The average γOs_i values for the dunites is 7.4 ± 1.3, for the ol-clinopyroxenites is 7.6 ± 1.2, for the two amphibolites measured is 8.1 and 14, and for the hornblende gabbro is 286.

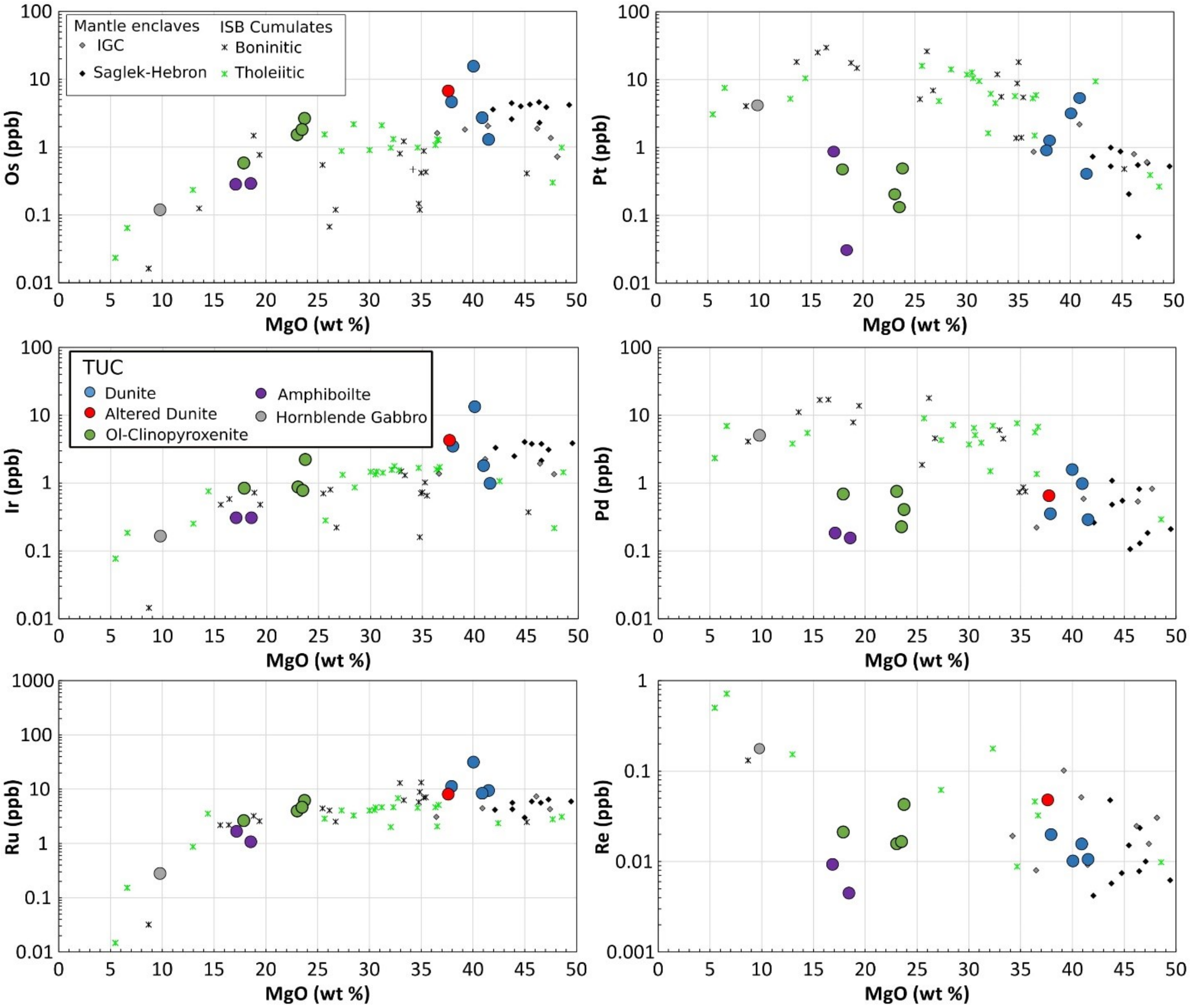

Fig. 2-9. MgO vs PGEs samples from the TUC and, for comparison, data from the literature for the Isukasia region. Sources are as follows: ISB cumulates from Szilas et al. (2015), and Rizo et al. (2016); Saglek-Hebron mantle enclaves from Ishikawa et al., (2017); IGC mantle enclaves from Bennet et al. (2002) and van de Locht et al., (2018). Only data from PPGE depleted peridotites south of the ISB are shown from van de Locht et al., (2018). In addition, only PPGE depleted lithospheric mantle peridotites are shown from Ishikawa et al., (2017). Note: there are no published data for the whole rock content of both MgO and PGEs for samples from the Ujaragssuit nunat layered intrusion.

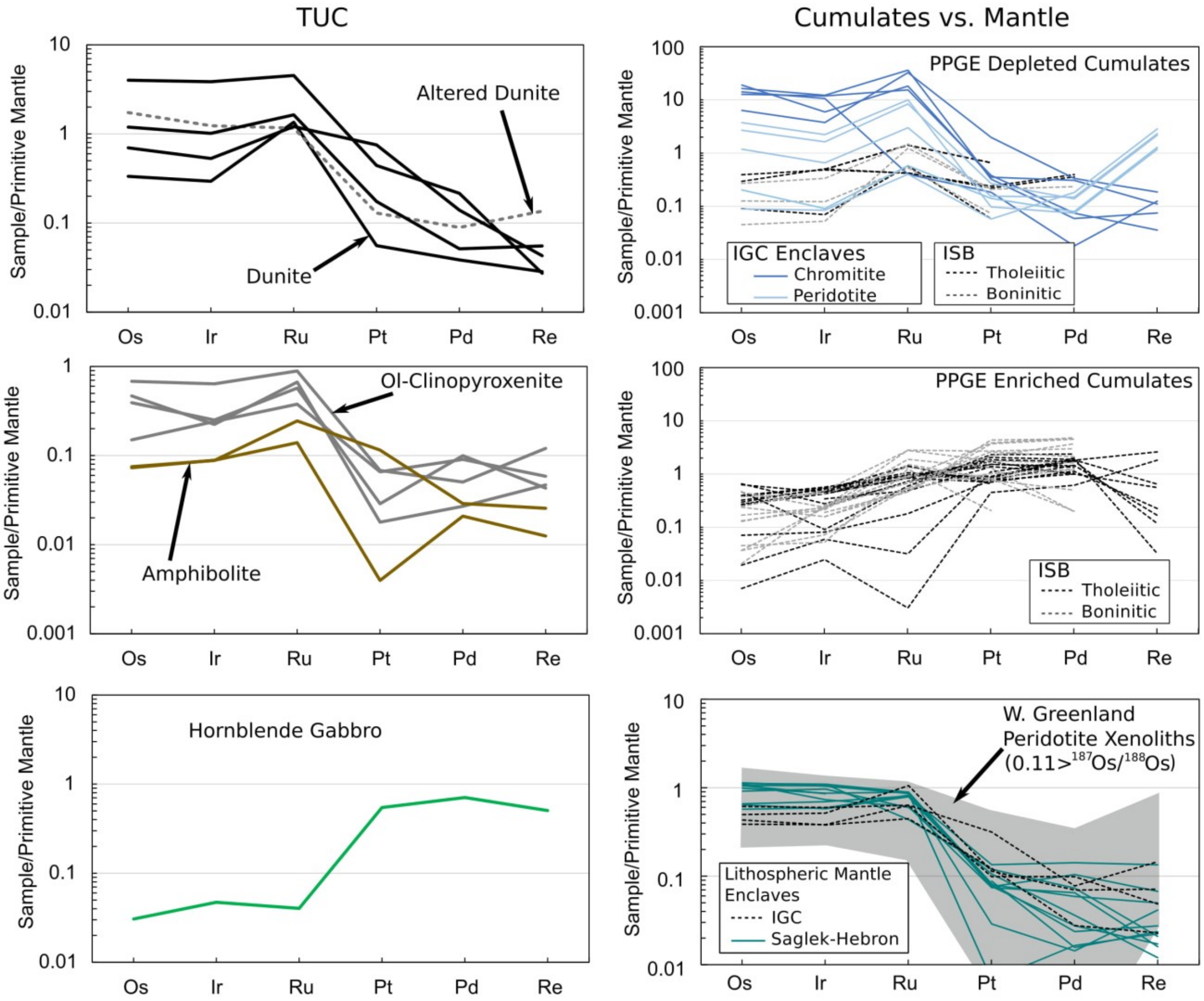

Fig. 2- 10. Primitive mantle normalized PGE concentrations of the TUC and, for comparison, data from the literature from the Isukasia region. Data sources are as in Fig. 2-9 with additional data from Coggon et al. (2015). NAC peridotite xenoliths from Wittig et al. (2010). Normalization values are from Becker et al. (2006).

Table 2. 2 – Summary of the Re-Os abundances and isotopic data from the TUC whole rock analyses.

Sample	Os (ppb)	2σ abs.	Re (ppb)	2σ abs.	^{187}Re/^{188}Os	Abs. 2σ	^{187}Os/^{188}Os	Abs. 2σ	γOs*	Abs. 2σ	T ma (PUM)	T rd (PUM)
Dunite												
565452	15.61	0.08	0.0095	0.0004	0.0031	0.0003	0.10906	0.00007	6.79	0.07	2.87	2.85
565470	4.65	0.03	0.0193	0.0104	0.0206	0.0108	0.11037	0.00008	6.96	0.70	2.81	2.67
565471	2.72	0.03	0.0150	0.0006	0.0277	0.0022	0.1140	0.0001	10.03	0.18	2.33	2.18
565472	1.30	0.02	0.0100	0.0005	0.0392	0.0043	0.1113	0.0001	6.65	0.30	2.81	2.55
565455	6.77	0.04	0.0476	0.0015	0.0342	0.0013	0.11071	0.00007	6.42	0.11	2.85	2.63
Ol-clinopyroxenite												
565451	2.66	0.03	0.0421	0.0009	0.0774	0.0019	0.1144	0.0002	7.20	0.24	2.60	2.13
565450	1.82	0.02	0.0164	0.0004	0.0439	0.0012	0.1119	0.0002	6.96	0.20	2.74	2.46
565467	0.59	0.02	0.0205	0.0005	0.1742	0.0083	0.1233	0.0003	9.73	0.60	1.51	0.89
565469	1.53	0.02	0.0151	0.0004	0.0497	0.0014	0.1119	0.0002	6.62	0.24	2.78	2.46
Amphibolite												
565464	0.29	0.02	0.0090	0.0003	0.152	0.011	0.1262	0.0002	13.99	0.72	0.76	0.49
565466	0.28	0.02	0.0044	0.0002	0.0790	0.0058	0.1153	0.0003	8.06	0.48	2.45	2.00
Hornblende Gabbro												
565463	0.12	0.01	0.1768	0.0038	7.79	0.95	0.904	0.003	285.82	61.05	5.99	N/A

Estimates for PUM are from Meisel et al. (2001) and Walker et al. (2002). Decay constant used from Selby et al. (2007).
*Relative to PUM at 3.81 Ga.

2.4 Discussion

2.4.1 Mineral chemistry – discerning primary and secondary effects

The mineral chemistry of the TUC has largely been affected by a redistribution of elements on a hand-sample scale. All olivine grains contain inclusions of tremolite, phlogopite, chromite, and magnetite which indicate a prograde metamorphic origin for the olivine (Dymek et al., 1988; Peltonen, 1990). Olivine from other ultramafic lithologies in the Isukasia region are not considered to reflect primary compositions, but rather compositions that re-equilibrated with alteration phases during metamorphism (Dymek et al., 1988; Szilas et al., 2015). Such metamorphic re-equilibration may result in an increase or decrease in the forsterite content of olivine in altered rocks (Dymek et al., 1988; Peltonen, 1990; Szilas et al., 2015). In addition, increases in NiO in olivine are the result of the lower affinity of NiO for amphibole relative to olivine (Peltonen, 1990). Indeed, the high NiO at low forsterite contents of the olivines observed in the TUC dunites are high relative to phanerozoic cumulates (Fig. 2-2). In addition, high MnO contents of olivine, similarly found in the TUC hydrous ol-clinopyroxenites (1.1 ± 0.2 wt%), have been attributed to prograde crystallization of olivine after serpentine in picritic basalts (Peltonen, 1990). However, MnO contents in olivines from other TUC lithologies (0.27 ± 0.04 wt%) are in the range of igneous olivines (e.g. Simkin and Smith, 1970). It is difficult to assess if any of the geochemical characteristics of the TUC olivines are preserved from the primary olivine compositions. More likely, much of the present-day composition of the olivine in the TUC is the product of whole-rock Mg # (Fig. 2-11), the partitioning of Fe and Mg between olivine and other Fe-Mg minerals, and the temperature of metamorphic equilibration.

Despite its advantage as a petrogenetic indicator, the chemistry of chromite in the peridotites of the TUC has largely been altered by secondary processes. Comparing the composition of chromite in the TUC to the igneous and mantle compositional trends of Barnes and Roeder (2001), variations in Fe^{2+}, Fe^{3+}, and Cr are inconsistent with either igneous or mantle processes. The TUC chromite compositional variations differ from chromite analyses from the Ujaragssuit nunat layered intrusion peridotites which have been interpreted as retaining igneous signatures (Rollinson et al., 2002) (Fig. 2-3). Instead, TUC chromite compositions likely indicate sub-solidus equilibration with olivine of low forsterite content at low temperature (Fig. 2-3). The low MgO and Al_2O_3 and high TiO_2, ZnO, MnO, CoO, Fe_2O_3, and FeO in the chromite cores, relative to, for example, eastern pacific MORB chromites (Fig. 2-4), is considered to reflect metamorphic equilibration with

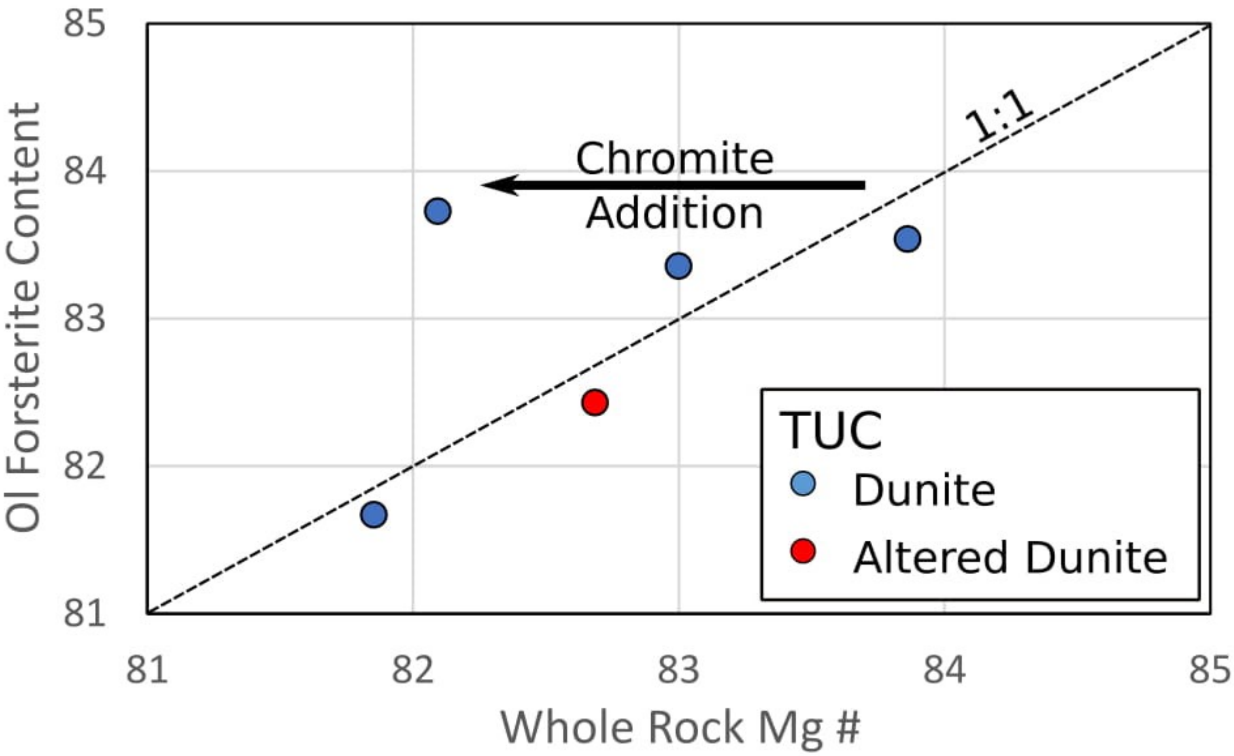

Fig. 2-11. The olivine forsterite contents in the dunites largely reflecting whole rock Mg #'s.

hydrous phases followed by chromite recrystallization (Gervilla et al., 2012; Colas et al., 2014). The result of this process is manifest in the major- and trace- element patterns characterizing the chromites of the TUC (Fig. 2-4), and also accounts for the presence of chlorite inclusions in otherwise homogeneous chromite (Fig. 2-1 D). Finally, magnetite rims on these chromite grains indicate further late alteration by oxidizing fluids. From these results, it is evident that, in the TUC peridotites, the composition of the original magmatic chromite has been obliterated by metamorphic processes and cannot be used as a petrogenetic indicator.

There are two types of clinopyroxene in the TUC ol-clinopyroxenites and amphibolites; those which have exsolved orthopyroxene plus oxides and those that lack exsolution lamellae and commonly contain inclusions of alteration phases, such as tremolite and phlogopite. Clinopyroxene without exsolution lamellae only occurs in hydrous ol-clinopyroxenites and amphibolites and is characterized by low Al_2O_3 at a given Mg # (Fig. 2-12). The very low Al_2O_3 is uncharacteristic of most mantle or igneous clinopyroxene, however, such low Al_2O_3, as well as low TiO_2 concentrations are found in secondary clinopyroxene closely associated with amphibole in metasomatized mafic and ultramafic igneous rocks (Fig. 2-12). As these compositions are a hallmark of the clinopyroxenes in the hydrous ol-clinopyroxenites of the TUC that have high modal amphibole, they are interpreted as metamorphic in origin and related to the recrystallization of the clinopyroxene and exchange of these elements between clinopyroxene and replacive amphibole.

Clinopyroxene with orthopyroxene exsolution lamellae only occur in anhydrous ol-clinopyroxenites. The exsolution of orthopyroxene and oxides from clinopyroxene is a feature both of slowly cooled magmatic rocks (Poldervaart and Hess 1951; Maeda et al., 2002; Zhu et al., 2017) and those that have experienced granulite-facies metamorphism (Liu et al. 2003). Calculated temperatures of clinopyroxene-orthopyroxene exsolution pairs, using the thermometer of Brey and Kohler (1990), gives a narrow temperature range of between 745 and 774 °C. Considering the CaO-SiO_2-MgO-H_2O system (Spear, 1993), this would be consistent with metamorphic equilibration of the mineral assemblage of anhydrous ol-clinopyroxenites; olivine, enstatite, and diopside. However, many of the peridotites in the TUC show olivine and tremolite to be in equilibrium and lack orthopyroxene, suggesting an upper temperature limit of ~700 °C. An exception is a single dunite sample that has orthopyroxene partially consumed by tremolite, perhaps indicating that the forsterite-tremolite assemblage was retrogressed from granulite-facies conditions. In addition, regional metamorphism is thought to have not exceeded amphibolite facies

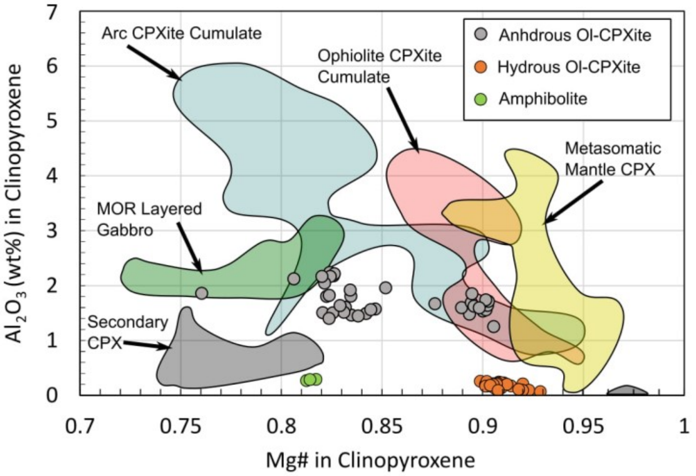

Fig. 2-12. Mg # vs Al_2O_3 in clinopyroxene for rocks of the TUC. Also, shown are the fields for secondary clinopyroxene in igneous mafic and ultramafic rocks (Dungan, 1979; Maeda et al., 2002), metasomatic mantle clinopyroxene (Coltorti et al., 1999; Franz et al., 2002; Simon et al., 2003; Pivin et al., 2009; Sun et al., 2012), and clinopyroxenes from mid-ocean ridge layered gabbros (Maeda et al., 2002), Arc clinopyroxenite cumulates (Himmelberg and Loney, 1995; Ma et al., 2016), ophiolite clinopyroxenite cumulates (Elthon et a., 1982; Parlak et al., 1996; Koga et al., 2001), and mantle peridotite xenoliths (Simon et al., 2003; Harvey et al., 2012).

metamorphism (Nutman et al., 2002). These results are speculative, in part because they depend on the presence of H_2O in the system. The modal mineralogy of the anhydrous ol-clinopyroxenites is similar to that expected in from igneous processes considering the major-element composition of these samples (see section *2.4.2*), and the composition of the clinopyroxenes may not significantly differ from a precursor pyroxene, if one existed. If the Mg # of the clinopyroxenes in the TUC are reflective of primary processes, a cumulate origin for clinopyroxenites is most plausible.

2.4.2 Constraints on the origin of the TUC – partial melting or crystal accumulation

It has been suggested that some massive peridotite enclaves within the IGC are relics of Eoarchean lithospheric mantle (Nutman et al., 1996; Friend et al., 2002), i.e., residues from partial melting, while other layered peridotite enclaves have been interpreted to be of a cumulate origin (Rollinson et al., 2002; Appel et al., 2002; Coggon et al., 2015). The geochemistry of the TUC is far too evolved to imply that the enclave, as a whole, is a fragment of unmodified mantle material as the whole rock Mg#'s are more fertile than estimates of primitive mantle (cf. Pearson et al., 2004, and references therein). However, being surrounded by more evolved rocks of the IGC and having a complex metamorphic history does not preclude that some areas of the TUC were derived from alteration of pristine mantle and this possibility is evaluated below on the basis of major-, trace-, and platinum-group element geochemistry.

Major-element systematics of peridotite enclaves in the IGC, interpreted as Eoarchean mantle, as well as other peridotites in the ISB, that are interpreted as cumulates, are very similar to each other, with the compositions of both overlapping with the composition of the dunites in the TUC for most elements (Fig. 2-6). However, those enclaves interpreted as lithospheric mantle have low FeO contents relative to the dunites of the TUC and some ISB ultramafic cumulates (Fig. 2-6). In their review of serpentinites, Deschamps et al. (2013) find that serpentinization causes only minor variations in FeO and MgO contents relative to the precursor rocks and so the elevation in FeO is unlikely to be due to this process. However, some increase in FeO in abyssal and subduction-related peridotites can occur via melt/rock interaction (Deschamps et al., 2013). Increases in FeO are also observed in melt metasomatized mantle xenoliths (Bodinier et al., 1990; Weyer and Ionov, 2007; Wittig et al., 2008). However, with the exception of some extreme cases, FeO enrichment via melt/rock interactions with mantle rocks does not produce the exceptionally high FeO content found in the dunites of the TUC (Fig. 2-13). In contrast, such elevated FeO contents (>12 wt%) are a common characteristic of cumulate dunites (Szilas et al., 2015) (Fig. 2-13). In addition, very few mafic rocks in the Isukasia area have FeO contents higher than those in the TUC (Fig. 2-6). The high proportion of mixing between primitive mantle and these basalts needed to generate the high FeO in the TUC dunites would result in a rock more similar to the basalts than the dunites.

To further evaluate a cumulate origin for the rocks of the TUC, hypothetical cumulates and melts resulting from fractional crystallization were modelled using the MELTS package (Ghiorso and Sack, 1995; Asimow and Ghiorso, 1998) (Fig. 2-6). The model parameters were set to 3 kbar pressure, FMQ of +1, and a starting composition of the least altered tholeiitic picritic basalts of Polat and Hofmann (2003) with 3.6 wt% H_2O. The H_2O content of the melt was set to saturation (3.6 wt% H_2O) as this is the approximate minimum H_2O required to produce clinopyroxenite cumulates, and the pressure of 3 kbar is the minimum pressure required to dissolve this amount of H_2O in the melt. The modelling was evaluated at various oxygen fugacities from FMQ -2 to FMQ +3. However, there are only slight variations in the results at different oxygen fugacities. An oxygen fugacity of FMQ+1 was chosen to be the approximate middle ground between modern MORB, ocean-island basalts, and island-arc basalts (cf. Ballhaus et al., 1990), and is consistent with the estimated parental melt composition of some >3.8 Ga cumulate peridotites enclaves in the IGC (Rollinson, 2002). The normalized starting composition of the modelled melt at the liquidus temperature of 1390 °C, 3 kbar, and +1 FMQ is given in Table 2.3. The model is only considered for a mass fraction of crystallization of 0.4. Initially olivine and minor chromite are precipitated to a mass fraction of ~0.28. This is followed by crystallization of clinopyroxene and minor Cr-rich magnetite to a mass fraction of ~0.12.

Table 2. 3 Normalized starting composition of the picritic basalts used in the MELTs modelling.

Oxide	SiO_2	TiO_2	Al_2O_3	Fe_2O_3	FeO	MnO	MgO	CaO	Na_2O	K_2O	NiO	Cr_2O_3	H_2O
Wt%	47.00	0.68	7.88	2.59	9.88	0.18	18.35	8.81	0.48	0.06	0.1	0.36	3.6

The model fits well with the major-element composition of the TUC (Fig. 2-6) in that the dunites can be produced as olivine/chromite cumulates with minor interstitial melt. In terms of Al_2O_3, TiO_2, SiO_2, and FeO, three ol-clinopyroxenites appear to be clinopyroxenite cumulates with

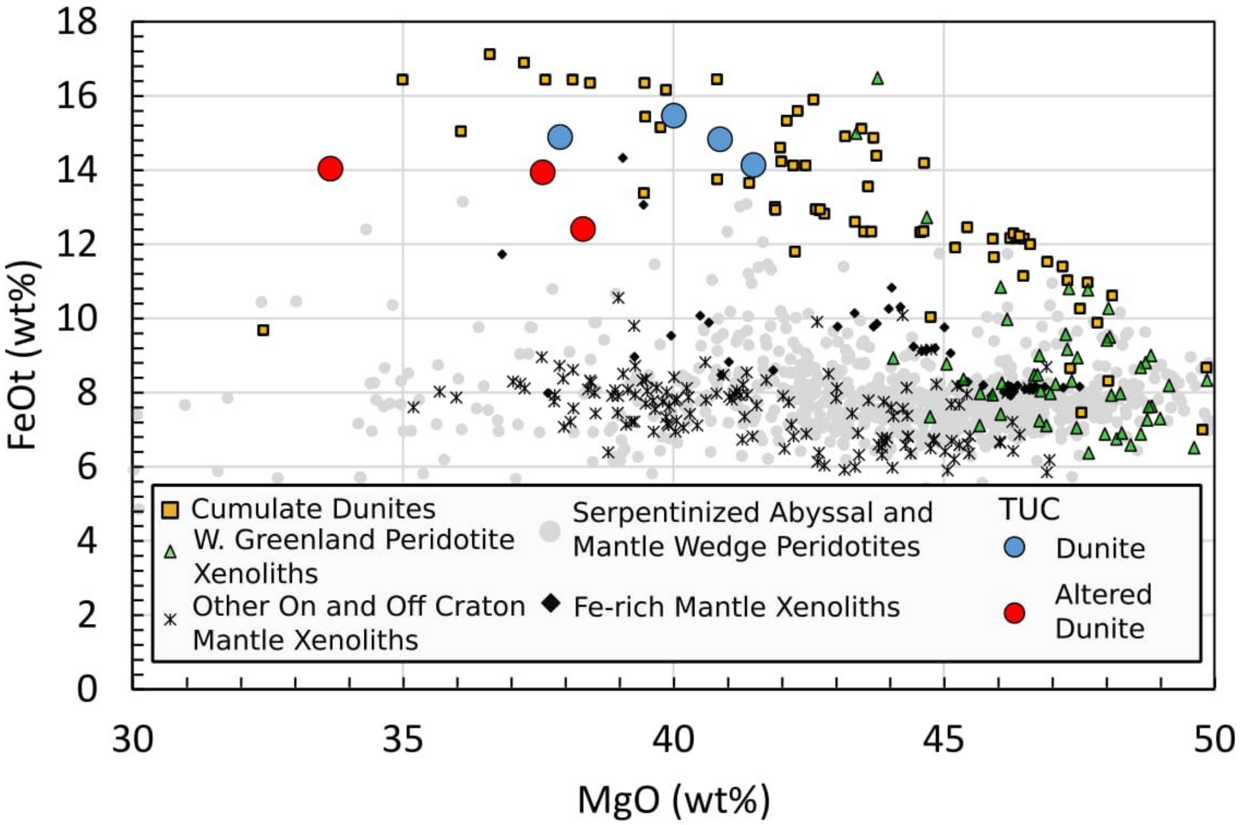

Fig. 2-13. MgO vs FeO content for mantle peridotites and cumulate dunite compared to the dunites from the TUC. Sources: Cumulate dunites from Day et al., (2008), Jagoutz and Schmidt (2012), Wang et al., (2013), and Li et al., (2013). On and off craton mantle xenoliths from Pearson et al., (2004) and Harvey et al., (2012), respectively. Metasomatised Fe-rich mantle xenoliths from Bodinier et al., (1990) and Ionov et al., (2005). Serpentinized peridotites from Deschamps et al., (2013). NAC peridotite xenoliths from Wittig et al. (2010).

variable olivine, and the amphibolites and one ol-clinopyroxenite plot with clinopyroxene cumulates. It must be noted that the MELTs modelling does not produce olvine-clinopyroxene cumulates resulting a large gap in MgO between largely olivine cumulates and clinopyroxene cumulates (Fig. 2-6). The reason for this is unknown, as ol-clinopyroxenite cumulates exist in the nature (e.g. Himmelberg and Loney; 1995; Day et al., 2008; Li et al., 2013). However, this may indicate some limitations to the MELTs program. The hornblende gabbros have compositions similar to melts resulting from the fractional crystallization of the cumulate sequence and/or with mafic rocks from ISB, and these are interpreted to be crystallized melt.

The similarity of the major-element composition of these samples to previously studied, geographically proximal volcanic rocks combined with their compositions being explicable as modelled cumulates and melts for most major elements, provides strong evidence against a melt modified mantle origin for the TUC. Instead, the dunites, ol-clinopyroxenites, and amphibolites are interpreted to be of cumulate origin. This origin also explains well the high Cr content of the dunites, which ranges to values far higher than typical cratonic mantle (Fig. 2-6) and is consistent with igneous chromite accumulation.

Archean mantle material and cumulate peridotites from the North Atlantic craton have a high degree of variability in both relative and absolute trace-element abundances (Fig. 2-7) and this may imply that many of these rocks have altered trace-element characteristics. Indeed, due to their lower trace element concentrations and the susceptibility of olivine and pyroxene to low pressure metasomatism, ultramafic rocks exhibit greater degrees of alteration and trace element variability than mafic to felsic rocks (Gruau et al., 1996, Frei et al., 2002, 2004; Wittig et al., 2008; Szilas et al., 2015). This is further evaluated in section *2.4.3* based on a cumulate model for the TUC. In addition, the trace-element characteristics that define the TUC (HFSE depletion, LREE enrichments, and negatively sloped HREEs) are found in both postulated mantle enclaves and cumulates (Fig. 2-7). Despite probable alteration, variations in LREEs relative to HREEs have been used to imply a residual mantle origin for ultramafic enclaves in the IGC (Friend et al., 2002; Rollinson, 2007). However, ultramafic cumulate lithologies in the IGC overlap with those of postulate mantle lithologies when investigating LREE enrichment relative to HREEs (Fig. 2-14). Thus, it is unlikely that REEs offer unequivocal constraints on a cumulate or residual mantle origin for ultramafic enclaves in the IGC, and therefore these elements are not further considered for this purpose here.

Primitive mantle normalized PGE abundances of cumulate rocks can be PPGE enriched or depleted relative to IPGEs, whereas depleted mantle lithologies are typically PPGE depleted (Fig. 2-10). The TUC are depleted in PPGEs and therefore resemble either cumulates or depleted mantle (Fig. 2-10). Differences in IPGE characteristics between PPGE depleted cumulates and lithospheric mantle material (Fig. 2-10) may allow cumulate and mantle peridotites to be differentiated. As IPGEs are resistant to alteration, they are ideal for petrogenetic interpretation in ancient metamorphosed rocks (Szilas et al., 2015). As noted by Ishikawa et al. (2017), there is a large range in IPGE abundances in cumulates whereas mantle peridotites tend to have a limited range from approximately primitive mantle normalized abundances and lower (Fig. 2-10). In addition, relative IPGE abundances in mantle rocks show little variability, whereas in cumulates these are highly variable, typically with negative Ir anomalies and positive Ru anomalies (Fig. 2-10) (Ishikawa et al., 2017). In these aspects the dunites, ol-clinopyroxenites, and amphibolites of the TUC resemble cumulates, as they have a large range of absolute and relative IPGE abundances (Fig. 2-10). The primitive mantle normalized PGE abundances of the hornblende gabbro sample are PPGE enriched relative to IPGEs and the pattern is consistent with a melt the has undergone fractional crystallization (e.g. Philipp et al., 2001; Woodland et al., 2002; Dale et al., 2012).

Combining FeO abundances with variation in IPGEs may offer a unique constraint for differentiating between mantle and cumulate origins for dunite/harzburgite rocks in metamorphic terranes (Fig. 2-15). In this way the variable IPGE abundance in the TUC dunites, combined with their high FeO content strongly implies that these samples are of cumulate origin.

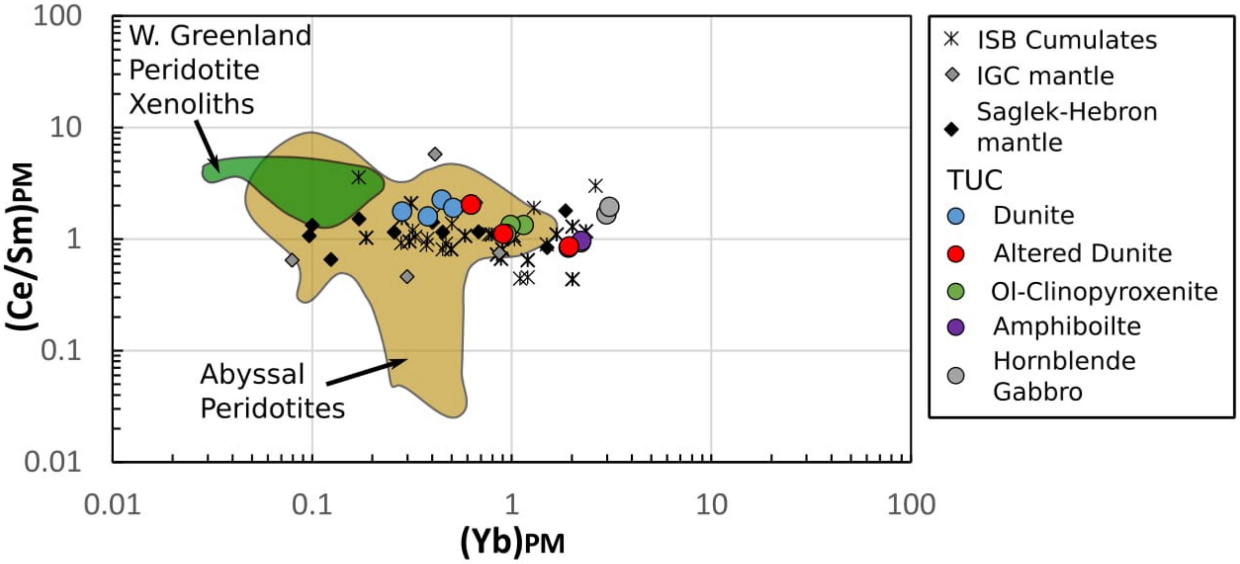

Fig. 2-14. REE Classification diagram for mantle enclaves from Rollinson (2007). Data sources are as follows: SW Greenland mantle xenoliths from Wittig et al. (2008 and 2010); Abyssal peridotites are from Niu (2002); IGC mantle enclaves are PPGE depleted samples from south of the ISB of van de Locht et al. (2018); Mantle enclaves from the Saglek-Hebron block are from Ishikawa et al. (2017); ISB cumulates are from Szilas et al. (2015). Primitve mantle (PM) normalization values are from of McDonough and Sun (1995)

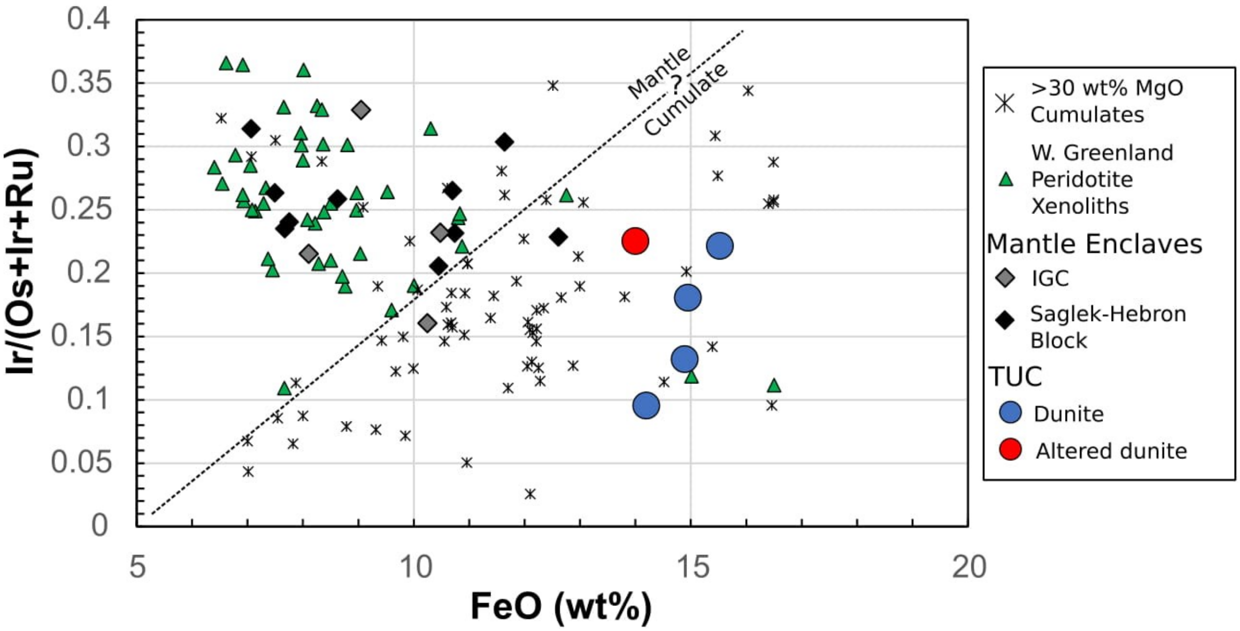

Fig. 2-15. A plot of FeO vs Ir/(Os+Ir+Ru) partially separating mantle and cumulate peridotites. Data sources are as follows: SW Greenland peridotite xenoliths from Wittig et al. (2008 and 2010); IGC mantle enclaves are PPGE depleted samples from south of the ISB of van de Locht et al. (2018); Mantle enclaves from the Saglek-Hebron block are from Ishikawa et al. (2017); Cumulates are from Day et al. (2008), Li et al., 2013, Wang et al. (2014), and Szilas et al. (2015 and 2017).

2.4.3 Trace element alteration characteristics

The Isukasia area has been subject to multiple phases of deformation and metamorphism up to at least amphibolite-facies conditions (Gruau et al., 1996; Frei et al., 2002; Nutman et a., 2002; Cruz et al., in prep), resulting in metasomatism that, in some cases, has extensively modified the trace-element compositions of the rocks in the region (e.g. Rosing and Rose, 1993; Rose et al., 1996; Rosing et al., 1996; Myers, 2001; Frei et al., 2002; Boyet et al., 2003). Presumably the TUC has experienced a similar alteration history. Previous studies of igneous rocks from the Isukasia region have concluded that fluid mobile elements, K, Na, Rb, Ba, Sr, Pb, U, are generally subject to significant mobilization in rocks that may be otherwise unaltered (Dymek et al., 1988; Polat et al., 2002; Polat and Hofmann, 2003; Hofmann et al., 2011; Szilas et al., 2015) and therefore these mobile elements are not considered here.

To assess the degree to which the concentration of less mobile trace elements in the TUC reflect crystal accumulation or alteration characteristics, the trace element variation in a hypothetical cumulate and resulting melt was modelled (Fig. 2-8). The methods, calculations, and partitioning coefficients used are given in Appendix 6. In the model, three stages of accumulation were used

1) olivine, 2) olivine and clinopyroxene, and 3) clinopyroxene. Trapped interstitial melt was estimated to be the amount of initial melt needed to account for the average Al_2O_3 in the dunites (~12 %). For most trace elements, this accumulation and melt-trapping model fits well with trace-element variations in the TUC. However, LREEs tend to be significantly more enriched in the samples than in the modelled results. This is consistent with results from studies on the assessment of trace element mobility in rocks from the ISB (Dymek et al., 1988; Polat et al., 2002; Polat and Hofmann, 2003; Frei et al., 2002), in which LREEs were found to be more mobile than most other trace elements considered here. That the HREE and HFSE distribution in the TUC mirrors that of the modelled results, and that many studies in the Isukasia region find that these elements are relatively immobile during alteration (e.g. Dymek et al., 1988; Polat et al., 2002; Polat and Hofmann, 2003; Szilas et al., 2015) indicates little significant redistribution of these elements in the TUC. In addition, the primitive mantle normalized trace-element patterns of these rocks are consistent and coherent between lithologies (Fig. 2-7), a characteristic typically associated with low degrees of alteration (Polat, et al., 2002).

2.4.4 Nature of the parent melts

In the Isukasia region, mafic and ultramafic magmatic rocks are classified as having either boninitic or tholeiitic affinities (Polat and Hofmann, 2003; Furnes et al., 2009; Jenner et al., 2009; Szilas et al., 2015). A useful parameter for distinguishing the two groups of rocks is the Al_2O_3/TiO_2 ratio, which, if above 30, designate boninitic affinities whereas values below 30 denote tholeiitic affinities. The samples from the TUC have a narrow range of Al_2O_3/TiO_2 ratios of 12 ± 2, a strong indication of a tholeiitic affinity for these rocks. In addition, mafic and ultramafic rocks in the Isukasia region with either boninitic and tholeiitic affinities are readily distinguishable in plots of Al_2O_3 vs trace-elements (Fig. 2-8). Samples from the TUC plot with tholeiitic-like rocks from the Isukasia region (Fig. 2-8). Relative to the boninitic-like rocks, tholeiitic-like samples from the Isukasia region and samples from the TUC are enriched in REEs and HFSEs and have high $(Gd/Yb)_{PM}$ ratios. The two groups of rocks are best distinguished on a plot of Al_2O_3/TiO_2 and $(Gd/Yb)_{PM}$ (Fig. 2-16), in which samples from the TUC are clearly defined as tholeiitic. Thus, the TUC likely formed from a melt that was similar in composition and origin to basalts with tholeiitic affinities in the Isukasia region.

Although Al/Ti ratios and trace elements can readily be used to distinguish between TUC cumulate lithologies with tholeiitic and boninitic affinities, most major elements in the TUC cumulates are not systematic enough to do so. For the dunites, this is largely because, with the exception of Al_2O_3, peridotites of boninitic and tholeiitic affinities in the Isukasia region with greater than 35 wt% MgO, have very similar major-element compositions (Fig. 2-8). This may reflect the mineralogical control on MgO, FeO, and SiO_2 by olivine. Other elements may be controlled by trapped interstitial melt, and some of these (CaO and Na_2O) do not significantly differ between boninitic and tholeiitic basalts in the Isukasia region (Fig. 2-8). The Al/Ti ratio is distinctive in that both elements are likely controlled by trapped interstitial melt in cumulate dunite lithologies and have significantly different concentrations between boninitic and tholeiitic basalts in the area (Fig. 8). Thus, in terms of major-element systematics, the dunites of the TUC can only be classified as boninitic and tholeiitic on the basis of Al/Ti ratios.

More problematic is that, with the exception of Al/Ti ratios, the major elements of the ol-clinopyroxenites and amphibolites of the TUC cannot be used to define them as belonging to either boninitic or tholeiitic suites. This is largely because clinopyroxenites have not previously been

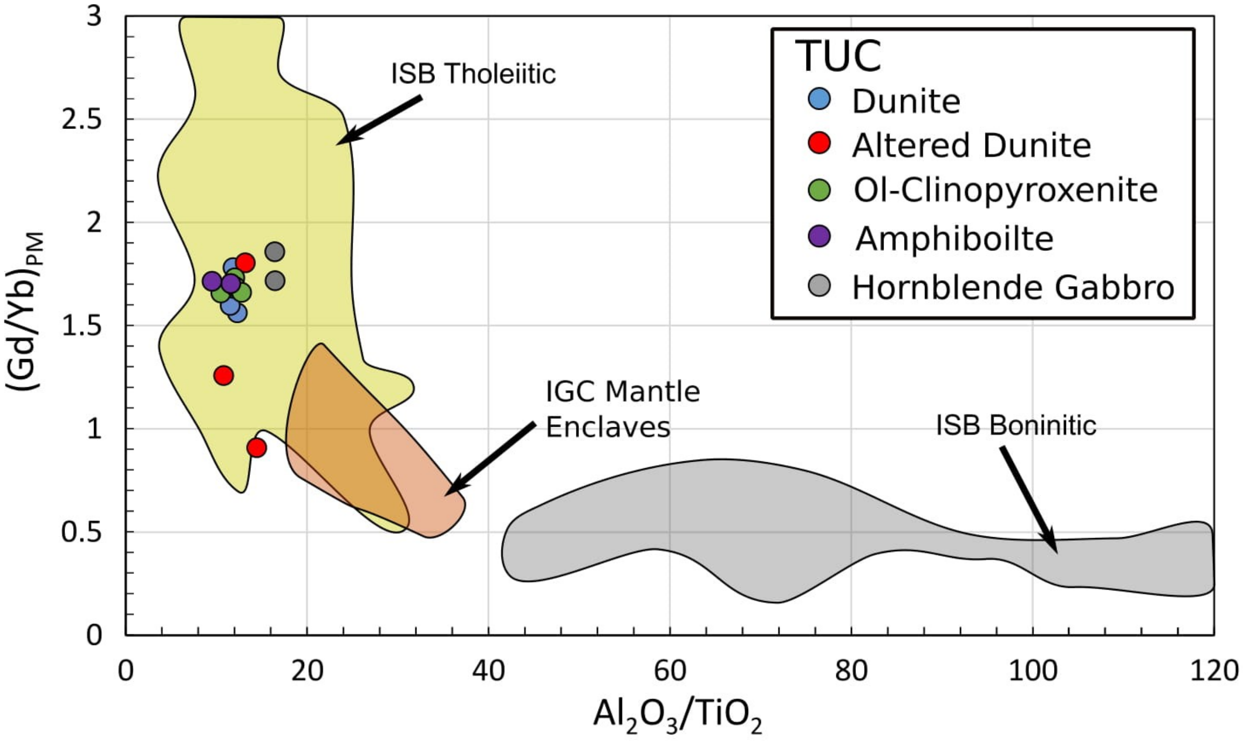

Fig. 2-16. Classification diagram after Jenner et al. (2009) for mafic and ultramafic rocks in the ISB. Data sources for the ISB are as in Fig. 2-6. Normalization values from McDonough and Sun (1995).

found in the ISB or peridotite enclaves in the IGC. The ol-clinopyroxenites and amphibolites plot towards or within the field of clinopyroxenite cumulates from arc environments. Arc clinopyroxenites are a possible affinity, as clinopyroxenites from other environments tend to be enriched in Al_2O_3 (e.g. Qi et al., 1994; Garuti et al., 2001; Scoates et al., 2008), which is uncharacteristic of similar rock types in the TUC. In addition, accumulation of clinopyroxene at low pressure may require precipitation from a hydrous melt, as this lowers the plagioclase liquidus relative to that of clinopyroxene (Gaetani et al., 1993). An interpretation in which the ol-clinopyroxenites and amphibolites largely formed from the accumulation of clinopyroxene from a hydrous melt can account for the overlap in some elements between these lithologies and the boninitic field for peridotites in the area (Fig. 2-6). A boninitic affinity is not a characteristic of the magmas which formed the TUC.

The hornblende gabbros of the TUC largely plot within the tholeiitic field for basalts in the area (Fig. 8), consistent with the interpretation that samples of this lithology originated as crystallized melts and the TUC formed from a melt with tholeiitic affinities.

Like the basaltic rocks of the ISB, hornblende gabbros and recalculated melts of the cumulates of the TUC display evidence for arc-like affinities in the most commonly used trace-element discrimination diagrams (Fig. 2-17). In the absence of evidence for extensive alteration of trace element signatures in the TUC, increases in Th relative to other HFSE and negative Ta, Nb, and Ti anomalies are proxies for crustal input (Pearce, 2008). Crustal contamination may occur through assimilation fraction crystallization, where the melt is contaminated by partial melts of a hydrous basaltic country rock during emplacement (Pearce, 2008). This may be a possible interpretation for the arc-like trace element signatures, as many of the ultramafic pods in the area have intruded into possible oceanic crustal lithologies (cf. Chadwick and Crewe, 1986). Alternatively, such trace-element signatures may have been genuinely produced in an arc-like environment - the typical interpretation for rocks with these signatures in the Isukasia region (e.g. Nutman et al., 1996; Polat et al., 2002; Jenner et al., 2009; Szilas et al., 2015). Although alternatives to generating arc-like geochemical signatures have been proposed (e.g. Bedard, 2006), such models depend on the delamination of anhydrous restites. If clinopyroxenite cumulates are abundant in the ultramafic

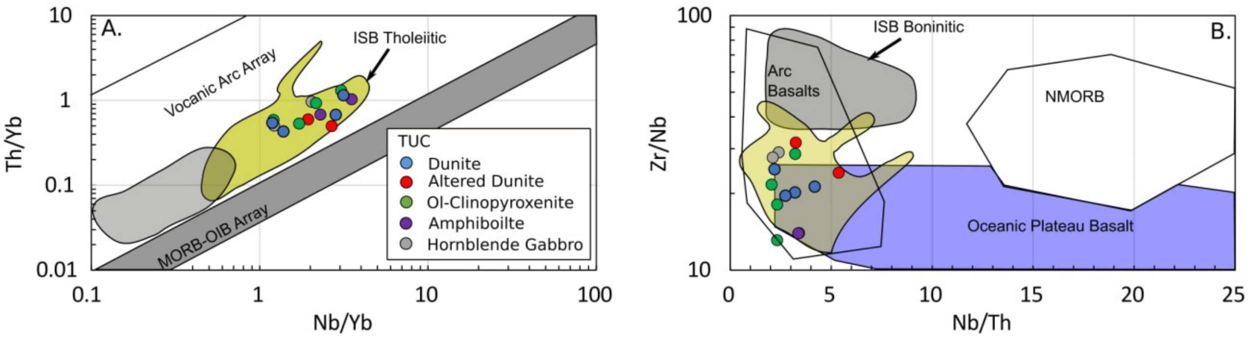

Fig. 2-17. Hornblende gabbros and recalculated melts for cumulate rocks of the TUC on A. the Nb/Yb vs. Th/Yb diagram of Pearce (2008), and B. Nb/Th vs. Zr/Nb discrimination diagram of Condie (2005). Also shown are basaltic rocks of tholeiitic and boninitic affinities from ISB. Data sources for the ISB rocks are the same as in Fig. 2-6. Partitioning coefficients used in recalculating the melts from which the TUC rocks formed are as in Fig. 2-8. An interstitial melt of 12 % was assumed. Concentrations were modelled with the equation: $C_{melt}=C_{sample}/(F+0.88*D_{mineral/melt})$, where C is the concentration of the element and D is the partitioning coefficient of that element in the mineral. Recalculated melt compositions are in Appendix 6.

enclaves south of the TSB it remains unclear if such non-uniformitarian models can generate the required H_2O to produce an extensive assemblage of clinopyroxenite cumulates.

2.4.5 Platinum group element geochemistry in Eoarchean cumulates

The ultramafic rocks of the TUC provide a rare opportunity to examine highly siderophile element abundances and behavior in an Eoarchean magmatic system. The altered nature of many of the TUC lithologies means that caution must be exercised in interpreting their behavior. Iridium group PGEs are largely immobile during alteration (Szilas et al., 2015). However, desulphurization by oxidizing fluids can cause a loss of PPGEs during metamorphism (Szilas et al., 2015; Rizo et al., 2016). Nonetheless, the melts of the TUC (hornblende gabbros) have high PPGE concentrations and are enriched in PPGEs relative to IPGEs (Fig. 2-10), consistent with magmas produced via fractional crystallization (e.g. Philipp et al., 2001; Woodland et al., 2002; Dale et al., 2012). The cumulate lithologies (dunites, ol-clinopyroxenites, and amphibolites) are depleted in PPGEs and enriched in IPGEs (Fig. 2-10), similar to some other peridotite cumulates in the southern West Greenland (e.g. Coggon et al., 2015; Szilas et al., 2017). It is possible that the low PPGE abundances in the TUC cumulates result from preferential loss of PPGEs during metamorphism. However, both cumulates and melts of the TUC have been metasomatically enriched in LREEs (Fig. 2-8), suggesting both experienced similar degrees of alteration. Alternatively, the low abundance of PPGEs relative IPGEs in the cumulates of the TUC may be accounted for if the magma was sulphide-undersaturated, and the abundances of PGEs in the TUC were controlled by the partitioning of PGEs into fractionating silicate and oxide phases, precipitating platinum group minerals (PGMs), and trapped interstitial melt.

In sulphide-saturated silicate magmas, exsolved sulphide will scavenge almost all PGEs from a silicate melt (Mungall and Brenan, 2014). Thus, to retain PGEs in cumulate rocks precipitated from sulphide-saturated magmas, sulphide would need to be trapped in growing minerals or interstitially. For all PGEs, the relative partition coefficients between sulphide and silicate melts are approximately the same (Mungall and Brenan, 2014), and exsolved sulphides should reflect the relative PGE abundances of the melt. Melts of the TUC (hornblende gabbro) are enriched in PPGEs relative to IPGEs (Fig. 2-10), like Phanerozoic melts (e.g. Philipp et al., 2001; Pitcher et al., 2009; Ireland et al., 2009; Hughes et al., 2015). Because the cumulate rocks of the TUC are enriched in IPGEs relative to PPGEs, the abundances of these elements are unlikely to be controlled by trapped sulphide, as such a characteristic is not consistent with inter-element PGE abundances in magmatic rocks. Furthermore, PGE evolution in sulphide-saturated magmas results in positively sloped primitive mantle normalized PGE patterns (e.g. Bezos et al., 2005; Dale et al., 2008), whereas, evolved sulphide-undersaturated magmas tend to display a stepped pattern of low abundances of IPGEs and a sharp increase in PPGEs (e.g. Woodland et al., 2002; Dale et al., 2012), similar to magmatic rocks of the TUC (Fig. 2-10).

Further insight requires more stringent constraints from other elements. To obtain a clinopyroxenite cumulate with the composition of that of the most evolved amphibolite sample with MELTS (section *2.4.2)* about 40 % fractional crystallization of a picritic basalt is required. The high $(Gd/Yb)_{PM}$ ratio of the hornblende gabbro samples and recalculated melts of the TUC (section *2.4.3*) indicates that the source of the melt for the TUC originated in the garnet stability field (see also Polat and Hofmann, 2003). At 1350 °C, garnet is stable in a fertile lherzolite composition above about 23 kbar (Klemme and O'Neill, 2000). A greater than 20 kbar decompression of basaltic melt, effectively doubles the sulphide content at sulphide saturation of that melt (Mavrogenes and O'Neill, 1999). Thus, unless the TUC melt assimilated abundant sulphide on route to surface, it is unlikely to have reached sulphide saturation.

The relative PGE abundance of the cumulate rocks of the TUC are similar throughout all lithologies (Fig. 2-10) and hence the major phases controlling these elements are likely the same. During fractional crystallization, IPGEs behave as compatible elements fractionating into early precipitating phases (Peck et al., 1992; Philipp et al., 2001; Putchel and Humayun, 2001; Coggon et al., 2015; Gannoun et al., 2016). Indeed, IPGEs in the TUC behave compatibly, positively correlating with MgO (Fig. 2-9). Iridium group PGEs are compatible in chromite (Coggon et al., 2015; Page and Barnes, 2016; Arguin et al., 2017; Park et a., 2017), which can also host the PGM laurite (Andrews and Brenan, 2002). The “zig-zag” primitive mantle normalized IPGE pattern of the TUC cumulates (Fig. 2-10) are characteristic of both chromite (Park et al. 2017) and laurite (Gannoun et al., 2016). Laurite requires a melt to be sulphide undersaturated but have high fS_2 and an fO_2 of about QFM at magmatic temperatures between 1200 and 1250°C (Andrews and Brenan, 2002). Such an fO_2 has been suggested for the melt which precipitated the Ujaragssuit nunat intrusion (Rollinson et al., 2002). However, differentiating between the contribution of laurite and chromite to the abundances of PGEs in the TUC is not necessary as both have similar PGE patterns, as discussed above, and commonly occur together.

Iridium group PGEs are also compatible in olivine with distribution coefficients of up to 3 (Brenan, 2003, 2005; Mungall and Brenan, 2014). In addition, PGMs are extremely insoluble in melts (Park et al., 2017) and tend to crystallize with early precipitating phases during fractional crystallization (e.g. Peck et al., 1992; Brenan and Andrew, 2001; Park et al., 2012, 2013 and 2017; Coggon et al., 2015). Experimental evidence suggests that Pt is compatible in clinopyroxene (Righter et al., 2004). However, Pt compatibility in clinopyroxene is unlikely to have affected the PGE systematics of the TUC, as Pt is significantly more depleted in the cumulates relative to gabbros.

In contrast to IPGEs, PPGEs do not correlate with other elements and occur in low abundances in the cumulate rocks of the TUC (Fig. 2-9). These elements are not compatible in olivine (Brenan, 2003, 2005) or chromite (Park et al., 2012 and 2017; Coggon et al., 2015; Arguin et al., 2016) and are absent or in low abundances in laurite (e.g. Zaccarini et al., 2004). In addition, Pt and Pd are more soluble in melts than IPGEs (cf. Mungall and Brenan, 2014). However, Pt-Fe alloys have been found to co-precipitate early with olivine and chromite (e.g. Peck et al., 1992; Coggon et al., 2015; Anguin et al., 2016), and may account for some elevated Pt in the dunites of the TUC. However, excluding one anomalously PGE-rich sample and another with elevated Pt, PPGEs in the other cumulate lithologies of the TUC can be accounted for by 4 to 15 % trapped interstitial melt with the composition of the hornblende gabbros.

In conclusion, the solubility of PGMs in the melt and partitioning of PGEs into fractionating phases can account for the PGE abundances in the TUC. The dunites have the highest concentration of IPGEs due to the partitioning of IPGEs into chromite, olivine, higher concentrations of PGEs in the melt, and precipitation of PGMs. Decreasing abundances of IPGEs in the melt and the lower modal abundances of olivine resulted in lower IPGE conents in the ol-clinopyroxenites and amphibolites relative to the dunites. The fractionation of IPGEs into the early forming cumulates depleted the melt in these elements, resulting in the low abundance IPGEs in the magmatic rocks of the TUC (Fig. 2-10). Although platinum may have been somewhat depleted by the formation of alloys, the lack of other significant host phases for Pt or Pd resulted in an increase in the abundance of these elements relative to IPGEs in the melts of the TUC (Fig. 2-10).

2.4.6 Source PGE characteristics

As there is significant interest in whether the PGE systematics of the Eoarchean and Archean mantle were different from those of the post-Archean mantle (e.g., Maier et al., 2009) a key aim of this study is to try to constrain the nature of the source of the melts parental to the TUC.

The PGE characteristics of the TUC melt source are ultimately difficult to estimate due to the fractionation of PGEs into precipitating phases as the melt travels towards the surface. Palladium is the most soluble PGE (cf. Mungall and Brenan, 2014) behaving incompatibly even at high degrees of fractional crystallization (e.g. Philipp et al., 2001; Pitcher et al., 2009; Dale et al., 2012). This behavior is clear in the TUC, as Pd behaves incompatibly in the most evolved cumulates. Hence the lithologies that best approximate melt compositions should be scrutinized instead. By comparing the concentrations of Pd in the hornblende gabbro to those of modern basalts at similar MgO contents (a proxy for the degree of fractional crystallization), some constraints can be placed on the PGE content of the melt source.

The concentration of Pd in the hornblende gabbro is 5.0 ppb. Except for arc basalts and some LIPs and OIBs, this concentration of Pd is high relative to Phanerozoic basalts with a similar MgO content (Fig. 2-18 A). If mantle melting and fractional crystallization processes were similar in the Eoarchean to that of today, any magmatic environment other than an arc, would imply that the mantle from which the TUC magmas were derived had higher Pd contents relative to that of the modern bulk silicate earth.

The degree of fractionation of IPGEs from PPGEs in the TUC hornblende gabbro is high relative to modern ocean island basalts and large igneous provinces (Fig. 2-18 B). Mid ocean ridge basalts have low PGE contents relative to that of the hornblende gabbro (e.g. Bezos et al., 2005; Dale et al., 2008), and this environment is not further considered here. The exceptionally low Ir/Pd ratios in the hornblende gabbro may reflect preferential PPGE transport from subducted or delaminated crustal components to the mantle source for the TUC (e.g. Woodland et al., 2002). As the hornblende gabbros display evidence for crustal contamination (Fig. 2-17), this possibility is implicated by these results. Alternatively, exogenous Pd may have been derived from assimilation of sulphide from the oceanic crust into which the magmas of the TUC intruded. Even in this scenario, the PGE systematics imply that the melt remained sulphide undersaturated which is consistent with the relatively S-poor and PGE-poor nature of oceanic crust.

As only one mafic sample was analyzed here, future work is required to target gabbroic and basaltic enclaves in the IGC, which are understudied and may yield additional information on the HSE systematics of the Eoarchean mantle and geodynamic setting of the earlier crust of which the TUC was a part. For now, the altered nature of these samples, their low melt fraction and their possible crustal contamination make their use for estimating the PGE systematics of the early Earth tenuous.

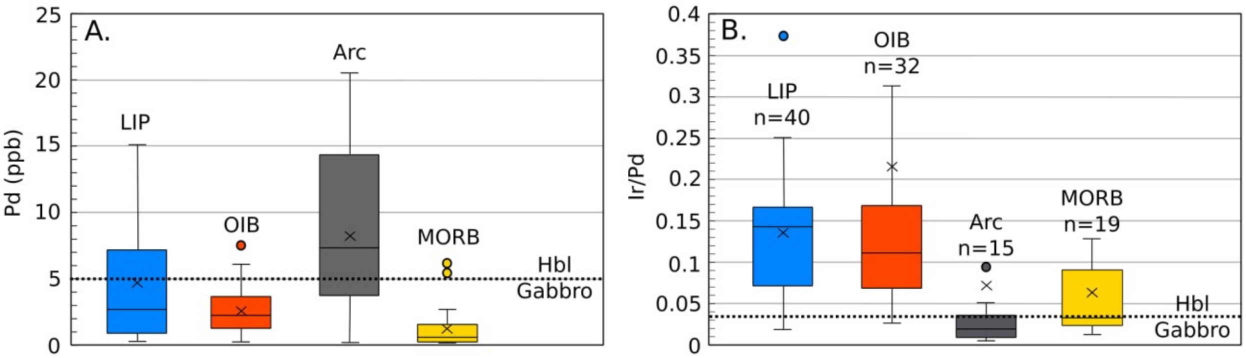

Fig. 2-18. Box plots of absolute concentrations of Pd and Ir/Pd ratios for the hornblende gabbro from the TUC and Phanerozoic basalts with MgO contents ranging from 7.5 to 12.5 wt%. Data sources are as follows: LIP from Song et al. (2009), Hughes et al. (2015), and Arguin et al. (2016); OIB from Ireland et al. (2009), Pitcher et al. (2009), and Day et al. (2009); Arc basalts from Woodland et al. (2002) and Dale et al. (2012); MORB from Rehkamper et al. (1999), Bezos et al. (2005), and Dale et al. (2008).

2.4.7 Re-Os isotope constraints on the age and origin of the TUC

Following the reasoning of previous studies of ultramafic bodies in the IGC, we infer the minimum age of 3.8 Ga for the TUC constrained by the age of the well-dated felsic IGC units in that area that intrude many of the ultramafic bodies (Nutman et al., 2002). Unfortunately, the Re-Os isotope systematics of the TUC measured here do not lead to a simple age interpretation for the body. Cumulate and magmatic rocks of the TUC scatter about a 3.8 Ga reference Re-Os isochron (Fig. 2-19) whose initial Os isotope composition is significantly more radiogenic than PUM at the inferred >3.8 Ga age of these rocks (Fig. 2-19). As such, T_{MA} model ages (Table 1) are young relative to the gneisses which enclose the TUC. There are three possible explanations for the modern Re and Os isotopic characteristics of the TUC: 1) Rhenium was higher in the protolith of the TUC, relative to the Re content at present, generating radiogenic Os, and was subsequently lost during metamorphism, in a way that did not totally disrupt the 3.8 Ga isochron slope. 2) The melt which formed the TUC was enriched in ^{187}Os relative estimates for PUM at 3.8 Ga. 3) The TUC is a Mesoarchean intrusion in the IGC, rather than of Eoarchean age. If the latter scenario is true, future work should should consider the possibility that other enclaves in the IGC, previously considered to be Eoarchean in age, may be younger intrusions.

In the first scenario, the TUC would have to have been affected by a major metamorphic event in which greater than 90 % of Re was systematically lost from most samples. The TUC has experienced multiple metamorphic events, the most significant likely being the ~3.0 Ga regional amphibolite-facies event (Gruau et al., 1996; Frei et al., 2002; Cruz et al., in prep). Magmas derived from an undepleted upper mantle that formed at 3.8 Ga and, underwent a large scale Re loss at 3.0 Ga would require ^{187}Re/^{188}Os ratios of about 0.51 to 0.6 prior to metamorphism to produce the current ^{187}Os/^{188}Os and ^{187}Re/^{188}Os ratios for most low ^{187}Re/^{188}Os cumulate samples. For cumulates of the TUC, this requires an initial Re content of between 0.03 and 1.9 ppb (sample dependent), not outside the range found in peridotites of the Ujaragssuit nunat layered intrusion (Rollinson et al., 2002; Coggon et al., 2015). However, this scenario requires the eight low ^{187}Re/^{188}Os samples that best fit this scenario to have roughly the same ^{187}Re/^{188}Os ratios in the protolith. The Os contents for these samples ranges from 0.28 to 15.6 ppb. As Os behaves compatibly and Re incompatibly during fractional crystallization (Ireland et al., 2009), it is unlikely that the cumulate lithologies had similar initial ^{187}Re/^{188}Os ratios prior to metamorphism. So, while we think that such systematic loss of Re to preserve a 3.0 Ga isochron is unlikely, we acknowledge that some of the scatter of the TUC samples about the 3.8 Ga reference isochron for radiogenic initial Os compositions (Fig. 2-19) may be the result of much lower degrees of late metamorphic Re redistribution.

In the second scenario, the magma which formed the TUC cumulates had a high initial ^{187}Os/^{188}Os ratio relative to estimates of PUM at 3.8 Ga. Modern mantle-derived melts with high ^{187}Os/^{188}Os ratios may have a source enriched by the introduction of radiogenic Os to a mantle wedge via slab dehydration (Brandon et al., 1996) or deep crustal recycling (Dale et al., 2009). Alternatively, the melts may have been contaminated by crustal assimilation (e.g., Lassiter and Luhr, 2001). It is necessary assess the potential for crustal contamination prior to making inferences about mantle source characteristics or slab contributions to Os isotopic abundances in the melts which formed the TUC. In addition, crustal assimilation in a layered intrusion can produce Re-Os isochron ages consistent with the crystallization age of cumulates, but at highly radiogenic initial ^{187}Os/^{188}Os (e.g. Schoenberg, et al., 1999). Crustal assimilation in modern mantle-derived melts can manifest itself as an inverse correlation between Os and ^{187}Os/^{188}Os (Lassiter and Luhr, 2001). However, as discussed above, Re is likely controlled by trapped interstitial melt in the TUC cumulates, which results in relatively low and invariable Re contents through all the cumulate lithologies (Table 1). In contrast, Os, which is controlled by cumulate phases, decreases with fractional crystallization.

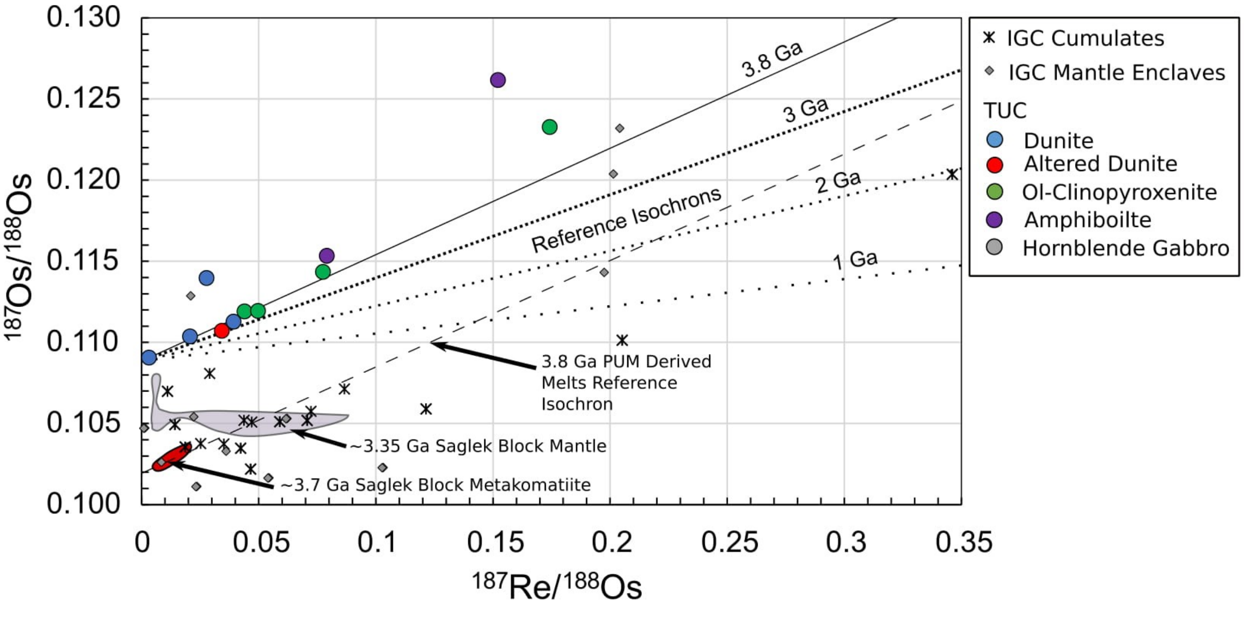

Fig. 2-19. ^{187}Re/^{188}Os vs ^{187}Os/^{188}Os plot for samples of the TUC, and cumulate and mantle peridotites in the IGC, which, for cumulates, includes the ISB. Data sources are as in Fig. 2-10 with additional data from Rollinson et al. (2002). The reference isochrons for the TUC were calculated using an initial ^{187}Os/^{188}Os ratio back calculated from the ^{187}Re/^{188}Os ratio of the least radiogenic TUC sample to 3.8 Ga. The primitive upper mantle derived melts utilize modern values of ^{187}Os/^{188}Os from Meisel et al. (2001) and Walker et al. (2002), back-calculated to the time of proposed interaction. The ^{187}Re decay constant use in the calculations is from Selby et al. (2007).

This causes Re/Os and, with time, $^{187}Os/^{188}Os$ to be approximately proportional to 1/Os. Hence, in cumulate igneous rocks, such a trend is not a definitive indicator of crustal assimilation.

A 3.8 Ga reference isochron for the TUC and hypothetical cumulates of PUM derived melts can be projected onto a plot of 1/Os vs $^{187}Os/^{188}Os$ if a constant Re content is assumed (Fig. 2-20). The cumulate lithologies of the TUC scatter about a reference isochron for a hypothetical cumulate precipitated from a melt with a higher initial $^{187}Os/^{188}Os$ ratio at 3.8 Ga relative to PUM-derived melts (Fig. 2-20). On such a plot, the effects of crustal assimilation on the cumulates from the assimilating melt are difficult to estimate, because the age, concentration of Os, and $^{187}Re/^{188}Os$ and $^{187}Os/^{188}Os$ ratios of the potential crustal assimilant are unknown. Nevertheless, an attempt is made to model this process to try to understand the general effects that it might have on the Re-Os isotope systematics. A fractional crystallization-crustal assimilation model is used to produce 3.8 Ga pseudo-isochrons for hypothetical cumulates on a plot of 1/Os vs $^{187}Os/^{188}Os$ (Fig. 2-20).

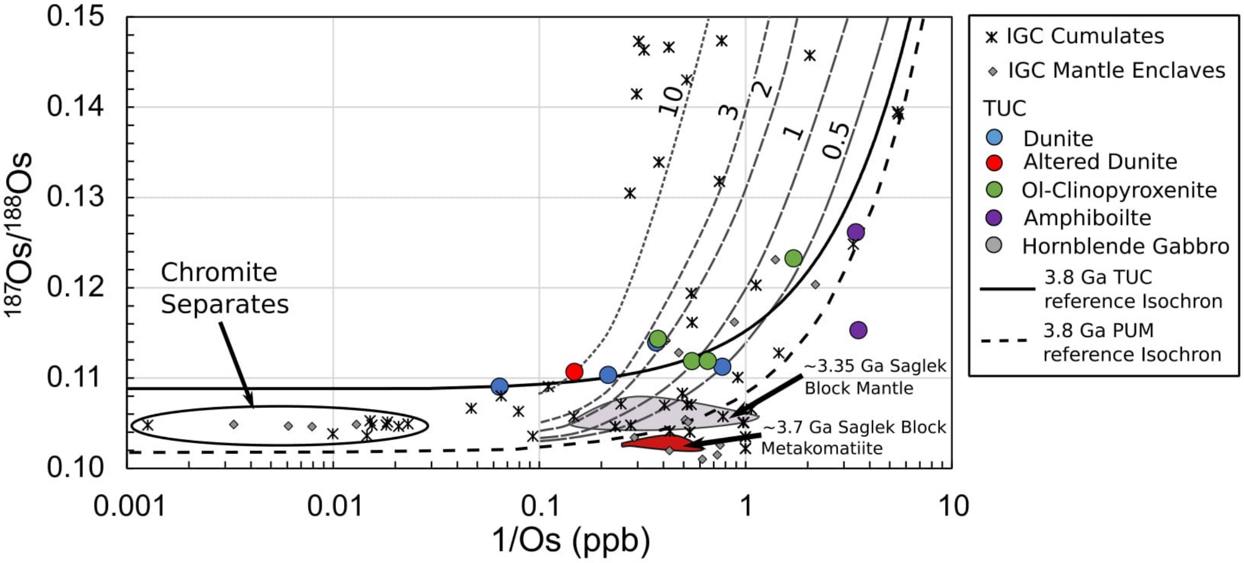

Fig. 2-20. Fig. 2-20. 1/Os vs $^{187}Os/^{188}Os$ for samples of the TUC, and cumulate and mantle peridotites in the IGC, which, for cumulates, includes the ISB. Data sources are as in Fig. 2-10, with additional data from Rollinson et al. (2002) and Coggon et al. (2015). Also shown are reference isochrons for hypothetical 3.8 Ga cumulates precipitated from a melt with $^{187}Os/^{188}Os$ ratios of PUM at 3.8 Ga and of that back calculated to 3.8 Ga of the least radiogenic sample in the TUC. The concentration of Re is held constant at 0.02 ppb, the average of the cumulate rocks of the TUC, while Os varies. Values for PUM and the ^{187}Re decay constant are as in Fig. 2-19. The dashed lines are the fractional crystallization-crustal assimilation model discussed in text and in Appendix 7. They are numbered for different $^{187}Os/^{188}Os$ ratios of the crustal assimilant.

Because many of the ultramafic enclaves in the area of the TUC are composed of oceanic lithologies (Chadwick and Crewe, 1986), it is assumed the assimilant was a basaltic crust. Calculated $^{187}Os/^{188}Os$ at 3.8 Ga for basaltic rocks in the area are highly variable, ranging as high as 13, with the wide range reflecting Re redistribution (Frei and Jensen, 2003; Frei et al., 2004; Rizo et al., 2016). This variability offers no valid reference point for a crustal assimilant. The Re/Os ratios of Phanerozoic basalts can range to values greater than 1000 (Gannoun et al., 2016), and given a potential 500 Myr evolution time (the approximate difference between the oldest Pt-Os model ages of the Ujaragssuit nunat layered intrusion (Coggon et al., 2013) and the age of the host gneiss to the TUC), $^{187}Os/^{188}Os$ ratios may reach as high as 40 in such basalts. For these reasons a broad range of $^{187}Os/^{188}Os$ was modeled, for various possible crustal assimilants, at a constant 1% crustal assimilation (Fig. 2-20). Further details of the model are available in Appendix 7.

The modelled crustal assimilation drives the pseudo-isochrons of hypothetical cumulates of PUM-derived melts to high $^{187}Os/^{188}Os$ ratios relative to the trajectory of the TUC peridotites and their projected reference isochron (Fig. 2-20). It is possible that higher degrees of crustal assimilation or a more radiogenic crustal assimilant can produce a melt with a high enough $^{187}Os/^{188}Os$ ratio to produce cumulates that replicate the high Os TUC cumulates. However, the TUC does not follow the general trajectories of the modelled pseudo-isochrons, implying that if crustal assimilation is responsible for the radiogenic Os isotopic compositions of the TUC, it was halted prior to the formation of the cumulates. Such a process could be envisioned if the magma interacted with high $^{187}Os/^{188}Os$ lithologies during migration within the crust. Such lithologies may include chemical or siliciclastic sediments (cf. Siebert et al., 2005; Ripley et al., 2008) or hydrothermally altered basalts (Gannoun et al., 2016). In addition, "least altered" boninitic basalts (Polat et al., 2002) may be a potential low $^{187}Os/^{188}Os$ lithology ($^{187}Os/^{188}Os$ at 3.8 Ga of 0.1± 0.02 (Frei et al., 2004)) in which to host the TUC and not affect the $^{187}Os/^{188}Os$ ratio of the melt even if crustal assimilation was continuing to occur. Alternatively, following crustal contamination of the melt, in some layered intrusions, crystal accumulation on the margins of intrusions may seal and buffer the fractionating magma from further crustal contamination (Day et al., 2008).

Additional radiogenic Os may be added to the TUC when the enclave was entrained in the host gneiss. However, using the Os content (0.006 ppb) and $^{187}Os/^{188}Os$ ratio (3.6) of the most radiogenic Archean tonalite of Putchel et al. (2016), there is no resolvable difference in hypothetical cumulates from PUM-derived melts unless this style of contamination reaches greater than 20 % addition of tonalitic melt to the cumulates. Even at such high mass fractions of crust addition, the effect will only be evident in cumulate rocks with ~1 ppb Os or less. Such a scenario cannot account for the radiogenic Os isotopic composition of the high Os cumulates of the TUC.

Although the above model scenario implies specific conditions for crustal assimilation to account for the more radiogenic Os isotopic nature of the TUC, relative to PUM, such conditions are plausible. Furthermore, late Re redistribution likely caused variations in $^{187}Re/^{188}Os$ vs $^{187}Os/^{188}Os$ space, as is suggested by the scattering of the TUC lithologies about the 3.8 Ga reference isochron (Fig. 2-19), obscuring some earlier Os isotopic variations. Thus, differentiating between contributions from the mantle source, slab melting or dehydration, and those from crustal assimilation to the Os isotopic composition of the TUC is not possible. However, it seems clear from the above considerations that if the TUC formed before the host gneiss, the initial $^{187}Os/^{188}Os$ ratio of the melts was moderately high relative to PUM.

In the third scenario, the TUC represents a Mesoarchean intrusion into the IGC. This contrasts with studies on other enclaves in the area that have Re-Os and Pt-Os systematics which constrain the age of some of the enclaves to be at least as old as the surrounding crustal gneisses (Rollinson et al., 2002; Coggon et al., 2013 and 2015). In addition, many of the ultramafic enclaves are intruded by the host gneiss (Chadwick et al., 1983). The TUC displays many of the same characteristics as other ultramafic enclaves in the area (Chadwick and Crewe, 1986), such as, concentric metasomatic zonation and a pod-like shape. These characteristics are possibly related to events that may be older than the 2.8 Ga model age of TUC (Chadwick and Crewe, 1986). However, this is speculative, as the age of these features is not well constrained (Chadwick and Crewe, 1986).

If the TUC represented a Mesoarchean intrusion it would likely be associated with the collision of the Kapisilik terrane, with the southern edge of the IGC in the Isukasia region at ~3.0 Ga (Nutman et al., 2015). The Kapisilik is thought to have collided with and partially overridden the gneisses south of the TSB (Nutman et al., 2015). Thus, in that scenario the TUC would have intruded the IGC in a forearc setting. This provides a plausible Mesoarchean tectonic event in the which the TUC may have intruded.

In summary, unfortunately, the Re-Os isotope systematics of the TUC do not provide definitive constraints on its age and evolution. The enrichment in ^{187}Os of the cumulate rocks within it may be due to crustal assimilation during migration of the melts within the crust or the addition of Re or may represent the introduction of radiogenic Os to the mantle source from the dehydration or partial melting of subducted or delaminated crust. Alternatively, Re-Os model age systematics could be interpreted as implying a possible Mesoarchean rather than Eoarchean age for the TUC rather than Eoarchean. To resolve this issue, it is suggested that future work targets multiple enclaves in the IGC which may clarify some of these issues.

2.5 Conclusions

The principal finding of this study is that the TUC largely formed by crystal accumulation. Major-element variations can be convincingly modelled via crystal accumulation, and the high FeO content of the dunites strongly argues against a mantle restite origin for these rocks. Similarly, trace-element patterns for relatively immobile elements track well with the proposed crystal accumulation melt trapping model. In addition, the wide variations in platinum group elements appear to be best explained by accumulating silicate, oxide, and PGM phases.

Concluding that the TUC is largely composed of ultramafic cumulates poses some difficulty in using this complex to constrain early plate tectonic processes and mantle source PGE characteristics because melt source characteristics must be inferred from partition coefficients. For lithophile/REE elements and HFSEs this is less problematic as most of the HFSE and HREE are hosted in the trapped melt phase of the cumulates. Hence, uncertainty in the partition coefficients of these elements is relatively insignificant in estimating the recalculated melt compositions. In contrast, this error is much larger for the PGEs due to uncertainties in our knowledge of the solubility of PGMs in melts and imprecision in the partition coefficients of PGEs into silicate and oxide phases. Thus, in terms of PGEs, assessments of plate tectonic and mantle source characteristics are restricted to Pd because this element would not significantly partition into crystallizaiong phases during fractional crystallization of a sulphide-undersaturated melt.

The inter-element fractionations of the modelled parental magma to the TUC have arc-like geochemical signatures. Although this signature may indicate that the complex formed in a convergent margin setting, these characteristics may also have been inherited from crustal assimilation and fractional crystallization. Distinguishing between these alternatives in Archean rocks is very challenging. Both scenarios can equally apply to Pd concentrations. The Pd concentration of the calculated TUC parent melt is high relative to Phanerozoic intra-plate basalts (Fig. 2-18). Alternatively, the high Pd may have been inherited from crustal assimilation of sulphide.

The radiogenic Os isotopic composition of the TUC offers limited insight into evaluating the origin of geochemical signatures that appear to suggest an arc-like setting for the TUC. Many modern and ancient layered intrusions tend to have high γOs values due to crustal assimilation (e.g. Schoenberg et al., 1999; Marques, et al., 2003; Day et al., 2008). Alternatively, radiogenic Os isotopic ratios in some primitive-subduction zone magmas cannot fully be accounted for by crustal assimilation and require a mantle source with radiogenic Os possibly related to subduction zone processes (e.g. Lessiter and Luhr, 1999; Woodland et al., 2002). However, given that many of the enclaves in the IGC are basaltic and intruded by ultramafic sills (Chadwick and Crewe, 1986), the likelihood of crustal contamination is high, and these results cannot be used with any confidence to support the idea that the TUC formed in an arc-like setting.

The possibility that the high Pd contents and radiogenic Os isotopic ratios of the TUC likely result from crustal contamination, complicates estimates for PGE contents in the melt source. It is unclear whether the high Pd content in the hornblende gabbro is due to high abundances of PGEs in the melt source, crustal assimilation, or arc-like volcanic processes. It seems unlikely that this is a mantle source characteristic, as other rocks in the area suggest their source had similar or lower PGE contents than the modern BSE (Bennett et al., 2002; Szilas et al., 2015; Rizo et al., 2016; van de Locht et al., 2018) or less (Dale et al., 2017).

There is uncertainty in the partitioning of Re and Os between mantle and core during core segregation (Walker et al., 2009). However, it has been suggested that Re may have been retained in the mantle during core formation to greater extent than Os (Dauphas, et al., 2002). At ~3.8 Ga, a source that had not received a chondritic late veneer, could have evolved to a highly radiogenic Os isotopic composition imparting this characteristic to the maficultrmafic rocks in the IGC (Rizo et al., 2016). This is observed in the Re-Os isotopic systematics of the TUC (Fig. 2-19 and 20). However, other ultramafic enclaves do not have radiogenic Os isotopic compositions relative to chondrites at ~3.8 Ga, outside the range that may be attributable to Re redistribution (e.g. Bennet et al., 2002; Rollinson et al., 2002; Rizo et al., 2016). Thus, the radiogenic Os isotopic composition of the TUC is likely the result of crustal assimilation or arc-like volcanic processes rather than an inherent feature of its mantle source. Furthermore, the more radiogenic Os isotopic composition relative to less evolved nearby cumulate rocks (e.g. Rollinson et al., 2002; Coggon et al., 2015), likely illustrates a significant effect of crustal assimilation on the TUC. Whether arc-like processes contributed to the Os isotopic character of the TUC remains unclear.

The radiogenic Os isotopic composition of the TUC also results in uncertainty about the age of the complex. Re-Os model ages suggest the TUC formed at ~2.8 Ga (Table 2.2). However, radiogenic Os isotopic compositions are not uncommon in cumulate rocks in which the melts experienced crustal assimilation fractional crystallization (e.g. Schoenberg et al., 1999; Marques, et al., 2003; Day et al., 2008). In addition, data for the TUC scatter about a 3.8 Ga Re-Os reference isochron (Fig. 2-19). Although, the excess scatter is likely the result of late Re redistribution, the data cannot be differentiated from a 3 Ga reference isochron, due to the very low $^{187}Re/^{188}Os$ ratios. Thus, age constraints from Re-Os isotopic systematics in these rocks are largely inconclusive.

Although the geochemistry of the TUC strongly implies the rocks originated as cumulates, in other encalves composed of more MgO-rich rocks, differentiating mantle and cumulate lithologies remains fraught with uncertainty, and the composition of the Eoarchean lithospheric mantle in the Isukasia region is still unclear. A recent study by van de Locht et al. (2018) supports the contention of Bennett et al. (2002), Friend et al. (2002), and Rollinson (2007) that some enclaves in the IGC are composed of lithospheric mantle material. Perhaps, future studies should target these specific enclaves to constrain the composition of the lithospheric mantle at ~3.8 Ga. Other ultramafic enclaves originating as cumulates or crystallized melts may offer a unique opportunity to understand the extent and effect of crustal contamination on magmatic rocks in the area. Finally, these data could be applied to understanding whether crustal contamination occurred via slab dehydration/partial melting or crustal assimilation and could be further used to place some constraints on the Eoarchean tectonic regime operating in the Isukasia region.

References

Andrews D. A. and Brenan J. M. (2002) The solubility of ruthenium in sulphide liquid: Implications for platinum-group mineral (PGM) stability and sulphide melt/silicate melt partitioning. *Chem. Geol.*, 192, 163-181.

Appel C. C., Appel P. W. U., and Rollinson H. R. (2002). Complex chromite textures reveal the history of an early Archean layered ultramafic body in West Greenland. *Min. Mag.* 66, 1029-1041.

Arguin J.P., Page P., Barnes S.J., Yu S.Y. and Song X.Y. (2016). The effect of chromite crystallization on the distribution of osmium, iridium, ruthenium and rhodium in picritic magmas: an example from the Emeishan Large Igneous Province, Southwestern China. J. *Petrology*, 57, 1019-1047.

Asimow, P.D. and Ghiorso, M.S. (1998). Algorithmic modifications extending MELTS to calculate subsolidus phase relations. *American Mineralogist*, 83, 1127-1132.

Ballhaus, C., Berry, R.F., and Green, D.H. (1990). Oxygen fugacity controls in the Earth's upper mantle. *Nature*, 348, 437-440.

Barnes, S.J. and Roeder, P.L. (2001). The Range of Spinel Compositions in Terrestrial Mafic and Ultramafic Rocks. *J. Petrology*, 42, 2279-2302.

Becker H., Horan M. F., Walker R. J., Gao S., Lorand J.P., and Rudnick, R.L. (2006). Highly siderophile element composition of the Earth's primitive upper mantle: constraints from new data on peridotite massifs and xenoliths. *Geochim. Cosmochim. Acta,* 70, 4528–4550.

Bédard, J.H. (2006). A catalytic delamination-drivenmodel for coupled genesis of Archaean crust and sub-continental lithospheric mantle. *Geochim. Cosmochim. Acta*, 70, 1188-1214.

Bennett, V.C., Nutman, A.P., and Esat, T.M., (2002). Constraints on mantle evolution from 187Os/188Os isotopic compositions from Archaean ultramafic rocks from southern west Greenland (3.8 Ga) and western Australia (3.46 Ga). *Geochim. Cosmochim. Acta*, 66, 2615-2630.

Bernstein, S., Szilas, K., Kelemen, P.B., 2013. Highly depleted cratonic mantle in West Greenland extending into diamond stability field in the Proterozoic. *Lithos*, 168, 160-172.

Bezos, A. B., Orand, J. L., Umler, E. H., and Ros, M. G. (2005). Platinum-group element systematics in Mid-Oceanic Ridge basaltic glasses from the Pacific, Atlantic, and Indian Oceans. *Geochim. Cosmochim. Acta*, 69, 2613-2627.

Bodinier, J.L., Vasseur, G., Vernieres, J., Dupuy, C., and Fabries, J. (1990). Mechanisms of Mantle Metasomatism: Geochemical Evidence from the Lherz Orogenic Peridotite. *J. Petrology*, 31, 597-628.

Boyet, M., Blichert-toft, J., Rosing, M., Storey, M., Albare, F., & Te, P. (2003). 142Nd evidence for early Earth differentiation. *Earth Planet. Sci. Lett.*, 214, 427-442.

Brandon, A. D., Creaser, R. A., Shirey, S. B., and Carlson, R. W. (1996). Osmium Recycling in Subduction Zones Author. *Science*, 272, 861-864.

Brenan, J. M., & Andrews, D. (2001). Higher-temperature stability of laurite and Ru-Os-lr alloy and their role in PGE fractionation in mafic magmas. *Canadian Mineralogist*, 39, 341-360.

Brenan, J.M., Mcdonough, W.F., and Dalpe, C. (2003). Experimental constraints on the partitioning of rhenium and some platinum-group elements between olivine and silicate melt. *Earth Planet. Sci. Lett.*, 212, 855-872.

Brenan J. M., McDonough W. F. and Ash R. (2005) An experimental study of the solubility and partitioning of iridium, osmium and gold between olivine and silicate melt. *Earth Planet. Sci. Lett.*, 237, 855-872.

Brey, G.P. and Köhler, T. (1990). Geothermobarometry in four-phase lherzolites II: new thermobarometers, and practical assessment of existing thermobarometers. *J. Petrology*, 31, 1353-1378.

Chadwick, B. and Crewe, M.A. (1986). Chromite in the early Archean Akilia Association (ca. 3,800 m.y.), Iviartoq region, inner Godthåbsfjord, southern West Greenland. *Econ. Geol.*, 81,184-191.

Chadwick, B., Crewe, M. A., and Park, J. F. W. (1983). Field work in the north of the Ivisortoq region, inner GodthSbsfjord, southern West Greenland. *Gronlands Geol. Undersogelse Rap.* 115, p. 49-56.

Coggon, J.A., Luguet, A., Fonseca, R.O.C., Lorand, J.-P., Heuser, A., and Appel, P.W.U. (2015). Understanding Re-Os systematics and model ages in metamorphosed Archean ultramafic rocks: A single mineral to whole-rock investigation: *Geochim. Cosmochim. Acta*, 167, 205-240.

Coggon, J.A., Luguet A., Nowell, G.M., and Appel, P.W.U. (2013). Hadean mantle melting recorded by southwest Greenland chromitite 186Os signatures. *Nat. Geo.*, 6, 871-874.

Colás, V., González-jiménez, J. M., Griffin, W.L., Fanlo, I., Gervilla, F., Reilly, S.Y.O., … Proenza, J.A. (2014). Fingerprints of metamorphism in chromite: New insights from minor and trace elements. *Chem. Geol.*, 389, 137-152.

Coltorti, M., Bonadiman, C., Hinton, R.W., Siena, F., and Upton, B.G.J. (1999). Carbonatite metasomatism of the oceanic upper mantle: evidence from clinopyroxenes and glasses in ultramafic xenoliths of Grande Comore, Indian Ocean. *J.Petrology*, 40, 133–165.

Condie, K.C. (2005). High field strength element ratios in Archean basalts: a window to evolving sources of mantle plumes? *Lithos*, 79, 491–504.

Dale, C. W., Luguet, A., Macpherson, C. G., Pearson, D. G., and Hickey-vargas, R. (2008). Extreme platinum-group element fractionation and variable Os isotope compositions in Philippine Sea Plate basalts: Tracing mantle source heterogeneity. *Chem. Geol.*, 248, 213-238.

Dale, C.W., Pearson, D.G., Starkey, N.A., Stuart, F.M., Ellam, R.M., … Macpherson, C.G. (2009). Osmium isotopes in Baffin Island and West Greenland picrites: Implications for the 187Os / 188Os composition of the convecting mantle and the nature of high. *Earth Planet. Sci. Lett.*, 278, 267–277.

Dale, C. W., Macpherson, C. G., Pearson, D. G., Hammond, S. J., and Arculus, R. J. (2012). Inter-element fractionation of highly siderophile elements in the Tonga Arc due to flux melting of a depleted source. *Geochim. Cosmochim. Acta*, *89*, 202–225.

Dale, C.W., Kruijer, T.S., and Burton, K.W. (2017). Highly siderophile element and 182 W evidence for a partial late veneer in the source of 3.8 Ga rocks from Isua, Greenland. *Earth Planet. Sci. Lett.*, 458, 394-404.

Dauphas, N., Reisberg, L., and Marty, B. (2002). An alternative explanation for the distribution of highly siderophile elements in the Earth. *Geochemical Journal*, 36, 409-419.

Day, J.M., Pearson, D.G., and Hulbert, L.J. (2008). Rhenium-Osmium Isotope and Platinum-Group Element Constraints on the Origin and Evolution of the 1.27 Ga Muskox Layered Intrusion. *J. Petrology*, 49, 1255-1295.

Deschamps, F., Godard, M., Guillot, S., and Hattori, K. (2013). Geochemistry of subduction zone serpentinites: a review. *Lithos*, 178, 96-127.

Droop, G.T.R. (1987. A general equation for estimating Fe 3+ concentrations in ferromagnesian silicates and oxides from microprobe analyses, using stoichiometric criteria. *Mineralogical magazine*, 51, 431-435.

Dungan, M.A. (1979). Bastite pseudomorphs after orthopyroxene, clinopyroxene, and tremolites. *Canadian Mineralogist*, 17, 729-740.

Dymek, R.F., Brothers, S.C., and Schiffries, C.M., (1988). Petrogenesis of ultramafic metamorphic rocks from the 3800 Ma Isua supracrustal belt, West Greenland. *J. Petrology*, 29, 1353-1397.

Elthon, D., J. F. Casey, and S. Komor (1982). Mineral chemistry of ultramafic cumulates from the North Arm Mountain Massif of the Bay of Islands ophiolite: Evidence for high-pressure crystal fractionation of oceanic basalts. *J. Geophys. Res.*, 87 (B10), 8717–8734

Franz, L. and Becker, K. (2002). Metasomatic Mantle Xenoliths from the Bismarck Microplate (Papua New Guinea)— Thermal Evolution, Geochemistry and Extent of Slab-induced Metasomatism. *J. Petrology,* 43, 315–343.

Frei, R., Rosing, M., Waight, T.E., and Ulfbeck D.G. (2002). Hydrothermal-metasomatic and tectono-metamorphic processes in the Isua greenstone belt (West Greenland): A multi-isotopic investigation of their effects on the Earth's oldest oceanic crustal sequence. *Geochim. Cosmochim. Acta*, 66, 467–486.

Frei, R. and Jensen, B.K. (2003). Re – Os, Sm – Nd isotope and REE systematics on ultramafic rocks and pillow basalts from the Earth's oldest oceanic crustal fragments (Isua Supracrustal Belt and Ujaragssuit nunat area, W Greenland). *Chem. Geol.*, 196, 163-191.

Frei, R., Polat, A., and Meibom, A. (2004). The Hadean upper mantle conundrum: evidence for source depletion and enrichment from Sm–Nd, Re–Os, and Pb isotopic compositions in 3.71 Gy boninite-like metabasalts from the Isua Supracrustal Belt, Greenland. *Geochim. Cosmochim. Acta*, 68, 1645-1660.

Friend, C.R.L., Bennett, V.C., and Nutman, A.P., (2002). Abyssal peridotites >3,800 Ma from southern west Greenland: field relationships, petrography, geochronology, wholerock and mineral chemistry of dunite and harzburgite inclusions in the Itsaq Gneiss Complex. *Contrib. Mineral Petrol.*, 143, 71-92.

Friend, C.R.L. and Nutman, A.P. (2005). New pieces to the Archaean terrane jigsaw puzzlein the Nuuk region, southern West Greenland: steps in transforming a simpleinsight into a complex regional tectonothermal model. *J. Geol. Soc. Lond.*, 162,147–163.

Furnes, H., Rosing, M., Dilek, Y., and DeWit, M. (2009). Isua supracrustal belt (Greenland) - A vestige of a 3.8 Ga suprasubduction zone ophiolite, and the implications for Archean geology. *Lithos*, 113, 115-132.

Gaetani, G.A., T.L. Grove, and W.B. Bryan (1993). The influence of water on the petrogenesis of subduction-related igneous rocks. *Nature*, 365, 332-334.

Gannoun, A., Burton, K. W., Day, J. M. D., Harvey, J., Schiano, P., & Parkinson, I. (2016). Highly Siderophile Element and Os Isotope Systematics of Volcanic Rocks at Divergent and Convergent Plate Boundaries and in Intraplate Settings. *Reviews in Mineralogy and Geochemistry*, 81, 651-724.

Garuti, G., Bea, F., Zaccarini, F., and Montero, P. (2001). Age, Geochemistry and Petrogenesis of the Ultramafic Pipes in the Ivrea Zone, NW Italy. *J. Petrology*, 42, 433-457.

Gervilla, F., Padro, J.A., Fanlo, I., and Gonza, J.M. (2012). Formation of ferrian chromite in podiform chromitites from the Golyamo Kamenyane serpentinite, Eastern Rhodopes, SE Bulgaria: a two-stage process. *Contrib. Mineral Petrol.*, 164, 643–657.

Ghiorso, M.S. and Sack, R.O. (1995). Chemical mass transfer in magmatic processes IV. A revised and internally consistent thermodynamic model for the interpolation and extrapolation of liquid–solid equilibria in magmatic systems at elevated temperatures and pressures. *Contrib. Mineral Petrol.*, 119, 197–212.

Gruau, G., Rosing, M., Bridgwater, D., and Gill, R.C.O. (1996). Resetting of Sm–Nd systematics during metamorphism of >3.7-Ga rocks: implications for isotopic models of early Earth differentiation. *Chem. Geol.*,133, 225-240.

Harvey J., Yoshikawa, M., Hammond, S.J., and Burton, K.W. (2012). Deciphering the Trace Element Characteristics in Kilbourne Hole Peridotite Xenoliths: Melt–Rock Interaction and Metasomatism beneath the Rio Grande Rift, SW USA. *J. Petrology*, 53, 1709–1742.

Helmy, H.M. and Mahallawi, M.M. (2003). Gabbro Akarem mafic-ultramafic complex, Eastern Desert, Egypt: a late Precambrian analogue of Alaskan-type Complexes. *Mineralology Petrology*, 77, 85–108.

Himmelberg, G.R. and Loney, R.A. (1995). Characteristics and petrogenesis of Alaskan type ultramafic-mafic intrusions, Southeastern Alaska. *US Geol. Surv. Prof. Pap.*, 1564, 1-47.

Hoffmann, J.E., Münker, C., Polat, A., Rosing,M.T., and Schulz, T. (2011). The origin of decoupled Hf–Nd isotope compositions in Eoarchean rocks from southern West Greenland. *Geochim. Cosmochim. Acta*, 75, 6610-6628.

Hughes, H.S.R., Mcdonald, I., and Kerr, A.C. (2015). Lithos Platinum-group element signatures in the North Atlantic Igneous Province: Implications for mantle controls on metal budgets during continental breakup. *Lithos*, 233, 89-110.

Ionov, D. A., Chanefo, I., and Bodinier, J. L. (2005). Origin of Fe-rich lherzolites and wehrlites fromTok, SE Siberia by reactive melt percolation in refractory mantle peridotites. *Contrib. Mineral Petrol.*, 150, 335-353.

Ireland, T.J., Walker, R.J., and Garcia, M O. (2009). Highly siderophile element and 187Os isotope systematics of Hawaiian picrites: Implications for parental melt composition and source heterogeneity. *Chem. Geol.*, 260, 112-128.

Ishikawa, A., Suzuki, K., Collerson, K.D., Liu, J., Pearson, D.G., and Komiya, T. (2017). Rhenium-osmium isotopes and highly siderophile elements in ultramafic rocks from the Eoarchean Saglek Block, northern Labrador, Canada: implications for Archean mantle evolution. *Geochim. Cosmochim. Acta*, 216, 286-311.

Jagoutz, O., Muntener, O., Ulmer, P., Pettke, T., Burg, J.P.m Dawood, H., and Husain, S (2007). Petrology and mineral chemistry of lower crustal intrusions: the Chilas Complex, Kohistan (NW Pakistan). *J. Petrology*, 48 (10), 1895–1953.

Jagoutz, O. and Schmidt, M. W. (2012). The formation and bulk composition of modern juvenile continental crust: The Kohistan arc. *Chem. Geol.*, *298-299*, 79-96.

Jenner, F.E., Bennett, V.C., Nutman, A.P., Friend, C.R.L., Norman, M.D., and Yaxley, G. (2009). Evidence for subduction at 3.8 Ga: geochemistry of arclike metabasalts from the southern edge of the Isua Supracrustal Belt. *Chem. Geol.*, 261, 82-99.

Klemme, S. and O'Neill., H.S. (2000). The near-solidus transition from garnet lherzolite to spinel lherzolite. *Contrib. Mineral Petrol.*, 138, 237-248.

Koga, K.T., P.B. Kelemen, and N. Shimizu (2001). Petrogenesis of the crust-mantle transition zone and the origin of lower crustal wehrlite in the Oman ophiolite. *Geochem. Geophys. Geosyst.*, 2, 1038,

Komiya, T., Maruyama, S., Hirata, T., Yurimoto, H., and Nohda, S. (2004). Geochemistry of the oldest MORB and OIB in the Isua supracrustal belt, southern West Greenland: implications for the composition and temperature of Early Archean mantle. *Island Arc*, 13, 47–72.

Lassiter, J. C., & Luhr, J. F. (2001). Osmium abundance and isotope variations in mafic Mexican volcanic rocks: Evidence for crustal co ntamination and constraints on the geochemical behavior of osmium during partial melting and fractional crystallization. *Geochem. Geophys. Geosyst.*, 2, 1027.

Li, C., Ripley, E. M., Thakurta, J., Stifter, E. C., and Qi, L. (2013). Variations of olivine Fo – Ni contents and highly chalcophile element abundances in arc ultramafic cumulates, southern Alaska. *Chem. Geol.*, 351, 15–28.

Liu, X.I., Zhao, Y., Chen, J., and Liu, X. (2003). Pyroxene exsolution in mafic granulites from the Grove Mountains, East Antarctica: constraints on Pan-African metamorphic conditions. *Eur. J. Mineral.*, 15, 55–65.

Locht, J., van de, Hoffmann, J.E., Li, C., Wang, Z., Becker, H., Rosing, M. T., Kleinschrodt, R., and Münker, C. (2018). Earth's oldest mantle peridotites show entire record of late accretion. *Geo. Society of America*, 46, 1–4.

Lowry D, Appel PWU, and Rollinson HR (2003). Oxygen isotopes of an early Archaean layered ultramafic body, southern West Greenland: implications for magma source and post-intrusion history. *Precambrian Res.* 126, 273–288.

Luguet A., Nowell, G.M., and Pearson, D.G. (2008). 184Os/188Os and 186Os/188Os measurements by Negative Thermal Ionization Mass Spectrometry (N-TIMS): effects of interfering element and mass fractionation corrections on data accuracy and precision. *Chem. Geol.*, 248, 342-362.

Maeda, J., Naslund, H.R., Jang, Y.D., Kikawa, E., Tajima, T., and Blackburn, W.H. (2002). High-temperature fluid within oceanic layer 3 gabbros, hole 735B, southwest Indian ridge:

implications for the magmatic-hydrothermal transition at slow-spreading mid-ocean ridges. Natland, J.H., Dick H.J.B., Miller, D.J., and Von Herzen, R.P. (Eds.), *Proceedings of the Ocean Drilling Program, Scientific Results Volume*, 176, 1-56.

Maier, W.D., Barnes, S.J., Campbell, I.H., Fiorentini, M.L., Peltonen, P., Barnes, S.J., and Smithies, R.H. (2009). Progressive mixing of meteoritic veneer into the early Earth's deep mantle. *Nature*, 460, 620-623.

Marques, J. C., Filho, C. F. F., Carlson, R. W., & Pimentel, M. M. (2003). Re-Os and Sm-Nd Isotope and Trace Element Constraints on the Origin of the Chromite Deposit of the Ipueira-Medrado Sill, Bahia, Brazil. *J. Petrology*, 44, 659-678.

Mavrogenes, J.A. and O'Neill, H.T. (1999). The relative effects of pressure, temperature and oxygen fugacity on the solubility of sulfide in mafic magmas. *Geochim. Cosmochim. Acta*, 63, 1173-1180.

McDonough, W.F. and Sun, S.S. (1995). The composition of the Earth. *Chem. Geol.*, 120, 223-253.

McGregor, V.R., Friend, C.R.L., and Nutman, A.P. (1991). The late Archaean mobile beltthrough Godthåbsfjord, southern West Greenland: a continent–continent colli-sion zone? *Bull. Geol. Soc. Den.*, 39, 179-197.

Meisel, T., Walker, R.J., Irving, A.J., and Lorand, J.P. (2001). Osmium isotopic compositions of mantle xenoliths: a global perspective. *Geochim. Cosmochim. Acta*, 65, 1311-1323.

Morimoto N (1988) Nomenclature of pyroxene. *Mineralogical Magazine*, 52, 535-550.

Mungall, J.E. and Brenan, J.M. (2014). Partitioning of platinum-group elements and Au between sulfide liquid and basalt and the origins of mantle-crust fractionation of the chalcophile elements. *Geochim. Cosmochim. Acta*, *125*, 265-289.

Myers, J.S. (2001). Protoliths of the 3.8–3.7 Ga Isua greenstone belt, West Greenland. *Precambrian Res.*, 105, 129-141.

Niu, Y. (2004). Bulk-rock Major and Trace Element Compositions of Abyssal Peridotites: Implications for Mantle Melting, Melt Extraction and Post-melting Processes Beneath Mid-Ocean Ridges. *J. Petrology*, 45, 2423-2458.

Nutman, A.P., Mcgregor, V.R., Friend, C.R.L., Bennett, V.C., and Kinny, P.D. (1996). The Itsaq Gneiss Complex of southern West Greenland; the world's most extensive record of early crustal evolution (3900–3600). *Precambrian Res.*, 78, 1-39.

Nutman, A.P., Friend, C.R.L., and Bennett, V.C. (2002). Evidence for 3650–3600 Ma assembly of the northern end of the Itsaq Gneiss Complex, Greenland: implication for early Archean tectonics. *Tectonics*, 21, No. 1, 1005.

Nutman, A. P., Bennett, V. C., Friend, C. R. L., Yi, K., and Lee, S.R. (2015). Mesoarchaean collision of Kapisilik terrane 3070 Ma juvenile arc rocks and > 3600 Ma Isukasia terrane continental crust (Greenland). *Precambrian Res.*, 258, 146-160.

Page, P. and Barnes, S.J. (2009). Using trace elements in chromites to constrain the origin of podiform chromitites in the Thetford Mines ophiolite, Québec, Canada. *Econ. Geol.*, 104, 997-1018.

Page P. and Barnes S.J. (2016). The influence of chromite on osmium, iridium, ruthenium and rhodium distribution during early magmatic processes. *Chem. Geol*., 420, 51-68.

Park, J., Hu, Z., Gao, S., Campbell, I. H., and Gong, H. (2012). Platinum group element abundances in the upper continental crust revisited – New constraints from analyses of Chinese loess. *Geochim. Cosmochim. Acta*, *93*, 63-76.

Park J.W., Campbell I.H., and Arculus R.J. (2013). Platinum-alloy and sulfur saturation in an arc-related basalt to rhyolite suite: evidence from the Pual Ridge lavas, the Eastern Manus Basin. *Geochim. Cosmochim. Acta*, 101, 76-95.

Park, J., Kamenetsky, V., Campbell, I., Park, G., Hanski, E., and Pushkarev, E. (2017). Empirical constraints on partitioning of platinum group elements between Cr-spinel and primitive terrestrial magmas. *Geochim. Cosmochim. Acta*, *216*, 393-416.

Parlak, O., Delaloye, M. & Bíngöl, E. Geol Rundsch (1996). Mineral chemistry of ultramafic and mafic cumulates as an indicator of the arc-related origin of the Mersín ophiolite (southern Turkey). *Geol. Rundsch*, 85, 647.

Pearce, J.A. (2008). Geochemical fingerprinting of oceanic basalts with applications to ophiolite classification and the search for Archean oceanic crust. *Lithos*, 100, 14-48.

Pearson, D.G. and Woodland, S.J. (2000). Solvent extraction/anion exchange separation and determination of PGEs (Os, Ir, Pt, Pd, Ru) and Re–Os isotopes in geological samples by isotope dilution ICP-MS. *Chem. Geol.*, 165, 87-107.

Pearson, D.G., Irvine, G.J., Ionov, D.A., Boyd, F.R., and Dreibus, G.E. (2004). Re – Os isotope systematics and platinum group element fractionation during mantle melt extraction: a study of massif and xenolith peridotite suites. *Chem. Geol.,* 208, 29-59.

Pearson, D.G. and Wittig, N. (2008). Formation of Archaean continental lithosphere and its diamonds: the root of the problem. *J. Geol. Soc.*, 165, 895-914.

Peck, D.C., Keays, R.R., and Ford, R.J. (1992). Direct crystallization of refractory platinum - group element alloys from boninitic magmas: Evidence from western Tasmania. *Australian J. Earth Sci.*, 39, 373-387.

Peltonen, P. (1990). Metamorphic olivine in picritic metavolcanics from southern Finland. *Bulletin of the Geological Society of Finland*, 62, 99-114.

Peters, D. and Pettke, T. (2017). Evaluation of Major to Ultra Trace Element Bulk Rock Chemical Analysis of Nanoparticulate Pressed Powder Pellets by LA-ICP-MS. *Geostand. Geoanal. Res.*, 41, 5-28.

Philipp, H., & Puchelt, H. (2001). Platinum-Group Elements (PGE) in Basalts of the Seaward-Dipping Reflector Sequence, SE Greenland Coast. *J. Petrology*, 42, 407-432.

Pitcher, L., Helz, R.T., Walker, R.J., and Piccoli, P, (2009). Fractionation of the platinum-group elements and Re during crystallization of basalt in Kilauea Iki lava lake, Hawaii. *Chem. Geol.*, 260, 196-210.

Pivin, M., Féménias, O., and Demaiffe, D. (2009). Lithos Metasomatic mantle origin for Mbuji-Mayi and Kundelungu garnet and clinopyroxene megacrysts (Democratic Republic of Congo). *Lithos*, *112*, 951–960.

Polat, A., Hofmann, A.W., and Rosing,M.T. (2002). Boninite-like volcanic rocks in the 3.7–3.8 Ga Isua greenstone belt, West Greenland: geochemical evidence for intra-oceanic subduction zone processes in the early Earth. *Chem. Geol.*, 184, 231-254.

Polat, A. and Hofmann, A.W. (2003). Alteration and geochemical patterns in the 3.7 – 3.8 Ga Isua greenstone belt, West Greenland. *Geochim. Cosmochim. Acta*, 126, 197-218.

Polat, A., Hofmann, A.W., Münker, C., Regelous, M., Appel, and P.W.U. (2003). Contrasting geochemical patterns in the 3.7–3.8 Ga pillowbasalt cores and rims, Isua greenstone belt, Southwest Greenland: implications for postmagmatic alteration processes. *Geochim. Cosmochim. Acta*, 67, 441–457.

Poldervaart, A. and Hess, H.H. (1951). Pyroxenes in the crystallization of basaltic magma. *Journal of Geology*, 59, 472-489.

Putchel, I. and Humayun, M. (2001). Platinum group elements in Kostomuksha komatiites and basalts: Implications for oceanic crust recycling and core-mantle interaction. *Geochim. Cosmochim. Acta*, 64, 4227-4242.

Puchtel, I.S., Touboul, M., Blichert-toft, J., Walker, R.J., Brandon, A.D., Nicklas, R.W., Kulikov, V.S., and Samsonov, A.V. (2016). Lithophile and siderophile element systematics of Earth ' s mantle at the Archean – Proterozoic boundary: Evidence from 2.4 Ga komatiites. *Geochim. Cosmochim. Acta*, 180, 227-255.

Qi, Q., Beard, B.L., Jin, Y., Taylor, L.A., Qi, Q., Beard, (1994). Petrology and Geochemistry of Al-Augite and Cr- Diopside Group Mantle Xenoliths from Tahiti, Society Islands. *International Geology Review*, 36, 152-178.

Rehkamper, M., Halliday, A.N., Fitton, J.G., Lee, D.C., Wieneke, M., and Arndt, N.T. (1999). Ir, Ru, Pt, and Pd in basalts and komatiites: new constraints for the geochemical behavior of the platinum-group elements in the mantle. *Geochim. Cosmochim. Acta*, 63, 3915-3934.

Righter K., Campbell A. J., Humayun M. and Hervig R. L. (2004). Partitioning of Ru, Rh, Pd, Re, Ir, and Au between Cr-bearing spinel, olivine, pyroxene and silicate melts. *Geochim. Cosmochim. Acta*, 68, 867-880.

Ripley, E.M., Shafer, P., Li, C., and Hauck, S.A. (2008). Re – Os and O isotopic variations in magnetite from the contact zone of the Duluth Complex and the Biwabik Iron Formation, northeastern Minnesota. *Chem. Geol.*, 249, 213-226.

Rizo, H., Boyet, M., Blichert-Toft, J., and Rosing, M. T. (2013). Early mantle dynamics inferred from 142Nd variations in Archean rocks from southwest Greenland. *Earth Planet. Sci. Lett.*, 377, 324-335.

Rizo, H., Walker, R.J., Carlson, R.W., Touboul, M., Horan, M.F., Puchtel, I.S., Boyet, M., and Rosing, M.T. (2016). Early Earth differentiation investigated through 142Nd, 182W, and highly siderophile element abundances in samples from Isua, Greenland: *Geochim. Cosmochim. Acta*, 175, 319-336.

Rollinson, H., Appel, P.W.U., and Frei, R. (2002). A metamorphosed, early Archean chromitite from West Greenland: Implications for the genesis of Archean anorthositic chromitites. *J. Petrology*, 43, 2143-2170.

Rollinson, H., (2007). Recognizing early Archaean mantle: a reappraisal. *Contrib. Mineral Petrol.*, 154, 241–252.

Rose, N.M., Rosing, M.T., and Bridgwater, D. (1996). The origin of metacarbonate rocks in the Archaean Isua supracrustal belt, West Greenland. *American Journal of Science*, 296, 1004-1044.

Rosing, M.T. and Rose, N.M. (1993). The role of ultramafic rocks in regulating the concentrations of volatile and non-volatile components during deep crustal metamorphism. *Chem. Geol.*, 108, 187-200.

Rosing, M.T., Rose, N.M., Bridgwater, D., and Thomsen, H.S. (1996). Earliest part of the Earth's stratigraphic record: a reappraisal of the N3.7 Ga Isua (Greenland) supracrustal sequence. *Geology*, 24, 43-46.

Schoenberg, R., Kruger, F.J., Nagler, T.F., Meisel, T., and Kramers, J.D. (1999). PGE enrichment in chromitite layers and the Merensky Reef of the western Bushveld Complex; a Re – Os and Rb – Sr isotope study. *Earth Planet. Sci. Lett.*, 172, 49-64.

Scoates, J. S., Weis, D., Franssens, M., Mattielli, N., Annell, H., Frey, F. A., … Giret, A. (2008). The Val Gabbro Plutonic Suite: A Sub-volcanic Intrusion Emplaced at the End of Flood Basalt Volcanism on the Kerguelen Archipelago. *J. Petrology*, 49, 79-105.

Selby, D., Creaser, R. A., Stein, H. J., Markey, R. J. & Hannah, J. L. (2007). Assessment of the 187Re decay constant by cross calibration of Re-Os molybdenite and U-Pb zircon chronometers in magmatic ore systems. *Geochim. Cosmochim. Acta*, 71, 1999-2013.

Siebert, C., Kramers, J.D., Meisel, T.H., Morel, P.H., and Nagler, T.F. (2005). PGE, Re-Os, and Mo isotope systematics in Archean and early Proterozoic sedimentary systems as proxies for redox conditions of the early Earth. *Geochim. Cosmochim. Acta*, 69, 1787-1801.

Simkin, T. & Smith, J. V. (1970). Minor-element distribution in olivine. *J. Geol.*, 78, 304-325.

Simon, N.S.C., Irvine, G.J., Davies, G.R., Pearson, D.G., and Carlson, R.W. (2003). The origin of garnet and clinopyroxene in “depleted” Kaapvaal peridotites. *Lithos*, 71, 289–322.

Spear, F.S. (1993). Metamorphic phase equilibria and pressure-temperature time paths. Monograph1. *Mineral. Soc. America*, Washingon, DC. Chapter 13.

Song, X.Y., Keays, R.R>, Xiao, L., Qi, H., and Ihlenfield, C. (2009). Platinum-group element geochemistry of the continental flood basalts in the central Emeisihan Large Igneous Province, SW China. *Chem. Geol.*, 262, 246-261.

Sun, J., Liu, C., Wu, F., Yang, Y., and Chu, Z. (2012). Metasomatic origin of clinopyroxene in Archean mantle xenoliths from Hebi , North China Craton : Trace-element and Sr-isotope constraints. *Chem. Geol.*, *328*, 123-136.

Szilas, K., Kelemen, P.B., and Rosing, M.T. (2015). The petrogenesis of ultramafic rocks in the >3.8 Ga Isua supracrustal belt, southern West Greenland: Geochemical evidence for two distinct magmatic cumulate trends: *Gondwana Res.*, 28, 565–580.

Szilas, K., Hinsberg, V., Van, Mcdonald, I., Næraa, T., Rollinson, H., Adetunji, J., and Bird, D. (2017). Highly refractory Archaean peridotite cumulates: Petrology and geochemistry of the Seqi Ultramafic Complex, SW Greenland. *Geoscience Frontiers*, 1-27.

Tilhac, R., Ceuleneer, G., Griffin, W.L., Reilly, S.Y.O., Pearson, N.J., … Gregoire, M. (2017). Primitive Arc Magmatism and Delamination: Petrology and Geochemistry of Pyroxenites from the Cabo Ortegal Complex, Spain. *J. Petrology*, 57, 1921-1954.

Wang, C.Y., Zhou, M., Yang, S., Qi, L., & Sun, Y. (2014). Geochemistry of the Abulangdang intrusion: Cumulates of high-Ti picritic magmas in the Emeishan large igneous province, SW China. *Chem. Geol.*, 378–379, 24–39.

Walker R. J., Prichard H. M., Ishiwatatari, A., and Pimentel, M. (2002) The osmium isotopic composition of convecting upper mantle deduced from ophiolitic chromites. *Geochim. Cosmochim. Acta*, 66, 329-345.

Walker, R.J. (2009). Highly siderophile elements in the Earth, Moon and Mars: Update and implications for planetary accretion and differentiation. *Chemie der Erde*, 69, 101-125.

Waterton, P. (2018). (PhD Thesis). University of Alberta, Edmonton, Alberta, Canada.

Weyer, S. and Ionov, D.A., (2007). Partial melting and melt percolation in the mantle: the message from Fe isotopes. *Earth Planet. Sci. Lett.*, 259, 119-133.

Wittig, N., Pearson, D.G., Webb, M., Ottley, C.J., Irvine, G.J., Kopylova, M.G., Jensen, S.M., and Nowell, G.M. (2008). Origin of cratonic lithospheric mantle roots: a geochemical study of peridotites from the North Atlantic Craton, West Greenland. *Earth Planet. Sci. Lett.*, 274, 24-33.

Wittig, N., Webb, M., Pearson, D.G., Dale, C.W., Ottley, C.J., Hutchison, M., Jensen, S.M., and Laguet, A. (2010). Formation of the North Atlantic Craton: Timing and mechanisms constrained from Re–Os isotope and PGE data of peridotite xenoliths from S.W. Greenland. *Chem. Geol.,* 276, 166-187

Wlotzka, F. (2005). Cr spinel and chromite as petrogenetic indicators in ordinary chondrites: Equilibration temperatures of petrologic types 3.7 to 6. *Meteoritics Planetary Science*, 40, 1673-1702.

Woodland, S. J., Pearson, D. G., and Thirlwall, M. F. (2002). A Platinum Group Element and Re – Os Isotope Investigation of Siderophile Element Recycling in Subduction Zones: Comparison of Grenada, Lesser Antilles Arc, and the Izu – Bonin Arc. *J. Petrology*, 43, 171-198.

Zaccarini, F., Pushkarev, E.V., Fershtater, B., and Garuti, G. (2004). Composition and mineralogy of PGE-rich chromitites in the Nurali lherzolite-gabbro complex, southern Urals, Russia. *Canadian Mineralogist*, 42, 545-562.

Zhu, Y., Chen, J., Xue, Y., Feng, W., and Jiang, J. (2017). Spinel and orthopyroxene exsolved from clinopyroxene in the Haladala pluton in the middle Tianshan (Xinjiang, China). *Mineralogy and Petrology*, 111, 1-15.

Chapter 3

Conclusions and Future Directions

3.1 Main Conclusions

This study has focused on one of the larger, until now unstudied ultramafic enclaves of the IGC – the Tussaap ultramafic complex (TUC). The main conclusions of this study are as follows:

- The geochemistry of the TUC strongly implies that the peridotites within it originated as cumulates. Fractional crystallization models of both major and trace elements fit very well with variations of these elements in the TUC (Figs. 2-6 and 8). In addition, PGE and Re-Os isotopic systematics are consistent with a cumulate origin.
- Interelement fractionation of trace elements, high Pd abundances, and Re-Os isotope systematics suggest significant crustal contamination of the TUC parental melts. Whether this was entirely the result of crustal assimilation or in part from arc-like volcanic processes is unclear. In conclusion, there is no significant geochemical evidence to implicate arc-like processes in the pretrogenesis of the TUC.
- Cumulate processes and significant crustal contamination has obscured PGE systematics that may have otherwise been used to estimate the abundance of PGEs in the parental melt source of the TUC.
- Furthermore, crustal contamination increased the ^{187}Os/^{188}Os ratio of the parental melts, leading to anomalously ^{187}Os/^{188}Os high ratios in the TUC, and casting some doubt on the the proposed Eoarchean age of the TUC.

3.2 Identifying Eoarchean lithospheric mantle

The positive identification of fragments of mantle rocks in Eoarchean crustal terranes has become a critical goal in understanding early mantle geochemistry and, particularly, in trying to constrain the continued flux of meteoritic material to Earth's mantle long after it had formed (e.g., Morino et al., 2017; Ishikawa et al., 2018; van de Locht et al., 2018). There are no explicit characteristics that can be used to identify remnants of Eoarchean or Hadean mantle hosted in crustal rocks. Because of this there is debate and uncertainty in what ultramafic constituents of the IGC originated from partial melting or crystal accumulation (Dymek et al., 1988; Bennet et al., 2002; Friend et al., 2002; Rollinson, 2007; Friend and Nutman, 2011; Szilas et al., 2015; van de Locht et al., 2018). The same uncertainty surrounds ultramafic enclaves in other Eoarchean terranes (e.g. Morino et al., 2016; Ishikawa et al., 2018).

As the geochemical characteristics of the TUC peridotites constrain their origin to crystal accumulation, a unique opportunity is available to evaluate discrimination diagrams used to differentiate between crustally hosted Eoarchean lithospheric mantle and ultramafic cumulates. Of interest is the ubiquitous use of the Al/Si vs Mg/Si weight ratio diagram as a rigorous discrimination of these rock types (e.g. Friend et al., 2002; Rollinson, 2007; van de Locht et al., 2018). However, olivine with varying forsterite contents and trapped interstitial melt, cumulate dunites, and the TUC dunites cover the same range in Al/Si and Mg/Si ratios as postulated Eoarchean mantle lithologies (Fig. 3-1). Thus, this diagram does not clearly differentiate cumulate and mantle lithologies.

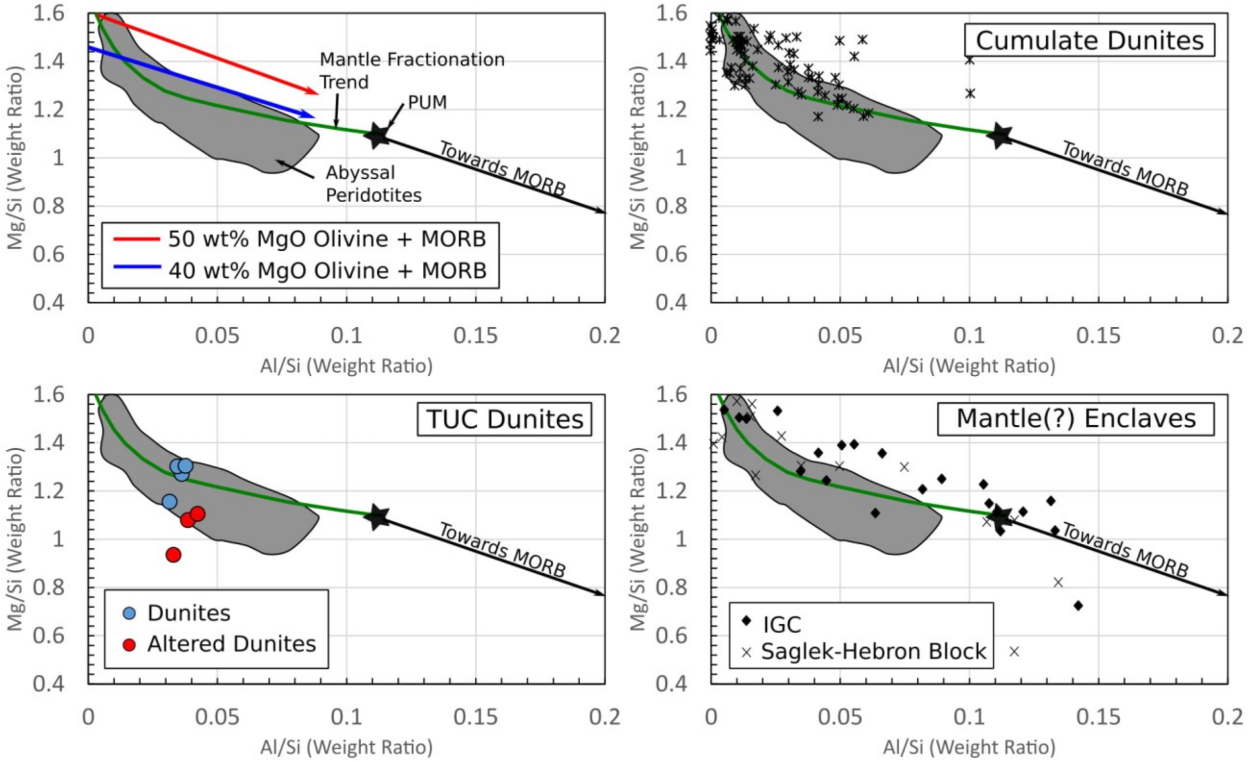

Fig. 3-1. Al/Si vs Mg/Si weight ratio diagram commonly used in the literature as a discrimination diagram for mantle rocks. Abyssal peridotites and mantle fractionation trend are from Rollinson (2007). Red and blue arrows are olivine MORB mixing lines for different wt% MgO in the olivine. The olivine is assumed to have 40 wt% SiO_2 and the length of the lines represents 0 to 20% mixing with MORB. MORB compositions are from Bezos et al. (2005). Cumulate dunites are from Himmelberg and loney (1995), Day et al. (2008), Jagoutz and Schmidt (2012), Li et al. (2013), Wang et al. (2014), and Szilas et al. (2017). The IGC mantle enclaves are from Friend et al. (2002) and van de Locht et al. (2018). The Saglek-Hebron data are from Ishikawa et al. (2018).

Chromite chemistry, Cr# and Fe#, is also used to evaluate cumulate and mantle origins for ultramafic rocks in the IGC (Friend et al., 2002; Rollinson, 2007). However, Cr# in chromites have similar ranges between layered and massive peridotite enclaves in the IGC (Rollinson, 2007), and, except for potential igneous trends, the Fe# in chromite appears to be controlled by equilibration with olivine in the TUC, layered peridotites, and postulated mantle lithologies in the IGC (Fig. 2-3). This implies that chromite chemistry is not a unique discriminator between ultramafic cumulate and mantle material in the IGC or other ultramafic enclaves in Eoarchean terranes.

Rare earth element systematics have been used to determine the origin of ultramafic enclaves in the IGC (Friend et al., 2002; Rollinson, 2007). However, the large variation and overlap of primitive mantle normalized REE abundances of both cumulate and postulated mantle lithologies in the IGC (Figs. 2-7 and 14) makes the use of these elements questionable for this purpose. In addition, the ubiquitous disturbance of the Sm-Nd isotopic system in the area strongly implies that LREEs were highly mobile during late Archean metamorphism (e.g. Gruau et al., 1996; Blichert-Toff et al., 1999; Frei et al., 2002; Polat et al., 2003; Boyet et al., 2003). These findings are consistent with REE systematics in the TUC that suggest that LREE have been mobilized in these rocks. Thus, LREEs should not be used to identify mantle lithologies in the IGC. It is suggested here that, given the uncertainty in the composition of the mantle in the Eoarchean, mantle material should be identified by other means, and then trace element characteristics of the mantle at this time can be assessed.

The inter-element distribution of PGEs has been used as a potential indicator of mantle or cumulate lithologies (e.g. Locht et al., 2018). Primitive mantle normalized PPGE depletion relative to IPGEs is not a definitive indicator of depleted mantle material as this signature is found in the TUC and both mantle and cumulate lithologies in the IGC (Fig. 2-10). However, as noted by Ishikawa et al. (2017), relatively flat IPGE patterns and consistent abundances may be used as evidence for a mantle origin. This signature should be used in combination with the concentration of FeO in the rocks, as this is elevated in most cumulate lithologies relative to cratonic mantle (Figs. 2-13 and 15).

Based on the combination of these geochemical indicators, we agree with Friend et al. (2002), Rollinson (2007), and van de Locht et al. (2018), that some ultramafic enclaves south of the ISB may be composed of lithospheric mantle material. The four samples of van de Locht et al. (2018), characterized as “group 1 peridotites south of the ISB”, are the most likely rocks studied thus far to represent fragments of depleted mantle in the Isukasia region (Fig. 2-15).

3.2 Crustal assimilation: arc-like geochemical signatures and modern BSE like PGE characteristics

Within the TUC suite the interelement fractionation of trace elements, Pd abundances, and Re-Os isotope systematics, indicate some addition of crustally derived geochemical signatures to the melts which formed the TUC. Whether this crustal contamination was entirely the result crustal assimilation or, in part, derived from arc-like processes transferring the crustal signature in the mantle remains unclear. Many studies in the Isukasia region have used trace element characteristics in mafic and ultramafic rocks to infer arc-like volcanic processes (e.g. Polat et al., 2002; Polat and Hofmann, 2003; Jenner et al., 2009; Nutman and Friend, 2009; Furnes et al., 2009; Szilas et al., 2015; Polat et al., 2015). However, the results of this study suggest a further need to evaluate crustal assimilation as a mechanism for producing arc-like geochemical signatures in the area.

Evaluating late veneer additions to the early mantle requires an understanding of the effects of crustal assimilation on PGE abundances and Re-Os isotope systematics. Crustal assimilation can result in contamination of melts with Pd and will elevate $^{187}Os/^{188}Os$ ratios making it difficult to estimate mantle source PGE characteristics and their time-integrated evolution. The TUC has high Pd and radiogenic $^{187}Os/^{188}Os$ ratios implying that some crustal components were added to the TUC melts. In contrast, other studies in the Isukasia region suggest that the source for many of the melts in the area had modern BSE-like PGE abundances implying that their source was replenished or partially replenished in PGEs by a late chondritic veneer (Bennett et al., 2002; Szilas et al., 2015; Dale et al., 2016; Rizo et al., 2016; van de Locht et al., 2018). Unfortunately, the evolved nature of the TUC offers little insight into this source characteristic for the melts. However, that these other studies suggest modern BSE-like PGE characteristics for the source of most rocks in the region, supports the case made here for the significant crustal contamination experienced by the melt which formed the TUC.

3.3 Future Direction

In the exploration of mantle enclaves in the IGC, it appears that some enclaves south of the ISB explored by van de Locht et al. (2018) are the best estimate for early Archean lithospheric mantle.

These have limited trace element, PGE, and Re-Os isotopic data available, and no data from other isotopic systems. Further studies of these enclaves may confirm the suggestion that they are in fact mantle material, in addition to providing a fundamental platform for understanding the composition of the lithospheric mantle in the area.

A complement to such studies would be the exploration of new ultramafic enclaves in the IGC in the Isukasia region that would help in understanding the possible role of crustal assimilation, if the enclaves originated as cumulates and underwent varying degrees of fractionation. In this latter scenario, indices of crustal contamination may covary with $^{187}Os/^{188}Os$ ratios across multiple enclaves possibly allowing for the extrapolation to a common source or, at least, a better understanding the degree of crustal assimilation. In addition, the enclaves south of the ISB are relatively underexplored and may yield additional Eoarchean mantle fragments. Finally, as far as the author is aware, there are no geochemical studies of mafic enclaves in the Isukasia region south of the ISB, and such studies would provide further insight into the nature of the early crust.

References

Bennett, V.C., Nutman, A.P., and Esat, T.M., (2002). Constraints on mantle evolution from 187Os/188Os isotopic compositions from Archaean ultramafic rocks from southern west Greenland (3.8 Ga) and western Australia (3.46 Ga). *Geochim. Cosmochim. Acta*, 66, 2615-2630.

Bezos, A. B., Orand, J. L., Umler, E. H., and Ros, M. G. (2005). Platinum-group element systematics in Mid-Oceanic Ridge basaltic glasses from the Pacific, Atlantic, and Indian Oceans. *Geochim. Cosmochim. Acta*, 69, 2613-2627.

Blichert-Toff, J., Albarede, F., Rosing, M., Frei, F., and Bridgwater, D (1999). The Nd and Hf isotopic evolution of the mantle through the Archean. Results from the Isua supracrustals, West Greenland, and from the Birimian terranes of West Africa. *Geochim. Cosmochim. Acta*, 63, 3901-3914.

Boyet, M., Blichert-toft, J., Rosing, M., Storey, M., Albare, F., & Te, P. (2003). 142Nd evidence for early Earth differentiation. *Earth Planet. Sci. Lett.*, 214, 427-442.

Day, J.M., Pearson, D.G., and Hulbert, L.J. (2008). Rhenium-Osmium Isotope and Platinum-Group Element Constraints on the Origin and Evolution of the 1.27 Ga Muskox Layered Intrusion. *J. Petrology*, 49, 1255-1295.

Dale, C.W., Kruijer, T.S., and Burton, K.W. (2017). Highly siderophile element and 182 W evidence for a partial late veneer in the source of 3.8 Ga rocks from Isua, Greenland. *Earth Planet. Sci. Lett.*, 458, 394-404.

Dymek, R.F., Brothers, S.C., and Schiffries, C.M., (1988). Petrogenesis of ultramafic metamorphic rocks from the 3800 Ma Isua supracrustal belt, West Greenland. *J. Petrology*, 29, 1353-1397.

Frei, R., Rosing, M., Waight, T.E., and Ulfbeck D.G. (2002). Hydrothermal-metasomatic and tectono-metamorphic processes in the Isua greenstone belt (West Greenland): A multi-isotopic investigation of their effects on the Earth's oldest oceanic crustal sequence. *Geochim. Cosmochim. Acta*, 66, 467–486.

Friend, C.R.L., Bennett, V.C., and Nutman, A.P., (2002). Abyssal peridotites >3,800 Ma from southern west Greenland: field relationships, petrography, geochronology, wholerock and mineral chemistry of dunite and harzburgite inclusions in the Itsaq Gneiss Complex. *Contrib. Mineral Petrol.*, 143, 71-92.

Friend, C.R.L. and Nutman, A.P. (2011). Dunites from Isua, Greenland: a ca. 3720 Ma window into subcrustal metasomatism of depleted mantle. *Geology*, 39, 663-666.

Furnes, H., Rosing, M., Dilek, Y., and DeWit, M. (2009). Isua supracrustal belt (Greenland) - A vestige of a 3.8 Ga suprasubduction zone ophiolite, and the implications for Archean geology. *Lithos*, 113, 115-132.

Gruau, G., Rosing, M., Bridgwater, D., and Gill, R.C.O. (1996). Resetting of Sm–Nd systematics during metamorphism of >3.7-Ga rocks: implications for isotopic models of early Earth differentiation. *Chem. Geol.*,133, 225-240.

Himmelberg, G.R. and Loney, R.A. (1995). Characteristics and petrogenesis of Alaskan type ultramafic-mafic intrusions, Southeastern Alaska. *US Geol. Surv. Prof. Pap.*, 1564, 1-47.

Ishikawa, A., Suzuki, K., Collerson, K.D., Liu, J., Pearson, D.G., and Komiya, T. (2017). Rhenium-osmium isotopes and highly siderophile elements in ultramafic rocks from the Eoarchean Saglek Block, northern Labrador, Canada: implications for Archean mantle evolution. *Geochim. Cosmochim. Acta*, 216, 286-311.

Jagoutz, O. and Schmidt, M. W. (2012). The formation and bulk composition of modern juvenile continental crust: The Kohistan arc. *Chem. Geol.*, *298-299*, 79-96.

Jenner, F.E., Bennett, V.C., Nutman, A.P., Friend, C.R.L., Norman, M.D., and Yaxley, G. (2009). Evidence for subduction at 3.8 Ga: geochemistry of arclike metabasalts from the southern edge of the Isua Supracrustal Belt. *Chem. Geol.*, 261, 82-99.

Locht, J., Van De, Hoffmann, J.E., Li, C., Wang, Z., Becker, H., Rosing, M. T., Kleinschrodt, R., and Münker, C. (2018). Earth's oldest mantle peridotites show entire record of late accretion. *Geo. Society of America*, 46, 1–4.

Li, C., Ripley, E.M., Thakurta, J., Stifter, E. C., and Qi, L. (2013). Variations of olivine Fo – Ni contents and highly chalcophile element abundances in arc ultramafic cumulates, southern Alaska. *Chem. Geol.*, 351, 15–28.

Morino, P., Caro, G., Reisberg, L., and Schumacher, A. (2017). Chemical stratification in the post-magma ocean Earth inferred from coupled 146,147Sm–142,143Nd systematics in ultramafic rocks of the Saglek block (3.25–3.9 Ga; northern Labrador, Canada). *Earth Planet. Sci. Lett.*, 463, 136-150.

Nutman, A.P. and Friend, C.R.L. (2009). New 1:20,000 scale geological maps, synthesis and history of investigation of the Isua supracrustal belt and adjacent orthogneisses, southern West Greenland: a glimpse of Eoarchaean crust formation and orogeny. *Precambrian Res.*, 172, 189-211.

Polat, A., Hofmann, A.W., and Rosing,M.T. (2002). Boninite-like volcanic rocks in the 3.7–3.8 Ga Isua greenstone belt, West Greenland: geochemical evidence for intra-oceanic subduction zone processes in the early Earth. *Chem. Geol.*, 184, 231-254.

Polat, A. and Hofmann, A.W. (2003). Alteration and geochemical patterns in the 3.7 – 3.8 Ga Isua greenstone belt, West Greenland. *Geochim. Cosmochim. Acta*, 126, 197-218.

Polat, A., Wang, L., and Appel, P.W.U. (2015). A review of structural patterns and melting processes in the Archean craton of West Greenland: Evidence for crustal growth at convergent plate margins as opposed to non-uniformitarian models: *Tectonophysics*, 662, 67-94.

Rizo, H., Walker, R.J., Carlson, R.W., Touboul, M., Horan, M.F., Puchtel, I.S., Boyet, M., and Rosing, M.T. (2016). Early Earth differentiation investigated through 142Nd, 182W, and highly siderophile element abundances in samples from Isua, Greenland: *Geochim. Cosmochim. Acta*, 175, 319-336.

Rollinson, H., (2007). Recognizing early Archaean mantle: a reappraisal. *Contrib. Mineral Petrol.*, 154, 241–252.

Szilas, K., Kelemen, P.B., and Rosing, M.T. (2015). The petrogenesis of ultramafic rocks in the >3.8 Ga Isua supracrustal belt, southern West Greenland: Geochemical evidence for two distinct magmatic cumulate trends: *Gondwana Res.*, 28, 565–580.

Szilas, K., Hinsberg, V., Van, Mcdonald, I., Næraa, T., Rollinson, H., Adetunji, J., and Bird, D. (2017). Highly refractory Archaean peridotite cumulates: Petrology and geochemistry of the Seqi Ultramafic Complex, SW Greenland. *Geoscience Frontiers*, 1-27.

Wang, C.Y., Zhou, M., Yang, S., Qi, L., & Sun, Y. (2014). Geochemistry of the Abulangdang intrusion: Cumulates of high-Ti picritic magmas in the Emeishan large igneous province, SW China. *Chem. Geol.*, 378–379, 24–39.

Appendices

Appendix 1: Mineral Chemistry

Mineral Standards Used in Analyses

Mineral	**Olivine**	**Chromite**	**Clinopyroxene**	**Orthopyroxene**	**Amphibole**
SiO_2	Fo83 or Fo90.5	Fo90.5, Fo 83, or Enstatite	Dopside	Enstatite	Gore Garnet
TiO_2	Rutile	Ilmenite	Rutile	Rutile	Rutile
ZnO	Gahnite, Willemite, or Sphalerite	Gahnite, Willemite, or Sphalerite	Gahnite or Sphalerite	Gahnite or Sphalerite	
Al_2O_3	Pyrope	Pyrope	Pyrope	Pyrope	Gore Garnet
Cr_2O_3	Chromium Oxide	Chromium Oxide	Chromium Oxide	Chromium Oxide	Chromium Oxide
V	Vanadium Metal	Vanadium Metal	Vanadium Metal	Vanadium Metal	
Co	Cobalt Metal	Cobalt Metal	Cobalt Metal	Cobalt Metal	
Ni	Nickel Metal	Nickel Metal	Nickel Metal	Nickel Metal	Nickel Metal
MnO	Spassertine	Spassertine	Spassertine	Spassertine	Spassertine
MgO	Fo83 or Fo90.5	Fo83, Fo90.5, or enstatite	Diopside	Enstatite	Diopside
CaO	Diopside	Diopside	Diopside	Diopside	Diopside
Na_2O			Albite	Albite	Tugtapite
K2O					Sanidine
F					Apatite
Cl					Tugtupite

Olivine

Sample	**Lithology**	**SiO_2**	**TiO_2**	**ZnO**	**Cr_2O_3**	**FeO**	**CoO**	**NiO**	**MnO**	**CaO**	**Total**	**Mg#**
565451	Anhydrous Ol-CPXite	39.03	0.00	0.00	0.00	19.01	0.00	0.39	0.29	0.01	100.31	79.59
565451	Anhydrous Ol-CPXite	39.02	0.00	0.01	0.00	19.16	0.09	0.39	0.29	0.01	100.49	79.44
565451	Anhydrous Ol-CPXite	39.11	0.00	0.00	0.00	18.96	0.00	0.39	0.28	0.01	100.44	79.67
565451	Anhydrous Ol-CPXite	39.08	0.00	0.01	0.00	18.95	0.06	0.40	0.28	0.01	100.36	79.64
565451	Anhydrous Ol-CPXite	38.99	0.00	0.01	0.02	18.90	0.00	0.40	0.29	0.01	100.20	79.68
565451	Anhydrous Ol-CPXite	39.40	0.00	0.00	0.06	18.55	0.03	0.40	0.28	0.01	99.11	79.67
565451	Anhydrous Ol-CPXite	39.28	0.00	0.01	0.00	18.65	0.03	0.38	0.28	0.01	99.34	79.55
565451	Anhydrous Ol-CPXite	39.28	0.00	0.00	0.00	18.71	0.04	0.39	0.28	0.01	99.43	79.51
565451	Anhydrous Ol-CPXite	39.06	0.00	0.00	0.00	18.78	0.03	0.37	0.29	0.01	99.24	79.43
565451	Anhydrous Ol-CPXite	39.01	0.00	0.00	0.00	18.82	0.04	0.39	0.28	0.01	99.23	79.39
565451	Anhydrous Ol-CPXite	38.98	0.00	0.00	0.01	18.60	0.03	0.35	0.28	0.01	99.19	79.69
565451	Anhydrous Ol-CPXite	39.04	0.00	0.00	0.00	18.59	0.03	0.36	0.28	0.01	99.18	79.67
565451	Anhydrous Ol-CPXite	39.23	0.00	0.01	0.08	18.75	0.03	0.36	0.28	0.01	99.55	79.51
565451	Anhydrous Ol-CPXite	39.24	0.00	0.00	0.00	18.55	0.03	0.37	0.28	0.01	99.36	79.71
565451	Anhydrous Ol-CPXite	39.32	0.00	0.00	0.00	18.54	0.03	0.36	0.28	0.01	99.41	79.71
565451	Anhydrous Ol-CPXite	38.71	0.00	0.00	0.00	18.52	0.03	0.36	0.28	0.01	98.74	79.72
565451	Anhydrous Ol-CPXite	39.71	0.00	0.00	0.00	18.46	0.03	0.36	0.27	0.01	99.74	79.79
565451	Anhydrous Ol-CPXite	39.11	0.00	0.00	0.01	18.52	0.03	0.36	0.27	0.01	99.26	79.76

Sample	Lithology	SiO_2	TiO_2	ZnO	Cr_2O_3	FeO	CoO	NiO	MnO	CaO	Total	Mg#
565451	Anhydrous Ol-CPXite	39.11	0.00	0.00	0.00	18.56	0.03	0.35	0.27	0.01	99.34	79.75
565451	Anhydrous Ol-CPXite	39.08	0.00	0.01	0.00	18.47	0.03	0.36	0.28	0.01	99.19	79.80
565451	Anhydrous Ol-CPXite	38.93	0.00	0.00	0.00	18.48	0.03	0.36	0.28	0.01	99.07	79.81
565451	Anhydrous Ol-CPXite	38.85	0.00	0.01	0.00	18.50	0.03	0.36	0.27	0.01	99.03	79.80
565451	Anhydrous Ol-CPXite	39.17	0.00	0.00	0.00	18.53	0.03	0.37	0.27	0.01	99.47	79.81
565451	Anhydrous Ol-CPXite	39.31	0.00	0.00	0.00	18.44	0.03	0.38	0.28	0.01	99.40	79.84
565451	Anhydrous Ol-CPXite	38.97	0.00	0.00	0.01	18.42	0.03	0.36	0.28	0.01	99.03	79.84
565451	Anhydrous Ol-CPXite	38.91	0.00	0.00	0.07	18.48	0.03	0.36	0.28	0.01	99.01	79.75
565451	Anhydrous Ol-CPXite	38.94	0.00	0.00	0.00	18.48	0.03	0.36	0.27	0.01	99.10	79.81
565451	Anhydrous Ol-CPXite	39.06	0.00	0.01	0.02	18.69	0.03	0.36	0.28	0.01	99.29	79.56
565451	Anhydrous Ol-CPXite	39.08	0.00	0.00	0.00	18.89	0.03	0.36	0.28	0.01	99.40	79.37
565451	Anhydrous Ol-CPXite	39.11	0.00	0.02	0.00	18.79	0.03	0.37	0.29	0.01	99.47	79.48
565451	Anhydrous Ol-CPXite	39.01	0.00	0.01	0.00	18.82	0.03	0.36	0.29	0.01	99.32	79.43
565451	Anhydrous Ol-CPXite	38.99	0.00	0.01	0.00	18.76	0.03	0.37	0.28	0.01	99.25	79.49
565451	Anhydrous Ol-CPXite	39.14	0.00	0.02	0.00	18.78	0.03	0.36	0.28	0.01	99.47	79.50
565451	Anhydrous Ol-CPXite	38.94	0.00	0.00	0.00	18.54	0.03	0.36	0.27	0.01	99.14	79.76
565451	Anhydrous Ol-CPXite	38.88	0.00	0.00	0.00	18.65	0.03	0.35	0.28	0.01	99.21	79.67
565451	Anhydrous Ol-CPXite	38.87	0.00	0.00	0.00	18.62	0.03	0.36	0.28	0.01	99.10	79.67
565451	Anhydrous Ol-CPXite	39.11	0.00	0.01	0.00	18.78	0.03	0.37	0.28	0.01	99.51	79.53
565451	Anhydrous Ol-CPXite	39.08	0.00	0.00	0.00	18.85	0.03	0.37	0.28	0.01	99.36	79.40
565451	Anhydrous Ol-CPXite	39.07	0.00	0.00	0.00	18.92	0.03	0.37	0.29	0.01	99.38	79.32

Sample	Lithology	SiO_2	TiO_2	ZnO	Cr_2O_3	FeO	CoO	NiO	MnO	CaO	Total	Mg#
565451	Anhydrous Ol-CPXite	38.74	0.00	0.00	0.00	18.79	0.03	0.37	0.29	0.01	99.04	79.47
565451	Anhydrous Ol-CPXite	38.97	0.00	0.01	0.00	18.88	0.03	0.37	0.29	0.01	99.31	79.38
565451	Anhydrous Ol-CPXite	39.10	0.00	0.01	0.00	18.88	0.03	0.37	0.28	0.01	99.51	79.39
565451	Anhydrous Ol-CPXite	39.14	0.00	0.00	0.20	18.35	0.03	0.37	0.27	0.01	99.37	79.93
565451	Anhydrous Ol-CPXite	39.16	0.00	0.00	0.02	18.81	0.03	0.38	0.29	0.01	99.49	79.46
565451	Anhydrous Ol-CPXite	39.31	0.00	0.00	0.00	18.84	0.03	0.37	0.28	0.00	99.61	79.42
565451	Anhydrous Ol-CPXite	39.32	0.00	0.00	0.00	18.84	0.03	0.38	0.29	0.01	99.64	79.42
565470	Dunite	39.62	0.00	0.00	0.02	16.37	0.00	0.35	0.28	0.01	99.67	82.42
565470	Dunite	38.97	0.00	0.01	0.01	16.64	0.03	0.36	0.28	0.00	98.22	81.79
565470	Dunite	39.17	0.00	0.01	0.00	16.63	0.03	0.35	0.28	0.01	98.39	81.80
565470	Dunite	39.17	0.00	0.00	0.00	16.70	0.03	0.35	0.28	0.01	98.42	81.72
565470	Dunite	39.32	0.00	0.01	0.00	16.69	0.03	0.35	0.29	0.00	98.65	81.76
565470	Dunite	39.01	0.00	0.00	0.00	16.75	0.03	0.35	0.28	0.01	98.28	81.66
565470	Dunite	39.40	0.00	0.00	0.00	16.76	0.03	0.35	0.28	0.01	98.72	81.67
565470	Dunite	39.26	0.00	0.00	0.01	16.85	0.03	0.34	0.29	0.00	98.55	81.54
565470	Dunite	39.01	0.00	0.00	0.00	16.85	0.03	0.35	0.28	0.01	98.31	81.55
565470	Dunite	39.18	0.00	0.02	0.00	16.80	0.03	0.34	0.28	0.00	98.46	81.61
565470	Dunite	39.27	0.00	0.00	0.00	16.88	0.03	0.35	0.29	0.01	98.56	81.50
565470	Dunite	39.38	0.00	0.02	0.00	16.81	0.03	0.35	0.28	0.01	98.68	81.60
565470	Dunite	39.37	0.00	0.01	0.01	16.72	0.02	0.36	0.28	0.00	98.70	81.71
565470	Dunite	39.55	0.00	0.00	0.00	16.91	0.02	0.35	0.28	0.01	98.96	81.52
565470	Dunite	37.87	0.00	0.02	0.00	16.89	0.03	0.34	0.28	0.00	97.26	81.53
565470	Dunite	39.29	0.00	0.02	0.00	16.89	0.03	0.34	0.28	0.00	98.66	81.53
565470	Dunite	39.44	0.00	0.01	0.00	16.86	0.03	0.35	0.28	0.00	98.94	81.60
565470	Dunite	39.38	0.00	0.00	0.03	16.67	0.02	0.35	0.28	0.01	98.76	81.80
565470	Dunite	39.23	0.00	0.00	0.00	16.82	0.02	0.35	0.28	0.00	98.79	81.68

Sample	Lithology	SiO_2	TiO_2	ZnO	Cr_2O_3	FeO	CoO	NiO	MnO	CaO	Total	Mg#
565470	Dunite	39.24	0.00	0.00	0.00	16.84	0.03	0.35	0.29	0.00	98.67	81.60
565470	Dunite	39.35	0.00	0.01	0.00	16.83	0.03	0.35	0.28	0.00	98.87	81.65
565470	Dunite	39.33	0.01	0.01	0.11	16.93	0.03	0.35	0.29	0.00	99.15	81.59
565470	Dunite	39.30	0.00	0.00	0.00	16.99	0.02	0.36	0.29	0.00	98.90	81.49
565470	Dunite	39.22	0.00	0.00	0.00	16.81	0.03	0.37	0.28	0.00	98.72	81.66
565470	Dunite	39.34	0.00	0.00	0.00	16.84	0.03	0.36	0.28	0.00	99.10	81.72
565470	Dunite	39.37	0.00	0.00	0.00	16.74	0.03	0.36	0.28	0.00	99.02	81.82
565470	Dunite	39.28	0.00	0.00	0.01	16.80	0.03	0.35	0.28	0.01	98.80	81.69
565470	Dunite	39.39	0.00	0.01	0.00	16.84	0.03	0.35	0.29	0.00	98.79	81.60
565470	Dunite	39.33	0.00	0.02	0.00	16.84	0.03	0.35	0.28	0.00	98.86	81.64
565470	Dunite	39.33	0.00	0.00	0.00	16.87	0.02	0.35	0.28	0.00	98.89	81.61
565470	Dunite	39.29	0.00	0.01	0.00	16.77	0.02	0.35	0.28	0.00	98.79	81.72
565455	Dunite	39.71	0.00	0.00	0.00	16.01	0.02	0.44	0.24	0.00	98.98	82.58
565455	Dunite	39.82	0.00	0.00	0.00	16.04	0.03	0.44	0.24	0.00	99.16	82.55
565455	Dunite	39.67	0.00	0.00	0.00	16.06	0.03	0.44	0.24	0.00	98.97	82.52
565455	Dunite	39.73	0.00	0.00	0.00	15.93	0.03	0.44	0.24	0.00	99.08	82.69
565455	Dunite	39.76	0.01	0.00	0.00	16.15	0.03	0.43	0.24	0.00	99.03	82.40
565455	Dunite	39.80	0.00	0.00	0.00	15.98	0.03	0.44	0.24	0.00	99.14	82.63
565455	Dunite	39.71	0.00	0.00	0.00	16.08	0.03	0.43	0.24	0.00	99.23	82.57
565455	Dunite	39.75	0.00	0.00	0.00	16.10	0.03	0.43	0.24	0.00	99.31	82.57
565455	Dunite	39.32	0.00	0.00	0.00	17.11	0.03	0.42	0.34	0.00	98.95	81.29
565455	Dunite	39.85	0.00	0.00	0.00	15.96	0.02	0.44	0.24	0.00	99.19	82.65
565455	Dunite	39.76	0.00	0.01	0.00	16.02	0.03	0.43	0.24	0.01	99.13	82.58
565455	Dunite	39.64	0.01	0.00	0.01	16.79	0.03	0.42	0.31	0.00	99.15	81.65
565455	Dunite	39.71	0.00	0.00	0.00	16.00	0.03	0.44	0.24	0.00	99.17	82.65
565455	Dunite	39.67	0.00	0.00	0.04	16.01	0.03	0.44	0.26	0.00	99.14	82.61
565455	Dunite	39.62	0.00	0.00	0.01	16.36	0.03	0.41	0.31	0.00	99.09	82.18
565455	Dunite	39.64	0.00	0.00	0.00	16.08	0.02	0.44	0.25	0.00	98.96	82.50

Sample	**Lithology**	**SiO_2**	**TiO_2**	**ZnO**	**Cr_2O_3**	**FeO**	**CoO**	**NiO**	**MnO**	**CaO**	**Total**	**Mg#**
565455	Dunite	39.55	0.00	0.01	0.00	16.05	0.02	0.44	0.24	0.00	99.04	82.59
565455	Dunite	39.45	0.00	0.01	0.00	15.95	0.03	0.44	0.24	0.00	98.91	82.71
565455	Dunite	39.68	0.00	0.00	0.00	15.97	0.03	0.44	0.24	0.00	99.11	82.67
565455	Dunite	39.40	0.00	0.00	0.01	18.07	0.03	0.16	0.39	0.01	99.09	80.19
565455	Dunite	39.60	0.00	0.01	0.00	16.53	0.03	0.44	0.27	0.00	99.12	82.00
565455	Dunite	39.48	0.00	0.00	0.01	16.10	0.02	0.44	0.24	0.00	99.03	82.55
565455	Dunite	39.55	0.00	0.01	0.00	16.03	0.03	0.44	0.24	0.00	99.01	82.61
565455	Dunite	39.49	0.00	0.00	0.00	15.96	0.03	0.44	0.23	0.00	98.79	82.64
565455	Dunite	39.18	0.00	0.00	0.00	16.16	0.02	0.43	0.27	0.01	98.61	82.43
565455	Dunite	39.36	0.00	0.00	0.01	16.10	0.03	0.43	0.25	0.01	98.77	82.50
565455	Dunite	40.05	0.00	0.00	0.01	15.94	0.03	0.46	0.24	0.00	99.45	82.69
565455	Dunite	40.10	0.00	0.00	0.00	16.00	0.03	0.46	0.24	0.00	99.62	82.66
565455	Dunite	40.00	0.00	0.00	0.03	15.96	0.03	0.46	0.25	0.00	99.47	82.69
565455	Dunite	39.99	0.00	0.00	0.01	15.97	0.03	0.47	0.24	0.00	99.52	82.69
565455	Dunite	40.05	0.00	0.00	0.00	15.83	0.03	0.47	0.24	0.00	99.40	82.81
565455	Dunite	39.93	0.00	0.00	0.00	15.91	0.02	0.44	0.24	0.00	99.30	82.72
565472	Dunite	39.64	0.00	0.00	0.00	15.31	0.02	0.43	0.29	0.00	99.04	83.46
565472	Dunite	39.70	0.00	0.00	0.00	15.13	0.02	0.42	0.28	0.00	99.08	83.68
565472	Dunite	39.60	0.00	0.00	0.00	15.78	0.03	0.42	0.33	0.00	98.94	82.85
565472	Dunite	39.80	0.00	0.01	0.00	14.94	0.02	0.42	0.25	0.00	99.11	83.89
565472	Dunite	39.73	0.00	0.02	0.00	15.11	0.02	0.41	0.26	0.00	99.07	83.69
565472	Dunite	39.82	0.00	0.01	0.00	15.13	0.02	0.42	0.26	0.00	99.22	83.69
565472	Dunite	39.77	0.00	0.00	0.02	14.94	0.02	0.42	0.25	0.01	98.92	83.84
565472	Dunite	39.81	0.00	0.02	0.00	15.03	0.02	0.42	0.26	0.00	99.20	83.81
565472	Dunite	39.82	0.00	0.01	0.00	15.06	0.03	0.41	0.25	0.01	99.23	83.78
565472	Dunite	39.67	0.00	0.00	0.00	15.10	0.02	0.41	0.26	0.00	98.95	83.69
565472	Dunite	39.56	0.00	0.01	0.00	16.18	0.03	0.43	0.37	0.00	99.01	82.38
565472	Dunite	39.79	0.00	0.00	0.03	15.11	0.02	0.42	0.28	0.00	99.11	83.67

Sample	Lithology	SiO_2	TiO_2	ZnO	Cr_2O_3	FeO	CoO	NiO	MnO	CaO	Total	Mg#
565472	Dunite	39.69	0.00	0.01	0.00	14.88	0.02	0.43	0.25	0.00	98.89	83.94
565472	Dunite	39.74	0.00	0.01	0.00	14.92	0.02	0.42	0.25	0.00	98.94	83.88
565472	Dunite	39.77	0.00	0.02	0.00	15.07	0.02	0.42	0.26	0.00	99.06	83.73
565472	Dunite	39.94	0.00	0.01	0.00	15.05	0.02	0.42	0.25	0.00	99.17	83.74
565472	Dunite	39.88	0.00	0.00	0.00	15.06	0.02	0.42	0.25	0.01	99.12	83.72
565472	Dunite	40.08	0.00	0.00	0.03	14.87	0.02	0.42	0.25	0.01	99.30	83.94
565472	Dunite	39.91	0.00	0.02	0.00	14.97	0.03	0.42	0.25	0.01	99.25	83.85
565472	Dunite	40.01	0.00	0.01	0.00	14.96	0.02	0.42	0.25	0.01	99.21	83.82
565472	Dunite	39.91	0.00	0.01	0.00	15.02	0.03	0.42	0.25	0.01	99.26	83.80
565472	Dunite	39.84	0.00	0.00	0.00	14.96	0.02	0.41	0.26	0.00	99.01	83.83
565472	Dunite	39.79	0.00	0.01	0.02	15.23	0.02	0.42	0.27	0.00	99.17	83.55
565472	Dunite	39.82	0.00	0.00	0.00	15.05	0.02	0.42	0.25	0.00	99.19	83.77
565472	Dunite	39.81	0.00	0.01	0.01	15.06	0.02	0.42	0.26	0.01	99.29	83.79
565472	Dunite	39.89	0.00	0.00	0.01	15.12	0.02	0.41	0.26	0.00	99.25	83.69
565472	Dunite	39.88	0.00	0.00	0.05	15.02	0.03	0.43	0.25	0.00	99.41	83.86
565472	Dunite	39.87	0.00	0.00	0.00	15.05	0.03	0.42	0.25	0.00	99.49	83.86
565472	Dunite	39.88	0.00	0.01	0.00	15.14	0.02	0.42	0.28	0.00	99.42	83.72
565472	Dunite	40.02	0.00	0.00	0.00	15.02	0.02	0.42	0.25	0.00	99.47	83.85
565472	Dunite	39.88	0.00	0.00	0.00	15.02	0.02	0.42	0.25	0.00	99.34	83.85
565472	Dunite	39.88	0.00	0.00	0.01	15.12	0.02	0.43	0.27	0.00	99.47	83.76
565472	Dunite	39.88	0.00	0.00	0.00	15.53	0.03	0.42	0.30	0.00	99.59	83.29
565472	Dunite	38.35	0.01	0.00	0.00	17.30	0.03	0.44	0.61	0.00	98.78	81.24
565472	Dunite	38.60	0.00	0.00	0.00	17.51	0.03	0.44	0.64	0.00	98.98	80.95
565471	Dunite	39.81	0.00	0.00	0.00	15.03	0.00	0.40	0.27	0.00	99.76	84.00
565471	Dunite	39.74	0.00	0.00	0.00	15.00	0.00	0.41	0.27	0.00	99.61	84.00
565471	Dunite	39.79	0.01	0.02	0.00	15.00	0.00	0.41	0.27	0.01	99.71	84.01
565471	Dunite	39.79	0.00	0.00	0.00	15.03	0.00	0.41	0.27	0.01	99.70	83.98
565471	Dunite	39.49	0.01	0.01	0.00	15.30	0.00	0.40	0.27	0.01	99.09	83.55

Sample	**Lithology**	**SiO_2**	**TiO_2**	**ZnO**	**Cr_2O_3**	**FeO**	**CoO**	**NiO**	**MnO**	**CaO**	**Total**	**Mg#**
565471	Dunite	39.82	0.00	0.00	0.05	15.47	0.02	0.41	0.27	0.00	99.35	83.30
565471	Dunite	39.87	0.00	0.00	0.00	15.50	0.02	0.41	0.28	0.00	99.37	83.27
565471	Dunite	38.99	0.06	0.04	1.20	16.45	0.03	0.41	0.28	0.00	100.68	82.37
565471	Dunite	39.73	0.00	0.01	0.00	15.70	0.02	0.42	0.27	0.00	99.17	83.00
565471	Dunite	39.97	0.00	0.01	0.00	15.44	0.02	0.41	0.27	0.00	99.44	83.33
565471	Dunite	39.91	0.00	0.01	0.00	15.35	0.03	0.42	0.27	0.00	99.35	83.42
565471	Dunite	40.27	0.00	0.02	0.03	15.23	0.02	0.41	0.27	0.00	99.72	83.57
565471	Dunite	40.22	0.00	0.01	0.00	15.30	0.02	0.41	0.27	0.01	99.54	83.46
565471	Dunite	40.13	0.00	0.00	0.00	15.32	0.02	0.39	0.27	0.00	99.56	83.47
565471	Dunite	40.19	0.00	0.01	0.00	15.29	0.02	0.42	0.27	0.01	99.54	83.48
565471	Dunite	38.97	0.05	0.03	1.04	16.13	0.03	0.41	0.28	0.01	99.75	82.49
565471	Dunite	40.23	0.00	0.01	0.00	15.36	0.02	0.41	0.28	0.00	99.64	83.41
565471	Dunite	40.44	0.00	0.02	0.01	15.49	0.02	0.41	0.28	0.01	100.04	83.31
565471	Dunite	39.73	0.00	0.00	0.00	15.45	0.02	0.42	0.28	0.00	99.21	83.32
565471	Dunite	39.67	0.01	0.01	0.08	15.55	0.02	0.42	0.28	0.00	99.20	83.18
565471	Dunite	39.79	0.00	0.02	0.00	15.42	0.02	0.42	0.27	0.00	99.23	83.34
565471	Dunite	39.68	0.00	0.02	0.01	15.39	0.02	0.41	0.27	0.00	99.11	83.38
565471	Dunite	39.47	0.00	0.01	0.00	15.44	0.03	0.42	0.27	0.00	98.88	83.32
565471	Dunite	39.70	0.00	0.01	0.00	15.42	0.02	0.42	0.27	0.00	99.20	83.36
565471	Dunite	39.63	0.00	0.00	0.00	15.45	0.02	0.42	0.27	0.00	99.21	83.36
565471	Dunite	39.52	0.00	0.01	0.00	15.45	0.02	0.42	0.27	0.00	99.00	83.32
565471	Dunite	39.73	0.00	0.01	0.00	15.45	0.03	0.42	0.28	0.00	99.21	83.32
565471	Dunite	39.69	0.00	0.01	0.00	15.44	0.02	0.42	0.27	0.00	99.16	83.33
565471	Dunite	39.51	0.00	0.01	0.00	15.43	0.02	0.42	0.27	0.00	98.88	83.31
565471	Dunite	39.88	0.00	0.00	0.00	15.53	0.02	0.42	0.28	0.00	99.58	83.29
565471	Dunite	39.37	0.00	0.01	0.00	15.56	0.02	0.43	0.27	0.00	99.01	83.24
565471	Dunite	39.63	0.00	0.01	0.00	15.65	0.02	0.41	0.27	0.00	99.17	83.11
565471	Dunite	39.54	0.00	0.00	0.04	15.44	0.02	0.42	0.27	0.00	99.20	83.38

Sample	**Lithology**	**SiO_2**	**TiO_2**	**ZnO**	**Cr_2O_3**	**FeO**	**CoO**	**NiO**	**MnO**	**CaO**	**Total**	**Mg#**
565471	Dunite	39.79	0.00	0.01	0.00	15.52	0.02	0.41	0.28	0.01	99.51	83.32
565471	Dunite	39.83	0.00	0.02	0.00	15.56	0.02	0.41	0.28	0.01	99.54	83.26
565471	Dunite	39.81	0.00	0.00	0.00	15.59	0.02	0.42	0.28	0.00	99.60	83.26
565452	Dunite	39.65	0.00	0.00	0.06	15.26	0.03	0.35	0.26	0.00	99.46	83.66
565452	Dunite	39.67	0.00	0.00	0.00	15.21	0.03	0.36	0.26	0.00	99.37	83.71
565452	Dunite	39.73	0.00	0.00	0.00	15.24	0.02	0.34	0.25	0.00	99.29	83.64
565452	Dunite	39.54	0.00	0.00	0.00	15.06	0.02	0.36	0.26	0.00	98.94	83.80
565452	Dunite	39.64	0.00	0.00	0.00	14.90	0.02	0.36	0.24	0.00	98.87	83.94
565452	Dunite	39.33	0.00	0.01	0.01	14.81	0.02	0.35	0.25	0.00	98.23	83.95
565452	Dunite	38.99	0.00	0.01	0.00	14.91	0.02	0.35	0.25	0.00	97.95	83.85
565452	Dunite	39.54	0.00	0.01	0.00	15.10	0.02	0.34	0.26	0.00	98.64	83.66
565452	Dunite	39.21	0.00	0.00	0.00	15.14	0.02	0.35	0.26	0.00	98.22	83.57
565452	Dunite	39.36	0.00	0.00	0.00	15.14	0.03	0.35	0.27	0.00	98.46	83.61
565452	Dunite	39.12	0.00	0.00	0.01	15.12	0.03	0.34	0.26	0.00	98.29	83.65
565452	Dunite	39.25	0.00	0.00	0.00	15.20	0.02	0.34	0.26	0.00	98.57	83.61
565452	Dunite	39.41	0.00	0.00	0.00	15.04	0.02	0.35	0.26	0.00	98.64	83.77
565452	Dunite	39.63	0.00	0.00	0.00	15.14	0.02	0.35	0.26	0.00	99.04	83.70
565452	Dunite	39.53	0.00	0.01	0.00	15.20	0.02	0.34	0.26	0.00	99.06	83.66
565452	Dunite	39.45	0.00	0.00	0.00	15.27	0.02	0.35	0.26	0.00	98.83	83.54
565452	Dunite	39.74	0.00	0.00	0.00	15.26	0.02	0.35	0.26	0.00	99.34	83.62
565452	Dunite	39.70	0.00	0.00	0.00	15.35	0.02	0.35	0.27	0.00	99.42	83.55
565452	Dunite	39.81	0.01	0.00	0.00	15.32	0.02	0.35	0.26	0.00	99.66	83.63
565452	Dunite	39.70	0.00	0.01	0.00	15.35	0.02	0.35	0.28	0.00	99.43	83.55
565452	Dunite	39.55	0.00	0.00	0.00	15.07	0.02	0.35	0.26	0.00	99.28	83.89
565452	Dunite	39.91	0.00	0.00	0.01	15.10	0.03	0.34	0.25	0.02	99.56	83.82
565452	Dunite	39.46	0.00	0.01	0.02	15.03	0.02	0.34	0.26	0.00	98.89	83.83
565452	Dunite	39.49	0.00	0.00	0.01	15.14	0.02	0.35	0.25	0.01	99.12	83.78
565452	Dunite	39.73	0.00	0.00	0.00	15.15	0.02	0.34	0.26	0.00	99.34	83.76

Sample	Lithology	SiO$_2$	TiO$_2$	ZnO	Cr$_2$O$_3$	FeO	CoO	NiO	MnO	CaO	Total	Mg#
565452	Dunite	39.79	0.00	0.00	0.00	15.02	0.02	0.34	0.26	0.00	99.33	83.90
565452	Dunite	39.68	0.00	0.00	0.01	14.88	0.02	0.34	0.25	0.00	99.13	84.04
565452	Dunite	39.48	0.00	0.00	0.00	15.12	0.03	0.35	0.26	0.00	99.10	83.80
565452	Dunite	39.81	0.00	0.00	0.04	15.10	0.02	0.33	0.26	0.00	99.35	83.78
565452	Dunite	39.42	0.00	0.00	0.01	15.22	0.03	0.34	0.25	0.00	98.97	83.66
565452	Dunite	39.49	0.00	0.00	0.00	15.24	0.02	0.34	0.26	0.00	99.17	83.67
565452	Dunite	39.65	0.00	0.00	0.00	15.13	0.02	0.34	0.25	0.00	99.11	83.74
565452	Dunite	39.75	0.00	0.00	0.00	15.13	0.02	0.34	0.26	0.00	99.21	83.74
565452	Dunite	39.66	0.00	0.00	0.03	15.07	0.02	0.34	0.25	0.00	99.01	83.76
565452	Dunite	39.80	0.00	0.00	0.00	15.19	0.02	0.35	0.25	0.00	99.32	83.68
565452	Dunite	39.71	0.00	0.00	0.01	15.25	0.03	0.34	0.26	0.00	99.24	83.61
565452	Dunite	39.50	0.00	0.00	0.00	15.07	0.03	0.34	0.25	0.01	98.80	83.75
565452	Dunite	39.44	0.00	0.01	0.01	15.03	0.03	0.35	0.25	0.00	98.82	83.83
565452	Dunite	39.67	0.00	0.00	0.00	15.13	0.02	0.35	0.25	0.00	99.11	83.73
565452	Dunite	39.62	0.00	0.00	0.01	15.02	0.02	0.35	0.26	0.00	98.98	83.83
565452	Dunite	39.52	0.00	0.01	0.00	15.32	0.02	0.34	0.27	0.00	99.05	83.53
565452	Dunite	39.35	0.00	0.00	0.00	15.13	0.02	0.34	0.26	0.01	98.74	83.72
565469	Hydrous Ol-CPXite	38.91	0.00	0.01	0.00	19.99	0.03	0.27	0.98	0.00	100.27	78.14
565469	Hydrous Ol-CPXite	38.80	0.00	0.01	0.00	20.50	0.03	0.26	0.93	0.00	100.15	77.50
565469	Hydrous Ol-CPXite	38.82	0.00	0.01	0.00	20.22	0.03	0.27	1.00	0.00	100.25	77.86
565469	Hydrous Ol-CPXite	38.87	0.00	0.01	0.00	20.11	0.03	0.27	0.96	0.00	100.23	77.99
565469	Hydrous Ol-CPXite	38.71	0.00	0.01	0.00	20.51	0.03	0.26	0.89	0.00	100.17	77.56
565469	Hydrous Ol-CPXite	38.99	0.00	0.01	0.00	18.94	0.03	0.26	1.25	0.00	100.44	79.40
565469	Hydrous Ol-CPXite	38.97	0.00	0.01	0.00	20.27	0.03	0.27	0.87	0.00	100.64	77.96
565469	Hydrous Ol-CPXite	39.01	0.00	0.00	0.00	16.96	0.03	0.25	1.35	0.00	100.02	81.68

Sample	Lithology	SiO_2	TiO_2	ZnO	Cr_2O_3	FeO	CoO	NiO	MnO	CaO	Total	Mg#
565469	Hydrous Ol-CPXite	38.95	0.00	0.01	0.00	17.91	0.03	0.25	1.33	0.00	100.23	80.60
565469	Hydrous Ol-CPXite	39.05	0.00	0.01	0.00	17.20	0.04	0.28	1.35	0.00	100.21	81.42
565469	Hydrous Ol-CPXite	38.57	0.00	0.01	0.01	20.03	0.04	0.25	0.93	0.00	99.85	78.08
565469	Hydrous Ol-CPXite	38.62	0.01	0.01	0.01	19.50	0.03	0.27	1.10	0.00	99.95	78.69
565469	Hydrous Ol-CPXite	39.02	0.00	0.00	0.00	17.33	0.04	0.26	1.38	0.00	99.88	81.15
565469	Hydrous Ol-CPXite	39.02	0.00	0.01	0.00	17.41	0.03	0.25	1.31	0.00	99.81	81.05
565469	Hydrous Ol-CPXite	38.53	0.00	0.01	0.00	20.02	0.03	0.25	1.11	0.00	99.87	78.04
565469	Hydrous Ol-CPXite	38.64	0.00	0.01	0.00	20.02	0.03	0.26	0.91	0.00	99.84	78.06
565469	Hydrous Ol-CPXite	38.63	0.00	0.00	0.00	19.57	0.03	0.26	1.14	0.00	99.85	78.55
565469	Hydrous Ol-CPXite	38.61	0.01	0.02	0.00	20.25	0.02	0.27	0.86	0.00	99.85	77.80
565469	Hydrous Ol-CPXite	39.00	0.00	0.01	0.00	17.36	0.04	0.25	1.33	0.01	99.93	81.15
565469	Hydrous Ol-CPXite	38.76	0.00	0.00	0.00	18.09	0.04	0.25	1.29	0.00	99.77	80.29
565469	Hydrous Ol-CPXite	38.59	0.00	0.00	0.00	18.49	0.03	0.25	1.33	0.00	99.76	79.84
565469	Hydrous Ol-CPXite	38.62	0.00	0.01	0.00	17.74	0.04	0.25	1.24	0.00	99.48	80.69
565450	Hydrous Ol-CPXite	38.18	0.00	0.02	0.00	19.61	0.05	0.24	0.97	0.00	99.24	78.49
565450	Hydrous Ol-CPXite	38.18	0.00	0.00	0.00	19.58	0.06	0.25	0.96	0.00	99.23	78.54
565450	Hydrous Ol-CPXite	38.10	0.00	0.01	0.00	19.88	0.06	0.23	1.24	0.01	99.34	78.11
565450	Hydrous Ol-CPXite	38.11	0.00	0.01	0.00	19.77	0.05	0.24	1.01	0.00	99.18	78.28
565450	Hydrous Ol-CPXite	38.18	0.00	0.02	0.01	19.67	0.06	0.23	0.93	0.01	99.08	78.36
565450	Hydrous Ol-CPXite	38.30	0.00	0.01	0.00	19.61	0.05	0.23	0.96	0.00	99.49	78.57

Chromite

Sample	Lithology	Core/Rim	Al_2O_3	MgO	SiO_2	CaO	TiO_2	Cr_2O_3	MnO	FeO	NiO	ZnO	SUM
565451	Anhydrous Ol-CPXite	Altered	18.66	3.74	0.02	0.03	0.53	39.34	0.45	34.56	0.09	0.55	97.98
565451	Dunite	Altered	2.19	0.93	0.02	0.00	1.71	34.42	0.62	54.30	0.19	0.31	94.69
565452	Dunite	Altered	0.00	0.45	0.53	0.00	0.08	0.20	0.03	88.50	0.34	0.00	90.13
565452	Dunite	Altered	0.96	0.85	0.09	0.01	1.37	29.11	0.54	61.67	0.26	0.14	95.00
565451	Anhydrous Ol-CPXite	C	18.90	4.09	0.00	0.00	0.98	37.53	0.43	35.70	0.13	0.46	98.22
565451	Anhydrous Ol-CPXite	C	18.94	4.10	0.00	0.00	0.98	37.51	0.43	35.73	0.14	0.47	98.30
565451	Anhydrous Ol-CPXite	C	18.49	3.66	0.01	0.01	0.62	39.34	0.46	34.94	0.10	0.61	98.24
565451	Anhydrous Ol-CPXite	C	17.18	3.28	0.03	0.03	0.60	40.06	0.46	35.07	0.10	0.68	97.50
565451	Anhydrous Ol-CPXite	C	18.34	3.28	0.03	0.02	0.69	38.61	0.47	35.21	0.11	0.71	97.47
565451	Anhydrous Ol-CPXite	C	16.64	3.15	0.02	0.00	0.68	39.15	0.47	36.97	0.11	0.54	97.74
565451	Anhydrous Ol-CPXite	C	18.68	3.76	0.00	0.00	0.55	39.66	0.44	34.42	0.09	0.56	98.17
565451	Anhydrous Ol-CPXite	C	17.90	3.81	0.00	0.00	0.93	37.81	0.45	36.97	0.13	0.45	98.44
565451	Anhydrous Ol-CPXite	C	17.83	3.74	0.01	0.00	0.92	37.86	0.46	37.00	0.12	0.45	98.39
565451	Anhydrous Ol-CPXite	C	18.67	3.60	0.02	0.00	0.84	37.24	0.45	36.77	0.13	0.50	98.21

Sample	**Lithology**	**Core/Rim**	**Al_2O_3**	**MgO**	**SiO_2**	**CaO**	**TiO_2**	**Cr_2O_3**	**MnO**	**FeO**	**NiO**	**ZnO**	**SUM**
565451	Dunite	C	6.48	1.81	0.02	0.00	1.95	33.37	0.57	51.40	0.24	0.33	96.17
565451	Dunite	C	6.71	1.75	0.00	0.00	1.62	33.63	0.62	51.16	0.24	0.38	96.11
565451	Dunite	C	4.87	1.36	0.02	0.00	1.51	34.97	0.62	51.78	0.19	0.43	95.75
565451	Dunite	C	5.98	1.43	0.00	0.02	1.57	36.02	0.67	49.90	0.18	0.42	96.19
565451	Dunite	C	6.02	1.82	0.00	0.00	1.77	36.01	0.58	49.47	0.20	0.33	96.21
565451	Dunite	C	5.53	1.58	0.01	0.00	1.98	35.08	0.63	50.94	0.20	0.34	96.29
565451	Dunite	C	4.28	1.43	0.03	0.00	2.03	34.66	0.62	52.26	0.22	0.29	95.82
565451	Dunite	C	4.36	1.12	0.02	0.02	1.54	35.03	0.64	52.16	0.18	0.40	95.47
565455	Dunite	C	9.13	1.75	0.02	0.00	1.53	37.37	0.82	45.06	0.21	0.70	96.58
565455	Dunite	C	1.05	0.75	0.03	0.01	1.40	34.59	0.74	55.08	0.18	0.39	94.22
565455	Dunite	C	9.23	2.12	0.02	0.02	1.03	37.65	0.59	45.37	0.18	0.46	96.68
565455	Dunite	C	8.33	1.82	0.01	0.00	1.70	35.68	0.79	47.57	0.25	0.62	96.78
565455	Dunite	C	1.31	0.79	0.02	0.00	1.40	33.15	0.71	57.17	0.20	0.36	95.10
565455	Dunite	C	2.01	0.86	0.01	0.00	1.33	33.33	0.71	56.56	0.19	0.38	95.38
565455	Dunite	C	0.06	0.37	0.46	0.00	0.36	9.46	0.16	82.24	0.29	0.04	93.43
565455	Dunite	C	8.74	1.48	0.00	0.00	0.98	36.76	0.84	46.90	0.14	0.68	96.52
565455	Dunite	C	1.27	0.77	0.03	0.00	1.26	34.06	0.74	55.60	0.17	0.38	94.29
565455	Dunite	C	9.15	1.96	0.04	0.00	1.25	37.33	0.56	45.37	0.20	0.44	96.31
565455	Dunite	C	9.28	1.78	0.02	0.00	1.41	36.55	0.80	46.02	0.21	0.66	96.73
565455	Dunite	C	9.13	1.68	0.00	0.00	1.28	35.77	0.80	47.34	0.18	0.64	96.82
565455	Dunite	C	1.32	0.79	0.02	0.00	1.45	32.61	0.69	57.47	0.13	0.34	94.83
565455	Dunite	C	0.93	0.74	0.02	0.00	1.38	31.98	0.68	58.50	0.13	0.33	94.69
565455	Dunite	C	2.54	1.04	0.03	0.02	1.43	35.10	0.63	53.41	0.29	0.45	94.95

Sample	**Lithology**	**Core/Rim**	**Al_2O_3**	**MgO**	**SiO_2**	**CaO**	**TiO_2**	**Cr_2O_3**	**MnO**	**FeO**	**NiO**	**ZnO**	**SUM**
565455	Dunite	C	8.59	1.94	0.02	0.01	1.34	37.06	0.56	46.12	0.23	0.47	96.32
565472	Dunite	C	0.00	0.10	0.08	0.00	0.19	0.19	0.01	91.54	0.39	0.00	92.50
565472	Dunite	C	1.02	1.98	2.13	0.04	0.18	0.09	0.02	86.33	0.37	0.00	92.15
565472	Dunite	C	7.76	1.66	0.02	0.01	1.24	40.97	0.91	43.33	0.17	0.70	96.76
565472	Dunite	C	0.00	0.06	0.02	0.01	0.14	0.19	0.02	92.05	0.38	0.00	92.88
565472	Dunite	C	7.65	1.88	0.01	0.00	1.61	39.65	0.89	44.09	0.20	0.66	96.64
565472	Dunite	C	1.41	0.77	0.01	0.00	1.19	36.11	0.86	54.20	0.24	0.40	95.19
565472	Dunite	C	0.00	0.07	0.03	0.00	0.15	2.26	0.03	90.65	0.39	0.01	93.60
565472	Dunite	C	6.27	1.52	0.02	0.00	1.66	37.84	0.93	46.99	0.23	0.58	96.03
565472	Dunite	C	2.40	0.84	0.03	0.00	0.95	38.53	0.92	49.85	0.20	0.49	94.20
565472	Dunite	C	7.22	1.42	0.02	0.00	1.20	36.29	0.91	48.12	0.22	0.58	95.98
565472	Dunite	C	1.47	0.76	0.02	0.00	1.19	34.60	0.81	55.10	0.27	0.40	94.60
565472	Dunite	C	7.64	1.71	0.02	0.00	1.36	40.38	0.90	43.75	0.18	0.68	96.64
565472	Dunite	C	1.14	0.74	0.02	0.00	1.13	37.70	0.90	52.19	0.21	0.44	94.48
565472	Dunite	C	0.01	0.08	0.04	0.00	0.13	4.18	0.04	87.24	0.46	0.00	92.19
565472	Dunite	C	8.50	2.38	0.01	0.01	1.26	40.83	0.63	42.22	0.17	0.51	96.51
565472	Dunite	C	8.56	2.20	0.02	0.01	1.10	40.77	0.65	42.46	0.16	0.51	96.43
565472	Dunite	C	7.67	1.68	0.02	0.00	1.15	40.02	0.91	44.75	0.18	0.67	97.04
565472	Dunite	C	1.87	0.83	0.01	0.00	1.06	37.76	0.89	52.38	0.22	0.45	95.46
565472	Dunite	C	7.74	1.65	0.02	0.00	1.51	39.73	0.91	43.82	0.19	0.67	96.25
565472	Dunite	C	7.79	1.56	0.02	0.00	1.34	39.38	0.92	43.90	0.20	0.69	95.81
565472	Dunite	C	1.76	0.82	0.02	0.00	1.06	37.58	0.88	51.86	0.22	0.45	94.65
565472	Dunite	C	0.05	0.16	0.04	0.00	0.41	8.65	0.19	81.60	0.43	0.06	91.59

Sample	Lithology	Core/Rim	Al_2O_3	MgO	SiO_2	CaO	TiO_2	Cr_2O_3	MnO	FeO	NiO	ZnO	SUM
565472	Dunite	C	8.07	2.15	0.01	0.00	1.30	39.65	0.62	43.96	0.19	0.49	96.44
565472	Dunite	C	8.09	2.10	0.02	0.02	1.20	39.34	0.62	43.94	0.19	0.50	96.02
565472	Dunite	C	7.40	1.66	0.01	0.00	1.51	38.91	0.93	45.07	0.20	0.64	96.32
565472	Dunite	C	7.88	1.55	0.02	0.00	1.18	39.66	0.92	44.13	0.18	0.69	96.21
565471	Dunite	C	4.55	1.62	0.01	0.01	1.58	36.65	0.64	50.04	0.25	0.50	95.86
565471	Dunite	C	4.01	1.37	0.00	0.00	1.73	38.72	0.73	48.75	0.22	0.51	96.04
565471	Dunite	C	6.95	2.26	0.01	0.00	1.26	40.42	0.60	44.47	0.18	0.49	96.64
565471	Dunite	C	2.79	1.33	0.00	0.00	1.82	39.20	0.74	49.27	0.21	0.48	95.83
565471	Dunite	C	6.81	2.00	0.01	0.00	1.45	39.78	0.69	45.05	0.19	0.64	96.61
565471	Dunite	C	3.63	1.47	0.01	0.01	1.44	38.48	0.65	49.00	0.20	0.54	95.40
565471	Dunite	C	2.93	1.31	0.01	0.00	1.99	38.55	0.74	49.70	0.24	0.46	95.93
565471	Dunite	C	2.37	1.05	0.00	0.00	1.66	36.91	0.71	52.06	0.23	0.45	95.43
565471	Dunite	C	6.50	1.48	0.00	0.00	1.31	37.48	0.72	47.85	0.20	0.61	96.16
565471	Dunite	C	5.17	4.46	1.39	0.00	1.33	36.92	0.61	44.80	0.22	0.84	95.74
565471	Dunite	C	2.79	1.35	0.01	0.00	2.00	39.01	0.74	49.68	0.24	0.47	96.29
565471	Dunite	C	2.74	1.33	0.01	0.00	1.79	39.93	0.73	48.92	0.22	0.48	96.17
565471	Dunite	C	7.87	2.33	0.01	0.00	0.96	39.91	0.66	44.47	0.18	0.53	96.92
565471	Dunite	C	7.27	1.86	0.02	0.01	1.20	38.29	0.66	46.13	0.20	0.57	96.21
565452	Dunite	C	7.97	2.26	0.01	0.00	1.00	41.47	0.62	43.02	0.14	0.33	96.82
565452	Dunite	C	7.43	2.11	0.01	0.00	1.13	40.85	0.73	43.41	0.14	0.30	96.11
565452	Dunite	C	7.78	2.08	0.02	0.00	0.98	39.84	0.61	43.29	0.14	0.34	95.10
565452	Dunite	C	7.69	2.11	0.02	0.00	1.00	40.58	0.62	43.05	0.13	0.33	95.53
565452	Dunite	C	7.93	2.08	0.01	0.00	1.00	41.44	0.72	42.98	0.13	0.32	96.61

Sample	**Lithology**	**Core/Rim**	**Al_2O_3**	**MgO**	**SiO_2**	**CaO**	**TiO_2**	**Cr_2O_3**	**MnO**	**FeO**	**NiO**	**ZnO**	**SUM**
565452	Dunite	C	7.64	2.38	0.01	0.00	1.05	41.64	0.73	43.00	0.14	0.28	96.88
565452	Dunite	C	8.18	2.15	0.01	0.00	0.96	41.49	0.73	42.87	0.12	0.32	96.83
565452	Dunite	C	7.82	2.41	0.00	0.00	1.06	41.82	0.71	42.73	0.14	0.28	96.97
565452	Dunite	C	8.16	2.31	0.01	0.00	0.96	41.32	0.59	42.79	0.13	0.28	96.56
565452	Dunite	C	8.08	2.18	0.01	0.00	0.98	41.12	0.72	43.01	0.13	0.31	96.55
565452	Dunite	C	7.75	2.28	0.01	0.00	1.10	41.27	0.72	43.03	0.13	0.30	96.58
565452	Dunite	C	8.00	2.09	0.01	0.00	1.08	41.43	0.71	42.84	0.13	0.31	96.60
565452	Dunite	C	8.12	2.11	0.02	0.00	1.01	39.53	0.65	43.57	0.14	0.32	95.47
565452	Dunite	C	8.02	2.41	0.00	0.00	1.07	41.64	0.70	42.42	0.14	0.27	96.67
565452	Dunite	C	7.20	1.73	0.00	0.00	1.43	40.32	0.91	44.17	0.20	0.65	96.62
565452	Dunite	C	8.12	1.69	0.02	0.00	1.31	39.80	0.93	43.96	0.20	0.71	96.73
565472	Dunite	Frature	1.23	0.84	0.01	0.00	1.37	38.40	0.90	51.72	0.23	0.42	95.13
565472	Dunite	M	2.08	0.88	0.02	0.00	1.15	37.02	0.87	52.46	0.23	0.44	95.15
565451	Anhydrous Ol-CPXite	Not	18.73	3.83	0.02	0.00	0.54	39.72	0.44	34.42	0.09	0.55	98.35
565451	Anhydrous Ol-CPXite	R	18.80	3.97	0.00	0.00	0.98	37.51	0.43	35.86	0.13	0.46	98.14
565451	Anhydrous Ol-CPXite	R	18.27	3.55	0.02	0.01	0.71	39.04	0.46	35.10	0.10	0.63	97.88
565451	Anhydrous Ol-CPXite	R	16.80	3.30	0.02	0.00	0.68	39.52	0.48	36.78	0.11	0.56	98.25
565451	Anhydrous Ol-CPXite	R	17.88	3.79	0.02	0.00	0.93	37.80	0.44	36.89	0.14	0.45	98.32
565451	Anhydrous Ol-CPXite	R	17.77	3.61	0.01	0.00	0.92	37.59	0.45	37.26	0.13	0.44	98.19

Sample	Lithology	Core/Rim	Al_2O_3	MgO	SiO_2	CaO	TiO_2	Cr_2O_3	MnO	FeO	NiO	ZnO	SUM
565451	Anhydrous Ol-CPXite	R	18.83	3.42	0.04	0.00	0.81	36.72	0.44	36.94	0.12	0.51	97.85
565451	Dunite	R	5.93	1.72	0.03	0.00	1.93	33.09	0.58	51.69	0.24	0.31	95.52
565451	Dunite	R	6.71	1.64	0.00	0.01	1.49	34.13	0.63	50.83	0.20	0.40	96.04
565451	Dunite	R	3.45	1.15	0.03	0.00	1.54	33.78	0.61	53.40	0.21	0.38	94.55
565451	Dunite	R	6.02	1.38	0.00	0.00	1.51	36.04	0.67	50.01	0.16	0.42	96.22
565451	Dunite	R	5.88	1.80	0.00	0.01	1.78	35.75	0.58	49.71	0.20	0.33	96.03
565455	Dunite	R	9.08	1.83	0.02	0.00	1.66	37.37	0.80	44.97	0.24	0.70	96.68
565455	Dunite	R	1.57	0.79	0.04	0.02	1.28	34.93	0.76	54.40	0.18	0.41	94.38
565455	Dunite	R	9.30	2.05	0.03	0.06	0.97	37.54	0.60	45.21	0.18	0.48	96.43
565455	Dunite	R	8.45	1.73	0.01	0.00	1.45	35.70	0.78	47.78	0.23	0.62	96.76
565455	Dunite	R	9.22	2.06	0.00	0.00	1.39	37.66	0.56	45.05	0.22	0.44	96.60
565455	Dunite	R	7.66	1.67	0.03	0.01	1.38	34.83	0.55	48.24	0.26	0.50	95.13
565472	Dunite	R	0.01	0.10	0.04	0.00	0.13	6.89	0.09	85.71	0.45	0.02	93.45
565472	Dunite	R	7.22	1.59	0.01	0.00	1.28	40.07	0.93	44.50	0.17	0.67	96.45
565472	Dunite	R	0.30	0.46	0.04	0.00	0.81	31.44	0.76	59.39	0.25	0.33	93.77
565471	Dunite	R	5.22	1.69	0.02	0.00	1.41	37.18	0.63	48.55	0.23	0.53	95.47
565471	Dunite	R	7.23	2.29	0.01	0.00	1.18	40.13	0.59	44.05	0.18	0.50	96.18
565471	Dunite	R	2.81	1.27	0.01	0.00	1.78	39.23	0.74	49.40	0.20	0.48	95.92
565471	Dunite	R	2.81	1.27	0.01	0.00	1.85	39.47	0.74	48.96	0.21	0.48	95.79
565471	Dunite	R	2.14	1.07	0.00	0.01	1.31	37.71	0.67	51.78	0.21	0.45	95.36
565471	Dunite	R	2.78	1.39	0.03	0.00	1.25	39.14	0.66	48.43	0.21	0.53	94.42
565471	Dunite	R	2.83	1.21	0.00	0.00	1.61	39.23	0.75	49.38	0.21	0.49	95.70

Sample	Lithology	Core/Rim	Al_2O_3	MgO	SiO_2	CaO	TiO_2	Cr_2O_3	MnO	FeO	NiO	ZnO	SUM
565471	Dunite	R	1.67	0.96	0.03	0.04	1.42	37.28	0.70	51.99	0.23	0.43	94.74
565471	Dunite	R	3.33	1.02	0.02	0.01	1.12	36.49	0.65	51.86	0.22	0.51	95.23
565471	Dunite	R	2.72	1.23	0.02	0.00	1.60	40.22	0.75	48.79	0.21	0.49	96.03
565471	Dunite	R	6.31	2.00	0.01	0.02	1.13	39.14	0.65	46.40	0.20	0.48	96.35
565452	Dunite	R	8.03	2.23	0.03	0.00	0.95	40.65	0.61	42.98	0.13	0.32	95.94
565452	Dunite	R	7.33	1.63	0.02	0.00	0.86	40.66	0.76	43.79	0.12	0.31	95.48
565452	Dunite	R	0.62	0.72	0.04	0.00	1.86	31.41	0.64	58.33	0.24	0.15	94.01
565452	Dunite	R	7.71	2.09	0.01	0.04	0.97	42.22	0.73	42.56	0.13	0.31	96.78
565452	Dunite	R	5.91	1.31	0.03	0.00	0.94	39.92	0.72	47.16	0.15	0.29	96.42
565452	Dunite	R	7.86	2.07	0.00	0.01	0.97	42.20	0.72	42.29	0.12	0.31	96.56
565452	Dunite	R	8.10	2.29	0.02	0.00	0.96	40.86	0.59	42.97	0.13	0.28	96.22
565452	Dunite	R	8.05	1.97	0.01	0.01	0.90	40.39	0.73	43.22	0.13	0.30	95.70
565452	Dunite	R	7.57	1.82	0.01	0.00	0.94	41.15	0.75	43.55	0.12	0.31	96.22
565452	Dunite	R	8.01	1.97	0.01	0.00	1.07	41.16	0.72	42.93	0.13	0.32	96.34
565452	Dunite	R	2.18	0.91	0.03	0.00	1.16	37.86	0.88	51.25	0.21	0.46	94.94
565452	Dunite	R	5.35	1.21	0.04	0.00	1.00	38.33	0.91	47.89	0.18	0.59	95.50
565469	Hydrous Ol-CPXite	Altered	2.90	1.21	0.00	0.31	2.19	28.64	1.39	58.81	0.20	0.21	95.87
565469	Hydrous Ol-CPXite	Altered	0.11	0.53	0.00	0.06	1.70	11.19	1.08	79.31	0.24	0.10	94.33
565469	Hydrous Ol-CPXite	Altered	0.16	0.66	0.00	0.14	1.88	16.32	1.55	73.57	0.24	0.18	94.71
565469	Hydrous Ol-CPXite	Altered	2.70	1.17	0.00	0.45	2.68	26.38	1.45	59.61	0.21	0.20	94.85

Sample	Lithology	Core/Rim	Al_2O_3	MgO	SiO_2	CaO	TiO_2	Cr_2O_3	MnO	FeO	NiO	ZnO	SUM
565469	Hydrous Ol-CPXite	Altered	0.15	0.51	0.00	0.04	1.03	15.74	1.30	75.53	0.16	0.16	94.63
565469	Hydrous Ol-CPXite	Altered	0.11	0.42	0.00	0.01	0.55	12.50	1.00	78.84	0.21	0.13	93.75
565469	Hydrous Ol-CPXite	Altered	0.15	0.64	0.00	0.06	2.06	16.49	1.66	73.57	0.12	0.18	94.92
565469	Hydrous Ol-CPXite	Altered	0.09	0.48	0.00	0.05	1.08	10.60	0.96	80.43	0.25	0.09	94.04
565469	Hydrous Ol-CPXite	Altered	0.15	0.69	0.00	0.34	1.79	13.91	1.42	74.58	0.25	0.14	93.25
565469	Hydrous Ol-CPXite	Altered	0.16	0.63	0.00	0.01	1.87	16.01	1.49	74.34	0.20	0.15	94.86
565450	Hydrous Ol-CPXite	Altered	0.11	0.40	0.00	0.06	1.80	12.93	1.29	77.10	0.14	0.14	93.98
565450	Hydrous Ol-CPXite	Altered	0.12	0.42	0.00	0.02	1.84	13.84	1.37	76.38	0.12	0.15	94.24
565450	Hydrous Ol-CPXite	Altered	0.11	0.36	0.00	0.12	1.22	13.63	1.28	76.67	0.12	0.15	93.65
565450	Hydrous Ol-CPXite	Altered	0.14	0.53	0.00	0.02	2.25	15.01	1.52	74.97	0.19	0.16	94.80
565450	Hydrous Ol-CPXite	Altered	0.11	0.50	0.00	0.06	2.16	13.16	1.38	76.36	0.20	0.14	94.07
565450	Hydrous Ol-CPXite	Altered	0.10	0.43	0.00	0.12	1.76	12.01	1.24	77.64	0.20	0.11	93.61
565450	Hydrous Ol-CPXite	Altered	0.08	0.33	0.00	0.09	0.97	10.18	1.00	80.34	0.15	0.11	93.26
565450	Hydrous Ol-CPXite	Altered	0.13	0.40	0.00	0.09	1.43	14.16	1.37	76.05	0.15	0.16	93.94

Sample	**Lithology**	**Core/Rim**	**Al_2O_3**	**MgO**	**SiO_2**	**CaO**	**TiO_2**	**Cr_2O_3**	**MnO**	**FeO**	**NiO**	**ZnO**	**SUM**
565450	Hydrous Ol-CPXite	Altered	0.14	0.45	0.00	0.02	1.99	15.24	1.50	74.82	0.19	0.16	94.51
565450	Hydrous Ol-CPXite	Altered	0.10	0.41	0.00	0.10	1.87	11.44	1.22	78.34	0.18	0.11	93.76
565450	Hydrous Ol-CPXite	Altered	0.02	0.20	0.00	0.02	0.40	5.83	0.39	85.87	0.09	0.02	92.83
565450	Hydrous Ol-CPXite	Altered	0.09	0.47	0.00	0.03	1.90	11.29	1.16	78.74	0.21	0.11	94.00
565450	Hydrous Ol-CPXite	Altered	0.13	0.41	0.00	0.06	1.68	15.22	1.51	74.68	0.18	0.18	94.04
565450	Hydrous Ol-CPXite	Altered	0.10	0.34	0.00	0.04	1.09	11.97	1.12	78.95	0.17	0.11	93.89
565450	Hydrous Ol-CPXite	Altered	0.01	0.14	0.01	0.02	0.26	0.27	0.09	92.71	0.14	0.00	93.63
565450	Hydrous Ol-CPXite	Altered	2.03	0.96	0.00	0.05	2.11	29.51	2.69	58.44	0.19	0.26	96.22
565450	Hydrous Ol-CPXite	Altered	2.34	0.97	0.00	0.01	2.14	29.56	2.70	58.11	0.19	0.27	96.28
565450	Hydrous Ol-CPXite	Altered	2.60	1.01	0.00	0.00	2.08	29.78	2.71	57.72	0.19	0.27	96.37
565450	Hydrous Ol-CPXite	Altered	2.51	0.98	0.00	0.03	2.10	29.77	2.72	57.86	0.18	0.27	96.43
565450	Hydrous Ol-CPXite	Altered	0.69	0.84	0.00	0.15	2.22	25.12	2.14	63.11	0.18	0.33	94.78
565450	Hydrous Ol-CPXite	Altered	0.25	0.70	0.00	0.00	2.56	24.37	2.31	65.02	0.16	0.32	95.69
565469	Hydrous Ol-CPXite	Altered	1.89	1.07	0.00	0.00	1.90	34.43	2.84	54.78	0.16	0.54	97.61

Sample	**Lithology**	**Core/Rim**	**Al_2O_3**	**MgO**	**SiO_2**	**CaO**	**TiO_2**	**Cr_2O_3**	**MnO**	**FeO**	**NiO**	**ZnO**	**SUM**
565469	Hydrous Ol-CPXite	Altered	0.82	0.94	0.00	0.01	1.97	33.48	2.82	55.74	0.15	0.48	96.40
565469	Hydrous Ol-CPXite	Altered	0.29	0.86	0.00	0.00	2.37	26.22	2.35	63.63	0.18	0.31	96.21
565469	Hydrous Ol-CPXite	Altered	0.30	0.85	0.00	0.00	2.32	26.15	2.36	63.64	0.18	0.31	96.12
565469	Hydrous Ol-CPXite	Altered	0.30	0.84	0.00	0.01	2.32	25.78	2.32	64.13	0.19	0.31	96.19
565469	Hydrous Ol-CPXite	Altered	0.28	0.82	0.00	0.01	2.21	25.43	2.30	64.18	0.20	0.32	95.75
565469	Hydrous Ol-CPXite	Altered	0.23	0.79	0.00	0.00	2.29	22.01	1.97	68.01	0.23	0.25	95.78
565469	Hydrous Ol-CPXite	Altered	0.23	0.79	0.00	0.00	2.29	21.82	1.97	68.23	0.22	0.25	95.80
565469	Hydrous Ol-CPXite	Altered	0.21	0.79	0.00	0.01	2.24	21.46	1.93	68.59	0.22	0.24	95.70
565469	Hydrous Ol-CPXite	Altered	0.20	0.76	0.00	0.03	1.96	20.78	1.86	69.09	0.21	0.25	95.14
565469	Hydrous Ol-CPXite	Altered	0.12	0.49	0.00	0.00	0.94	13.36	1.14	77.68	0.15	0.14	94.02
565469	Hydrous Ol-CPXite	Altered	0.22	0.71	0.00	0.00	2.25	19.42	1.82	70.98	0.22	0.21	95.82
565469	Hydrous Ol-CPXite	Altered	0.21	0.66	0.00	0.00	1.92	19.26	1.76	71.54	0.20	0.22	95.77
565469	Hydrous Ol-CPXite	Altered	0.21	0.70	0.00	0.00	1.86	19.50	1.80	70.81	0.20	0.23	95.31

Clinopyroxene

Sample	**Lithology**	**SiO_2**	**TiO_2**	**ZnO**	**Al_2O_3**	**Cr_2O_3**	**FeO**	**NiO**	**MnO**	**MgO**	**CaO**	**Na_2O**	**TOTAL**
565469	Hydrous Ol-CPXite	55.57	0.02	0.00	0.18	0.10	3.26	0.03	0.23	17.04	24.04	0.12	100.59
565469	Hydrous Ol-CPXite	55.53	0.03	0.00	0.18	0.11	3.17	0.03	0.25	17.06	24.14	0.11	100.62
565469	Hydrous Ol-CPXite	55.50	0.01	0.00	0.14	0.08	3.07	0.03	0.27	17.13	24.26	0.08	100.56
565469	Hydrous Ol-CPXite	55.38	0.02	0.01	0.09	0.02	2.59	0.03	0.25	17.22	24.55	0.03	100.19
565469	Hydrous Ol-CPXite	54.68	0.03	0.00	0.18	0.09	3.30	0.03	0.25	17.04	23.95	0.10	99.65
565469	Hydrous Ol-CPXite	55.42	0.03	0.00	0.19	0.10	3.08	0.03	0.27	16.98	24.17	0.10	100.38
565469	Hydrous Ol-CPXite	55.04	0.03	0.00	0.19	0.10	3.25	0.03	0.25	17.15	23.96	0.12	100.12
565469	Hydrous Ol-CPXite	55.01	0.03	0.00	0.23	0.17	2.99	0.03	0.27	16.93	24.18	0.12	99.96
565469	Hydrous Ol-CPXite	54.89	0.03	0.00	0.25	0.20	3.07	0.02	0.27	16.88	24.12	0.11	99.84
565469	Hydrous Ol-CPXite	55.02	0.03	0.00	0.20	0.12	3.04	0.02	0.28	16.97	24.16	0.10	99.94
565469	Hydrous Ol-CPXite	54.91	0.03	0.00	0.21	0.12	2.68	0.02	0.30	17.16	24.33	0.06	99.82
565469	Hydrous Ol-CPXite	55.09	0.03	0.00	0.17	0.12	2.87	0.02	0.29	17.03	24.32	0.09	100.04
565469	Hydrous Ol-CPXite	55.03	0.03	0.00	0.18	0.10	3.22	0.03	0.23	16.97	23.94	0.11	99.83
565469	Hydrous Ol-CPXite	54.76	0.03	0.00	0.20	0.11	3.20	0.06	0.25	16.99	24.04	0.12	99.74
565469	Hydrous Ol-CPXite	55.01	0.04	0.01	0.23	0.29	3.04	0.03	0.26	16.95	24.15	0.15	100.16
565469	Hydrous Ol-CPXite	54.50	0.05	0.00	0.26	0.63	3.44	0.03	0.28	17.02	24.01	0.13	100.34
565469	Hydrous Ol-CPXite	54.94	0.03	0.00	0.22	0.27	3.11	0.02	0.26	16.96	24.12	0.14	100.07
565469	Hydrous Ol-CPXite	55.02	0.01	0.01	0.10	0.04	2.57	0.03	0.24	17.12	24.65	0.05	99.82
565450	Hydrous Ol-CPXite	55.56	0.03	0.00	0.20	0.16	2.98	0.02	0.32	17.20	24.12	0.10	100.70
565450	Hydrous Ol-CPXite	54.86	0.03	0.00	0.22	0.19	3.22	0.03	0.26	17.12	23.75	0.13	99.80
565450	Hydrous Ol-CPXite	55.96	0.02	0.00	0.10	0.09	2.68	0.03	0.30	17.09	24.37	0.10	100.73
565450	Hydrous Ol-CPXite	55.72	0.03	0.00	0.11	0.12	2.74	0.02	0.30	17.05	24.32	0.11	100.53

Sample	**Lithology**	**SiO_2**	**TiO_2**	**ZnO**	**Al_2O_3**	**Cr_2O_3**	**FeO**	**NiO**	**MnO**	**MgO**	**CaO**	**Na_2O**	**TOTAL**
565450	Hydrous Ol-CPXite	55.43	0.03	0.00	0.19	0.10	3.19	0.03	0.21	17.08	23.85	0.12	100.24
565450	Hydrous Ol-CPXite	55.55	0.03	0.00	0.18	0.11	3.19	0.03	0.25	17.09	23.83	0.11	100.39
565450	Hydrous Ol-CPXite	55.54	0.03	0.01	0.20	0.14	3.35	0.03	0.23	17.06	23.76	0.14	100.50
565450	Hydrous Ol-CPXite	55.59	0.03	0.00	0.19	0.14	3.36	0.03	0.24	17.09	23.78	0.12	100.57
565450	Hydrous Ol-CPXite	55.69	0.04	0.00	0.26	0.15	3.31	0.03	0.31	16.99	23.83	0.13	100.74
565450	Hydrous Ol-CPXite	55.88	0.03	0.00	0.19	0.17	3.16	0.03	0.26	17.03	24.00	0.11	100.85
565450	Hydrous Ol-CPXite	55.65	0.04	0.00	0.17	0.12	3.22	0.03	0.33	17.01	23.94	0.08	100.59
565450	Hydrous Ol-CPXite	55.70	0.02	0.00	0.12	0.07	3.16	0.03	0.31	17.07	24.07	0.09	100.65
565450	Hydrous Ol-CPXite	55.71	0.04	0.00	0.21	0.17	3.13	0.02	0.31	16.99	24.05	0.11	100.72
565450	Hydrous Ol-CPXite	55.56	0.03	0.00	0.20	0.17	3.20	0.03	0.31	17.01	23.93	0.10	100.53
565450	Hydrous Ol-CPXite	55.57	0.04	0.00	0.17	0.12	3.33	0.03	0.30	16.94	23.86	0.08	100.44
565450	Hydrous Ol-CPXite	55.56	0.03	0.00	0.18	0.14	3.25	0.03	0.29	17.01	23.89	0.08	100.47
565450	Hydrous Ol-CPXite	55.99	0.01	0.00	0.07	0.04	2.38	0.02	0.27	17.27	24.58	0.06	100.69
565450	Hydrous Ol-CPXite	55.62	0.02	0.00	0.09	0.07	3.12	0.02	0.31	17.06	24.11	0.08	100.51
565467	Anhydrous Ol-CPXite	54.20	0.26	0.00	2.18	0.29	5.61	0.05	0.25	14.84	22.80	0.45	100.93
565467	Anhydrous Ol-CPXite	54.21	0.24	0.00	2.24	0.29	5.67	0.05	0.25	14.80	22.68	0.46	100.90
565467	Anhydrous Ol-CPXite	54.15	0.26	0.00	2.22	0.30	5.60	0.05	0.26	14.85	22.78	0.46	100.92
565467	Anhydrous Ol-CPXite	54.20	0.24	0.00	2.17	0.30	5.68	0.05	0.26	14.85	22.64	0.45	100.83
565467	Anhydrous Ol-CPXite	54.40	0.22	0.00	2.13	0.28	6.59	0.05	0.28	15.28	20.93	0.45	100.60
565467	Anhydrous Ol-CPXite	53.26	0.17	0.00	1.86	0.24	10.54	0.06	0.39	18.64	15.70	0.17	101.03
565467	Anhydrous Ol-CPXite	54.27	0.20	0.00	1.80	0.29	5.80	0.05	0.25	14.98	22.73	0.43	100.81
565467	Anhydrous Ol-CPXite	54.48	0.19	0.00	1.46	0.27	5.41	0.05	0.23	15.23	23.10	0.36	100.79
565467	Anhydrous Ol-CPXite	54.34	0.24	0.01	2.05	0.29	5.79	0.04	0.26	14.85	22.85	0.42	101.14

Sample	**Lithology**	**SiO_2**	**TiO_2**	**ZnO**	**Al_2O_3**	**Cr_2O_3**	**FeO**	**NiO**	**MnO**	**MgO**	**CaO**	**Na_2O**	**TOTAL**
565467	Anhydrous Ol-CPXite	54.74	0.18	0.00	1.51	0.27	5.95	0.05	0.25	15.17	22.99	0.38	101.50
565467	Anhydrous Ol-CPXite	54.14	0.26	0.00	2.17	0.27	5.82	0.04	0.25	14.80	22.82	0.41	100.99
565467	Anhydrous Ol-CPXite	54.76	0.14	0.00	1.49	0.30	5.17	0.05	0.22	15.36	23.28	0.36	101.14
565467	Anhydrous Ol-CPXite	54.37	0.17	0.00	1.61	0.30	5.50	0.04	0.24	15.16	23.03	0.38	100.80
565467	Anhydrous Ol-CPXite	54.31	0.20	0.00	1.81	0.32	5.43	0.05	0.23	15.25	22.76	0.38	100.74
565467	Anhydrous Ol-CPXite	54.78	0.15	0.01	1.45	0.27	5.31	0.05	0.23	15.33	23.18	0.38	101.14
565467	Anhydrous Ol-CPXite	54.74	0.15	0.00	1.52	0.28	5.52	0.05	0.25	15.14	23.07	0.37	101.10
565467	Anhydrous Ol-CPXite	54.37	0.20	0.00	1.92	0.55	5.35	0.05	0.23	15.00	22.93	0.48	101.08
565467	Anhydrous Ol-CPXite	54.60	0.16	0.00	1.57	0.28	5.04	0.04	0.21	15.50	23.22	0.40	101.03
565467	Anhydrous Ol-CPXite	54.60	0.17	0.00	1.57	0.31	5.13	0.05	0.21	15.51	23.10	0.40	101.03
565467	Anhydrous Ol-CPXite	54.24	0.25	0.01	1.96	0.30	4.88	0.05	0.20	15.63	22.63	0.44	100.58
565467	Anhydrous Ol-CPXite	54.36	0.16	0.00	1.50	0.28	5.71	0.04	0.26	15.04	22.93	0.38	100.65
565467	Anhydrous Ol-CPXite	54.55	0.18	0.00	1.64	0.27	5.57	0.04	0.26	15.08	23.16	0.38	101.13
565467	Anhydrous Ol-CPXite	54.27	0.22	0.00	1.82	0.30	5.76	0.04	0.25	15.01	22.85	0.41	100.94
565451	Anhydrous Ol-CPXite	54.45	0.09	0.00	1.40	0.85	7.92	0.05	0.20	20.61	18.22	0.31	104.09
565451	Anhydrous Ol-CPXite	53.91	0.13	0.00	1.48	0.86	3.51	0.04	0.14	16.38	23.06	0.57	100.07
565451	Anhydrous Ol-CPXite	53.34	0.13	0.00	1.60	1.27	3.63	0.05	0.14	16.29	23.05	0.57	100.06
565451	Anhydrous Ol-CPXite	53.85	0.11	0.02	1.58	0.68	3.30	0.05	0.13	16.60	22.78	0.60	99.71
565451	Anhydrous Ol-CPXite	54.06	0.13	0.00	1.54	0.72	3.28	0.05	0.14	16.48	23.34	0.59	100.33
565451	Anhydrous Ol-CPXite	53.93	0.17	0.00	1.56	0.76	3.23	0.04	0.13	16.51	23.40	0.51	100.25
565451	Anhydrous Ol-CPXite	53.83	0.15	0.02	1.64	0.84	3.20	0.04	0.13	16.46	23.29	0.61	100.20
565451	Anhydrous Ol-CPXite	53.82	0.20	0.00	1.72	0.80	3.14	0.05	0.12	16.27	23.30	0.53	99.93
565451	Anhydrous Ol-CPXite	53.84	0.19	0.00	1.74	0.67	3.21	0.05	0.13	16.38	23.48	0.57	100.26

Sample	**Lithology**	**SiO_2**	**TiO_2**	**ZnO**	**Al_2O_3**	**Cr_2O_3**	**FeO**	**NiO**	**MnO**	**MgO**	**CaO**	**Na_2O**	**TOTAL**
565451	Anhydrous Ol-CPXite	53.88	0.15	0.00	1.69	0.96	3.45	0.05	0.13	16.28	23.14	0.68	100.41
565451	Anhydrous Ol-CPXite	53.66	0.17	0.00	1.86	0.90	3.43	0.05	0.13	16.21	23.11	0.68	100.18
565451	Anhydrous Ol-CPXite	53.08	0.15	0.00	1.67	0.97	4.28	0.05	0.15	16.89	20.78	0.61	98.63
565451	Anhydrous Ol-CPXite	53.82	0.17	0.00	1.63	0.84	3.41	0.04	0.13	16.30	23.02	0.68	100.03
565451	Anhydrous Ol-CPXite	53.86	0.16	0.00	1.60	0.65	3.35	0.04	0.13	16.45	23.54	0.56	100.34
565451	Anhydrous Ol-CPXite	53.80	0.12	0.00	1.26	0.62	3.15	0.04	0.12	16.80	23.44	0.46	99.80
565464	Amphibolite	53.97	0.03		0.30	0.12	6.20	0.00	0.27	15.45	23.61	0.31	100.25
565464	Amphibolite	53.74	0.04		0.27	0.10	6.48	0.02	0.28	15.65	23.00	0.24	99.84
565464	Amphibolite	53.42	0.06		0.29	0.12	6.37	0.03	0.27	15.56	23.07	0.27	99.46

Orthopyroxene

Sample	Lithology	SiO2	TiO2	ZnO	Al2O3	Cr2O3	FeO	NiO	MnO	MgO	CaO	Na2O	TOTAL
565467	Anhydrous Ol-CPXite	53.25	0.05	0.01	1.65	0.15	19.44	0.07	0.64	23.70	1.59	0.00	100.56
565467	Anhydrous Ol-CPXite	53.11	0.04	0.01	1.60	0.14	19.72	0.08	0.65	23.91	1.05	0.06	100.37
565467	Anhydrous Ol-CPXite	53.52	0.06	0.01	1.66	0.16	19.00	0.07	0.64	23.23	1.73	0.05	100.14
565467	Anhydrous Ol-CPXite	53.46	0.10	0.02	1.26	0.13	19.88	0.08	0.66	24.20	0.42	0.00	100.20
565467	Anhydrous Ol-CPXite	53.60	0.04	0.02	1.01	0.09	20.20	0.06	0.67	24.24	0.36	0.00	100.30
565467	Anhydrous Ol-CPXite	53.22	0.04	0.01	1.59	0.14	19.65	0.07	0.65	23.99	1.18	0.00	100.53
565467	Anhydrous Ol-CPXite	53.35	0.03	0.02	1.36	0.12	20.09	0.07	0.66	24.05	0.40	0.00	100.16
565467	Anhydrous Ol-CPXite	53.69	0.05	0.02	1.18	0.09	20.26	0.06	0.68	24.08	0.40	0.00	100.51
565467	Anhydrous Ol-CPXite	53.67	0.17	0.01	1.44	0.14	17.83	0.07	0.58	24.08	2.54	0.03	100.57
565467	Anhydrous Ol-CPXite	53.75	0.33	0.02	1.42	0.15	18.39	0.07	0.58	24.44	1.56	0.00	100.69
565467	Anhydrous Ol-CPXite	53.96	0.05	0.00	1.48	0.15	18.08	0.07	0.58	24.45	1.96	0.02	100.80
565467	Anhydrous Ol-CPXite	53.77	0.27	0.01	1.59	0.16	18.43	0.07	0.58	24.40	1.62	0.00	100.91
565467	Anhydrous Ol-CPXite	53.70	0.05	0.01	1.51	0.15	18.57	0.07	0.61	24.39	1.59	0.01	100.66
565467	Anhydrous Ol-CPXite	53.50	0.52	0.01	1.39	0.15	18.81	0.07	0.62	24.10	1.74	0.02	100.93
565467	Anhydrous Ol-CPXite	53.76	0.06	0.02	1.50	0.16	18.36	0.07	0.60	24.36	1.72	0.02	100.63
565467	Anhydrous Ol-CPXite	53.44	0.05	0.01	1.34	0.13	19.34	0.06	0.63	24.70	0.38	0.00	100.09
565467	Anhydrous Ol-CPXite	53.58	0.08	0.02	1.21	0.12	20.09	0.07	0.68	24.33	0.32	0.00	100.51
565467	Anhydrous Ol-CPXite	53.48	0.04	0.02	1.43	0.12	20.04	0.07	0.66	24.05	0.36	0.00	100.27
565467	Anhydrous Ol-CPXite	53.67	0.07	0.02	1.59	0.15	18.33	0.07	0.59	24.42	1.64	0.02	100.56
565467	Anhydrous Ol-CPXite	53.71	0.07	0.02	1.59	0.15	17.79	0.07	0.56	24.30	2.41	0.03	100.72
565467	Anhydrous Ol-CPXite	53.78	0.05	0.02	1.54	0.14	18.43	0.07	0.59	25.08	0.80	0.00	100.49
565467	Anhydrous Ol-CPXite	53.67	0.06	0.01	1.61	0.16	17.54	0.07	0.54	24.60	2.19	0.02	100.49

Sample	**Lithology**	**SiO_2**	**TiO_2**	**ZnO**	**Al_2O_3**	**Cr_2O_3**	**FeO**	**NiO**	**MnO**	**MgO**	**CaO**	**Na_2O**	**TOTAL**
565467	Anhydrous Ol-CPXite	53.88	0.05	0.02	1.40	0.14	17.85	0.07	0.56	25.12	1.53	0.01	100.64
565467	Anhydrous Ol-CPXite	54.07	0.05	0.02	1.19	0.13	18.58	0.07	0.58	25.43	0.36	0.00	100.47
565467	Anhydrous Ol-CPXite	53.47	0.04	0.01	0.96	0.08	20.30	0.07	0.68	24.06	0.33	0.00	100.00
565467	Anhydrous Ol-CPXite	53.51	0.05	0.02	1.17	0.12	20.35	0.06	0.67	24.00	0.38	0.00	100.35
565451	Anhydrous Ol-CPXite	54.31	0.05	0.00	1.04	0.14	12.90	0.08	0.34	30.00	0.36	0.00	99.22
565451	Anhydrous Ol-CPXite	54.33	0.07	0.00	1.31	0.25	12.16	0.09	0.32	28.87	1.90	0.01	99.31
565451	Anhydrous Ol-CPXite	54.17	0.05	0.00	1.37	0.26	12.37	0.08	0.33	29.15	1.40	0.00	99.19
565451	Anhydrous Ol-CPXite	54.33	0.06	0.00	1.29	0.24	12.53	0.07	0.34	29.55	1.14	0.00	99.55
565451	Anhydrous Ol-CPXite	53.79	0.07	0.00	1.78	0.31	12.91	0.08	0.33	28.96	1.04	0.00	99.26
565451	Anhydrous Ol-CPXite	55.11	0.04	0.00	0.85	0.15	11.95	0.07	0.31	30.96	0.29	0.00	99.74
565451	Anhydrous Ol-CPXite	54.65	0.05	0.00	1.15	0.17	12.39	0.07	0.34	30.52	0.34	0.00	99.69
565451	Anhydrous Ol-CPXite	54.35	0.06	0.00	1.11	0.18	12.67	0.08	0.34	29.72	0.33	0.00	98.84
565451	Anhydrous Ol-CPXite	54.45	0.06	0.00	1.09	0.17	12.67	0.09	0.34	29.91	0.28	0.00	99.06
565451	Anhydrous Ol-CPXite	54.50	0.06	0.00	1.28	0.19	12.79	0.08	0.35	30.02	0.35	0.00	99.63
565451	Anhydrous Ol-CPXite	54.14	0.08	0.00	1.43	0.31	12.19	0.08	0.32	29.14	1.70	0.00	99.38
565451	Anhydrous Ol-CPXite	54.71	0.06	0.00	1.06	0.16	12.22	0.07	0.33	30.58	0.34	0.00	99.52
565451	Anhydrous Ol-CPXite	54.50	0.09	0.00	1.27	0.24	11.30	0.06	0.31	30.06	1.81	0.00	99.65
565470	Dunite	55.95	0.04	0.00	0.24	0.07	10.68	0.06	0.33	32.20	0.21	0.00	99.78
565470	Dunite	55.67	0.04	0.00	0.17	0.05	11.16	0.04	0.33	31.81	0.09	0.00	99.36
565470	Dunite	55.82	0.04	0.00	0.22	0.05	10.71	0.05	0.34	32.16	0.13	0.00	99.52
565470	Dunite	55.93	0.04	0.00	0.23	0.08	10.73	0.05	0.32	32.17	0.13	0.00	99.67
565470	Dunite	55.93	0.04	0.01	0.24	0.07	10.57	0.05	0.33	32.15	0.21	0.00	99.59
565470	Dunite	55.81	0.03	0.00	0.22	0.07	10.66	0.05	0.32	32.12	0.13	0.00	99.41

Amphibole

Sample	Lithology	SiO_2	TiO_2	Al_2O_3	Cr_2O_3	FeO	NiO	MnO	MgO	CaO	Na2O	K2O	P2O5	Cl	F	O	TOTAL
565450	*Hydrous Ol-clinopyroxenite*	56.78	0.07	1.52	0.20	3.50	0.05	0.13	22.46	12.74	0.46	0.12	0.00	0.02	0.00	0.00	98.05
565450	*Hydrous Ol-clinopyroxenite*	55.90	0.10	1.96	0.32	3.75	0.08	0.14	22.27	12.72	0.56	0.20	0.02	0.02	0.00	0.00	98.02
565450	*Hydrous Ol-clinopyroxenite*	55.90	0.09	1.45	0.26	3.71	0.07	0.16	22.43	12.68	0.45	0.17	0.00	0.01	0.00	0.00	97.39
565450	*Hydrous Ol-clinopyroxenite*	57.67	0.06	0.90	0.11	3.48	0.07	0.16	23.03	12.68	0.29	0.09	0.00	0.01	0.00	0.00	98.54
565450	*Hydrous Ol-clinopyroxenite*	57.80	0.05	0.84	0.09	3.80	0.08	0.15	22.81	12.53	0.27	0.11	0.03	0.00	0.00	0.00	98.55
565450	*Hydrous Ol-clinopyroxenite*	56.61	0.07	0.96	0.13	3.90	0.06	0.15	22.76	12.44	0.34	0.13	0.00	0.01	0.00	0.00	97.57
565450	*Hydrous Ol-clinopyroxenite*	57.21	0.04	0.95	0.14	3.66	0.04	0.17	22.77	12.51	0.34	0.12	0.02	0.01	0.00	0.00	97.98
565450	*Hydrous Ol-clinopyroxenite*	57.17	0.06	0.89	0.09	3.55	0.06	0.15	22.87	12.73	0.32	0.11	0.00	0.02	0.00	0.00	98.02
565450	*Hydrous Ol-clinopyroxenite*	57.74	0.04	0.99	0.16	3.37	0.11	0.15	22.90	12.90	0.28	0.12	0.00	0.00	0.00	0.00	98.76
565450	*Hydrous Ol-clinopyroxenite*	57.20	0.06	1.00	0.17	3.39	0.08	0.15	22.98	12.80	0.26	0.12	0.00	0.01	0.00	0.00	98.23
565450	*Hydrous Ol-clinopyroxenite*	57.14	0.06	1.08	0.17	3.39	0.09	0.17	22.84	12.70	0.31	0.14	0.03	0.01	0.00	0.00	98.13
565450	*Hydrous Ol-clinopyroxenite*	57.03	0.05	0.82	0.13	3.45	0.05	0.17	22.91	12.77	0.22	0.10	0.00	0.02	0.00	0.00	97.72
565450	*Hydrous Ol-clinopyroxenite*	56.94	0.06	0.81	0.12	3.17	0.07	0.15	22.98	12.85	0.22	0.08	0.00	0.00	0.00	0.00	97.46
565450	*Hydrous Ol-clinopyroxenite*	56.92	0.06	0.80	0.12	3.31	0.10	0.15	22.96	12.76	0.26	0.10	0.02	0.00	0.00	0.00	97.54
565450	*Hydrous Ol-clinopyroxenite*	56.83	0.05	1.01	0.16	3.46	0.07	0.16	22.78	12.70	0.35	0.12	0.00	0.02	0.00	0.00	97.72
565450	*Hydrous Ol-clinopyroxenite*	58.38	0.05	0.92	0.13	3.69	0.05	0.19	22.67	12.64	0.31	0.10	0.00	0.01	0.00	0.00	99.14
565450	*Hydrous Ol-clinopyroxenite*	56.29	0.07	1.03	0.18	3.98	0.08	0.18	22.74	12.33	0.33	0.13	0.00	0.01	0.00	0.00	97.35

Sample	Lithology	SiO_2	TiO_2	Al_2O_3	Cr_2O_3	FeO	NiO	MnO	MgO	CaO	Na2O	K2O	P2O5	Cl	F	O	TOTAL
565450	*Hydrous Ol-clinopyroxenite*	56.37	0.05	0.98	0.13	3.87	0.05	0.15	22.59	12.46	0.35	0.13	0.03	0.02	0.00	0.00	97.19
565450	*Hydrous Ol-clinopyroxenite*	56.96	0.04	0.94	0.14	3.28	0.05	0.15	22.95	12.77	0.26	0.10	0.03	0.00	0.00	0.00	97.66
565450	*Hydrous Ol-clinopyroxenite*	56.21	0.07	0.90	0.13	3.85	0.07	0.15	22.73	12.46	0.30	0.13	0.02	0.01	0.00	0.00	97.03
565450	*Hydrous Ol-clinopyroxenite*	55.95	0.05	0.96	0.11	3.53	0.07	0.17	22.94	12.72	0.27	0.12	0.02	0.02	0.00	0.00	96.92
565450	*Hydrous Ol-clinopyroxenite*	55.11	0.05	0.93	0.08	3.51	0.09	0.16	22.68	12.98	0.26	0.09	0.03	0.00	0.00	0.00	95.97
565450	*Hydrous Ol-clinopyroxenite*	55.30	0.04	0.95	0.14	3.81	0.09	0.17	22.73	12.63	0.30	0.13	0.02	0.02	0.00	-0.01	96.33
565450	*Hydrous Ol-clinopyroxenite*	54.86	0.05	1.02	0.17	4.10	0.09	0.15	22.55	12.29	0.38	0.14	0.02	0.00	0.00	0.00	95.81
565450	*Hydrous Ol-clinopyroxenite*	54.39	0.08	1.26	0.21	4.09	0.10	0.16	22.26	12.24	0.37	0.17	0.01	0.01	0.00	0.00	95.35
565450	*Hydrous Ol-clinopyroxenite*	55.58	0.04	0.80	0.11	3.79	0.08	0.15	22.63	12.50	0.27	0.11	0.00	0.01	0.00	0.00	96.08
565450	*Hydrous Ol-clinopyroxenite*	55.78	0.03	0.60	0.08	3.74	0.06	0.16	22.74	12.47	0.22	0.09	0.02	0.01	0.00	0.00	96.01
565450	*Hydrous Ol-clinopyroxenite*	56.01	0.06	0.63	0.11	3.73	0.08	0.15	22.83	12.54	0.22	0.08	0.02	0.00	0.00	0.00	96.47
565450	*Hydrous Ol-clinopyroxenite*	56.13	0.06	0.63	0.09	3.70	0.06	0.18	22.81	12.52	0.20	0.09	0.01	0.01	0.00	0.00	96.50
565450	*Hydrous Ol-clinopyroxenite*	55.94	0.03	0.71	0.09	3.35	0.09	0.15	22.86	12.74	0.26	0.08	0.00	0.01	0.00	0.00	96.30
565450	*Hydrous Ol-clinopyroxenite*	55.85	0.06	0.82	0.11	3.73	0.06	0.17	22.79	12.48	0.24	0.11	0.00	0.00	0.00	0.00	96.41
565455	*Dunite*	50.91	0.42	6.55	0.71	4.75	0.15	0.10	20.51	11.87	1.65	0.23	0.00	0.06	0.00	-0.01	97.89
565455	*Dunite*	49.91	0.44	7.31	0.90	4.88	0.12	0.10	20.22	11.94	1.81	0.24	0.02	0.05	0.00	-0.01	97.93

Sample	Lithology	SiO_2	TiO_2	Al_2O_3	Cr_2O_3	FeO	NiO	MnO	MgO	CaO	Na2O	K2O	P2O5	Cl	F	O	TOTAL
565455	*Dunite*	50.73	0.39	6.82	0.84	4.67	0.11	0.10	20.53	11.81	1.76	0.10	0.02	0.04	0.00	-0.01	97.91
565455	*Dunite*	50.92	0.36	6.60	0.80	4.56	0.09	0.14	20.77	11.90	1.67	0.07	0.00	0.03	0.00	-0.01	97.90
565455	*Dunite*	50.11	0.47	7.25	0.95	4.99	0.11	0.10	20.25	11.84	1.80	0.19	0.02	0.05	0.00	-0.01	98.13
565455	*Dunite*	49.83	0.45	7.35	0.89	4.76	0.13	0.09	20.21	11.87	1.81	0.19	0.00	0.06	0.00	-0.01	97.61
565455	*Dunite*	48.89	0.45	7.19	0.90	4.87	0.11	0.10	20.07	11.72	1.81	0.16	0.02	0.05	0.00	-0.01	96.33
565455	*Dunite*	50.89	0.40	6.72	0.83	4.62	0.13	0.11	20.61	11.88	1.70	0.10	0.00	0.03	0.00	-0.01	98.01
565455	*Dunite*	49.85	0.43	7.19	0.98	4.69	0.11	0.09	20.02	11.69	1.78	0.23	0.00	0.05	0.00	-0.01	97.10
565455	*Dunite*	51.44	0.30	5.87	0.65	4.01	0.13	0.14	21.03	11.85	1.46	0.07	0.03	0.03	0.00	-0.01	97.00
565455	*Dunite*	49.12	0.44	7.46	0.98	4.88	0.12	0.10	19.98	11.80	1.78	0.27	0.00	0.05	0.00	-0.01	96.96
565455	*Dunite*	49.23	0.46	7.45	0.99	4.86	0.12	0.10	19.99	11.79	1.86	0.22	0.01	0.05	0.00	-0.01	97.12
565455	*Dunite*	50.29	0.37	6.69	0.79	4.43	0.09	0.11	20.53	11.73	1.71	0.09	0.00	0.03	0.00	-0.01	96.87
565455	*Dunite*	50.13	0.36	6.96	0.89	4.56	0.12	0.11	20.41	11.81	1.76	0.15	0.02	0.05	0.00	-0.01	97.33

Sample	Lithology	SiO_2	TiO_2	Al_2O_3	Cr_2O_3	FeO	NiO	MnO	MgO	CaO	Na2O	K2O	P2O5	Cl	F	O	TOTAL
565455	*Dunite*	50.19	0.35	6.59	0.84	4.59	0.12	0.12	20.72	11.77	1.65	0.11	0.00	0.03	0.00	-0.01	97.06
565455	*Dunite*	48.44	0.43	7.28	0.95	4.74	0.11	0.12	20.31	11.76	1.83	0.17	0.02	0.04	0.00	-0.01	96.21
565455	*Dunite*	50.06	0.37	6.80	0.85	4.51	0.10	0.10	20.62	11.76	1.69	0.12	0.03	0.03	0.00	-0.01	97.02
565471	*Dunite*	55.56	0.12	1.68	0.43	2.84	0.11	0.13	23.08	12.38	0.55	0.05	0.03	0.00	0.00	0.00	96.97
565471	*Dunite*	52.47	0.33	5.21	0.78	4.01	0.10	0.12	21.28	12.06	1.36	0.21	0.00	0.03	0.00	0.00	97.96
565471	*Dunite*	53.15	0.21	3.92	0.61	3.70	0.13	0.13	21.91	11.91	1.13	0.13	0.03	0.02	0.00	0.00	96.97
565471	*Dunite*	51.92	0.28	4.93	0.77	3.90	0.11	0.13	21.56	11.95	1.34	0.13	0.04	0.03	0.00	0.00	97.07
565471	*Dunite*	53.38	0.26	4.71	0.74	3.90	0.10	0.12	21.77	12.04	1.34	0.11	0.00	0.03	0.00	0.00	98.49
565471	*Dunite*	53.38	0.28	4.32	0.65	3.69	0.13	0.11	21.60	12.10	1.21	0.13	0.00	0.02	0.00	0.00	97.61
565471	*Dunite*	52.58	0.25	4.66	0.74	3.80	0.10	0.12	21.55	12.06	1.30	0.20	0.01	0.03	0.00	0.00	97.41
565471	*Dunite*	54.85	0.18	2.81	0.36	3.39	0.11	0.10	22.46	12.28	0.82	0.09	0.00	0.01	0.00	0.00	97.47
565471	*Dunite*	52.58	0.29	4.64	0.73	3.79	0.11	0.12	21.56	12.14	1.24	0.19	0.02	0.02	0.00	0.00	97.41
565471	*Dunite*	53.95	0.24	3.82	0.65	3.62	0.10	0.11	22.05	12.05	1.09	0.11	0.02	0.00	0.00	0.00	97.81
565471	*Dunite*	52.67	0.24	4.17	0.58	3.75	0.11	0.11	21.71	12.07	1.13	0.19	0.01	0.02	0.00	0.00	96.77
565471	*Dunite*	52.27	0.30	4.49	0.69	3.79	0.12	0.09	21.51	12.18	1.24	0.18	0.02	0.02	0.00	0.00	96.91
565471	*Dunite*	52.98	0.22	4.22	0.61	3.62	0.13	0.10	22.26	11.72	1.03	0.20	0.02	0.02	0.00	0.00	97.15
565471	*Dunite*	57.96	0.00	0.07	0.06	10.69	0.13	0.46	27.50	0.59	0.07	0.00	0.00	0.00	0.00	0.00	97.52

Sample	Lithology	SiO_2	TiO_2	Al_2O_3	Cr_2O_3	FeO	NiO	MnO	MgO	CaO	Na2O	K2O	P2O5	Cl	F	O	TOTAL
565471	*Dunite*	56.80	0.02	0.22	0.23	11.26	0.12	0.51	27.10	0.46	0.03	0.00	0.00	0.00	0.00	0.00	96.74
565471	*Dunite*	53.74	0.22	3.61	0.59	3.42	0.09	0.11	22.12	12.15	1.06	0.10	0.02	0.01	0.00	0.00	97.25
565471	*Dunite*	52.67	0.28	4.65	0.72	3.74	0.11	0.11	21.55	11.90	1.30	0.12	0.00	0.02	0.00	0.00	97.16
565471	*Dunite*	55.91	0.14	2.03	0.31	3.04	0.10	0.13	22.94	12.42	0.62	0.05	0.00	0.01	0.00	0.00	97.69
565471	*Dunite*	52.37	0.28	5.02	0.75	3.89	0.10	0.12	21.47	11.99	1.39	0.12	0.02	0.02	0.00	0.00	97.55
565471	*Dunite*	52.04	0.34	5.31	0.79	3.93	0.10	0.14	21.35	11.98	1.43	0.12	0.01	0.03	0.00	0.00	97.56
565471	*Dunite*	52.51	0.31	4.97	0.74	3.89	0.10	0.11	21.42	11.98	1.34	0.11	0.00	0.04	0.00	0.00	97.53
565471	*Dunite*	55.53	0.11	2.11	0.37	2.85	0.09	0.09	23.11	12.31	0.63	0.05	0.03	0.02	0.00	0.00	97.31
565471	*Dunite*	58.64	0.00	0.04	0.02	1.29	0.10	0.12	24.29	13.24	0.05	0.01	0.00	0.00	0.00	0.00	97.80
565471	*Dunite*	53.16	0.23	4.02	0.60	3.67	0.13	0.11	21.74	12.11	1.10	0.15	0.00	0.03	0.00	0.00	97.05
565471	*Dunite*	52.61	0.27	4.49	0.69	3.72	0.12	0.09	21.61	12.14	1.17	0.18	0.02	0.02	0.00	0.00	97.13
565471	*Dunite*	51.66	0.31	4.95	0.77	3.84	0.11	0.12	21.57	12.00	1.29	0.21	0.01	0.03	0.00	0.00	96.88
565471	*Dunite*	53.45	0.22	3.77	0.60	3.54	0.11	0.13	21.99	12.13	1.08	0.10	0.00	0.02	0.00	0.00	97.14
565471	*Dunite*	58.29	0.02	0.16	0.08	10.39	0.12	0.43	27.75	0.62	0.05	0.00	0.00	0.01	0.00	0.00	97.92
565471	*Dunite*	53.45	0.24	3.81	0.57	3.63	0.10	0.10	22.07	12.10	1.07	0.10	0.00	0.02	0.00	0.00	97.29
565471	*Dunite*	53.38	0.23	3.74	0.56	3.53	0.12	0.12	22.21	12.11	1.10	0.09	0.02	0.02	0.00	0.00	97.24
565471	*Dunite*	52.83	0.25	3.99	0.58	3.50	0.12	0.12	21.96	12.07	1.12	0.13	0.02	0.03	0.00	0.00	96.71
565471	*Dunite*	52.52	0.26	4.19	0.59	3.64	0.09	0.10	21.84	12.15	1.19	0.14	0.01	0.02	0.00	0.00	96.74

Sample	**Lithology**	**SiO_2**	**TiO_2**	**Al_2O_3**	**Cr_2O_3**	**FeO**	**NiO**	**MnO**	**MgO**	**CaO**	**Na2O**	**K2O**	**P2O5**	**Cl**	**F**	**O**	**TOTAL**
565471	*Dunite*	52.36	0.26	4.11	0.63	3.69	0.10	0.11	21.88	12.10	1.14	0.13	0.00	0.03	0.00	0.00	96.55
565471	*Dunite*	51.33	0.28	4.57	0.65	3.87	0.11	0.13	21.59	12.10	1.27	0.20	0.02	0.03	0.00	0.00	96.14
565451	*Anhydrous Ol-Clinopyroxenite*	44.51	0.92	11.50	1.31	5.33	0.13	0.08	17.99	12.17	2.80	0.52	0.00	0.00	0.00	0.00	97.25
565452	*Dunite*	52.33	0.21	4.72	0.74	3.68	0.09	0.12	21.63	12.13	1.27	0.12	0.00	0.02	0.00	0.00	97.05
565452	*Dunite*	52.27	0.25	4.88	0.73	3.86	0.12	0.10	21.47	12.19	1.31	0.15	0.00	0.02	0.00	0.00	97.35
565452	*Dunite*	53.10	0.19	4.42	0.71	3.67	0.10	0.11	21.78	12.27	1.20	0.09	0.00	0.01	0.00	0.00	97.65
565452	*Dunite*	52.35	0.21	4.75	0.75	3.78	0.11	0.11	21.65	12.18	1.29	0.13	0.00	0.02	0.00	0.00	97.32
565452	*Dunite*	53.24	0.19	4.38	0.66	3.70	0.09	0.10	21.75	12.21	1.20	0.11	0.02	0.02	0.00	0.00	97.68
565452	*Dunite*	52.29	0.23	4.71	0.75	3.87	0.10	0.09	21.55	12.26	1.26	0.20	0.00	0.02	0.00	0.00	97.34
565452	*Dunite*	53.08	0.21	4.39	0.64	3.65	0.08	0.11	21.85	12.23	1.12	0.17	0.03	0.03	0.00	0.00	97.60
565452	*Dunite*	52.02	0.18	4.67	0.68	3.78	0.10	0.11	21.66	12.19	1.23	0.18	0.02	0.02	0.00	0.00	96.87
565452	*Dunite*	54.77	0.11	2.52	0.34	3.23	0.07	0.10	22.73	12.42	0.74	0.04	0.01	0.01	0.00	0.00	97.10
565452	*Dunite*	53.39	0.13	3.36	0.65	3.38	0.07	0.13	22.45	12.16	0.93	0.06	0.00	0.02	0.00	0.00	96.73
565452	*Dunite*	51.30	0.23	4.79	1.50	4.11	0.07	0.13	21.53	12.01	1.26	0.18	0.00	0.02	0.00	0.00	97.14
565452	*Dunite*	54.29	0.15	3.13	0.48	3.20	0.08	0.13	22.51	12.35	0.89	0.07	0.00	0.01	0.00	0.00	97.29
565452	*Dunite*	51.82	0.24	5.24	0.73	3.96	0.14	0.09	21.33	12.08	1.35	0.21	0.02	0.03	0.00	0.00	97.24
565452	*Dunite*	51.73	0.22	4.99	0.71	3.87	0.11	0.09	21.27	12.15	1.28	0.20	0.00	0.03	0.00	0.00	96.64
565452	*Dunite*	52.25	0.23	5.07	0.74	3.87	0.09	0.11	21.39	12.09	1.31	0.18	0.03	0.03	0.00	0.00	97.37

Sample	Lithology	SiO_2	TiO_2	Al_2O_3	Cr_2O_3	FeO	NiO	MnO	MgO	CaO	Na2O	K2O	P2O5	Cl	F	O	TOTAL
565452	*Dunite*	52.63	0.24	4.56	0.62	3.74	0.08	0.12	21.66	12.07	1.21	0.15	0.02	0.02	0.00	0.00	97.12
565452	*Dunite*	52.88	0.18	3.70	0.59	3.41	0.11	0.10	22.10	12.14	1.02	0.05	0.03	0.02	0.00	0.00	96.33
565452	*Dunite*	52.32	0.24	4.78	0.69	3.85	0.09	0.09	21.45	12.12	1.29	0.19	0.01	0.02	0.00	0.00	97.13
565452	*Dunite*	51.85	0.20	4.67	0.73	3.85	0.09	0.09	21.62	11.96	1.25	0.11	0.00	0.02	0.00	0.00	96.44
565452	*Dunite*	52.18	0.22	4.81	0.71	3.80	0.10	0.09	21.53	12.12	1.29	0.16	0.02	0.02	0.00	0.00	97.06
565452	*Dunite*	57.92	0.06	0.18	0.04	0.97	0.09	0.07	24.19	13.46	0.04	0.04	0.00	0.00	0.00	0.00	97.06
565464	*Amphibolite*	53.01	0.29	2.96	0.25	9.03	0.07	0.23	18.58	11.81	0.67	0.25	0.00	0.04	0.00	0.00	97.19
565464	*Amphibolite*	51.94	0.23	3.52	0.15	9.20	0.07	0.22	18.44	11.96	0.74	0.32	0.00	0.04	0.00	0.00	96.83
565464	*Amphibolite*	52.35	0.25	3.35	0.13	9.21	0.06	0.24	18.55	11.88	0.75	0.29	0.02	0.03	0.00	0.00	97.10
565464	*Amphibolite*	52.60	0.24	3.15	0.12	9.11	0.05	0.24	18.55	12.00	0.60	0.28	0.01	0.05	0.00	0.00	97.01
565464	*Amphibolite*	52.94	0.29	2.96	0.15	8.89	0.07	0.22	18.64	12.04	0.65	0.26	0.03	0.03	0.00	0.00	97.16
565464	*Amphibolite*	53.13	0.27	2.86	0.20	8.79	0.05	0.22	18.62	12.32	0.56	0.25	0.00	0.03	0.00	0.00	97.30
565464	*Amphibolite*	54.19	0.19	2.52	0.23	8.56	0.05	0.14	18.62	12.84	0.40	0.22	0.02	0.03	0.00	0.00	98.01
565464	*Amphibolite*	52.48	0.23	2.97	0.24	8.80	0.08	0.20	18.60	12.31	0.51	0.23	0.00	0.02	0.00	0.00	96.68
565464	*Amphibolite*	53.19	0.25	2.89	0.30	8.72	0.06	0.22	18.60	12.34	0.58	0.23	0.03	0.04	0.00	0.00	97.47
565464	*Amphibolite*	53.52	0.26	2.82	0.27	8.86	0.07	0.21	18.66	12.01	0.68	0.23	0.00	0.04	0.00	0.00	97.63
565464	*Amphibolite*	52.82	0.29	3.00	0.27	9.13	0.08	0.24	18.70	11.59	0.64	0.26	0.01	0.03	0.00	0.00	97.06
565464	*Amphibolite*	53.46	0.24	2.60	0.26	9.06	0.04	0.27	18.93	11.67	0.54	0.23	0.00	0.03	0.00	0.00	97.32

Sample	Lithology	SiO_2	TiO_2	Al_2O_3	Cr_2O_3	FeO	NiO	MnO	MgO	CaO	Na2O	K2O	P2O5	Cl	F	O	TOTAL
565464	*Amphibolite*	52.64	0.27	3.04	0.29	9.03	0.07	0.23	18.63	11.58	0.79	0.32	0.03	0.13	0.00	0.00	97.05
565464	*Amphibolite*	53.21	0.30	2.83	0.29	9.10	0.03	0.26	18.70	11.85	0.58	0.24	0.00	0.03	0.00	0.00	97.42
565464	*Amphibolite*	53.24	0.27	2.88	0.28	8.90	0.07	0.23	18.79	11.78	0.63	0.23	0.00	0.03	0.00	0.00	97.33
565464	*Amphibolite*	53.45	0.28	2.85	0.27	9.20	0.05	0.25	18.78	11.65	0.62	0.26	0.02	0.04	0.00	0.00	97.72
565464	*Amphibolite*	53.16	0.28	2.86	0.26	8.95	0.04	0.23	18.68	11.86	0.64	0.25	0.02	0.03	0.00	0.00	97.26
565464	*Amphibolite*	53.32	0.25	2.64	0.24	9.27	0.08	0.28	18.38	11.91	0.57	0.25	0.03	0.09	0.00	0.00	97.30
565464	*Amphibolite*	53.67	0.24	2.66	0.25	9.11	0.05	0.25	18.74	11.68	0.57	0.23	0.00	0.03	0.00	0.00	97.49
565464	*Amphibolite*	53.25	0.29	2.84	0.27	9.19	0.06	0.27	18.41	11.93	0.61	0.25	0.03	0.05	0.00	0.00	97.43
565464	*Amphibolite*	52.28	0.32	2.89	0.30	8.78	0.06	0.21	18.66	12.36	0.55	0.26	0.00	0.07	0.00	0.00	96.73
565464	*Amphibolite*	52.47	0.27	2.86	0.24	9.46	0.06	0.17	18.24	12.21	0.53	0.26	0.02	0.04	0.00	0.00	96.83
565464	*Amphibolite*	53.85	0.25	2.84	0.22	8.81	0.05	0.23	18.64	12.59	0.52	0.25	0.00	0.03	0.00	0.00	98.26
565464	*Amphibolite*	53.12	0.24	2.80	0.25	8.71	0.05	0.18	18.74	12.37	0.56	0.24	0.01	0.03	0.00	0.00	97.29
565464	*Amphibolite*	53.31	0.26	2.89	0.33	8.70	0.05	0.18	18.46	12.82	0.57	0.25	0.03	0.03	0.00	0.00	97.88
565464	*Amphibolite*	54.03	0.26	2.81	0.32	9.00	0.05	0.25	18.71	11.90	0.66	0.25	0.00	0.04	0.00	0.00	98.29
565464	*Amphibolite*	52.06	0.24	2.93	0.32	8.94	0.00	0.20	18.41	12.42	0.54	0.23	0.00	0.03	0.00	0.00	96.33
565464	*Amphibolite*	52.08	0.27	2.74	0.28	9.08	0.05	0.25	18.63	11.74	0.72	0.22	0.00	0.03	0.00	0.00	96.09
565464	*Amphibolite*	52.23	0.26	2.90	0.31	9.41	0.06	0.23	18.67	11.63	0.72	0.25	0.00	0.03	0.00	0.00	96.69
565464	*Amphibolite*	52.56	0.32	3.01	0.31	9.22	0.09	0.23	18.54	11.58	0.77	0.25	0.02	0.03	0.00	0.00	96.94

Sample	**Lithology**	**SiO_2**	**TiO_2**	**Al_2O_3**	**Cr_2O_3**	**FeO**	**NiO**	**MnO**	**MgO**	**CaO**	**Na2O**	**K2O**	**P2O5**	**Cl**	**F**	**O**	**TOTAL**
565464	*Amphibolite*	52.80	0.27	2.94	0.32	9.25	0.05	0.25	18.54	11.72	0.73	0.27	0.00	0.03	0.00	0.00	97.17
565464	*Amphibolite*	53.40	0.27	2.91	0.31	9.08	0.05	0.23	18.72	11.93	0.70	0.24	0.02	0.04	0.00	0.00	97.90
565464	*Amphibolite*	53.02	0.28	2.99	0.33	9.27	0.05	0.23	18.66	11.85	0.62	0.26	0.00	0.03	0.00	0.00	97.58
565464	*Amphibolite*	52.99	0.23	2.78	0.30	9.19	0.06	0.28	18.60	12.04	0.59	0.25	0.04	0.04	0.00	0.00	97.40
565464	*Amphibolite*	52.74	0.27	2.93	0.31	9.32	0.03	0.27	18.62	11.77	0.67	0.26	0.00	0.04	0.00	0.00	97.23
565464	*Amphibolite*	52.70	0.25	2.88	0.30	9.33	0.06	0.30	18.64	11.63	0.62	0.26	0.02	0.03	0.00	0.00	97.03
565464	*Amphibolite*	52.82	0.27	2.87	0.29	9.15	0.06	0.24	18.68	11.80	0.67	0.25	0.00	0.04	0.00	0.00	97.15
565464	*Amphibolite*	52.32	0.26	2.95	0.31	9.16	0.06	0.24	18.64	11.70	0.61	0.26	0.00	0.04	0.00	0.00	96.55
565463	*Hornblende Gabbro*	45.05	0.82	9.72	0.11	15.65	0.00	0.27	11.72	11.89	1.12	0.92	0.01	0.25	0.00	-0.06	97.48
565463	*Hornblende Gabbro*	45.05	0.92	9.70	0.10	15.72	0.00	0.29	11.61	11.89	1.14	0.90	0.02	0.19	0.00	-0.04	97.48
565463	*Hornblende Gabbro*	45.77	0.78	9.12	0.09	15.35	0.04	0.26	12.19	11.91	1.15	0.83	0.00	0.16	0.00	-0.04	97.62
565463	*Hornblende Gabbro*	47.33	0.64	7.66	0.07	14.72	0.00	0.27	13.01	11.98	0.92	0.62	0.00	0.14	0.00	-0.03	97.34
565463	*Hornblende Gabbro*	48.87	0.49	6.67	0.07	14.26	0.03	0.25	13.70	12.11	0.86	0.49	0.00	0.10	0.00	-0.02	97.88
565463	*Hornblende Gabbro*	49.09	0.44	6.83	0.09	14.06	0.05	0.27	13.54	12.16	0.79	0.50	0.00	0.13	0.00	-0.03	97.91
565463	*Hornblende Gabbro*	46.34	0.80	8.62	0.06	15.00	0.04	0.27	12.44	12.02	0.97	0.74	0.00	0.22	0.00	-0.05	97.46

Sample	Lithology	SiO_2	TiO_2	Al_2O_3	Cr_2O_3	FeO	NiO	MnO	MgO	CaO	Na2O	K2O	P2O5	Cl	F	O	TOTAL
565463	*Hornblende Gabbro*	44.32	0.90	9.90	0.12	15.80	0.03	0.26	11.30	11.88	1.10	0.88	0.02	0.24	0.00	-0.05	96.67
565463	*Hornblende Gabbro*	48.03	0.55	7.64	0.09	14.35	0.00	0.26	13.30	12.11	0.94	0.59	0.03	0.11	0.00	-0.03	97.98
565463	*Hornblende Gabbro*	49.22	0.50	5.89	0.00	13.57	0.00	0.26	14.22	12.16	0.83	0.38	0.01	0.08	0.00	-0.02	97.10
565463	*Hornblende Gabbro*	44.93	0.79	10.35	0.13	15.86	0.00	0.29	11.06	11.83	1.08	0.93	0.02	0.24	0.00	-0.05	97.44
565463	*Hornblende Gabbro*	44.93	0.80	10.09	0.11	15.70	0.00	0.28	11.24	11.97	1.13	0.91	0.00	0.19	0.00	-0.04	97.30
565463	*Hornblende Gabbro*	44.38	0.87	9.79	0.13	15.53	0.04	0.27	11.61	11.91	1.12	0.93	0.01	0.19	0.00	-0.04	96.73
565463	*Hornblende Gabbro*	44.53	0.87	10.08	0.10	15.83	0.04	0.27	11.34	11.88	1.11	0.93	0.02	0.23	0.00	-0.05	97.18
565463	*Hornblende Gabbro*	51.91	0.16	3.99	0.08	12.49	0.03	0.24	15.42	12.29	0.50	0.15	0.00	0.05	0.00	-0.01	97.30
565463	*Hornblende Gabbro*	53.03	0.06	2.67	0.09	12.15	0.05	0.25	16.05	12.51	0.32	0.05	0.00	0.02	0.00	0.00	97.24
565463	*Hornblende Gabbro*	45.64	0.74	8.92	0.06	15.09	0.00	0.26	12.07	11.95	1.04	0.78	0.00	0.15	0.00	-0.03	96.65
565463	*Hornblende Gabbro*	47.66	0.62	7.30	0.15	13.45	0.00	0.28	13.76	11.99	0.92	0.58	0.00	0.11	0.00	-0.02	96.79
565463	*Hornblende Gabbro*	44.82	0.86	9.60	0.15	15.00	0.00	0.27	11.94	11.74	1.18	0.92	0.01	0.19	0.00	-0.04	96.66

Sample	**Lithology**	**SiO_2**	**TiO_2**	**Al_2O_3**	**Cr_2O_3**	**FeO**	**NiO**	**MnO**	**MgO**	**CaO**	**Na2O**	**K2O**	**P2O5**	**Cl**	**F**	**O**	**TOTAL**
565463	*Hornblende Gabbro*	44.58	0.89	9.69	0.12	15.19	0.00	0.25	11.84	11.77	1.19	0.94	0.00	0.21	0.00	-0.05	96.63
565463	*Hornblende Gabbro*	44.78	0.87	9.81	0.09	15.38	0.00	0.29	11.71	11.91	1.13	0.96	0.00	0.20	0.00	-0.04	97.07
565463	*Hornblende Gabbro*	54.63	0.06	1.49	0.06	10.76	0.00	0.24	17.37	12.60	0.18	0.04	0.01	0.02	0.00	0.00	97.46
565463	*Hornblende Gabbro*	46.62	0.91	7.87	0.07	14.26	0.03	0.27	12.76	12.09	0.92	0.65	0.02	0.19	0.00	-0.04	96.62
565463	*Hornblende Gabbro*	52.82	0.06	2.25	0.02	11.48	0.00	0.25	16.53	12.44	0.32	0.05	0.00	0.02	0.00	0.00	96.22
565472	*Dunite*	51.96	0.26	4.73	0.66	3.87	0.12	0.11	21.66	12.21	1.17	0.24	0.00	0.03	0.00	0.00	97.03
565472	*Dunite*	51.15	0.31	5.50	0.85	4.02	0.12	0.11	21.22	12.25	1.34	0.26	0.00	0.04	0.00	0.00	97.18
565472	*Dunite*	51.31	0.29	5.06	0.75	3.91	0.14	0.11	21.49	12.26	1.27	0.23	0.00	0.04	0.00	0.00	96.86
565472	*Dunite*	52.20	0.29	4.59	0.67	3.68	0.14	0.12	21.81	12.25	1.16	0.17	0.02	0.03	0.00	0.00	97.12
565472	*Dunite*	51.84	0.29	4.86	0.67	3.90	0.12	0.11	21.50	12.21	1.17	0.23	0.00	0.03	0.00	0.00	96.92
565472	*Dunite*	52.11	0.25	4.76	0.69	3.74	0.11	0.12	21.69	12.18	1.22	0.16	0.00	0.03	0.00	0.00	97.09
565472	*Dunite*	50.63	0.32	5.65	0.86	4.10	0.12	0.08	21.21	12.30	1.34	0.29	0.02	0.03	0.00	0.00	96.96
565472	*Dunite*	52.99	0.20	4.03	0.65	3.63	0.12	0.12	22.15	12.05	1.08	0.08	0.00	0.02	0.00	0.00	97.12
565472	*Dunite*	52.16	0.23	4.53	0.67	3.91	0.08	0.13	21.91	11.97	1.17	0.10	0.00	0.03	0.00	0.00	96.89
565472	*Dunite*	51.48	0.24	4.95	0.76	3.94	0.13	0.09	21.48	12.00	1.28	0.14	0.00	0.03	0.00	0.00	96.54
565472	*Dunite*	51.18	0.29	4.52	0.59	3.80	0.09	0.09	21.72	12.12	1.17	0.13	0.00	0.02	0.00	0.00	95.73

Sample	**Lithology**	**SiO_2**	**TiO_2**	**Al_2O_3**	**Cr_2O_3**	**FeO**	**NiO**	**MnO**	**MgO**	**CaO**	**Na2O**	**K2O**	**P2O5**	**Cl**	**F**	**O**	**TOTAL**
565472	*Dunite*	52.65	0.21	4.41	0.69	3.60	0.13	0.13	21.88	12.07	1.18	0.11	0.01	0.02	0.00	0.00	97.09
565472	*Dunite*	52.27	0.23	4.29	0.65	3.77	0.10	0.14	21.92	12.13	1.09	0.10	0.00	0.02	0.00	0.00	96.72
565472	*Dunite*	52.50	0.23	4.08	0.67	3.57	0.11	0.12	22.06	12.12	1.14	0.08	0.02	0.02	0.00	0.00	96.73
565472	*Dunite*	53.12	0.30	4.83	0.70	4.07	0.12	0.11	21.64	12.05	1.26	0.17	0.00	0.03	0.00	0.00	98.41
565472	*Dunite*	52.35	0.27	4.58	0.60	3.86	0.14	0.11	21.57	12.11	1.22	0.19	0.03	0.03	0.00	0.00	97.06
565472	*Dunite*	52.23	0.28	4.62	0.58	4.00	0.13	0.11	21.64	12.13	1.16	0.16	0.03	0.03	0.00	0.00	97.10
565472	*Dunite*	53.11	0.23	3.72	0.39	3.65	0.09	0.10	22.06	12.18	1.04	0.16	0.00	0.03	0.00	0.00	96.77
565472	*Dunite*	52.54	0.18	3.67	0.51	3.57	0.11	0.11	22.11	12.07	1.02	0.12	0.00	0.03	0.00	0.00	96.05
565472	*Dunite*	53.33	0.22	3.68	0.38	3.55	0.11	0.11	22.13	12.10	1.01	0.13	0.00	0.03	0.00	0.00	96.79
565472	*Dunite*	53.08	0.20	3.43	0.32	3.57	0.10	0.08	22.20	12.17	0.96	0.15	0.00	0.03	0.00	0.00	96.29
565472	*Dunite*	52.95	0.22	3.92	0.47	3.70	0.10	0.10	21.95	12.14	1.02	0.16	0.02	0.02	0.00	0.00	96.77
565472	*Dunite*	51.98	0.27	4.24	0.55	3.83	0.12	0.13	21.93	12.19	1.12	0.13	0.02	0.04	0.00	0.00	96.55
565472	*Dunite*	53.40	0.25	4.20	0.60	3.72	0.10	0.10	21.83	12.20	1.07	0.17	0.00	0.02	0.00	0.00	97.66
565472	*Dunite*	51.88	0.29	5.11	0.70	3.88	0.09	0.11	21.39	12.14	1.30	0.22	0.00	0.04	0.00	0.00	97.15
565472	*Dunite*	51.72	0.31	5.19	0.75	3.87	0.14	0.10	21.30	12.13	1.29	0.24	0.00	0.03	0.00	0.00	97.06
565469	*Hydrous Ol-clinopyroxenite*	54.20	0.20	3.18	0.40	4.63	0.09	0.15	21.85	12.34	0.86	0.20	0.00	0.04	0.00	-0.01	98.12
565469	*Hydrous Ol-clinopyroxenite*	53.54	0.15	2.81	0.40	4.29	0.08	0.18	22.00	12.54	0.73	0.15	0.01	0.04	0.00	-0.01	96.91

Sample	Lithology	SiO_2	TiO_2	Al_2O_3	Cr_2O_3	FeO	NiO	MnO	MgO	CaO	Na2O	K2O	P2O5	Cl	F	O	TOTAL
565469	*Hydrous Ol-clinopyroxenite*	53.17	0.16	3.30	0.43	4.56	0.06	0.21	21.88	12.08	0.92	0.12	0.00	0.05	0.00	-0.01	96.93
565469	*Hydrous Ol-clinopyroxenite*	53.11	0.22	3.93	0.50	4.62	0.09	0.24	21.55	11.95	1.08	0.12	0.00	0.04	0.00	-0.01	97.45
565469	*Hydrous Ol-clinopyroxenite*	54.30	0.13	2.65	0.39	3.97	0.09	0.13	22.07	12.69	0.74	0.22	0.01	0.03	0.00	-0.01	97.44
565469	*Hydrous Ol-clinopyroxenite*	55.92	0.08	1.34	0.13	3.56	0.08	0.12	22.60	12.87	0.41	0.10	0.02	0.01	0.00	0.00	97.24
565469	*Hydrous Ol-clinopyroxenite*	56.59	0.04	0.52	0.05	3.61	0.11	0.14	23.02	12.78	0.22	0.03	0.01	0.01	0.00	0.00	97.11
565469	*Hydrous Ol-clinopyroxenite*	55.64	0.06	1.76	0.24	3.51	0.08	0.10	22.75	13.03	0.54	0.13	0.01	0.01	0.00	0.00	97.85
565469	*Hydrous Ol-clinopyroxenite*	54.13	0.12	2.48	0.31	4.18	0.08	0.16	22.18	12.65	0.71	0.18	0.00	0.04	0.00	-0.01	97.23
565469	*Hydrous Ol-clinopyroxenite*	56.16	0.06	1.42	0.15	3.68	0.08	0.13	22.61	12.84	0.45	0.11	0.00	0.00	0.00	0.00	97.70
565469	*Hydrous Ol-clinopyroxenite*	56.12	0.05	1.24	0.22	3.31	0.06	0.14	22.99	12.97	0.35	0.07	0.02	0.02	0.00	0.00	97.55
565469	*Hydrous Ol-clinopyroxenite*	53.72	0.14	2.96	0.50	4.68	0.10	0.16	21.85	12.38	0.81	0.19	0.02	0.03	0.00	-0.01	97.55
565469	*Hydrous Ol-clinopyroxenite*	54.33	0.13	2.47	0.29	4.26	0.09	0.14	22.18	12.59	0.71	0.20	0.02	0.04	0.00	-0.01	97.42
565469	*Hydrous Ol-clinopyroxenite*	55.25	0.05	1.21	0.11	3.15	0.06	0.15	23.07	12.90	0.37	0.10	0.00	0.01	0.00	0.00	96.42
565469	*Hydrous Ol-clinopyroxenite*	54.44	0.10	2.07	0.24	3.71	0.07	0.12	22.34	12.82	0.58	0.18	0.02	0.02	0.00	0.00	96.71
565469	*Hydrous Ol-clinopyroxenite*	57.20	0.06	1.37	0.10	3.57	0.08	0.14	22.76	12.92	0.45	0.10	0.00	0.00	0.00	0.00	98.76
565469	*Hydrous Ol-clinopyroxenite*	55.06	0.11	2.30	0.38	3.92	0.05	0.13	22.36	12.86	0.66	0.16	0.05	0.02	0.00	-0.01	98.06

Sample	Lithology	SiO_2	TiO_2	Al_2O_3	Cr_2O_3	FeO	NiO	MnO	MgO	CaO	Na2O	K2O	P2O5	Cl	F	O	TOTAL
565469	*Hydrous Ol-clinopyroxenite*	54.45	0.09	2.49	0.37	3.78	0.07	0.11	22.35	12.90	0.73	0.19	0.00	0.03	0.00	-0.01	97.55
565469	*Hydrous Ol-clinopyroxenite*	55.57	0.06	0.88	0.04	3.42	0.10	0.14	23.10	13.01	0.33	0.07	0.02	0.01	0.00	0.00	96.75
565469	*Hydrous Ol-clinopyroxenite*	55.31	0.17	2.68	0.37	4.22	0.08	0.15	22.09	12.62	0.77	0.19	0.00	0.03	0.00	-0.01	98.67
565469	*Hydrous Ol-clinopyroxenite*	54.46	0.15	2.83	0.41	4.17	0.08	0.17	21.99	12.67	0.74	0.23	0.00	0.04	0.00	-0.01	97.93

Appendix 2: Major and Trace Element Geochemistry XRF

Sample	**565458**	**565463**	**565466**	**565464**	**565467**	**565451**	**565469**	**565450**
Lithology	*Hornblende Gabbro*	*Hornblende Gabbro*	*Amphibolite*	*Amphibolite*	*Anhydrous Ol-CPXite*	*Anhydrous Ol-CPXite*	*Hydrous Ol-CPXite*	*Hydrous Ol-CPXite*
Latitude (N)	64° 58.967	64° 58.832	64° 58.859	64° 58.910	64° 58.817	64° 58.780	64° 58.810	64° 58.772
Longitude (W)	50° 02.994	50° 03.993	50° 03.529	50° 03.606	50° 03.692	50° 03.967	50° 03.867	50° 03.965
SiO_2	52.70	52.64	53.50	54.48	53.14	50.81	52.37	51.96
TiO_2	0.45	0.71	0.28	0.26	0.25	0.19	0.14	0.12
Al_2O_3	7.33	11.70	3.29	2.51	2.66	2.33	1.72	1.56
FeO	11.99	11.68	10.86	9.23	9.90	8.88	8.07	8.18
MnO	0.22	0.19	0.24	0.21	0.21	0.20	0.19	0.21
MgO	13.67	9.77	17.07	18.54	17.85	23.72	23.02	23.48
CaO	11.20	10.05	13.85	14.07	15.49	13.22	13.95	13.86
Na_2O	1.86	2.49	0.64	0.47	0.33	0.54	0.27	0.16
K_2O	0.50	0.70	0.24	0.19	0.16	0.09	0.25	0.46
P_2O_5	0.07	0.08	0.03	0.04	0.02	0.02	0.02	0.01
LOI	0.38	0.47	0.98	0.35	0.84	0.23	0.93	1.37
V	159	165	161	144	158	78	62	58
Ni	324	177	423	397	437	810	730	759
Cr	739	446	1398	1816	1384	4274	4049	4229
Co	67	49	71	53	62	64	63	65

Sample	**565452**	**565470**	**565472**	**565471**	**565455**	**565462**	**565453**
Lithology	*Dunite*	*Dunite*	*Dunite*	*Dunite*	*Altered Dunite*	*Altered Dunite*	*Altered Dunite*
Latitude (N)	64° 58.792	64° 58.795	64° 58.819	64° 58.811	64° 58.809	64° 58.767	64° 58.798
Longitude (W)	50° 03.981	50° 03.971	50° 03.994	50° 03.993	50° 04.011	50° 04.134	50° 03.993
SiO_2	51.96	40.49	42.26	41.16	40.49	43.64	45.61
TiO_2	0.12	0.10	0.10	0.10	0.11	0.12	0.14
Al_2O_3	1.56	1.29	1.19	1.23	1.34	1.63	1.55
FeO	8.18	15.52	14.95	14.20	14.89	14.00	12.47
MnO	0.21	0.29	0.26	0.30	0.26	0.24	0.22
MgO	23.48	40.03	37.92	41.50	40.88	37.60	38.35
CaO	13.86	1.89	2.89	1.04	1.38	2.37	1.56
Na_2O	0.16	0.14	0.19	0.10	0.12	0.27	0.04
K_2O	0.46	0.23	0.22	0.35	0.51	0.11	0.03
P_2O_5	0.01	0.02	0.02	0.02	0.03	0.03	0.03
LOI	1.37	0.70	-0.06	1.42	0.06	1.33	9.92
V	56	37	35	32	38	42	42
Ni	2386	2064	2453	2865	2548	1794	2050
Cr	16545	6191	7517	5968	4508	5155	5583
Co	180	173	181	159	155	160	188

Note: Oxides in wt % and elements in ppm

Analyses of the reference material MUH-1

Specimen	MUH-1 (A)	MUH-1 (B)	MUH-1 (C	MUH-1 (D)	MUH-1 (E)	AVERAGE	Standard Deviation	RSD%	Certified Values	Anhydours Certified Values	Percent Difference in Accuracy
SiO_2	43.92	44.20	43.98	43.81	44.10	44.00	0.15	0.35	40.38	44.85	-1.88
TiO_2	0.03	0.03	0.03	0.04	0.03	0.03	0.00	12.20	0.03	0.04	-12.05
Al_2O_3	1.53	1.49	1.48	1.52	1.49	1.50	0.02	1.44	1.33	1.48	1.38
Fe_2O_3T	9.81	9.91	9.85	10.04	9.67	9.86	0.14	1.38	8.59	9.54	3.31
MnO	0.129	0.127	0.127	0.128	0.127	0.13	0.00	0.70	0.12	0.13	-2.63
MgO	42.44	42.16	42.26	41.97	42.12	42.19	0.17	0.41	38.25	42.48	-0.68
CaO	1.36	1.34	1.34	1.40	1.35	1.36	0.02	1.84	1.21	1.35	0.79
Na_2O	0.12	0.11	0.11	0.11	0.11	0.11	0.00	4.29	0.10	0.12	-3.55
K_2O	0.012	0.010	0.009	0.019	0.017	0.01	0.00	32.78	0.01	0.01	0.55
P_2O_5	0.008	0.008	0.008	0.009	0.006	0.01	0.00	14.04	0.01	0.01	-6.36
Total	99.362	99.389	99.190	99.046	99.021	99.20	0.17	0.17	90.04	100.00	
LOI	9.84	9.87	9.79	9.87	9.80	9.83	0.04	0.38	9.38	9.38	4.84
V	38	44	34	43	45	40.80	4.66	11.42	41	45.53	-10.40
Ni	2921	3060	3068	3021	2866	2987.20	89.50	3.00	2104	2336.66	27.84
Cr	2954	2946	2917	2828	2871	2903.20	53.14	1.83	2710	3009.68	-3.54
Co	119	127	111	106	108	114.20	8.70	7.62	106.7	118.50	-3.63

Certified values are from the International Association of Geoanalysts.

Appendix 3: Trace Elements ICPMS

Sample	**565458**	**565463**	**565466**	**565464**	**565467**	**565451**	**565469**	**565450**
Lithology	*Hornblende Gabbro*	*Hornblende Gabbro*	*Amphibolite*	*Amphibolite*	*Anhydrous Ol-CPXite*	*Anhydrous Ol-CPXite*	*Hydrous Ol-CPXite*	*Hydrous Ol-CPXite*
Th	0.77	1.50	0.31	0.18	0.21	0.10	0.15	0.20
Nb	1.84	3.17	1.07	0.61	0.45	0.33	0.35	0.47
Ta	0.12	0.21	0.08	0.04	0.03	0.02	0.02	0.02
La	8.08	9.46	2.63	1.80	2.50	2.21	1.66	1.22
Ce	22.47	24.30	8.21	6.03	7.49	6.19	5.13	3.89
Pr	3.04	3.04	1.38	1.06	1.25	0.94	0.78	0.62
Sr	97.87	222.55	48.42	21.41	19.57	43.45	13.48	9.47
Nd	14.17	13.33	7.38	5.86	6.68	4.57	3.73	3.14
Zr	53.46	87.82	21.44	12.20	12.81	12.36	8.45	8.23
Hf	1.54	2.35	0.73	0.47	0.54	0.39	0.26	0.26
Sm	3.38	3.12	2.13	1.81	2.02	1.16	0.96	0.87
Eu	0.94	0.94	0.53	0.47	0.50	0.31	0.25	0.20
Gd	3.40	3.23	2.33	2.05	2.27	1.22	1.02	0.96
Tb	0.52	0.51	0.38	0.34	0.37	0.19	0.16	0.15
Dy	3.11	3.10	2.32	2.08	2.30	1.17	1.00	0.95
Y	15.45	15.70	11.41	10.15	11.40	5.67	4.81	4.62
Ho	0.62	0.62	0.47	0.42	0.46	0.23	0.20	0.19
Er	1.72	1.75	1.30	1.15	1.29	0.66	0.56	0.54
Yb	1.51	1.56	1.13	0.99	1.13	0.58	0.50	0.48
Lu	0.22	0.23	0.17	0.14	0.16	0.09	0.07	0.07

Sample	**565452**	**565470**	**565472**	**565471**	**565455**	**565462**	**565453**
Lithology	*Dunite*	*Dunite*	*Dunite*	*Dunite*	*Altered Dunite*	*Altered Dunite*	*Altered Dunite*
Th	0.10	0.09	0.13	0.11	0.16	0.18	0.13
Nb	0.22	0.29	0.36	0.46	0.52	0.96	1.44
Ta	0.02	0.02	0.02	0.03	0.03	0.04	0.19
La	1.34	1.40	0.67	0.96	2.37	0.78	0.76
Ce	3.87	3.55	1.98	2.60	5.65	2.73	2.81
Pr	0.53	0.48	0.29	0.38	0.75	0.47	0.49
Sr	4.43	11.31	2.58	4.18	26.55	3.00	3.47
Nd	2.25	2.12	1.27	1.76	3.27	2.39	2.48
Zr	5.53	6.07	7.21	10.02	16.87	23.72	8.23
Hf	0.16	0.19	0.19	0.27	0.42	0.61	0.27
Sm	0.43	0.47	0.28	0.41	0.69	0.61	0.82
Eu	0.10	0.13	0.07	0.09	0.19	0.05	0.12
Gd	0.39	0.47	0.27	0.40	0.67	0.62	0.98
Tb	0.06	0.07	0.04	0.06	0.10	0.10	0.18
Dy	0.34	0.43	0.24	0.35	0.58	0.60	1.23
Y	1.70	2.10	1.13	1.71	2.81	3.30	7.83
Ho	0.07	0.09	0.05	0.07	0.12	0.13	0.27
Er	0.20	0.25	0.13	0.20	0.33	0.38	0.82
Yb	0.21	0.24	0.13	0.19	0.31	0.41	0.91
Lu	0.03	0.04	0.02	0.03	0.05	0.07	0.14

Note: all values in ppm

OKUM analyses reported in Waterton et al. (2018)

Sample number	**OKUM-724-1**	**OKUM-724-2**	**OKUM-724-3**	**OKUM-724-4**	**OKUM-724-5**	**OKUM-724-6**	**OKUM-724-7**	**OKUM-724-8**	**OKUM-724-9**
Th	0.027	0.026	0.027	0.025	0.026	0.026	0.028	0.027	0.028
Nb	0.363	0.354	0.369	0.359	0.355	0.361	0.386	0.357	0.387
Ta									
La	0.389	0.386	0.390	0.388	0.388	0.387	0.400	0.385	0.404
Ce	1.259	1.248	1.246	1.255	1.247	1.264	1.277	1.219	1.276
Pr	0.229	0.229	0.227	0.230	0.228	0.230	0.238	0.226	0.239
Sr	15.308	15.233	15.329	15.492	15.453	15.680	16.064	15.370	16.036
Nd	1.455	1.441	1.440	1.469	1.443	1.461	1.508	1.459	1.503
Zr	14.855	14.602	15.593	14.742	14.458	15.442	16.361	14.708	16.820
Hf	0.526	0.510	0.529	0.528	0.508	0.532	0.545	0.517	0.556
sm	0.712	0.685	0.699	0.699	0.702	0.703	0.702	0.680	0.712
Eu	0.305	0.304	0.301	0.304	0.298	0.307	0.313	0.301	0.311
Gd	1.168	1.147	1.155	1.178	1.167	1.186	1.178	1.129	1.183
Tb	0.219	0.218	0.219	0.219	0.219	0.223	0.229	0.221	0.230
Dy	1.540	1.522	1.533	1.546	1.523	1.542	1.606	1.537	1.606
Y	9.248	9.231	9.274	9.342	9.298	9.406	9.670	9.306	9.688
Ho	0.336	0.332	0.335	0.341	0.336	0.340	0.345	0.334	0.345
Er	0.990	0.990	0.987	1.002	0.980	0.997	1.031	0.990	1.034
Yb	0.993	0.971	0.973	0.989	0.978	0.994	1.006	0.977	1.014
Lu	0.147	0.145	0.148	0.150	0.147	0.150	0.149	0.145	0.151

Sample number	OKUM-724-10	OKUM-724a-11	OKUM-724b-12	Average	(%RSD)	Certified Reference Values	Percent Difference from Certified Values
Th	0.027	0.027	0.027	0.027	3.0	0.031	-13.8
Nb	0.370	0.344	0.347	0.363	3.6	0.370	-2.0
Ta							
La	0.396	0.387	0.401	0.392	1.7	0.412	-4.9
Ce	1.255	1.215	1.246	1.251	1.4	1.270	-1.5
Pr	0.232	0.231	0.233	0.231	1.7	0.235	-1.7
Sr	15.735	15.726	15.943	15.614	1.8	16.100	-3.0
Nd	1.466	1.431	1.464	1.462	1.6	1.494	-2.2
Zr	15.333	16.456	16.468	15.486	5.2	17.000	-8.9
Hf	0.535	0.538	0.557	0.532	2.9	0.551	-3.5
sm	0.704	0.676	0.699	0.698	1.6	0.715	-2.4
Eu	0.307	0.302	0.302	0.304	1.4	0.300	1.5
Gd	1.161	1.170	1.194	1.168	1.5	1.170	-0.2
Tb	0.228	0.224	0.223	0.223	1.8	0.229	-2.8
Dy	1.580	1.526	1.563	1.552	1.9	1.610	-3.6
Y	9.525	9.274	9.392	9.388	1.6	9.080	3.4
Ho	0.339	0.330	0.335	0.337	1.3	0.355	-5.0
Er	1.025	0.991	1.018	1.003	1.8	1.041	-3.7
Yb	0.993	0.978	0.999	0.989	1.3	1.009	-2.0
Lu	0.147	0.147	0.150	0.148	1.3	0.148	0.1

Appendix 4: Platinum Group Element Chemistry

sample	Lithology	Os	2σ abs.	Ir	2σ abs.	Ru	2σ abs.	Pt	2σ abs.	Pd	2σ abs.	Re	2σ abs.
565463	*Hornblende Gabbro*	0.12	0.01	0.17	0.00	0.28	0.01	4.15	0.10	5.02	0.12	0.1768	0.0038
565464	*Amphibolite*	0.29	0.02	0.31	0.01	1.71	0.11	0.87	0.02	0.21	0.02	0.0090	0.0003
565466	*Amphibolite*	0.28	0.02	0.31	0.01	0.98	0.02	0.030	0.009	0.15	0.02	0.0044	0.0002
565451	*Ol-CPXite*	2.66	0.03	2.23	0.05	6.23	0.14	0.52	0.02	0.36	0.02	0.0421	0.0009
565450	*Ol-CPXite*	1.82	0.02	0.78	0.02	4.68	0.10	0.14	0.01	0.19	0.02	0.0164	0.0004
565467	*Ol-CPXite*	0.59	0.02	0.84	0.02	2.64	0.07	0.50	0.02	0.64	0.02	0.0205	0.0005
565469	*Ol-CPXite*	1.53	0.02	0.88	0.02	4.00	0.10	0.22	0.01	0.71	0.05	0.0151	0.0004
565452	*Dunite*	15.61	0.08	13.46	0.31	31.69	0.68	3.36	0.07	1.53	0.04	0.0095	0.0004
565470	*Dunite*	4.65	0.03	3.55	0.29	11.46	0.49	1.33	0.22	0.36	0.08	0.0193	0.0104
565471	*Dunite*	2.72	0.03	1.86	0.04	8.47	0.17	5.73	0.12	0.99	0.05	0.0150	0.0006
565472	*Dunite*	1.30	0.02	1.03	0.02	9.48	0.19	0.42	0.02	0.27	0.02	0.0100	0.0005
565455	*Altered Dunite*	6.77	0.04	4.33	0.09	8.12	0.17	0.98	0.03	0.63	0.10	0.0476	0.0015

Note: values in ppb

Appendix 5: Cr as an Interference on Ru

Ratios of ^{100}Ru/^{99}Ru and ^{101}Ru/^{99}Ru, largely in the dunite samples, do not lay on a mixing line between Ru isotopic ratios in the spike used and natural Ru (Fig. A-1). A potential interference on Ru is Cr, as samples with high Cr deviate in their Ru isotopic ratios from the mixing line between spike and natural Ru (Fig. A-1). Furthermore, a correlation exists between Cr and Ru isotopic ratios in all lithologies of the TUC (Fig. A-1), and further investigation may be required if this is prevalent among dunite samples from other unrelated studies. Thus, it is unclear if large Ru anomalies in the TUC are real or reflect unsolved analytical issues.

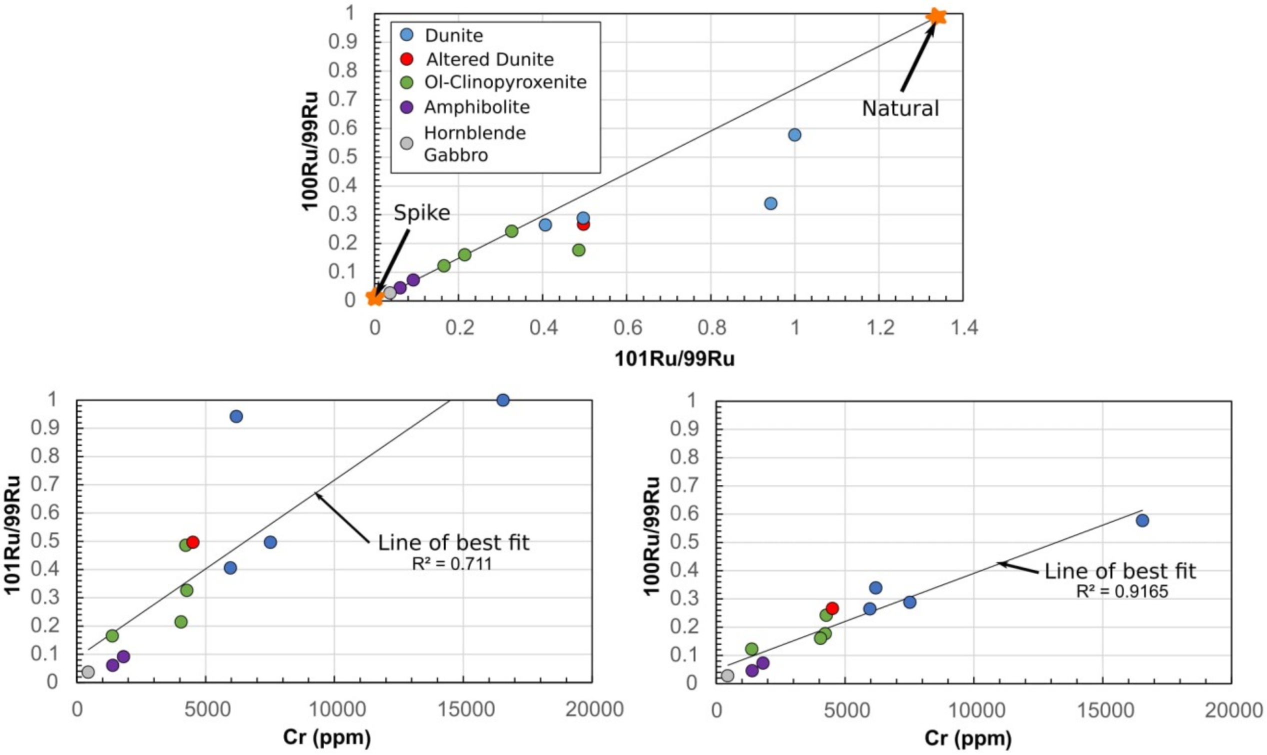

Fig. A- 1. Ruthenium ratios in some samples do not lie on a sample spike mixing line, potentially resulting in erroneous data. Correlation in Ru isotopic ratios and Cr may indicate a potential interference by Cr.

Appendix 6: Trace Element Modelling

The model follows the order of crystallization and degree of fractionation of the MELTS modeling in section 2.4.2, as well as using the same samples for the initial starting composition (least altered tholeiitic basalts of Polat and Hofmann (2003)). In the initial stage, olivine is precipitated to a mass fraction of 0.28. Although in the modelling from MELTS there is no significant cotectic olivine and clinopyroxene precipitation, the petrography of the TUC indicates that either such a stage existed or olivine and clinopyroxene cumulates were mechanically mixed. Thus, in the second stage, olivine and clinopyroxene are precipitated to a mass fraction of 0.1 with a modal proportion of 25:75, the approximate modal minerology of the TUC ol-CPXites. A third stage consists of clinopyroxene precipitation to a mass fraction of 0.1. Because of the low partitioning coefficients used for all trace elements in olivine (Bedard, 2005) and some in clinopyroxene (Norman et al., 2005), trace elements in the cumulate rocks of the TUC may be significantly affected by trapped interstitial melt. For this reason, trapped interstitial melt was estimated from the minimum initial melt that would need to be added to account for the average concentration of Al_2O_3 in the dunite samples, about 12 %. This quantity of melt, with the trace element concentration of melt at the end of each stage, was added to the cumulate fraction of that stage. The results were extrapolated through the calculated cumulate and melts from each stage.

Calculations were done using the model of Albarede and Bottinga (1972), in which diffusion rates in cumulate crystals precipitating and settling from a finite reservoir are too slow to allow re-equilibration with the liquid (i.e. fractional crystallization). The equations used to calculate the change in precipitate and liquid compositions are $C_{solid}=C_{initial}(1/F)(1-[1-F]^{D})$ and $C_{liquid}=C_{initial}[1-F]^{(D-1)}$, respectively, where C is the concentration of element i, D is the distribution coefficient of i between precipitate and melt, and F is the mass fraction of precipitate. Distribution coefficients for olivine are from Bedard (2005) and clinopyroxene from (Norman et al., 2005).

The concentration of elements in the minerals and melt at the end of each stage are given below.

	F*	**Al_2O_3**	**TiO_2**	**Th**	**Nb**	**La**	**Nd**	**Zr**	**Hf**	**Yb**
Initial melt		7.72	0.65	0.93	1.73	2.84	6.13	41.6	1.85	1.32
D (mineral/melt)										
Ol		0.002	0.02	0	0	0.006	0.002	0.003	0.005	0.02
CPX		0.2	0.27	0	0.004	0.03	0.15	0.07	0.13	0.40
BULK 0.25Ol 0.75CPX		0.15	0.21	0.00	0.00	0.03	0.11	0.05	0.10	0.31
Stage 1: Olivine										
Olivine + Melt	0.25	1.29	0.17	0.16	0.29	0.48	1.02	6.93	0.32	0.27
Final Liquid Stage 1	0.25	10.28	0.87	1.24	2.31	3.78	8.17	55.42	2.46	1.75

	F*	**Al_2O_3**	**TiO_2**	**Th**	**Nb**	**La**	**Nd**	**Zr**	**Hf**	**Yb**
Stage 2: Olivine/CPX										
CPX										
	0.02	2.07	0.23	0.00	0.01	0.12	1.23	3.74	0.32	0.71
	0.04	2.09	0.24	0.00	0.01	0.12	1.24	3.78	0.32	0.71
	0.06	2.11	0.24	0.00	0.01	0.12	1.25	3.81	0.32	0.71
	0.08	2.13	0.24	0.00	0.01	0.12	1.26	3.85	0.33	0.72
	0.1	2.14	0.24	0.00	0.01	0.13	1.28	3.89	0.33	0.72
Ol										
	0.02	0.021	0.017	0.000	0.000	0.023	0.017	0.168	0.012	0.035
	0.04	0.021	0.018	0.000	0.000	0.023	0.017	0.170	0.013	0.036
	0.06	0.021	0.018	0.000	0.000	0.023	0.017	0.171	0.013	0.036
	0.08	0.021	0.018	0.000	0.000	0.024	0.017	0.173	0.013	0.036
	0.1	0.022	0.018	0.000	0.000	0.024	0.017	0.175	0.013	0.037
Ol:CPX:Melt 22:66:12										
	0.02	2.77	0.28	0.17	0.33	0.61	1.93	10.15	0.55	0.71
	0.04	2.78	0.28	0.17	0.33	0.61	1.94	10.17	0.55	0.71
	0.06	2.79	0.28	0.17	0.33	0.61	1.95	10.20	0.55	0.71
	0.08	2.81	0.28	0.17	0.33	0.61	1.95	10.22	0.56	0.72
	0.1	2.82	0.28	0.17	0.33	0.61	1.96	10.25	0.56	0.72
Final Liquid Stage 2										
	0.1	11.25	0.94	1.38	2.56	4.19	8.97	61.25	2.71	1.88

Stage 3 CPX										
CPX + Melt										
	0.02	3.51	0.35	0.19	0.36	0.70	2.41	12.06	0.68	0.92
	0.04	3.53	0.35	0.19	0.36	0.70	2.42	12.10	0.68	0.92
	0.06	3.55	0.35	0.19	0.36	0.70	2.43	12.14	0.68	0.92
	0.08	3.56	0.35	0.19	0.37	0.70	2.44	12.17	0.69	0.93
	0.1	3.58	0.36	0.19	0.37	0.70	2.45	12.21	0.69	0.93
Liquid Stage 3 End										
	0.1	12.24	1.02	1.53	2.85	4.64	9.81	67.57	2.97	2.01

*Fraction factor.

Recalculated TUC melts for Fig. 2-17. Partitioning coefficients are as in the trace element modelling above.

Sample	**Lithology**	**Zr/Nb**	**Nb/Th**	**Th/Yb**	**Nb/Yb**
565466	*Amphibolite*	13.97	3.41	1.03	3.52
565464	*Amphibolite*	13.95	3.37	0.68	2.30
565467	*Anhydrous Ol-CPXite*	21.66	2.05	0.59	1.21
565451	*Anhydrous Ol-CPXite*	28.61	3.22	0.53	1.72
565469	*Hydrous Ol-CPXite*	18.10	2.33	0.93	2.16
565450	*Hydrous Ol-CPXite*	13.10	2.33	1.31	3.05
565452	*Dunite*	24.90	2.19	0.54	1.19
565470	*Dunite*	20.17	3.21	0.43	1.38
565472	*Dunite*	19.59	2.73	1.15	3.14
565471	*Dunite*	21.28	4.18	0.68	2.83
565455	*Altered Dunite*	31.68	3.25	0.60	1.94
565462	*Altered Dunite*	24.15	5.37	0.50	2.68
565453	*Altered Dunite*	5.60	10.91	0.17	1.81

Note: Melt is assumed to be 12%. The Ol:CPX ratio in the Ol-clinopyroxenites is assumed to be 25:75.

References:

Albarede, F. and Bottinga, Y. (1972). Kinetic disequilibrium in trace element partitioning between phenocrysts and host lava. *Geochim. Cosmochim. Acta*, 36, 156.

Bedard, J.H. (2005). Partitioning coefficients between olivine and silicat melts. *Lithos*, 83, 394-419.

Norman, M., Garcia, M. O., and Pietruszka A. J. (2005). Trace-element distribution coefficients for pyroxenes, plagioclase, and olivine in evolved tholeiites from the 1955 eruption of

Kilauea Volcano, Hawaii, and petrogenesis of differentiated rift-zone lavas. *American Mineralogist*, 90, 888-899.

Polat, A. and Hofmann, A.W. (2003). Alteration and geochemical patterns in the 3.7 – 3.8 Ga Isua greenstone belt, West Greenland. *Geochim. Cosmochim. Acta*, 126, 197-218.

Appendix 7: Fractional Crystallization Crustal Assimilation Pseudo Isochron Model

The model for fractional crystallization-crustal assimilation first calculates the relative increase in $^{187}Os/^{188}Os$ in the melt by the addition of a crustal assimilant. It is somewhat subjective to estimate the timing of initiation of fractional crystallization in the model. This is because realistically the precipitation of anomalously high abundances of Os rich minerals, such as chromite (Putchel et al., 2001; Arguin et al., 2016), may form at any point in the fractional crystallization process due variations in melt chemistry (cf. Splander et al., 2005). Were this to occur late in the crustal assimilation-fractional crystallization process, anomalously high and variable $^{187}Os/^{188}Os$ ratios at high Os contents should be produced if a significant amount of crustal assimilation has occurred. However, this is unlikely to have occurred in the TUC as high Os samples do not have significantly scattered $^{187}Os/^{188}Os$ ratios (Fig. 2-20). Thus, the model assumes that the samples with the highest Os contents formed earlier in the fractional crystallization sequence than those with lower Os contents. The highest Os sample in the TUC is anomalous, for this reason a lesser Os content in the hypothetical cumulates was used to estimate the initial starting point of fractional crystallization. For simplicity fractional crystallization initiates at 10 ppb Os in the hypothetical cumulates.

The model assumes that prior to fractional crystallization, the melt as 50% more Os than the basaltic assimilant. When fractional crystallization commences, Os in the melt is decreased via the fractional crystallization equation of Albarede and Bottinga (1972): $C_{liquid}=C_{initial}[1-F]^{D-1}$, where D is bulk distribution coefficient in the cumulates for Os, and F is the degree of fractional crystallization. Due to the evolved nature of the TUC cumulates relative to others in the area (e.g. Rollinson et al., 2002), the melt was modelled to have assimilated 0.2% crust prior to fractional crystallization.

The model follows the fractional crystallization sequence of the MELTS modelling in Section 2.5.3. Olivine and chromite are precipitated from the melt to a mass fraction of 0.28. The proportion of chromite in the cumulate was estimated by dividing the whole rock Cr concentration by that of the average Cr content of chromite in each dunite. The average chromite content was 2.6%. Following the formation of the dunite, chromite bearing clinopyroxenite was a precipitated to mass fraction of 0.15. Chromite content was estimated as in the dunite samples and averaged

1%. Partitioning coefficients used for chromite and olivine were 150 and 1.7, respectively (Putchel et al., 2001). Clinopyroxene was assumed to not be a significant host for Os (Righter et al., 2004).

Between the precipitation of 10 and 1 ppb Os cumulates, 0.4% crustal assimilation occurred in the melt and, in this interval, chromite bearing dunite was modelled to have precipitated. Between 1 and 0.1 ppb Os, another 0.4 % crustal assimilation occurred and chromite bearing CPXite was modelled to have precipitated. Finally, to produce the pseudo-isochrons Re was assumed to be 0.02 ppb, the average of the TUC cumulates. The decay constant used was 1.666e-11 (Selby et al., 2007). Initial of ^{187}Os/^{188}Os ratios for PUM were calculated at 3.8 Ga from the of ^{187}Os/^{188}Os ratios of Meisel et al. (2001) (0.1296) and the Re/Os ratio from Becker et al. (2006) (Calculated ^{187}Re/^{188}Os of 0.434).

References:

Albarede, F. and Bottinga, Y. (1972). Kinetic disequilibrium in trace element partitioning between phenocrysts and host lava. *Geochim. Cosmochim. Acta*, 36, 156.

Arguin J.P., Page P., Barnes S.J., Yu S.Y. and Song X.Y. (2016). The effect of chromite crystallization on the distribution of osmium, iridium, ruthenium and rhodium in picritic magmas: an example from the Emeishan Large Igneous Province, Southwestern China. J. *Petrology*, 57, 1019-1047.

Becker H., Horan M. F., Walker R. J., Gao S., Lorand J.P., and Rudnick, R.L. (2006). Highly siderophile element composition of the Earth's primitive upper mantle: constraints from new data on peridotite massifs and xenoliths. *Geochim. Cosmochim. Acta,* 70, 4528–4550.

Meisel, T., Walker, R.J., Irving, A.J., and Lorand, J.P. (2001). Osmium isotopic compositions of mantle xenoliths: a global perspective. *Geochim. Cosmochim. Acta*, 65, 1311-1323.

Putchel, I. and Humayun, M. (2001). Platinum group elements in Kostomuksha komatiites and basalts: Implications for oceanic crust recycling and core-mantle interaction. *Geochim. Cosmochim. Acta*, 64, 4227-4242.

Righter K., Campbell A. J., Humayun M. and Hervig R. L. (2004). Partitioning of Ru, Rh, Pd, Re, Ir, and Au between Cr-bearing spinel, olivine, pyroxene and silicate melts. *Geochim. Cosmochim. Acta*, 68, 867-880.

Rollinson, H., Appel, P.W.U., and Frei, R. (2002). A metamorphosed, early Archean chromitite from West Greenland: Implications for the genesis of Archean anorthositic chromitites. *J. Petrology*, 43, 2143-2170.

Selby, D., Creaser, R. A., Stein, H. J., Markey, R. J. & Hannah, J. L. (2007). Assessment of the 187Re decay constant by cross calibration of Re-Os molybdenite and U-Pb zircon chronometers in magmatic ore systems. *Geochim. Cosmochim. Acta*, 71, 1999-2013.

Spandler, C., Mavrogenes, J., & Arculus, R. (2005). Origin of chromitites in layered intrusions: Evidence from chromite-hosted melt inclusions from the Stillwater Complex. *Geological Society of America*, 33, 893-896.